THE ANGEL GAS FIELD,

NORTH WEST SHELF, AUSTRALIA:

AN INTEGRATED 3D SEISMIC AND PETROPHYSICAL STUDY

Sarah Ryan, B.Sc. (Hons)

National Centre for Petroleum Geology and Geophysics,
University of Adelaide,
Australia.

Submitted in fulfilment of the requirements
of the degree of Doctor of Philosophy,
University of Adelaide.

April 1996

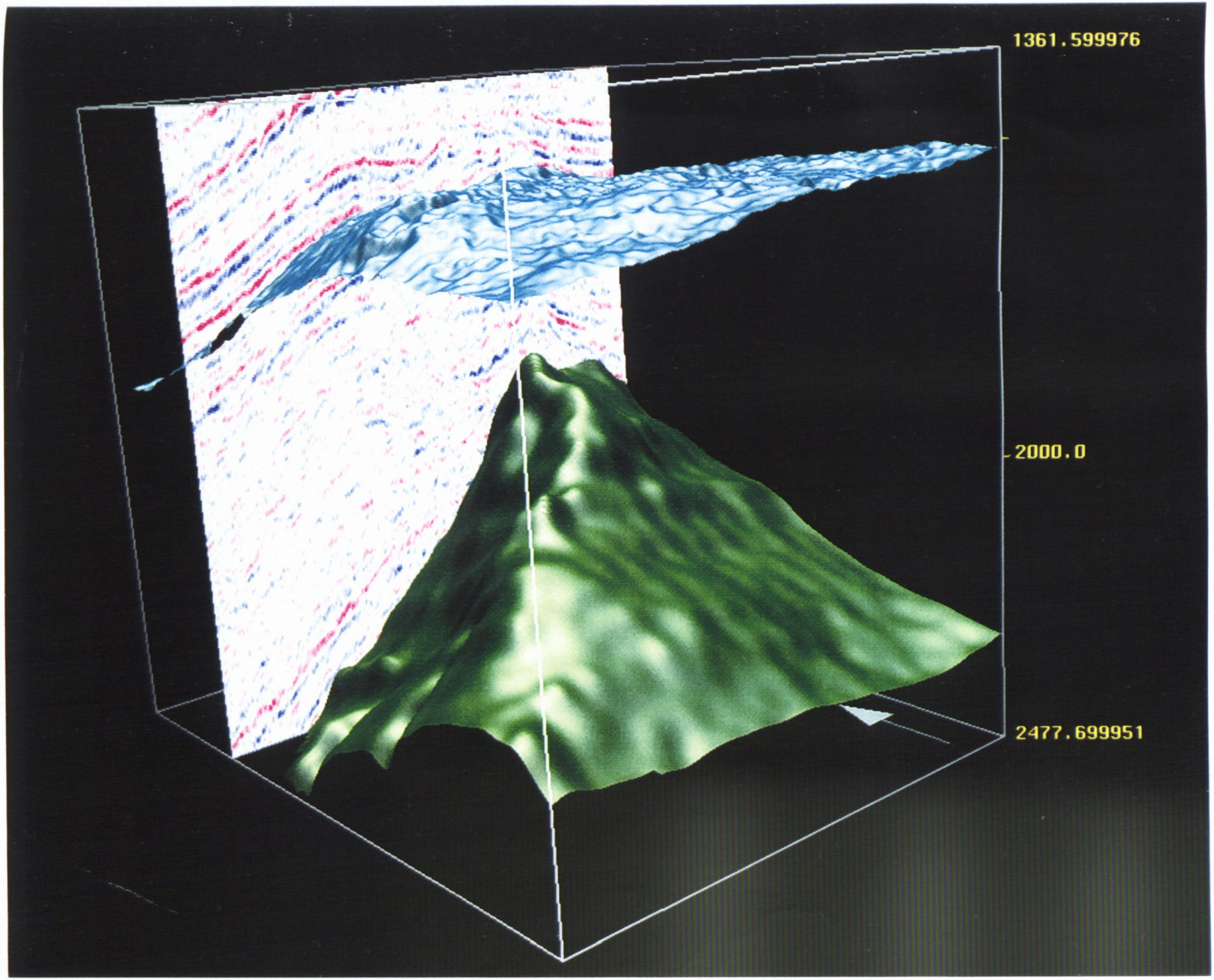
1361.599976
2000.0
2477.699951

This thesis is dedicated to Dr W. J. (Bill) Stuart,
Founding director of the National Centre for
Petroleum Geology and Geophysics.
(1939-1996)

Table of Contents

Reprint of: RYAN-GRIGOR, S., and SCHULZ-ROJAHN, J.P., 1995, Seismic delineation of structure-controlled carbonate cement and potential economic implications, Angel Field, North West Shelf. The APEA Journal, 35, 280-295.

List of Tables

List of Figures

Abstract

The Angel Gas Field on the North West Shelf, offshore Western Australia was studied by integrating a number of geological and geophysical disciplines. The aim of the study was to use all available information, primarily 3D seismic data, to describe and predict the geometry, petrophysical characteristics, and fluid content of the reservoir unit of the Angel Field. This integrated approach has also generated new ideas and methods such as recognition and mapping of massive dolomite-cemented zones in the sandstone from the 3D seismic data, and development of a model for the age and mode of formation of the dolomite cement in the sandstone from integration of 3D seismic mapping and carbon isotope and other petrographic data. It has focussed on the use of 3D seismic data, specifically analysis of the pre-stack gathers and the stacked data, to delineate the reservoir quality.

AVO analysis, using intercept-gradient crossplots, was a useful and robust method, especially when empirically calibrated to the well control via Biot-Gassman fluid replacement modelling, a new approach developed in this study. AVO analysis gave a good gas indicator, and a semi-quantitative porosity and V_{clay} indicator. The AVO gas response, as calculated by the R_p-R_s method, shows anomalies that are in accordance with the relative change predicted by theory. These anomalies coincide with the time closures at top reservoir level. It appears that in the study area the method provides a useful hydrocarbon indicator, except when the reservoir sandstone contains dolomite-cemented layers. The presence of dolomite-cemented zones severely reduces the usefulness of AVO analysis, by overwhelming any potential gas effect. The properties of the overlying shale also have a significant effect on the AVO response, with the potential to cause false gas anomalies. The extent of the dolomite-cemented zones of the Angel Formation was mapped from the 3D seismic data. The dolomite cement is interpreteted to occur only in the northern part of the field, in a roughly oval-shaped area along the crest of the structural trend. The dolomite cement formed in the Miocene, synchronous with hydrocarbon migration into the structure.

The Dampier Sub-basin appears to be underlain by a low-angle detachment fault which dips towards the west, and has a ramp-flat-ramp geometry. Extension and subsidence during the Triassic and Early Jurassic caused rotation and uplift of the Madeleine Trend, the narrow linear intra-basin high which underlies the Angel Field. Miocene-to-Present E-W compression caused right-lateral strike-slip movement along the Madeleine Trend, and the formation of the

faults that cut the reservoir interval. Only the NW-SE normal faults are likely to be open to fluid flow, while the three other fault sets recognised are likely to be closed. The main E-W fault zone in the Angel Field appears to be acting as a seal, as different hydrocarbon-water contacts are interpreted to the north and the south of the fault zone.

The Angel Formation was sub-divided into three units by integrating 3D seismic and palynological data. The seismic horizons that separate these layers are very close to time-synchronous in the study area. Each of the three units is interpreted to have been sourced from a different area, in contrast to the usual assumption that the Legendre Trend in the east was the major sediment source, by combining seismic reflection patterns with heavy mineral data. The Lower Unit was sourced from the south-west, probably from the Rankin Trend high via the Kendrew Terrace. The Middle Unit was sourced mostly from the north, with a minor contribution from the south. The northern source was probably local areas of uplift such as the DeGrey Nose and the uplifted fault blocks of the Beagle Sub-basin. The Upper Unit was sourced mostly from the southeast, probably from the Legendre Trend, with a small amount from the Rankin Trend.

The best reservoir quality (cleanest sandstone and highest porosity) in the Upper Unit is interpreted to occur along the Madeleine Trend, and the lowest quality within the Kendrew Terrace, to the north-west of the Angel Field. The dolomite cement in the Angel Formation drastically reduces porosity, and therefore also reservoir quality, in the northern portion of the field. Eleven time closures at Upper Unit level were studied using both the pre- and post-stack 3D seismic data. Ten of these showed an AVO gas anomaly, and the other was within the dolomite-cemented zone. The one gas anomaly that did not occur within a time closure, on the northern flank of the Angel Field, can be explained by offset-dependent tuning from an intra-formation reflector.

This example demonstrates the potential for integrated studies of known oil and gas fields, now that 3D seismic surveys of increasing quality and resolution are being routinely acquired over old acreage as basins become mature for petroleum exploration, and emphasis shifts to efficiency of development of known fields.

Statement of Authenticity and Availability

This thesis contains no material which has been accepted for the award of any other degree or diploma in any university and that, to the best of my knowledge and belief, the thesis contains no material previously published or written by another person, except where due reference is made in the text of the thesis. I consent to the thesis being made available for photocopying and loan if applicable if accepted for the award of the degree.

Sarah Ryan

Acknowledgments

This project was made possible by a University of Adelaide Faculty of Science PhD Scholarship. Woodside Offshore Petroleum Pty. Ltd. provided most of the data used in this study and provided four months in their offices in Perth, and I thank especially John Turner (now with Brown and Root), Larry Tilbury and Eleanor Witt for their help, also all in North West Shelf Development. Palynological data was supplied by Morgan Palaeo Associates, and digital log data was supplied by Wiltshire Geological Services. Danny Burns of the Schlumberger Geoquest office in Adelaide helpfully provided access to the Geoquest 3D visualisation software.

This study was done at the National Centre for Petroleum Geology and Geophysics in Adelaide, under the supervision of Mr Andy Mitchell, whom I thank for his untiring support and enthusiasm, and Professor Jim Applegate. Professor Tony Ryan, Mr Larry Tilbury, Dr Nick Lemon and Professor Cedric Griffiths read the manuscript and made helpful comments. I thank especially Dr Bill Stuart firstly for persuading me to come to the National Centre to do my Honours year, and for his care and concern over the years.

Finally but most importantly I thank my husband Darryl Grigor, and my family, for their support and encouragement.

1. INTRODUCTION

As petroleum provinces become mature, emphasis shifts from exploration to production, and from discovering new fields to ensuring optimal development of known fields. Efficient development requires a detailed knowledge of all aspects of the oil or gas field. This is best achieved by utilising all available data from geophysics, geology, petrophysics, and geochemistry in an integrated and cross-disciplinary study. The use of 3D seismic data is critical, due to its ability to accurately image and provide quantitative information about structure, reservoir continuity, and fluid content.

The aim of this study is to use all available information, primarily 3D seismic, to describe and predict the geometry, petrophysical characteristics, and fluid content of the reservoir unit of the Angel Gas Field, Dampier Sub-basin, offshore Western Australia.

Regional Geology

The Dampier Sub-basin is part of the greater Northern Carnarvon Basin, Australia's richest oil and gas province. The greater Northern Carnarvon Basin contains reserves of approximately 9.1 BBOE (billion barrels oil equivalent). The Dampier Sub-basin contains 1.1 BBOE, and the Angel Field contains 1700 BCF (billion cubic feet) of gas and 83 MMB (million barrels) of oil/condensate (367 MBOE in total) (Kopsen, 1994).

The Dampier Sub-basin forms part of the Westralian Superbasin, the major Permo-Carboniferous to Cretaceous basin system that bounds the west coast of Australia (Bradshaw et al., 1988). It is a sub-basin, together with the Barrow Sub-basin to the south, of the Carnarvon Basin (Fig 1). It is bounded by the Beagle Sub-basin to the north, the Exmouth Plateau to the west, and the Pilbara Craton to the east. It has been affected by at least five tectonic events since its initiation in the Permo-Carboniferous.

The western boundary of the Dampier Sub-basin, and the eastern margin of the Exmouth Plateau, is formed by the Rankin Fault System, a major fault system that extends over 500 km (Stagg and Colwell, 1994). The portion of the Exmouth Plateau immediately to the west of the Rankin Fault System is a structurally high area, known as the Rankin Trend. The Rankin Trend consists of tilted Triassic fault blocks, and contains the major gas/condensate fields of Goodwyn and North Rankin, and many smaller fields (Vincent and Tilbury, 1988). The

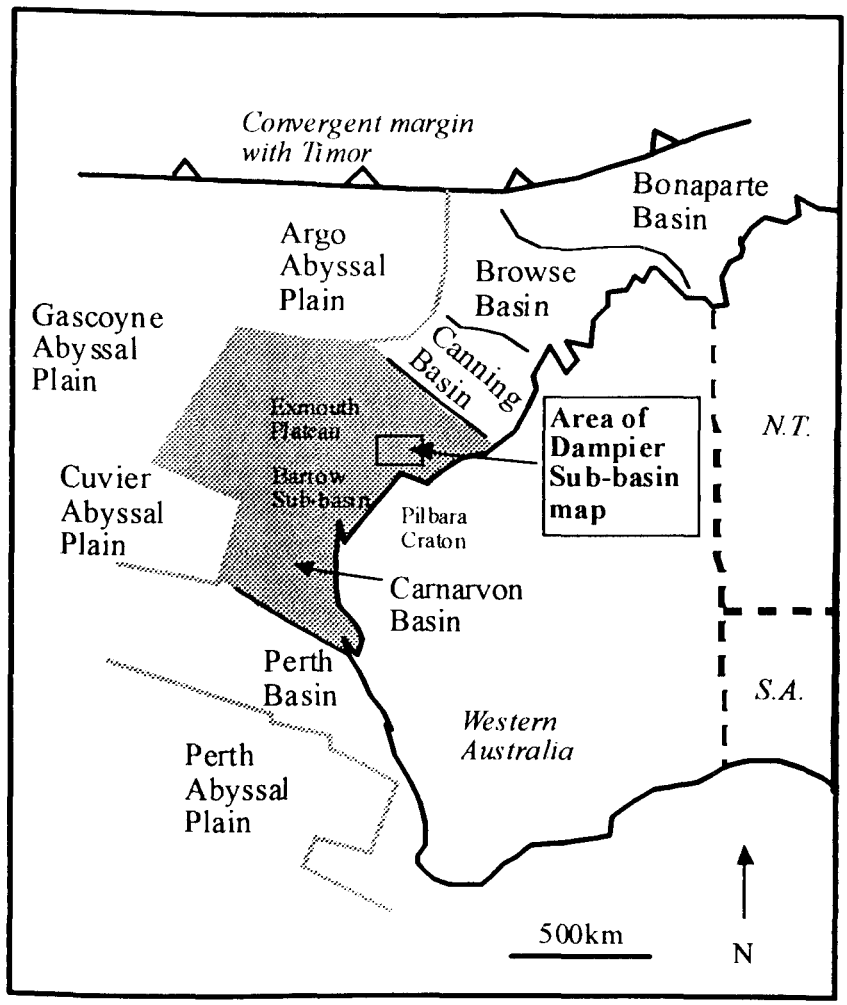

Figure 1(a). Map of western margin of Australia, showing the elements of the Westralian Superbasin, and the location of the Dampier Sub-basin.

Figure 1(b). Map of the Dampier Sub-basin, showing structural elements, selected wells and fields, and location of the study area. Line A-A' marks the location of the cross-section in Figure 2. Modified from Miller (1995).

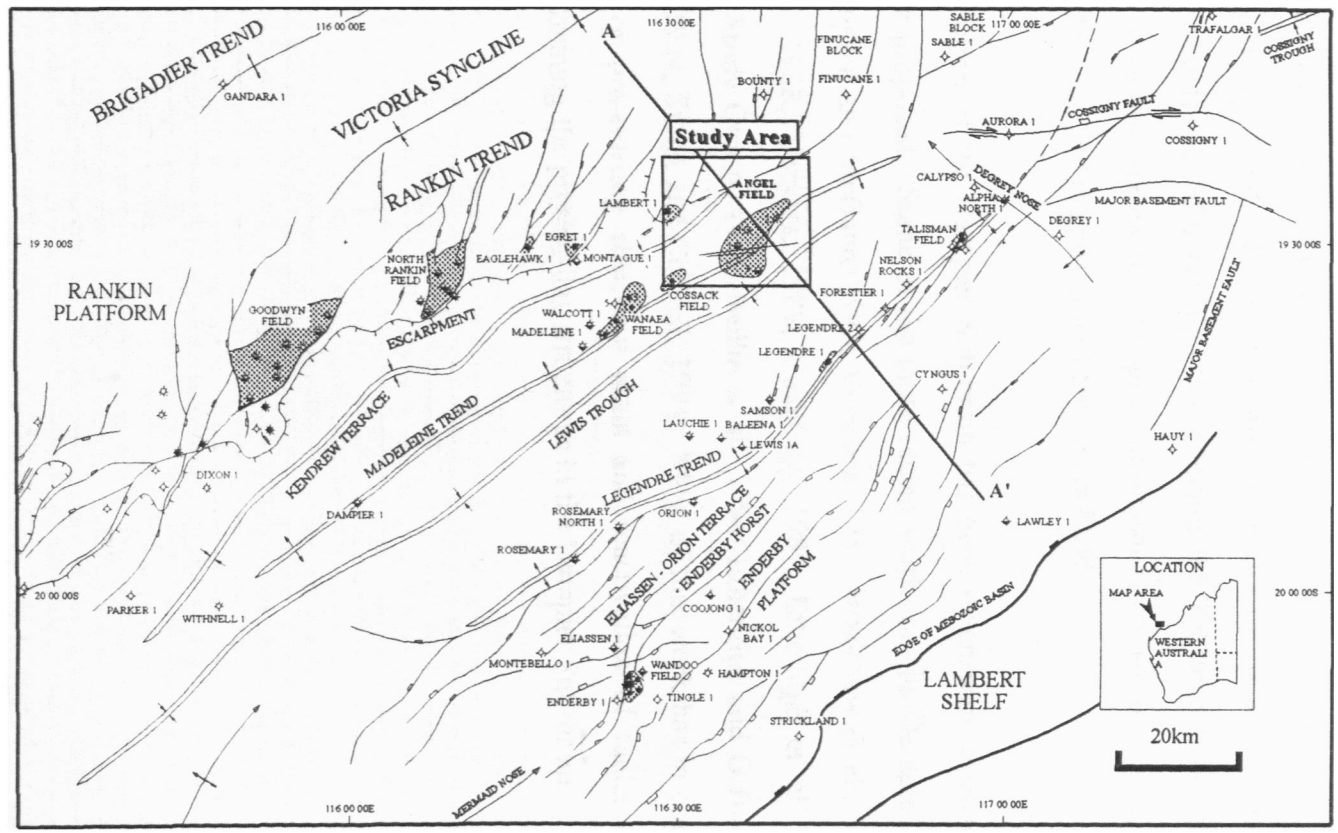
BRIGADIER TREND
VICTORIA SYNCLINE
RANKIN TREND
GANDARA 1
116 00 00E
116 30 00E
117 00 00E
A
A'
Study Area
BOUNTY 1
FINUCANE BLOCK
FINUCANE 1
SABLE BLOCK
SABLE 1
TRAFALGAR
COSSIGNY TROUGH
AURORA 1
COSSIGNY FAULT
COSSIGNY 1
CALYPSO 1
DEGREY NOSE
ALPHA NORTH 1
MAJOR BASEMENT FAULT
DEGREY 1
19 30 00S
ANGEL FIELD
LAMBERT 1
EGRET 1
MONTAGUE 1
EAGLEHAWK 1
NORTH RANKIN FIELD
TALISMAN FIELD
NELSON ROCKS 1
FORESTIER 1
COSSACK FIELD
WANAEA FIELD
WALCOTT 1
MADELEINE 1
LEGENDRE 2
LEGENDRE 1
CYNGUS 1
RANKIN PLATFORM
GOODWYN FIELD
ESCARPMENT
KENDREW TERRACE
MADELEINE TREND
LEWIS TROUGH
LAUCHIE 1
BALEENA 1
SAMSON 1
LEWIS 1A
HAUY 1
DIXON 1
LEGENDRE TREND
DAMPIER 1
ROSEMARY NORTH 1
ORION 1
LAWLEY 1
ROSEMARY 1
ELIASSEN - ORION TERRACE
ENDERBY HORST
ENDERBY PLATFORM
20 00 00S
PARKER 1
WITHNELL 1
COOJONG 1
NICKOL BAY 1
ELIASSEN 1
EDGE OF MESOZOIC BASIN
MONTEBELLO 1
WANDOO FIELD
HAMPTON 1
ENDERBY 1
TINGLE 1
STRICKLAND 1
LAMBERT SHELF
MERMAID NOSE
LOCATION
MAP AREA
WESTERN AUSTRALI
20km

structural development and exploration potential of the Rankin Trend is discussed by Stein (1994), and that of the Exmouth Plateau by Exon and Von Rad (1994).

To the east of the Rankin Trend, within the Dampier Sub-basin, is the Madeleine Trend. This is a narrow linear high that runs parallel to the Rankin Trend and hosts the Wanaea/Cossack Oil Fields and the Angel Gas Field. Between the Rankin Trend and the Madeleine Trend is the Kendrew Terrace, also called the Kendrew Trough. To the east of the Madeleine Trend is the Lewis Trough, the main depocentre in the Dampier Sub-basin. There is no major faulting within the Lewis Trough itself. The eastern margin of the Lewis Trough is the Legendre Trend, a narrow, heavily faulted linear high that contains the Talisman Oil Field (Vincent and Tilbury, 1988). A section across the Dampier Sub-basin is shown in Fig. 2, indicating the major structural elements and the position of the Angel Field.

The tectonic evolution of the Dampier Sub-basin has been extensively discussed, and many models have been proposed. Some of the more recent work on the Dampier Sub-basin and environs is in: Kopsen and McGann, 1985; Veenstra, 1985; Bradshaw et al., 1988; Hocking, 1988; Woodside, 1988; Veevers, 1988; Cockbain, 1989; Etheridge et al., 1991; AGSO Northwest Shelf Study Group, 1994; Baillie et al., 1994; Etheridge and O'Brien, 1994; Hill, 1994; Newman, 1994; Stagg and Colwell, 1994. Most of this work has in common the idea that inheritance of pre-existing structural grain and reactivation of faults has been very important in determining the present-day structures in the Dampier Sub-basin.

Figure 2. Section across the Dampier Sub-basin, showing structural elements and location of the Angel Field. Modified from Veenstra (1985).

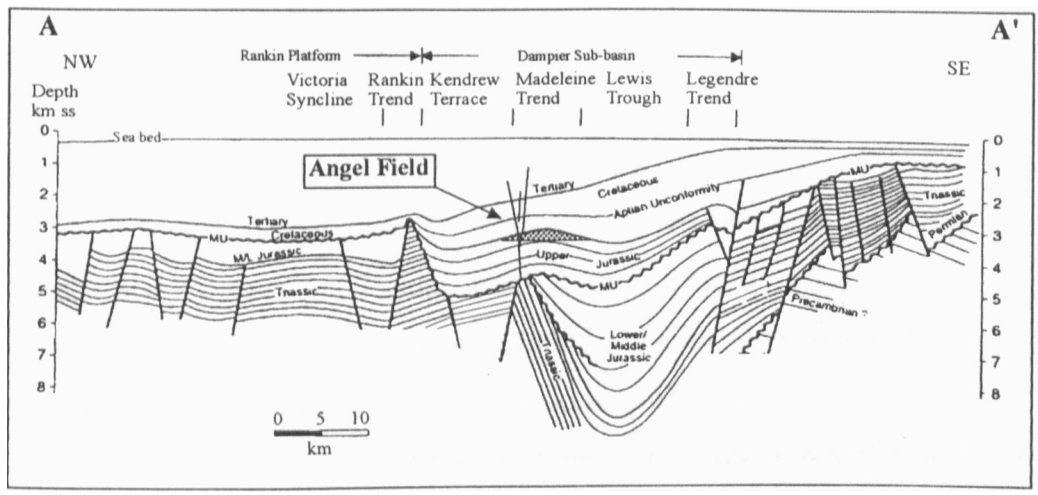
A
A'
NW
SE
Depth
km ss
Rankin Platform
Dampier Sub-basin
Victoria Syncline
Rankin Trend
Kendrew Terrace
Madeleine Trend
Lewis Trough
Legendre Trend
Sea bed
Angel Field
Tertiary
Cretaceous
MU
Upper Jurassic
Triassic
Aptian Unconformity
Lower/ Middle Jurassic
Precambrian ?
Permian
0 5 10
km

Petroleum Exploration on the Madeleine Trend

The first offshore well in the Dampier Sub-basin was Legendre-1 (Fig. 1b), drilled in 1968 by British Oil Co. of Australia Ltd., now Woodside Offshore Petroleum. It flowed 1014 BOPD from a 6.7m net pay sandstone (Vincent and Tilbury, 1988). Following this success on the Legendre Trend, the Madeleine Trend was tested with Madeleine-1 and Dampier-1 in 1969, and Angel-1 in 1972. Angel-1 was a gas discovery, with 82m gross pay and an estimated 1.7 TCF gas in place. Madeleine-1 was found to be off-structure, and in 1979 Walcott-1 was drilled to re-test the structure. Wanaea-1 (1989) and Cossack-1 (1990) discovered the Wanaea and Cossack Oil Fields, which have estimated combined recoverable reserves of approximately 264 MMBOE (Kopsen, 1994). The reservoir in the Madeleine Trend is Upper Jurassic sandstone sealed by Lower Cretaceous shales, and sourced from underlying Middle to Upper Jurassic shales (oil) or Triassic carbonaceous claystones and coals (gas). The closure is formed mostly by drape and differential compaction over an eroded fault crest, and partly by right-lateral transpression during the Miocene.

The Angel Field

The Angel Field lies in approximately 80m of water, in Production Licenses WA-3-L and WA-4-L, and was discovered in 1972 by Angel-1. It measures approximately 10km by 15km and contains an estimated 1.7 TCF gas in place. Three appraisal wells were drilled (Angel-2, 3, and 4) and confirmed major gas reserves at the same stratigraphic level, the sandstone of the Late Jurassic Angel Formation, which occurs at a depth of about 2700m subsea. Angel-3 tested gas at 13.6 MMscf/day with 704 bbls/day of condensate. The field has not been brought on line, and is currently suspended (Vincent and Tilbury, 1988). The reservoir is a massive sandstone approximately 200m thick with around 18% porosity, 700mD permeability, and a net-to-gross ratio of over 90%. The seal is the regional Early Cretaceous Barrow Group shales, and the source for the gas is thought to be the underlying Triassic carbonaceous claystones and coals (Woodside, 1988; Brikke, 1982). In 1992, Woodside Offshore Petroleum Pty Ltd and its Joint Venture partners acquired what was then the world's biggest marine 3D seismic survey, the East Dampier Survey. Part 5 of this survey (the study area, marked by a square in Figure 1b) covered Production Licenses WA-3-L and WA-4-L, an area of approximately 1600km^2.

Methods Used

The stacked volume and selected pre-stack gathers from Part 5 of the East Dampier survey were used in this study. The stacked data were interpreted, with particular attention to the reservoir interval, which was divided into three units. Various time, isochron, and attribute maps were prepared for the seismic horizons. These maps were examined for information on the depositional and structural history of the Angel Formation. The seismic character of each unit within the Angel Formation was analysed, and this gave information on the sediment transport direction in each unit. This was combined with a heavy mineral study (DiBona and Scott, 1990) to determine the source area(s) for each unit.

The effects of each of the five main tectonic episodes on the study area was determined. These ranged from mild synsedimentary movement to major basin-wide structuring. An amplitude analysis of the stacked 3D seismic data, using various techniques, including crossplots of amplitude versus two-way time, was conducted and showed the effect of gas, and also possibly oil, on the data. A similar technique was used to map the area in the field where the sandstone is almost completely cemented by dolomite. The origin and mode of emplacement of the dolomite cement was determined by integration of this work with petrography, X-ray diffraction (XRD), scanning electron microscopy (SEM), backscattered electron microprobe (BSE), and carbon and oxygen isotope data, which were conducted by Dr. Jorg Schulz-Rojahn, (Ryan-Grigor and Schulz-Rojahn, 1995 and Schulz-Rojahn et al., 1996).

The prestack gathers were analysed for amplitude variation with offset (AVO). The interpretation process used in this study was empirical and semi-quantitative. The presence of gas was determined by using the R_p-R_s method of Castagna and Smith (1994). This involved simply taking the average of the intercept and gradient pairs along selected inlines. The values were contoured and smoothed, to produce a map of R_p-R_s over the study area. Biot-Gassman modelling and Shuey's simplification of the Zoeppritz equations were used to predict the AVO response at Angel-4, under various conditions such as variable porosity, water saturation and so on. A new AVO analysis technique was developed, which calibrates the AVO response from the logs to the seismic data at the well location, and this empirical calibration was used to generate values of AVO-derived porosity and V_{clay}, which were then contoured over the study area to produce maps. The final step was to integrate all the information in order to produce a map of reservoir quality for the Angel Field, and also to predict the likelihood of hydrocarbons in the ten other time closures at reservoir level in the study area.

2. TECTONIC EVOLUTION OF THE DAMPIER SUB-BASIN

The most widespread and well-documented tectonic events will be outlined here, together with their effects on the Dampier Sub-basin. They are also summarised in Table 1. The effect of these tectonic events on the study area will be discussed later.

Age	Tectonic Event	Tectonic Stress	N W Shelf	Dampier Sub-basin	Angel area
Precambrian	Mobile rift surrounding Pilbara craton	N-NNW (Pinjarra) and W-WSW (Paterson Orogen)	Development of original tectonic grain	Intersection of orogen fabrics focussed structural weakness	
Carboniferous to Permian	Initiation of Westralian Superbasin	NW-SE extension	Initiated major basin structures	Initiated basin structures eg. Lewis Trough, Rankin Fault	Madeleine Fault initiated?
L. Triassic to E. Jurassic	Opening of Neo-Tethys and separation of Sibumasu	N-S compression (E-W extension)	Uplift and erosion on basin margins, left-lateral reactivation of faults	Lewis Trough deepens	Madeleine Trend formed as Lewis Trough deepens?
Mid-Late Jurassic (Callovian - Oxfordian)	Start of seafloor spreading in Argo Abyssal Plain	NNW extension	Uplift, then subsidence and normal faulting	Main Breakup Unconformity (MUC)	Main Breakup Unconformity (MUC), faulting in Kendrew Tce
L. Jurassic to E. Cret. (Tithonian)	Slowing of seafloor spreading in Argo Abyssal Plain	WNW extension	Uplift and erosion on basin margins, left-lateral reactivation of faults	Left-lateral reactivation of faults eg. Legendre Trend	Normal movement on Madeleine Fault during Tithonian
E. Cretaceous (Valanginian)	Start of seafloor spreading further south along margin, in Gascoyne, Perth Abyssal Plains	NW extension	Extension, regional unconformity formed (KV)	Unconformity (KV)	Unconformity (KV)
Miocene to present	North Australia - Melanesian Arc collision	E-W compression	Right-lateral reactivation of faults, uplift and erosion at basin margins	Right-lateral transpressional reactivation of Madeleine Fault	Formation of faults in reservoir

Table 1. Major tectonic events and their effect on the study area. Compiled from Powell, 1976; Veenstra, 1985; Kopsen and McGann, 1985; Bradshaw et al., 1988; Hocking, 1988; Woodside, 1988; Cockbain, 1989; Etheridge et al., 1991; AGSO, 1994; Baillie et al, 1994; Hill, 1994; Newman, 1994; Stagg and Colwell, 1994; Etheridge and O'Brien, 1994; Miller, 1995.

Precambrian

The Archaean Pilbara Craton forms the eastern boundary of the Westralian Superbasin. The Precambrian mobile belts that surround the Pilbara Craton, the Pilbara Orogen (oriented N to NNW) and the Pinjarra Orogen (oriented W to WSW) partially underlie the Westralian Superbasin. These ancient zones of weakness have probably influenced deformation in subsequent tectonic events (Veevers, 1984; Hill, 1994), and their intersection may have focussed structural weakness in the area of the Lewis Trough (Hill, 1994).

Carboniferous to Permian

The Westralian Superbasin was initiated by NW-SE extension, thought to be between 100% and 500%, in the Permo-Carboniferous (Etheridge and O'Brien, 1994). The extension was accommodated by detachment or delamination zones within the crust, and thinning in the lower crust, by a mechanism involving pure shear (AGSO, 1994). Most of the lower crust was removed below a mid-crust discontinuity, identified as the prominent C2 reflector (Stagg and Colwell, 1994). This tectonic event, the Alice Springs Orogeny, formed the major structures along the North West Shelf, such as the Barrow and Dampier Sub-basins, and major features within the Dampier Sub-basin such as the Rankin Trend and the Lewis Trough (Hill, 1994). These structures formed during development of a rift-valley system, which was followed by a Permo-Triassic sag phase. The major structural features of the North West Shelf are often separated by N to NNW trending features, such as the boundary between the Barrow and Dampier Sub-basins. The N to NNW grain is thought to have been inherited from Archaean N to NNW trends visible within the Pilbara and Kimberley cratons, and it determined the orientation of accommodation and transfer zones during Permo-Carboniferous extension (AGSO, 1994).

Late Triassic to Early Jurassic

An Australia-wide phase of tectonism, the Fitzroy Movement, was associated with the breakup and separation of the Sibumasu continental sliver from northwest Australia, and the initiation of NeoTethys (Veevers, 1988). This tectonism formed a rifted-arch system with block-faulting and uplift during the Late Triassic to Early Jurassic. The Fitzroy movement is considered by some workers on the Dampier Sub-basin to be N-S extensional (Veevers, 1984; Hill, 1994; Newman, 1994, Stagg and Colwell, 1994) and by others to be N-S compressional (Etheridge and O'Brien, 1994; Etheridge et al., 1991). The difference in interpretation hinges on whether the Lewis Trough is interpreted to have been caused by compression or extension. On the

scale of the western margin of Australia, there appears to be an element of E-W extension and also of N-S compression (AGSO, 1994) which acted to form a series of grabens and synclines along the coast and caused right-lateral shear in the Canning Basin (Veevers, 1984; Veevers, 1988).

Middle to Late Jurassic (Callovian to Oxfordian)

In the Middle to Late Jurassic, NNW extension occurred, associated with the breakup of Gondwanaland and the start of seafloor spreading along the western margin of Australia. Seafloor spreading was initiated in the Indian Ocean to the north in the Argo Abyssal Plain and spread southwards along the margin. The Callovian to Oxfordian tectonic pulse is associated with relative uplift followed by rapid subsidence in the troughs (eg. the Lewis Trough) and the formation of a regional unconformity which is mapped as the Main Breakup Unconformity (MUC) seismic horizon (Fig. 5).

Jurassic to Early Cretaceous (Tithonian)

In the latest Jurassic to Early Cretaceous, a further extensional tectonic pulse occurred, this time oriented WNW-ESE. This was due to a major plate reorganisation and change in seafloor spreading orientation (Etheridge and O'Brien, 1994), specifically the slowing of the seafloor spreading rate in the Argo Abyssal Plain (AGSO, 1994). The tectonic movement has been dated to the *P. iehiense* and *K. wisemaniae* palynological zones in the Vulcan Sub-basin (Etheridge and O'Brien, 1994). There is evidence of a basin-wide hiatus in the Dampier Sub-basin during the *K. wisemaniae* zone, with this interval missing in some wells (Kopsen and McGann, 1985; Hocking, 1992, Barber, 1994; Ross and Vail, 1994; Miller, 1995).

Early Cretaceous (Valanginian)

Extension during the Early Cretaceous, oriented NW-SE, was caused by the onset of seafloor spreading in the Gascoyne and Cuvier Abyssal Plains, west and south of the Exmouth Plateau. This resulted in subsidence and normal faulting, and the creation of the widespread intra-Valanginian unconformity (seismic horizon KV).

Tertiary

An open ramp shelf developed, with a large carbonate wedge, up to four kilometres thick, prograding north and west. A regional northwest tilt of the shelf began in the Cretaceous and continued throughout the Tertiary (Bradshaw et al., 1988; Baillie et al., 1994), caused by the

transition from a divergent to a convergent plate boundary, as the Australian plate started moving north towards the Eurasian plate (Veevers, 1988).

In the Miocene, a major E-W compressional event related to subduction of the Australian plate beneath the Banda Arc near Timor affected the entire western margin of the Australian continent (Baillie et al., 1994; Coblentz et al., 1995). By the Middle Miocene, the north-west Australian continental margin had collided with Indonesia, and by the Late Miocene, the Melanesian Arc was accreting onto the Papuan Basin, forming the Papuan Thrust Belt (Etheridge and O'Brien, 1994). The E-W compression is generally expressed as reactivation of older structures and faults, which had been repeatedly reactivated throughout the Mesozoic. The style of reactivation depends on the angle that the older faults make with the compressional vector. This reactivation is of great importance in the North West Shelf, as it has formed many of the hydrocarbon traps in the Barrow, Dampier, and Bonaparte Basins and the Timor Sea (Kopsen and McGann, 1985; Parry and Smith, 1988; Etheridge et al., 1991; Etheridge and O'Brien, 1994).

Effect of Beagle Sub-basin structure

The Beagle Sub-basin lies directly to the north of the Dampier Sub-basin and the study area, and is separated from the Dampier Sub-basin by several large-scale ENE-WSW faults, such as the Cossigny Fault, and by the De Grey Nose, a large ENE-WSW anticline. The structural grain of the Beagle Sub-basin is dominantly N-S, as compared to NE-SW in the Dampier Sub-basin (Fig 3). The structural development and exploration potential of the Beagle Sub-basin is discussed in more detail by Blevin et al. (1994).

In the northern part of the study area, the Madeleine Fault curves around from NE-SW to run N-S, in line with the Beagle Sub-basin structural grain. There may also be a continuation of the Cossigny Fault, or a smaller fault associated with it, running through the study area. Together, these structural elements indicate that the study area lies on the boundary between the Dampier and Beagle Sub-basins, and that the Angel Field is on the very northern edge of the Dampier Sub-basin and is consequently influenced by the structural grain of the Beagle Sub-basin.

Figure 3. Map of the northern Dampier Sub-basin and the southern Beagle Sub-basin, showing structural elements and the location of the study area at the boundary between the two basins. Modified from Lemon and Mahmood (1994).

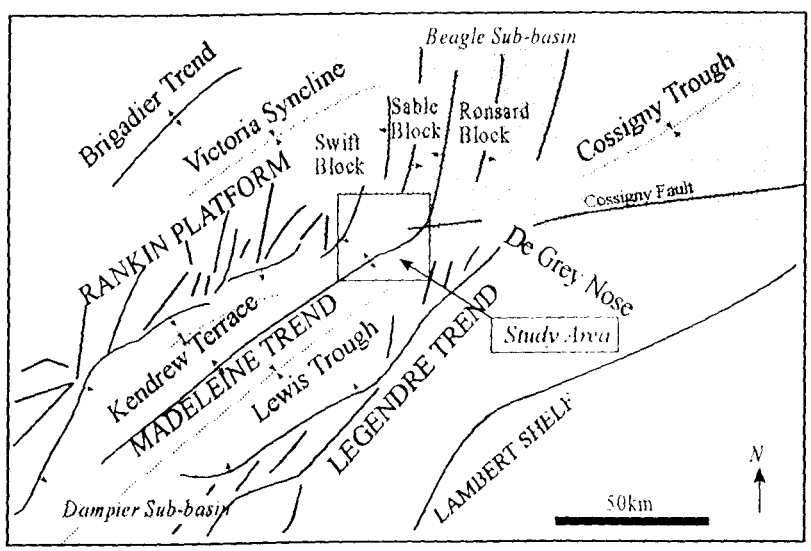
Beagle Sub-basin
Brigadier Trend
Victoria Syncline
Sable Block
Ronsard Block
Cossigny Trough
Swift Block
RANKIN PLATFORM
Cossigny Fault
De Grey Nose
Kendrew Terrace
MADELEINE TREND
Lewis Trough
Study Area
LEGENDRE TREND
LAMBERT SHELF
Dampier Sub-basin
50km
N

3. STRATIGRAPHY OF THE DAMPIER SUB-BASIN

The post-Carboniferous stratigraphic column for the Dampier Sub-basin is shown in Figure 4, and a detailed stratigraphic column for the study area during the Late Jurassic and early Cretaceous in shown in Figure 5. The local relative sealevel curve derived by Miller (1995) is used in this study (Fig. 5), unless otherwise specified. The relative age of rock units was determined using palynostratigraphical data from Morgan Palaeo Associates, which are available for most wells in the area. The palynostratigraphy of the North West Shelf is based on assemblages of dinoflagellate cysts (Helby et al., 1987) and is summarised in Ingram and Morgan (1988). Relative age dating using the dinoflagellate zones has been applied to several absolute time scales, causing errors in age of up to 13Ma at the Jurassic-Cretaceous boundary (Miller, 1985). Exact determination of the absolute age of each rock layer is not an aim of this study, so rock units will be referred to by their palynological zone name only.

Carboniferous to Permian

The oldest rocks in the Westralian Superbasin are Late Carboniferous to Permian. They rest unconformably on Precambrian or older rocks in the western Canning and Northern Carnarvon Basins. The lower part of the section consists of glacial siliciclastics (Lyons Group) and the upper section is a mixed siltstone/sandstone, which was deposited in a shallow marine environment (Kennedy Group, Byro Group). Deposition of these sediments was terminated by the Alice Springs orogeny, which caused uplift, faulting, and volcanism. (Cockbain, 1989; Woodside Offshore Petroleum, 1988; Kopsen and McGann, 1985; Bradshaw et al., 1988)

Triassic

The earliest Triassic sediment is the Scythian to early Carnian Locker Shale, a thick widespread claystone, which is overlain by the Ladinian to Rhaetian fluvial/deltaic interbedded shale, siltstone, coal, and sandstone of the Mungaroo Formation (Kopsen and McGann,1985; Bint and Helby, 1988). The Locker Shale is thought to be the source for the gas/condensate fields in the Rankin Trend, for instance Goodwyn and North Rankin (Brikke, 1982), and probably for the Angel and Lambert fields as well. Tilted fault blocks of the Mungaroo Formation are the reservoir for the fields along the Rankin Trend (Woodside, 1988). Triassic sedimentation was terminated by the Late Triassic to Early Jurassic tectonic event.

Figure 4. Stratigraphic column for the Barrow and Dampier Sub-basin, showing post-Carboniferous sediments.

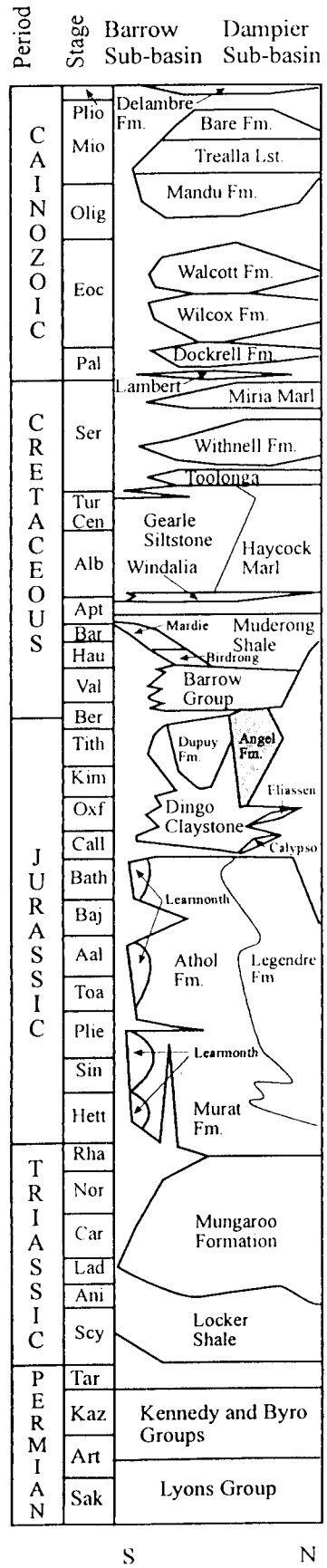
Period
Stage
Barrow Sub-basin
Dampier Sub-basin
CAINOZOIC
CRETACEOUS
JURASSIC
TRIASSIC
PERMIAN
Plio
Mio
Olig
Eoc
Pal
Ser
Tur
Cen
Alb
Apt
Bar
Hau
Val
Ber
Tith
Kim
Oxf
Call
Bath
Baj
Aal
Toa
Plie
Sin
Hett
Rha
Nor
Car
Lad
Ani
Scy
Tar
Kaz
Art
Sak
Delambre Fm.
Bare Fm.
Trealla Lst.
Mandu Fm.
Walcott Fm.
Wilcox Fm.
Dockrell Fm.
Lambert
Miria Marl
Withnell Fm.
Toolonga
Gearle Siltstone
Windalia
Haycock Marl
Mardie
Muderong Shale
Birdrong
Barrow Group
Dupuy Fm.
Angel Fm.
Fliassen
Dingo Claystone
Calypso
Learmonth
Athol Fm.
Legendre Fm
Learmonth
Murat Fm.
Mungaroo Formation
Locker Shale
Kennedy and Byro Groups
Lyons Group
S
N

Figure 5. Upper Jurassic and Lower Cretaceous stratigraphic column for the Dampier Sub-basin, with the seismic horizons used in this study, and the local sealevel curve from Miller (1995).

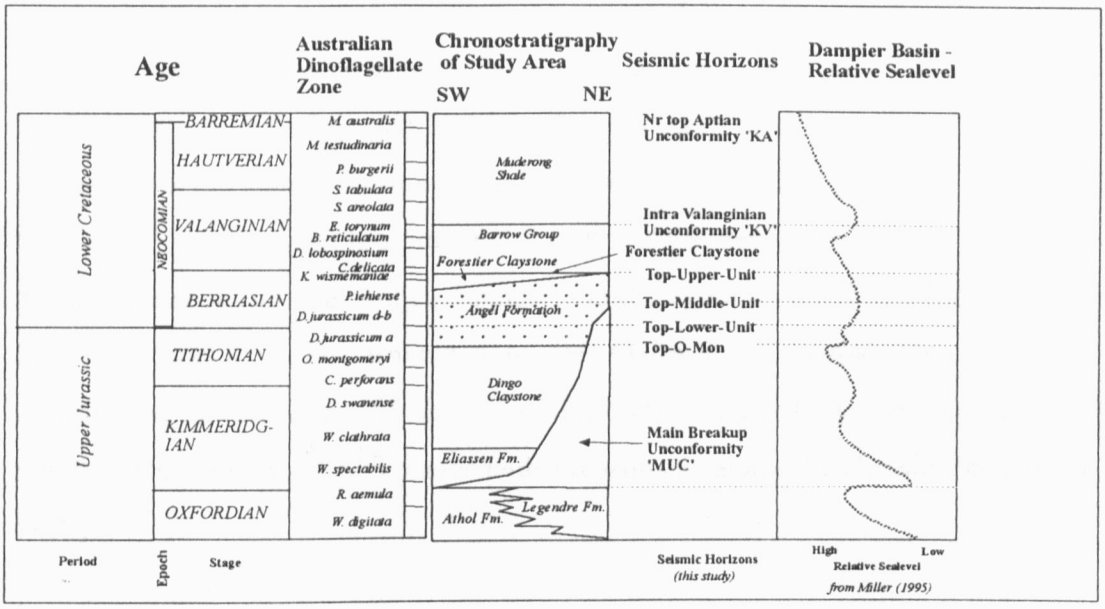
Age
Australian Dinoflagellate Zone
Chronostratigraphy of Study Area
SW
NE
Seismic Horizons
Dampier Basin - Relative Sealevel
Lower Cretaceous
Upper Jurassic
NEOCOMIAN
BARREMIAN
HAUTVERIAN
VALANGINIAN
BERRIASIAN
TITHONIAN
KIMMERIDG-IAN
OXFORDIAN
M. australis
M. testudinaria
P. burgerii
S. tabulata
S. areolata
E. torynum
B. reticulatum
D. lobospinosium
C. delicata
K. wismaniae
P. iehiense
D. jurassicum d-b
D. jurassicum a
O. montgomeryi
C. perforans
D. swanense
W. clathrata
W. spectabilis
R. aemula
W. digitata
Muderong Shale
Barrow Group
Forestier Claystone
Angel Formation
Dingo Claystone
Eliassen Fm.
Legendre Fm.
Athol Fm.
Nr top Aptian Unconformity 'KA'
Intra Valanginian Unconformity 'KV'
Forestier Claystone
Top-Upper-Unit
Top-Middle-Unit
Top-Lower-Unit
Top-O-Mon
Main Breakup Unconformity 'MUC'
High
Low
Relative Sealevel
Period
Epoch
Stage
Seismic Horizons (this study)
from Miller (1995)

Early to Middle Jurassic

The Early to Middle Jurassic section is dominated by Toarcian to Callovian siltstone of the Athol Formation, sometimes called Middle Dingo Claystone, with a restricted deltaic to delta-front unit, the mainly Bajocian Legendre Formation, in the northeast of the basin. The Athol Formation is the source for the oil in the Wanaea and Cossack Fields (DiToro, 1994). The Legendre Formation also has potential for oil and gas generation, and may have contributed to the hydrocarbons in the Angel, Lambert, and Legendre fields (Woodside, 1988). Middle Jurassic deposition was terminated by the Oxfordian-Callovian rifting event. Substantial erosion and development of secondary porosity occurred on the exposed Rankin Trend, together with formation of a major fault escarpment along the Rankin Fault (Bint and Helby, 1988).

Late Jurassic

The sediment that was deposited in the Dampier Sub-basin between the onset and the completion of the Callovian-Oxfordian rifting (*W. digitata* to *W. spectabilis* zones) consists of fine-grained clastics (Calypso Formation) and mass-flow sandstone (Eliasson Formation) (Hocking, 1992). The Calypso Formation is absent in the Angel and Talisman areas.

The shale and siltstone (*W. spectabilis* to *O. montgomeryi* zones) that overlies these sediments is named the Dingo Claystone (Hocking, 1992). In the northern Dampier Sub-basin, the Dingo Claystone is overlain by the Angel Formation, a Tithonian (*D. jurassicum* to *K.wisemaniae* zones) sequence that consists of massive sandstone with thin shale breaks. In the northern Dampier Sub-basin, sandstone deposition became dominant in the Tithonian when reactivation of the basin-bounding faults resulted in erosion and higher sand input from the edges of the basin (Hocking, 1988). By this time the Lewis Trough was full of sediment, and the Tithonian sand started spilling over the Madeleine Trend and filling up the Kendrew Terrace, which was the depocentre during all of the Tithonian (Miller, 1995). The Angel Formation is the reservoir for several fields in the Dampier Sub-basin (Angel, Wanaea, Cossack, Talisman, Dixon, Lambert, and Legendre) and will be discussed in more detail. In the southern Dampier sub-basin, the Angel Formation is absent, and Dingo Claystone deposition continued until the *K.wisemaniae* zone. Deposition of the Angel and Dingo Formations was terminated by the Late Jurassic/Early Cretaceous tectonic event.

Early Cretaceous

The Early Cretaceous rocks in the Dampier Sub-basin are dominantly siltstones and shales of the Barrow Group and Muderong Shale equivalents, and form the regional seal for the Dampier Sub-basin. The earliest shales were deposited in lows in pre-existing topography and later covered higher areas such as the Rankin Trend, as the sealevel rose during the major Valanginian transgression. Ryan-Grigor and Griffiths (1996) have suggested that the Early Cretaceous in the Dampier Sub-basin may be a potential source rock in the topographic lows, such as the Kendrew Terrace. Later the circulation changed from restricted to open marine. The Barrow Group, which in the Barrow Sub-basin contains the Mardie Greensand Member and the Birdrong Sandstone, amongst others, in the Dampier Sub-basin consists only of shale and siltstone, ranging in age from *C. delicata* to *E. torynum*. Overlying this, and separated by the intra-Valanginian Unconformity (seismic horizon KV) is the Muderong Shale, which ranges in age from *E. torynum* to *M. australis*. The Barrow Group equivalent in the Dampier Sub-basin is also sometimes referred to as the Forestier Claystone (Hocking, 1992). In this study, Forestier Claystone is used for the basinal shales deposited prior to the Barrow Group, as described by Thompson et al. (1990), which in the study area are mostly *K. wisemaniaea* in age.

Late Cretaceous

The Late Cretaceous marks the change from dominantly clastic to dominantly carbonate sedimentation. The pelagic Windalia Radiolarite (Aptian to Albian) was followed by fine-grained carbonates and marl (the Albian to Santonian Gearle Siltstone and correlative Haycock Marl), deposited in an outer-shelf to upper-slope marine environment. In the latest Cretaceous, the Campanian Toolonga Calcilutite and Maastrichtian Miria Marl were deposited in a passive margin environment with open ocean circulation.

Tertiary

The Tertiary section of the North West Shelf consists of four main sedimentary depsitional units, of mixed carbonates and clastics, which together make up a large prograding carbonate wedge. These units were described in detail by Apthorpe (1988) and will be summarised here, together with the nature of the breaks between them.

Unit 1A is the early Palaeocene Lambert Formation, a middle to outer shelf claystone and Unit 1B is the late Palaeocene Dockrell Formation and early to Middle Eocene Wilcox Formation, both outer shelf calcareous claystones. The boundary between units 1 and 2 is a Mid Eocene disconformity, caused by a change in water temperature and sediment type. It marks the change from predominantly clastic to predominantly carbonate sedimentation.

Unit 2 is Mid-Eocene to Early Oligocene in age, and consists of the Walcott Formation, a cherty calcilutite. It was deposited in a middle to outer shelf environment. There is evidence of mild tectonism and downwarping during the deposition of unit 2, which in the Angel area is expressed as tilting towards the west. The boundary between unit 2 and 3A is an Oligocene to Late Miocene global hiatus, caused by the retreat of the sea to the edge of the continental shelf (Bradshaw, 1988).

Unit 3A is Oligocene to Early Miocene, and consists of the Mandu Limestone, a 'large prograding wedge of unsorted sediment, consisting of quartz silt, molluscan and other bioclastic debris and middle to outer shelf foraminifera, in a matrix of calcareous silt, variably cemented by calcite' (Apthorpe, 1988). The boundary between units 3A and $3B_{LOWER}$ is an Early Miocene disconformity, and in places a submarine erosion surface, marked by an angular unconformity.

Unit $3B_{LOWER}$ is the Early Miocene to Late Miocene Trealla Limestone, an inner shelf marly limestone/calcarenite. The boundary between units $3B_{LOWER}$ and $3B_{UPPER}$ is a Late Miocene disconformity caused by a sealevel drop, and the subsequent deposition of unit $3B_{UPPER}$. Unit $3B_{UPPER}$ is the Late Miocene Bare Formation, an inner shelf/coastal sediment consisting of quartz sandstone and dolomites. The boundary between units $3B_{UPPER}$ and 4 is a Late Miocene to Pliocene unconformity caused by the large-scale downwarping and tilting due to the collision of the Australian Plate with Timor. Unit 4 is the Late Miocene to Pliocene Delambre Formation, which is made up of carbonates. It is not well known as it occurs above the depth at which samples are collected in the wells.

The Angel Formation

Definition and Subdivision

The Angel Formation was first proposed by Hocking (1985) as the Upper Jurassic sand-dominated sequence that consists of massive sandstone with thin shale breaks. This encompasses the *D. jurassicum* and *P. iehiense* palynological zones, except in Angel-1, where sandstone deposition continued into the *K. wisemaniae* zone. Hocking (1992) and Di Toro (1994) place the base of the Angel Formation at the boundary between the *D. jurassicum* and *O. montgomeryi* zones. The correlative Dupuy Formation in the Barrow Sub-basin has a similar age range (*O. montgomeryi* to *P. iehiense*). In this study, the Angel Formation has been sub-divided into three units: Lower, Middle, and Upper. The justification for this subdivision is discussed in Chapter 4. Briefly, the horizons within the Angel Formation were picked solely from the seismic data, and then correlated to the logs and the palynological data. The three units used in this study to subdivide the Angel Formation are 'genetic stratigraphic units' as defined by Galloway (1994). A genetic stratigraphic unit

'(1) is bounded by stratal surfaces that reflect major reorganisations in the array of depositional surfaces, and

(2) is a meaningful mappable unit that fosters interpretation of the depositional systems, their component facies and historical evolution. The practical application is prediction of the distribution of reservoir sand bodies and stratigraphic geometries that form traps.'

The relationship between these units and other published subdivisions of the Angel Formation (Hocking, 1992; Wulff, 1992; Barber, 1994; Miller, 1995) is shown in Figure 6, using Lambert-1 as an example. Figure 7 is a structural cross-section across the study area, showing the Angel Formation interval.

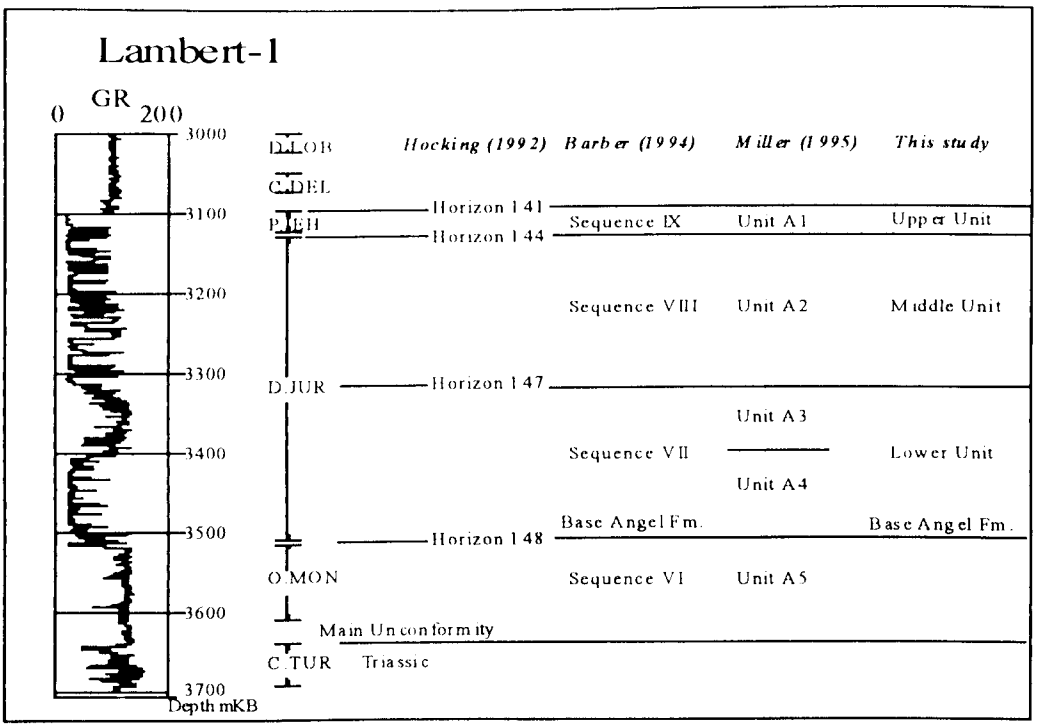

Figure 6. The subdivisions of the Angel Formation used in this study compared to the subdivisions used in previous studies, using Lambert-1 as an example.

The Lower Unit corresponds to the lower part of the *D. jurassicum* zone (sub-zone *a*), and Barber's (1994) sequence VII. The base of the Lower Unit (Horizon 148 of Hocking, 1992) is marked in the study area by a change from interbedded sandstone and shale to massive blocky sandstone with thin shale breaks (Fig. 6 and 7). It is thought (Hocking, 1992) that this horizon marks a tectonic pulse that triggered sand deposition. The top of the Lower Unit (Horizon 147 of Hocking, 1992) is the top of a small shaly interval, which may represent a period of low sand input. Miller (1995) defined the shaly interval as a separate unit (A3) but it must be noted that he could find no seismic evidence for this separate unit and therefore combined the units A3 and A4 in his interpretation, which corresponds to the Lower Unit used in this study.

Figure 7. Structural cross-section across the study area, showing the GR and smoothed acoustic impedance for each well, and the units of the Angel Formation.

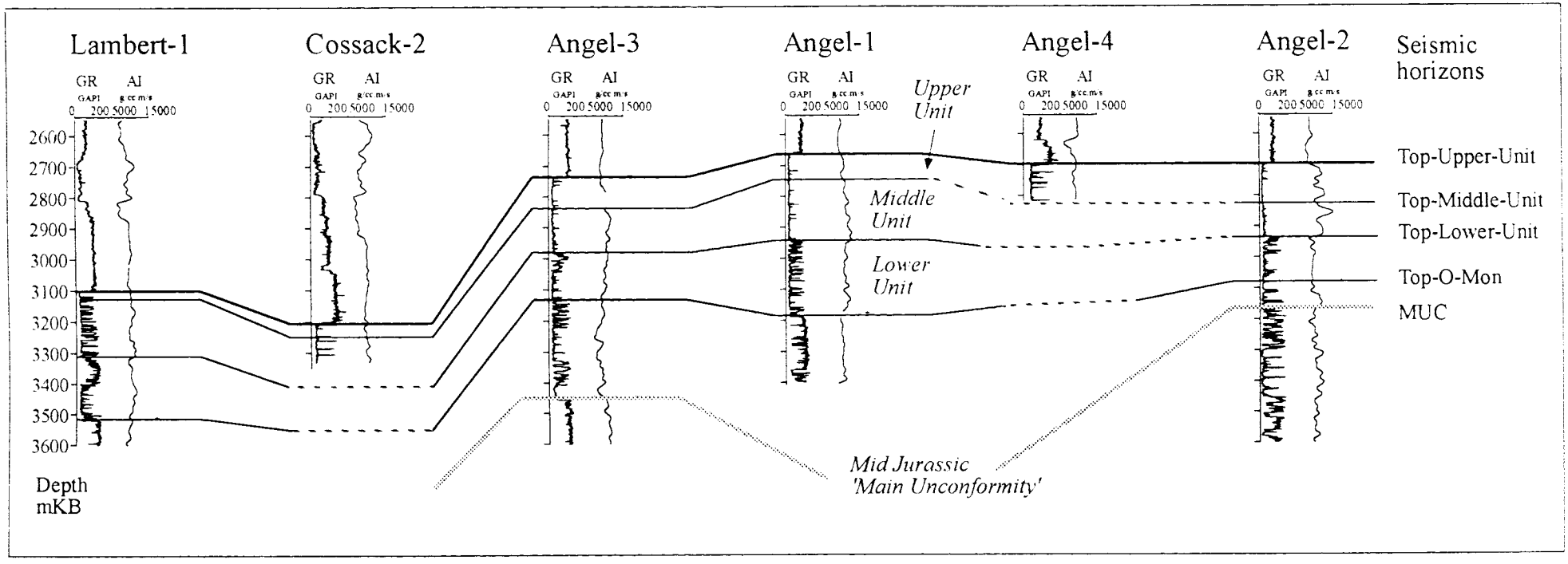
Lambert-1
Cossack-2
Angel-3
Angel-1
Angel-4
Angel-2
GR AI
GAPI g/cc m/s
0 200 5000 15000
2600
2700
2800
2900
3000
3100
3200
3300
3400
3500
3600
Depth
mKB
Upper
Unit
Middle
Unit
Lower
Unit
Mid Jurassic
'Main Unconformity'
Seismic
horizons
Top-Upper-Unit
Top-Middle-Unit
Top-Lower-Unit
Top-O-Mon
MUC

The Middle Unit consists of massive blocky sandstone with thin shale streaks, and corresponds to the upper part of the *D. jurassicum* (sub-zone *b-d*) and Barber's (1994) sequence VIII. The top of the Middle Unit is marked by a change from massflow sands (massive blocky sands) to transgressive silty sandstones above. This is seen throughout the northern Carnarvon Basin (Hocking, 1992).

The Upper Unit is the *P. iehiense* palynological zone and Barber's (1994) sequence IX. The top of the Upper Unit (Horizon 141 of Hocking, 1992) is marked by a hiatus which spans the *K. wisemaniae* zone in most wells, is present throughout the Barrow and Dampier Sub-basins, and has been ascribed variously to: Neocomian uplift (Kopsen and McGann, 1985), 'an event which changed depositional style, at least subtly, at the base of *K.Wisemaniae* rather than simple diachronous changes' (Hocking, 1992), a sealevel drop (Barber, 1994), and submarine erosion during a transgression (Miller, 1995).

Environment of Deposition

The Angel Formation was deposited as a sand-rich deep-water mass-flow submarine fan (Hocking, 1992; Miller, 1995) into the deep marine trough of the Dampier Sub-basin, which was closed to the northeast and open to the sea in the southwest (Hocking, 1992; Bradshaw,1988).

Miller (1995) studied the Late Jurassic depositional systems of the Dampier Sub-basin. His conclusions are paraphrased briefly here, as they give a more regional picture of the stratigraphic development of the Angel Formation.

> The Lewis Trough depocentre was non-existent during Angel Formation deposition, due to fill by previous sedimentation. The Lewis Trough was instead a ramp with a wide shallow-marine margin. During deposition of the Lower Unit (his units A3 and A4), slope aprons were present along the eastern margin of the Lewis Trough. The Angel and Montague areas are interpreted to contain depositional lobe sheet sands that are part of a wide-spread channel-lobe complex that formed in a basin with low submarine topographic relief. During deposition of the Middle Unit (Unit A2), the depositional systems present are interpreted to be characteristic of a ramp-style setting, with a relative fall in sealevel. The ramp is self-fed, eg the sediments deposited within the basin are from reworking of sediments from a shallow marine margin. The Angel area is interpreted to contain depositional lobe massive sands, and the Wanaea area to

have depositional lobe sheet sands. Depositional lobe massive sand is also interpreted at Finucane-1 and Bounty-1, which lie to the north, on the margin of the Beagle Sub-basin. The Upper Unit (A1) is interpreted to reflect a relative rise in sea level and waning sedimentation. Sand-rich systems such as this tend to pile sand up rather than transport it over great distances (Pickering et al., 1990). This results in depositional relief occurring where the sand concentration is highest, which in this case is in the Angel area, with rapidly decreasing sand content in more distal areas (Miller, 1995)

The Angel Formation in the study area has a net-to-gross ratio of over 90%, compared to approximately 60% in Cossack, 40% in Wanaea, and less than 30% in Madeleine, indicating that these fields are more distal from the sediment source. The Angel Formation in the Wanaea and Cossack Fields was deposited as laterally extensive sheet sands from high-density sandy turbidites (DiToro, 1994). The increase in number and thickness of intraformational shale beds indicates the possibility of intraformational seals.

The sandstones are dominantly massive with occasional faint bedding and common dewatering structures, such as dish structures (Woodside, 1988). The massive sandstones are classified as Facies B1.1 (Pickering et al., 1990), which is characteristic of rapid mass deposition and non-channelised decelerating flow, while the bedded sandstones (most common in Angel-4) are classified as Facies B2.1, which is characteristic of amalgamated channel and chute sands on a gradient.

Mineralogy and diagenesis

The Angel Formation in the study area is a glauconitic sub-arkosic sandstone. It is dominantly medium-grained, moderately well sorted, and well lithified. The quartz grains are sub-angular to sub-rounded. The mineralogy of the framework grains is: dominant monocrystalline igneous quartz; common detrital pelletal glauconite; minor orthoclase, microcline, feldspar, and chert; and trace muscovite, zircon, hornblende, ferromagnesian minerals, and sedimentary and volcanic rock fragments. The clay mineralogy is glauconite with minor authigenic kaolinite. The cement is predominantly authigenic quartz with pyrite, calcite, and non-ferroan dolomite. At Angel-2, poikilotopic ferroan dolomite is the dominant cement, together with anhydrite (Woodside, 1971, 1972, 1973, 1988, 1990d).

The diagenetic sequence consists of formation of early pyrite cement, followed by quartz overgrowths, feldspar dissolution, and formation of authigenic kaolin (Figure 8). The late diagenetic events are precipitation of dolomite cement and microfracturing, which occurred synchronously with oil staining, and this was followed by formation of anhydrite cement (Schluz-Rojahn et al., 1996).

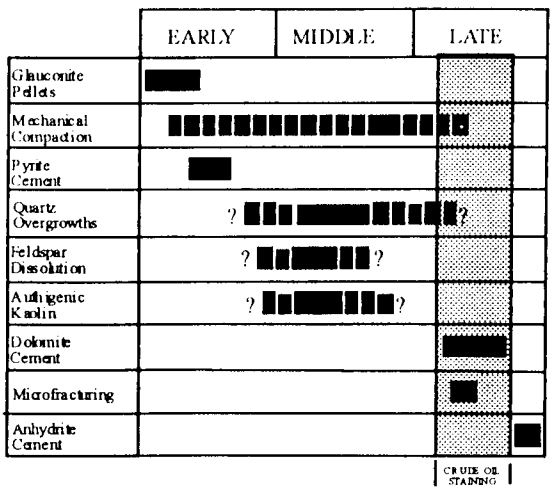

Figure 8. Diagenetic sequence of the Angel Formation in the Angel Field, from Schulz-Rojahn et al. (1996).

4. SEISMIC INTERPRETATION

Introduction

The study area was Part 5 of the East Dampier Marine 3D Seismic Survey, at the time of acquisition the world's largest 3D survey in terms of amount of data recorded with a total area of 2,746 km^2 (Vaughan, 1993). It was acquired in 1992 by Western Geophysical for Woodside Offshore Petroleum and its Joint Venture partners, using a triple-streamer, dual-source configuration, acquiring 6 CMP lines with 25m spacing per sail line. The area of Part 5 is approximately 1600 km^2, and covers the Production Licence areas WA-3-L and WA-4-L, in which lies the Angel Field (Fig 1b). The data acquisition parameters are listed in Table 2. The data were processed by Halliburton Geophysical Services, now part of Western Geophysical.

Streamer Config'n	Triple 320 trace, 100m separation
Source Config'n	Dual 1790 in^3 Airgun Array, 50m separation
Streamer Depth	9m
Source Depth	6m
Group Interval	12.5m
Shotpoint Interval	50m (25m alternating pops)
Nominal Fold	40
Sample Rate	2 msec
Record Length	6 seconds
Lo,Hicut Filter	2Hz/12dB per octave, 196Hz/214dB per octave
Array Type	Tapered array, centre weighted, 15.2m overall, 121% overlap of adjacent groups, 16 phones per group.
Data Polarity	Increase of acoustic impedance with depth gives a trough, and negative numbers on tape (SEG normal polarity).

Table 2 Acquisition parameters for Part 5 of the East Dampier 3D Marine Seismic Survey.

In the final 3D volume, the bin dimensions are 50mx25m. The processing sequence applied to this data is discussed in Chapter 9. The data have been migrated and converted to zero-phase. The conversion did not work properly, and the data is thus closer to minimum phase than zero phase, and was assumed to be minimum phase for interpretation. The survey has since been

reprocessed to zero-phase, but was not available in time for this study. The entire Part 5 volume was used in the poststack interpretation.

The data were interpreted at the NCPGG on a Sun Sparc 10 workstation using Western Geophysical's 3D seismic interpretation package AIS-3D. Also used was a Landmark workstation, and the Schlumberger Geoquest 3D seismic interpretation program IESX. Other programs used were ERMAPPER for horizon visualisation, and Schlumberger Geoquest's 3D visualisation program GEOVIZ, running on a Silicon Graphics Indigo 2 workstation.

Each horizon was interpreted on a regular grid of inlines and crosslines, typically every 32nd inline and every 16th crossline, giving a square grid of 800 m. If this was not sufficient to define the horizon, the grid was tightened to 16x8 where needed. The AIS-3D autotracking program 'Spacetrack' was then used to pick the horizon between the grid of seed lines. Certain horizons with variable character could not be Spacetracked, and a smoothed linear fill was used instead.

Fault Interpretation Methods

The major faults were picked on a 32 by 16 grid, ie on every 32nd inline and 16th crossline, and also on timeslices spaced at 100 ms intervals. To assist the fault mapping, selected horizons were loaded into the image analysis program ERMAPPER, where artificial illumination of the horizon from various directions and angles was used to illuminate features on the horizon such as small offsets caused by faults. This allowed subtle features to be mapped that were not seen in the vertical sections, and helped to determine fault orientation. The main faults in the Angel Field were individually picked and the fault planes were imported into the 3D visualisation program GEOVIZ. This enabled the geometrical relationship between the faults to be clearly seen in 3D, and greatly assisted in interpretation.

Well Ties

All six wells in the study area (Angel-1, 2, 3, 4, Cossack-2, Lambert-1) were used to tie the seismic data. The formation tops were picked from the composite logs in the Well Completion Reports, together with palynological data supplied by Morgan and Associates. All of the wells have velocity surveys, which appear to be of good quality, and were used to correct the sonic log. Synthetic seismograms were generated in Western Atlas' QUIKLOG program, using the sonic and density logs. These logs were first edited to remove bad hole effects, which commonly occur at washouts just below the casing shoe and in caving in the overpressured

Cretaceous shales. The borehole condition in the reservoir section was good to excellent. Bad hole was primarily determined from the caliper, and also from the density log itself, as it is a pad tool, and reads close to the mud density when the borehole wall is rugose. The density quality control curve DRHO is the best indicator of bad hole, but it was only available in the most recent wells.

Synthetic seismograms generated using a minimum-phase wavelet with a Ricker amplitude spectrum, a peak frequency of 35Hz, and displayed according to the SEG normal polarity convention (an increase of acoustic impedance with depth gives a trough for the leading half cycle of a minimum-phase wavelet) gave a good match over the zone of interest. The well ties are considered to be reliable, due to the simple overall lithology and the presence of several strong distinct reflections, which can be confidently correlated with the seismic data.

Interpreted Horizons

Thirteen horizons were interpreted in the study area. Their names, ages, seismic response and interpretation methods used are detailed in Table 3. The nomenclature for the horizons is based on that used internally by Woodside Offshore Petroleum Pty Ltd. All of the horizons except the two intra-Angel Formation horizons Top-Middle-Unit and Top-Lower-Unit were picked from the synthetic seismograms at the well locations. Eight of these horizons were chosen for detailed study, and are discussed below. The remaining five horizons in the Late Cretaceous to Pliocene overburden were picked to aid the interpretation process, and were not studied in detail. These are included in Table 3 for completeness. The horizon picks at the well locations are listed in Table 4.

Horizon Name	Age	Horizon Character	Angular Relationships	Picking Method	Confidence in Picks
MUC	Callovian to Oxfordian	Very variable	Erosional terminations below, onlaps above	Linear Fill	High
Top-O-Mon	Tithonian	Moderately strong and continuous peak	Conformable below, onlaps and downlaps above	Spacetrack	High
Top-Lower-Unit	Tithonian	Mostly weak trough, sometimes weak peak.	Low-angle terminations below, onlaps and downlaps above	Linear Fill	Med (flanks)-Low (crest)
Top-Middle-Unit	Tithonian	Mostly weak trough, sometimes weak peak.	Low-angle terminations below, onlaps and downlaps above	Linear Fill	Med (flanks)-Low (crest)
Top-Upper-Unit	Latest Jurassic to Earliest Cretaceous	Weak to moderate, variable	Low-angle terminations below, onlaps above.	Linear Fill	Med (flanks)-Low (crest)
Top-FC	Earliest Cretaceous	Variable to strong trough in Nth.	Low angle onlap above	Linear Fill	Med (flanks)-Low (crest)
KV	Valanginian	medium to weak trough, weak peak on crest.	Low-angle angular terminations below and onlaps above, conformable in basin	Spacetrack/ Linear Fill	High
KA	Nr Top Aptian	Strong to weak peak	Low-angle angular teminations below and onlaps above, conformable in basin	Spacetrack	High
TE	Middle Eocene	Strong to moderate peak	Conformable	Spacetrack	High
TO	Oligocene to late Miocene	Moderate to weak peak	Erosional terminations below and onlaps above	Spacetrack	High
TME	Early Miocene	Moderate to weak peak	Erosional terminations below and downlaps above	Spacetrack/ Linear Fill	High
TML1	Late Miocene	Variable	Erosional terminations below and onlaps above	Linear Fill	High
TML2	Late Miocene to Pliocene	Variable	Onlap above, erosional terminations below	Linear Fill	High

Table 3. Description of seismic horizons used in this study. The name, age, seismic character, angular relationships, method of picking used, and confidence in the picks are listed for each horizon.

Horizon	Angel-1 (msecs)	Angel-2 (msecs)	Angel-3 (msecs)	Angel-4 (msecs)	Cossack-2 (msecs)	Lambert-1 (msecs)
TML2	238	266	213	264	328	448
TML1	335	364	274	348	368	460
TME	442	475	372	458	480	662
TO	638	682	565	674	772	868
TE	1030	1070	940	1054	1150	1350
KA	1537	1553	1519	1553	1654	1854
KV	1625	1647	1618	1634	1740	1892
Top-FC	1737	1762	1720	1752	1854	2058
Top-Upper-Unit	1737	1762	1772	1752	1854	2058
Top-Middle-Unit	1795	1793	1820	(1804)	1880	2072
Top-Lower-Unit	1860	1866	1884	(1868)	(1990)	2170
Top-O-Mon	1975	1917	1942	(1973)	(2068)	2242
MUC	(2242)	1934	(2158)	(2215)	(2296)	2290

Table 4. Horizon picks at the well locations in msecs. Brackets indicate that the well did not penetrate the horizon.

The oldest horizon mapped is the Mid Jurassic Main Break-up Unconformity (MUC), which is the extensional event associated with the separation of Australia during the breakup of Gondwana. This was picked because it represents the palaeotopography on which the post-breakup sediment was deposited. Two events were picked within the Angel Formation: Top-Lower-Unit and Top-Middle-Unit. The Angel Formation has not been seismically mapped in detail before, so the intra-formation reflections had not been previously described. The reflections were chosen by extracting an arbitrary line that runs through all wells in the study area, and examining the seismic data within the Angel Formation on this line. No palynological or other data were used to pick the two intra-Angel Formation reflections, only the character of the seismic data. The reflections are not very strong events in places, but they are mappable over the entire study area and are often indicated by termination of the overlying and/or underlying reflections.

It was found when matching the seismic data to the synthetic seismograms that the Top-O-Mon, Top-Lower-Unit horizon, and Top-Upper-Unit horizons also corresponded to palynological boundaries. The Top-Middle-Unit horizon appears to slightly cross-cut palynological boundaries. This implies that most seismic horizons represent time boundaries in the Angel Formation in the study area. Miller (1995) found that the Jurassic and Cretaceous

seismic horizons are time synchronous on the scale of the northern Dampier Sub-basin. Vail et al. (1977) first suggested that seismic reflections (stratal surfaces and unconformities) were approximately time-synchronous, to within +/- 1/2 cycle accuracy. Stratal surfaces represent periods of non-deposition or change in the depositional sequence, and are differentiated from unconformities by their smaller time breaks and lack of erosion. Each seismic layer bounded by stratal surfaces is a separate depositional sequence with a particular geological history (Vail et al., 1977).

The four Late Jurassic reflections mapped in the study area represent stratal horizons which divide the Angel Formation into three discrete units, the Upper, Middle and Lower Units. Figure 9 shows portions of the seismic data along an arbitrary line that runs through all of the wells in the study area, and the interpreted Angel Formation horizons near each well location, together with the GR, smoothed acoustic impedance and palynological zones for each well. Figure 9(d) shows the entire arbitrary line that runs through all of the wells in the study area, together with the Cretaceous and Jurassic horizons used in this study. The Upper Unit consists of the *P. iehiense* zone, the Middle Unit of the upper *D. jurassicum* zone, and the Lower Unit of the lower *D. jurassicum* zone. The correspondence of the palynological boundaries to the seismic horizons is within the 1/2 cycle error specified by Vail et al. (1977), except in Angel-2, where the high-amplitude reflections from the dolomite-cemented layers (visible on the acoustic impedance log) may have swamped the lower-amplitude Top-Middle-Unit horizon. There are no palynological data available for Angel-4, but the seismic interpretation indicates that the Angel Formation intersected in this well is probably part of the Upper Unit. The Upper Unit appears to start earlier (in the late upper *D. jurassicum* zone) in the north of the field (at Angel-2), and becomes progressively younger towards the south. This could be due to a mispick of the seismic horizon, or evidence that the deposition of the Upper Unit started in the north and moved southwards with time.

The KV horizon is an Early Cretaceous unconformity separating the Barrow Group from the overlying Muderong Shale. The KA horizon is the boundary between the Muderong Shale and the overlying Windalia Radiolarite. Both the KV and KA events are moderate to strong regional reflectors, and are approximately conformable with the Top-Upper-Unit. Five horizons were picked in the Tertiary carbonate wedge. The earliest is the Eocene TE horizon, and the other four (TO, TME, TML1, and TML2) are Oligocene to Late Miocene/Pliocene in age.

Data Quality

Seismic event continuity and strength are good to excellent in the Rankin Trend and Lewis Trough, and deteriorate over the Madeleine Trend. The quality of the events is fair to very poor over the Angel Field, in contrast to fields further south, such as Goodwyn and Wanaea-Cossack, where most of the horizons are strong continuous events. The decrease in data quality along the structural high is attributed to faulting, which is concentrated on the structural high.

The Tertiary and Cretaceous horizons (TML2, TML1, TME, TO, TE, KA, KV) are considered to be of good quality with high confidence, grading to fair at the crest of the field. The Late Jurassic horizons (Top-FC, Top-Upper-Unit, Top-Middle-Unit, Top-Lower-Unit) are of fair quality, grading to poor along the crest of the field, even with the well control. The reasons for the particular difficulties encountered in mapping the Top-Upper-Unit horizon are discussed later. Top-O-Mon and MUC are of good quality, grading to fair at the crest of the field.

Figure 9(a) Arbitrary line through the 3D seismic data volume through wells Angel-1, Angel-4 and Angel-2, together with interpreted seismic horizons, overlain by the GR, smoothed acoustic impedance and palynological zones at each well. Note that the Top-Upper-Unit seismic horizon coincides with the top of the *P. iehiense* palynological zone, the Top-Middle-Unit horizon with the uppermost *D. jurassicum* zone, the Top-Lower-Unit with the lower *D. jurassicum* zone, and the Top-O-Mon horizon with the top of the *O. montgomeryi* palynological zone.

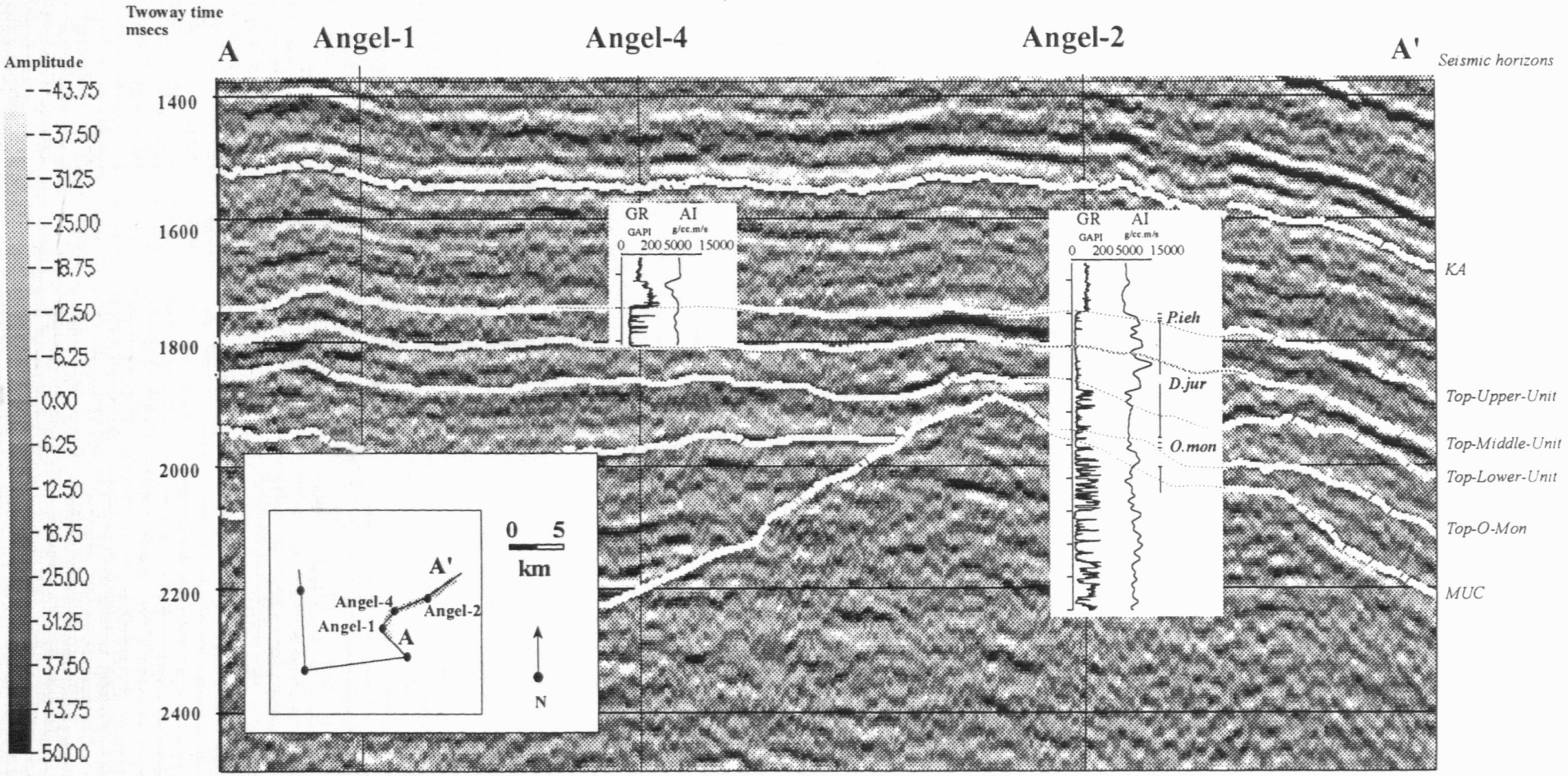
Twoway time
msecs
Amplitude
-43.75
-37.50
-31.25
-25.00
-18.75
-12.50
-6.25
0.00
6.25
12.50
18.75
25.00
31.25
37.50
43.75
50.00
A
Angel-1
Angel-4
Angel-2
A'
Seismic horizons
1400
1600
1800
2000
2200
2400
GR AI
GAPI g/cc.m/s
0 200 5000 15000
KA
P.ieh
D.jur
O.mon
Top-Upper-Unit
Top-Middle-Unit
Top-Lower-Unit
Top-O-Mon
MUC
0 5
km
N

Figure 9(b) Arbitrary line through the 3D seismic data volume through wells Angel-3, and Angel-1, together with interpreted seismic horizons, overlain by the GR, smoothed acoustic impedance and palynological zones at each well. Note that the Top-Upper-Unit seismic horizon coincides with the top of the *P. iehiense* palynological zone, the Top-Middle-Unit horizon with the uppermost *D. jurassicum* zone, the Top-Lower-Unit with the lower *D. jurassicum* zone, and the Top-O-Mon horizon with the top of the *O. montgomeryi* palynological zone.

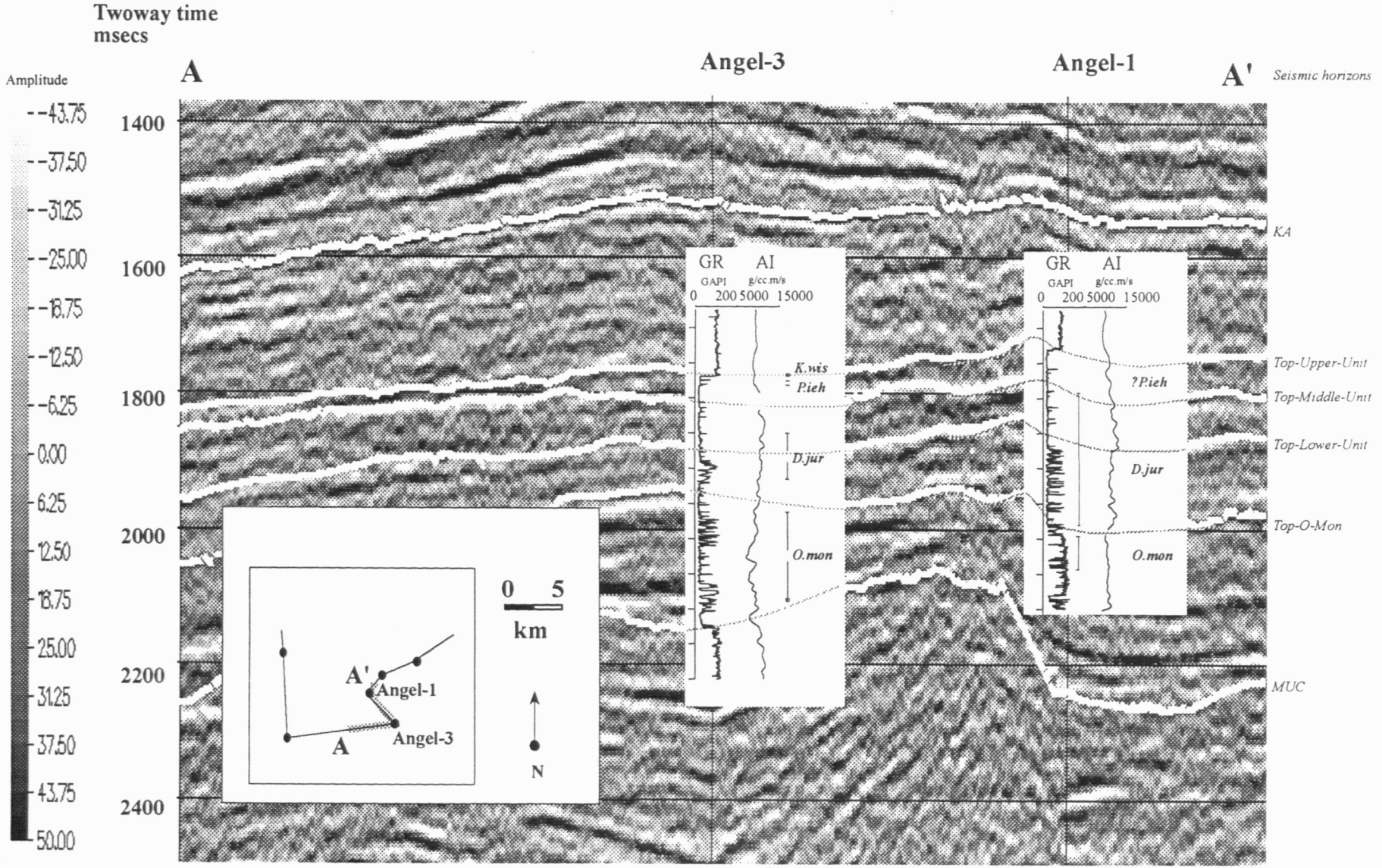
Twoway time
msecs
Amplitude
--43.75
--37.50
--31.25
--25.00
--18.75
--12.50
--6.25
0.00
6.25
12.50
18.75
25.00
31.25
37.50
43.75
50.00
1400
1600
1800
2000
2200
2400
A
Angel-3
Angel-1
A'
Seismic horizons
KA
Top-Upper-Unit
Top-Middle-Unit
Top-Lower-Unit
Top-O-Mon
MUC
GR AI
GAPI g/cc.m/s
0 200 5000 15000
K.mis
P.ieh
D.jur
O.mon
?P.ieh
D.jur
O.mon
0 5
km
A'
Angel-1
A
Angel-3
N

Figure 9(c) Arbitrary line through the 3D seismic data volume through wells Lambert-1 and Cossack-2, together with interpreted seismic horizons, overlain by the GR, smoothed acoustic impedance and palynological zones at each well. Note that the Top-Upper-Unit seismic horizon coincides with the top of the *P. iehiense* palynological zone, the Top-Middle-Unit horizon with the uppermost *D. jurassicum* zone, the Top-Lower-Unit with the lower *D. jurassicum* zone, and the Top-O-Mon horizon with the top of the *O. montgomeryi* palynological zone.

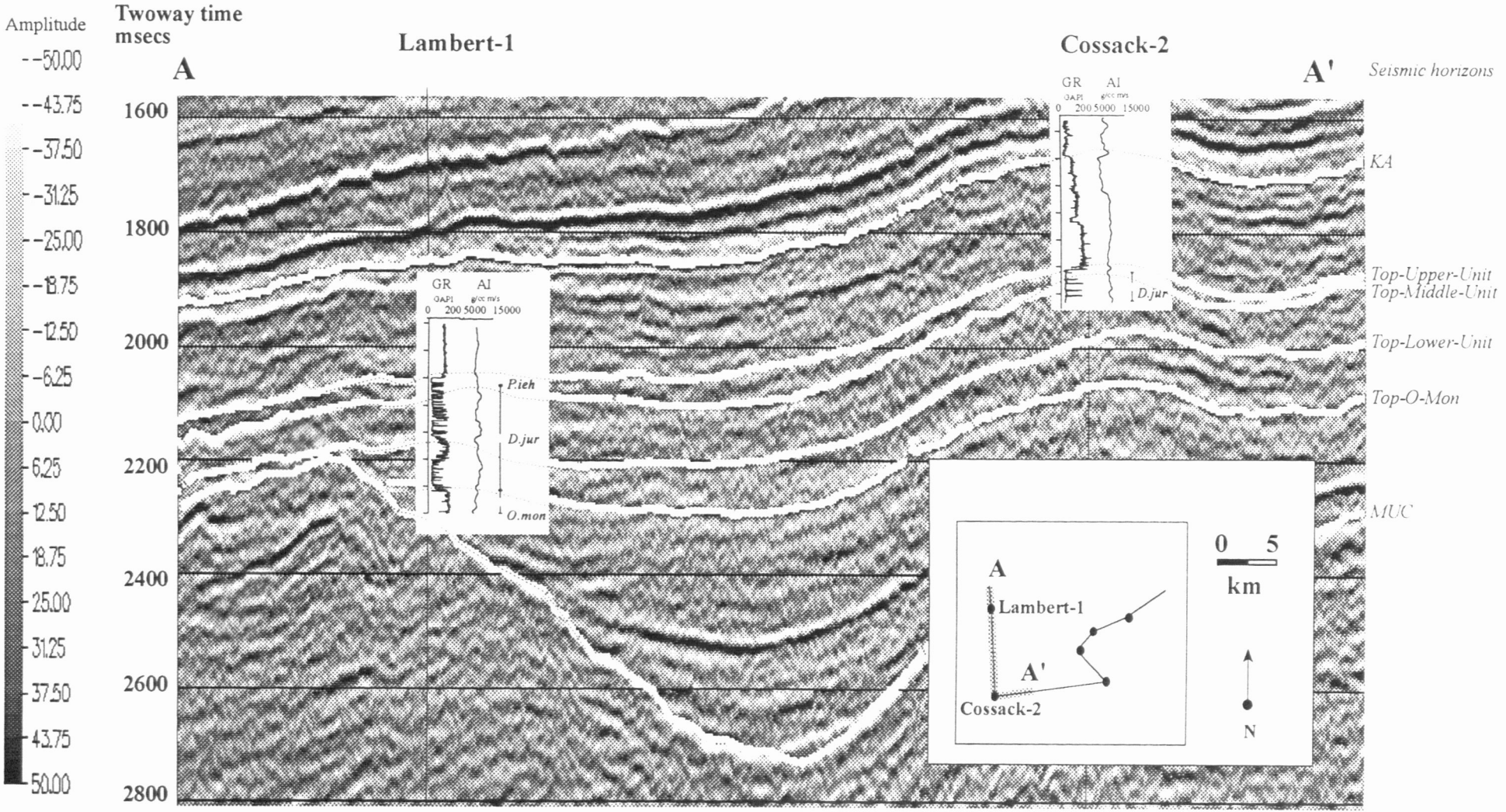
Amplitude
-50.00
-43.75
-37.50
-31.25
-25.00
-18.75
-12.50
-6.25
0.00
6.25
12.50
18.75
25.00
31.25
37.50
43.75
50.00
Twoway time
msecs
1600
1800
2000
2200
2400
2600
2800
A
A'
Lambert-1
Cossack-2
GR AI
GAPI g/cc m/s
0 200 5000 15000
P.ieh
D.jur
O.mon
Seismic horizons
KA
Top-Upper-Unit
Top-Middle-Unit
Top-Lower-Unit
Top-O-Mon
MUC
0 5
km
N

Figure 9(d). The entire arbitrary line through all the wells in the study area shown in Figures 9(a), 9(b), and 9(c), showing all of the Cretaceous and Jurassic seismic horizons picked in this study, as well as three of the overlying Tertiary horizons.

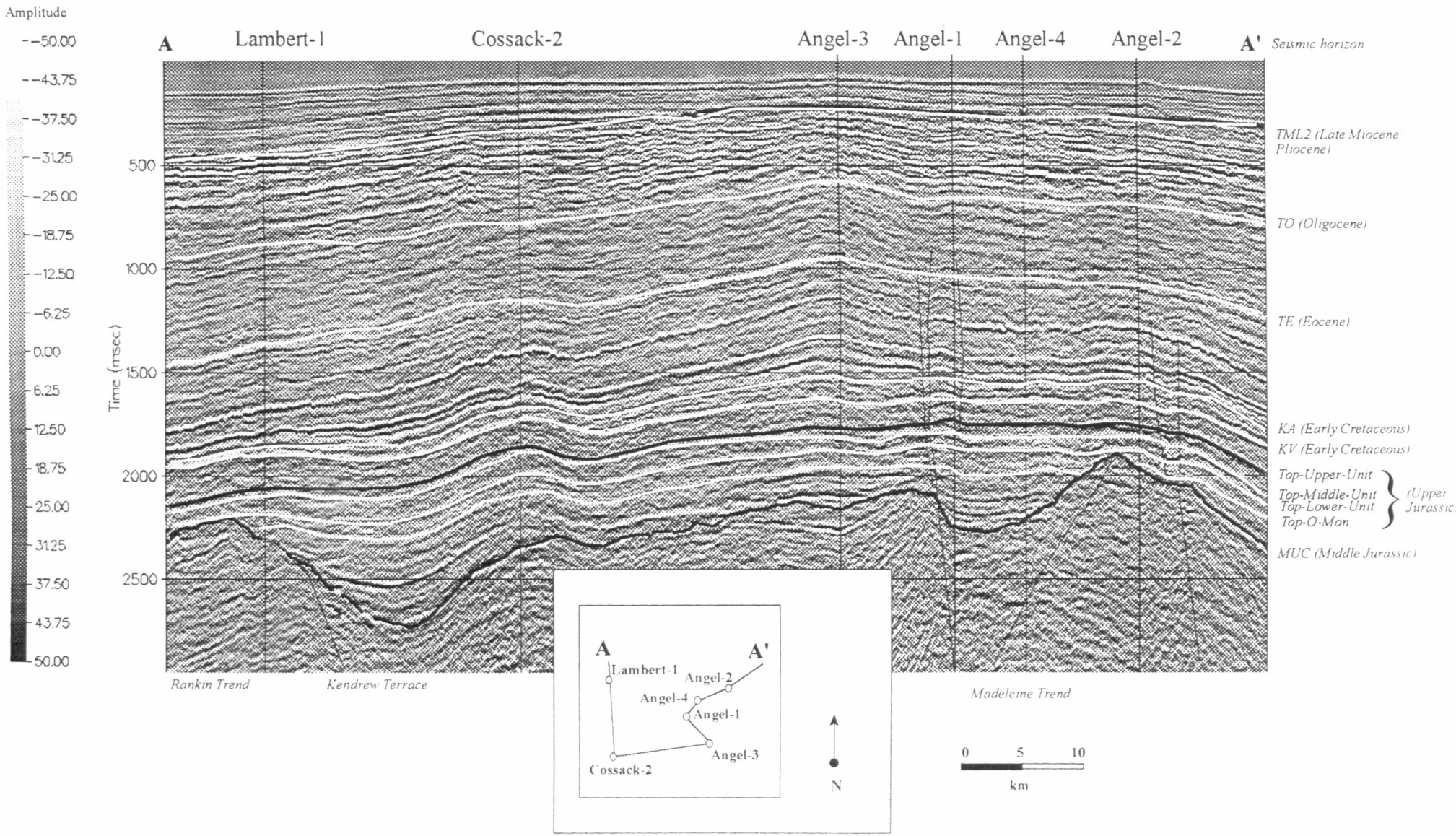
Amplitude
-50.00
-43.75
-37.50
-31.25
-25.00
-18.75
-12.50
-6.25
0.00
6.25
12.50
18.75
25.00
31.25
37.50
43.75
50.00
A
Lambert-1
Cossack-2
Angel-3
Angel-1
Angel-4
Angel-2
A'
Seismic horizon
Time (msec)
500
1000
1500
2000
2500
TML2 (Late Miocene Pliocene)
TO (Oligocene)
TE (Eocene)
KA (Early Cretaceous)
KV (Early Cretaceous)
Top-Upper-Unit
Top-Middle-Unit
Top-Lower-Unit
Top-O-Mon
(Upper Jurassic)
MUC (Middle Jurassic)
Rankin Trend
Kendrew Terrace
Madeleine Trend
A
A'
Lambert-1
Angel-2
Angel-4
Angel-1
Angel-3
Cossack-2
N
0
5
10
km

The Top Angel Formation Horizon (Top-Upper-Unit) is very difficult to map over most of the study area, as it does not have a consistent character or phase. This is due to:

1. Forestier Claystone in the southeast of the study area,
2. Dolomite cement in the Angel Fm. in the northeast, and
3. Variable acoustic impedance in the Barrow Group shales.

Forestier Claystone

In the south-east of the study area, the Angel Formation is overlain by a Late Jurassic claystone (the Forestier Claystone, *K. wisemaniae* in age at Angel-3), the top of which coincides with event Top-FC at Angel-3. The claystone is 52 msec thick at Angel-3, and lies between the Angel Formation sandstones and the overlying Barrow Group. shales. It was noted also in the 1982 and 1990 2D seismic interpretation reports, and occurs also in Forestier-1, which lies on the Legendre Trend to the east (Woodside, 1990c).

Dolomite Cement in the Angel Formation

In the north-east of the field, the Angel Formation sandstones contain massive layers of dolomite cement, between 10m and 40m thick, which have reduced the porosity from around 18% to less than 5%, and greatly increased the acoustic impedance. These dolomite-cemented layers are discussed further in Chapter 7. At Angel-2, it is signficant that the top of the uppermost layer of dolomite cement lies 8 m below the top of the sandstone, within the reservoir. The Top-Upper-Unit reflection is generated from a combination of the seismic response of the sandstone and the overlying shale, and the seismic response of the sandstone and the underlying dolomite-cemented layer. There is no well control on the thickness between the top of the sandstone and the top of the uppermost dolomite-cemented layer, away from Angel-2. The dolomite-cemented layers act to shift the Top-Upper-Unit reflection below the true level of the top of the Angel Formation by a small but unknown time, and change the character of the horizon to the start of a strong trough.

Variable Acoustic Impedance in Barrow Group Shales

The Barrow Group shales, which overlie the Angel Formation in all wells except Angel-3, have a variable acoustic impedance, caused primarily by variations in density. The shales at Angel-1 and Angel-2 have densities of around 2.2 g/cc, while at Angel-3 and Angel-4 their density is around 2.6 g/cc. The Barrow Group and overlying Muderong Shale were divided into 'time

slices' using palynological zones, and the average density in each zone was calculated (Table 5).

Formation	Palynological Zone	Angel-1	Angel-2	Angel-3	Angel-4	Cossack-1	Lambert-1
Muderong Shale	*M.australis*	2.45	2.25	2.45	2.15	2.45	2.45
Muderong Shale	*M.testudinaria / P. burgerii*	2.45	2.2	2.5	2.15	2.45	2.45
Barrow Gp. equivalent	*E. torynum/ B.reticulatum*	2.6	2.2	2.55	2.35	2.5	2.45
Barrow Gp. equivalent	*D. lobospinosium*	2.35	2.4	2.6	2.6	2.65	2.65
Barrow Gp. equivalent	*C. delicata/ K.wisemaniae*	2.2/ss	2.2	2.65*	2.45	2.65	2.6

Table 5. Palynological zonation of the Barrow Group and Muderong Shale and mean density at each well in g/cc. An 'ss' indicates that sandstone was deposited at the base of the *K.wisemaniae* zone. *=Forestier Claystone.

It can be seen that the lower density rocks only occur at Angel-1 and Angel-2, which were topographic highs at the end of sandstone deposition. It is suggested that during deposition, the heavier, siltier shale was deposited in the lows, and a more argillaceous shale was deposited on the highs. As deposition and compaction continued, the shale at the crest of the field (which was probably of a different lithology originally) became more overpressured than the surrounding shale, which enhanced the difference in density. The Cretaceous shales in all four Angel wells are overpressured to varying degrees, with the mudweight used to drill this section varying from 12ppg (1.4g/cc) at Angel-3 up to 13.2ppg (1.6g/cc) at Angel-2 (Woodside Offshore Petroleum, 1971, 1972, 1973, 1990d). Wells Angel-1 and Angel-2 are more overpressured than the other wells, as predicted by this hypothesis.

The hypothesis of a single layer of shale with varying density was tested by 2D seismic modelling of an arbitrary line through the field that intersects Angel-1, Angel-4, and Angel-2, using the density data in Table 5 and velocity data from the wireline logs, and then comparing it to the real seismic data. A 2D seismic model was set up using the Western Atlas program MIMIC, raytraced using QUIKCDP, and a synthetic seismic section produced using SLIPR. The wavelet used was the same 35Hz minimum phase Ricker wavelet of normal SEG polarity used in the synthetic seismograms. Figure 10 shows the 2D model used, the synthetic seismic section, and the real seismic data for comparison. It can be seen that the pattern of reflectors produced by the model is very close to that seen in the real data. In effect the 2D model was a

constant velocity model, with only the density varying, as all of the shales have velocities that vary less than 10% between wells, even the low density shales.

The implication of this is that lower density shales or 'soft shales' could be localised to the palaeo-high that was formed after Angel Formation deposition and the start of differential compaction. In the study area it appears to be restricted to around Angel-1 and Angel-2, as confirmed by the KV to Top-Upper-Unit isochron map (Fig 15b). The acoustic impedance of the 'soft shale' is very close to the Angel Fm. sandstone, and their interface is therefore seismically invisible. A stronger reflection comes from the interface between the 'soft shale' and the overlying denser shale. This has also been noted in the Wanaea Oil Field, which lies about 15km to the south (DiToro, 1994). The effect of the low density shales on the Top-Upper-Unit event is to decrease its amplitude and make it hard to pick over the crest of the field.

Time Maps

Time maps were prepared for the Cretaceous and Jurassic horizons, and isochron maps were generated to give an idea of the thickness of each unit. The isochron to KV maps define the horizons as they were up to the early Cretaceous, before the development of the regional north-west tilt. Amplitude maps were generated where it was felt that they would be useful in interpretation, and concentrated on the horizons within the Angel Formation. Time-to-depth conversion and the generation of depth maps was beyond the scope of this study. The time maps will be discussed as if they represent depth maps: a constant interval velocity is assumed,

Figure 10. Seismic model to test hypothesis of the presence of a shale layer with variable density above the Angel Formation.

(a) 2D seismic model. Velocity and density at well locations from well log data. Only density shown, as velocity is almost constant in Barrow Group shales.

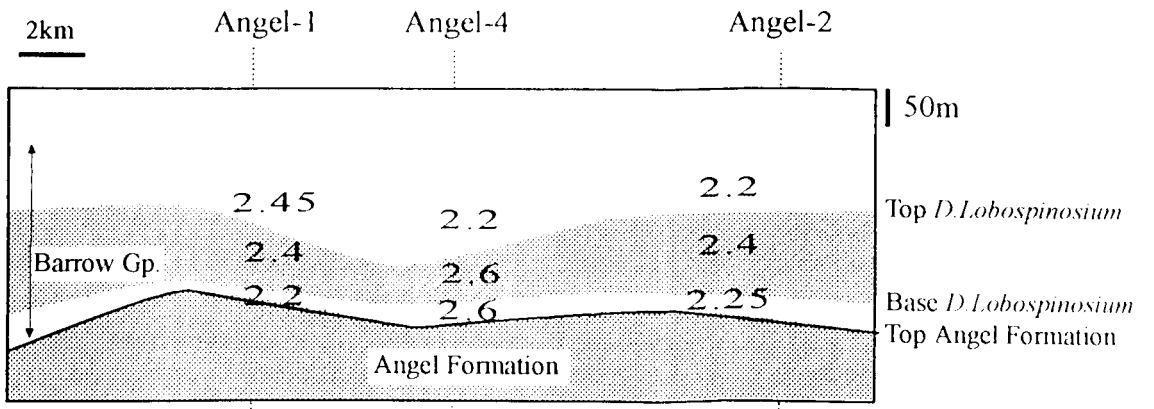

(b) Synthetic seismic section

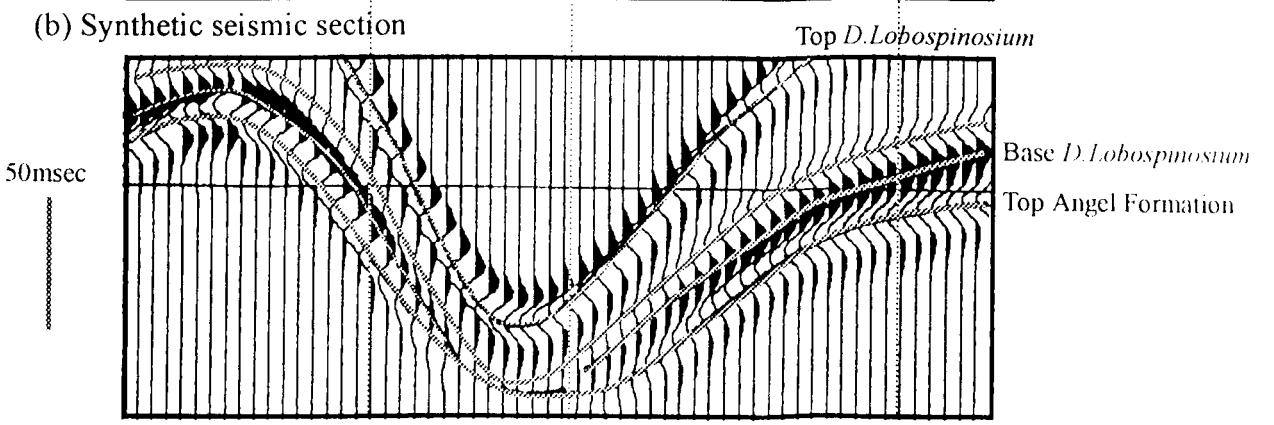

(c) 3D Seismic traverse through field

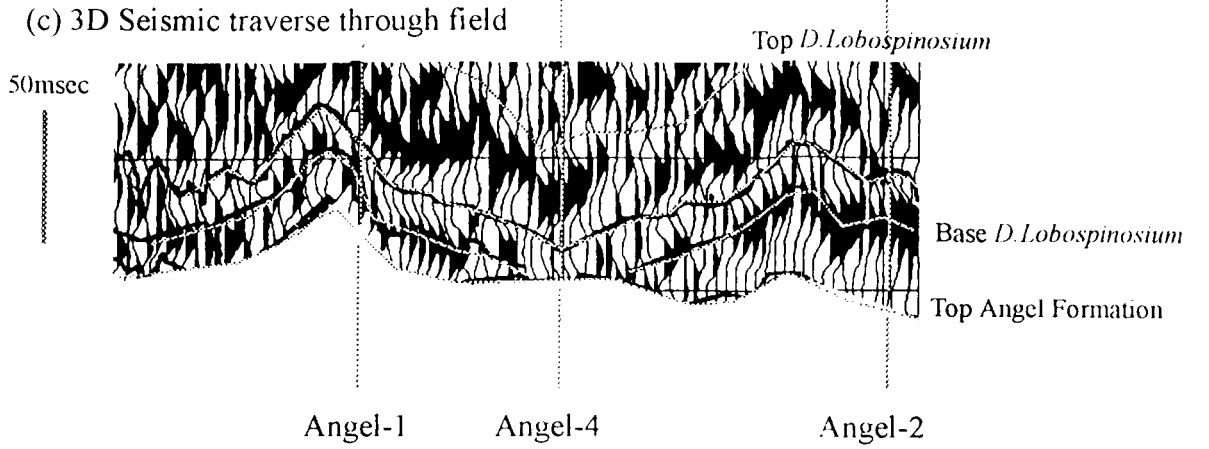

and therefore an increase in time thickness represents an increase in rock thickness. However, in all of the isochron maps discussed below, the variation in the time thickness may also be at least partly due to variations in interval velocity, with the thinner regions reflecting areas of higher interval velocity. In order to assess the variation in interval velocity in the study area and the applicability of the constant velocity assumption, the interval velocity was calculated for two layers in the overburden: surface to TE (Eocene) and TE to Top-Upper-Unit, and for the three units within the Angel Formation. The interval velocity for the overburden layers was calculated from the well depths and times picked from the seismic data at the wells. The interval velocity for the three Angel Formation layers was calculated from the sonic log. The interval velocities at the wells varied by less than 10% in each layer, as shown in Table 6, so the assumption of a constant velocity is reasonable, provided that the velocity variation between the wells is representative of the variation across the whole study area. A 10% variation implies that isochron maps with relief of this scale or smaller, for instance a feature with 20ms relief on an isochron map with average value of 200ms, should be treated with caution. The very high interval velocity in the Middle Unit at Angel-2 is caused by the presence of thick dolomite-cemented layers. Interval velocities were not calculated when a well did not fully penetrate a unit.

	Lambert-1	Cossack-2	Angel-1	Angel-2	Angel-3	Angel-4
Surface to TE	3060	3020	3060	3100	3100	3040
TE to Top-Upper-Unit	3210	3260	3050	2970	3030	3060
Upper Unit	4060	4070	3980	4120	3940	3790
Middle Unit	4240	-	4290	4570	4370	-
Lower Unit	4260	-	4260	3880	4070	-

Table 6. Interval velocity in m/s for selected layers in the study area, illustrating that interval velocity varies by 10% or less within each layer. The velocities are rounded off to the nearest 10m/s.

MUC (Main Breakup Unconformity)

The time structure and isochron to KV maps of the MUC (Figure 11) both show the large topographic relief of this horizon. The Rankin Trend runs across the northwestern corner of the study area, showing the large fault scarp typical of the main Rankin Fault. The most visible

features are the deep half-graben of the Kendrew Terrace, and the large 'headland' of the Madeleine Trend. The isochron map suggests that at Valanginian time, the Madeleine Trend plunged to the southwest. At the present, the Madeleine Trend also plunges towards the northeast, due to the northwest regional tilt.

Figure 11(a). Time structure of seismic horizon MUC (Mid Jurassic Unconformity). Note the prominent Rankin Trend to the northwest with the bounding Rankin Fault, marked by the arrow, also the Madeleine Trend which runs NE-SW across the study area and is highest near Angel-2.

Figure 11(b). Time interval between seismic horizon KV (Valanginian Unconformity) and MUC. Note the prominent Rankin Trend to the northwest with the bounding Rankin Fault, and the Madeleine Trend which runs NE-SW across the study area, and is highest in the northeast.

(a) Map of two-way time to seismic horizon MUC (Mid Jurassic Unconformity).

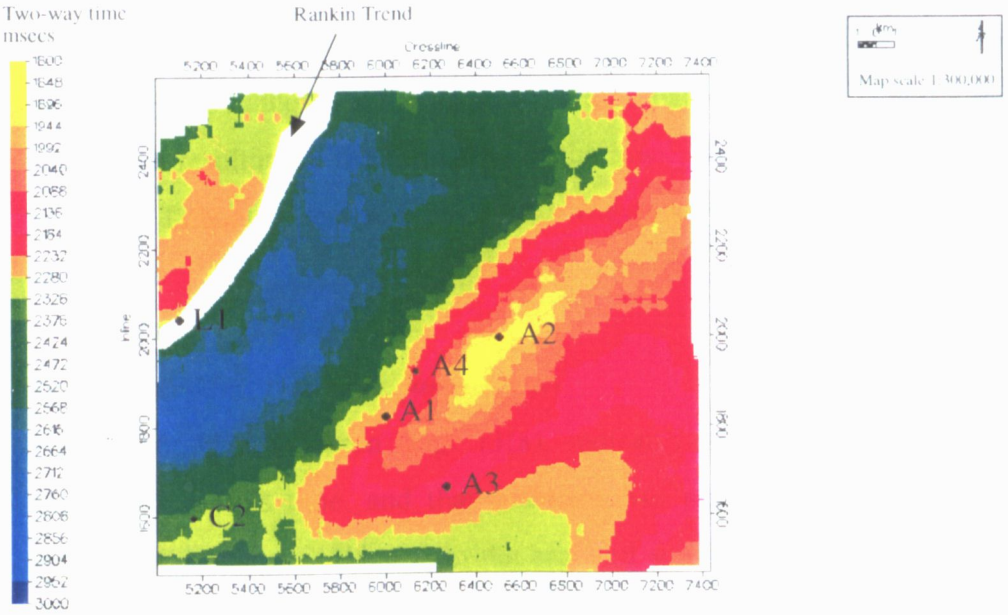

(b) Map of time interval between seismic horizons KV (Valanginian Unconformity) and MUC (Mid Jurassic Unconformity).

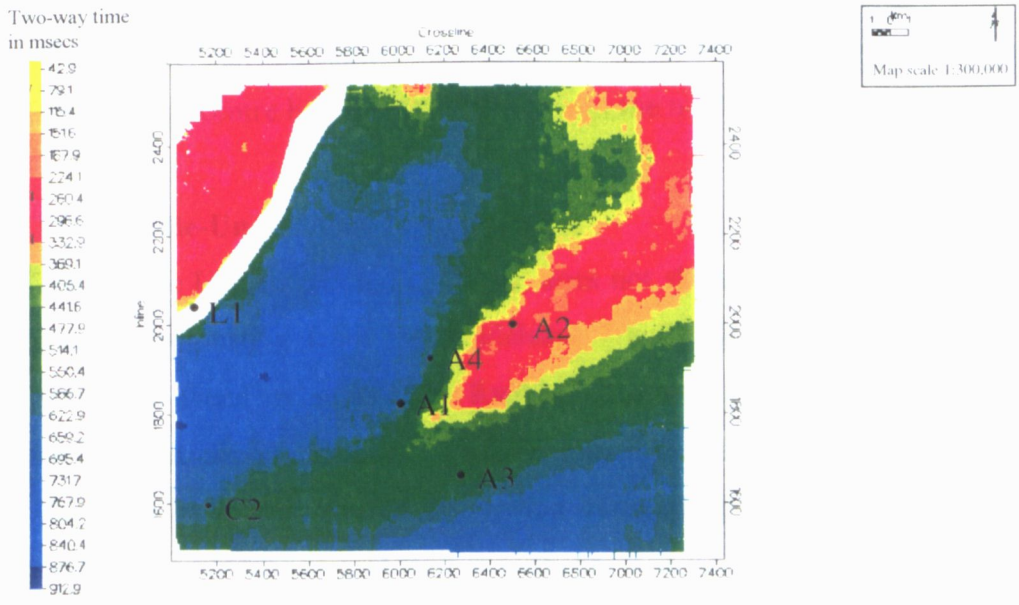

Top-O-Mon (base of Angel Fm., top *O. montgomeryi*, base *D. jurassicum*)

The Top-O-Mon to MUC isochron (Fig. 12a) shows that Dingo Claystone was mainly deposited in the Kendrew Terrace and the Lewis Trough, and onlapped onto the Madeleine Trend. The KV to Top-O-Mon isochron (Fig. 12b) shows that after the deposition of the Dingo Claystone, the Kendrew Terrace half-graben was still a low. This could also have been caused by the filling of the Kendrew Terrace half-graben by Dingo Claystone, then further subsidence resulting in the formation of the low. The subsidence could have been associated with the Tithonian tectonic pulse that triggered the deposition of the Angel Formation sandstones.

Top-Lower-Unit (lower *D. jurassicum*)

The Lower Unit isochron, Fig. 13(a), indicates that the Kendrew Terrace was still the depocentre at this time, and that sediment had not yet covered the Madeleine Trend. In general the isochron is thinnest in the east and south and thickens towards the Rankin Trend. Thickening of the sediment immediately adjacent to the Madeleine and Rankin faults is evidence for syndepositional normal fault movement on these faults. The linear trends running approximately northeast and northwest across the study area have been interpreted to be syndepositional faults, and these are discussed in Chapter 5. This movement may be associated with the Tithonian tectonic pulse. The KV to Top-Lower-Unit (Fig. 13b) isochron shows that after Lower Unit deposition the Madeleine Trend extended south to Cossack. The Kendrew Trough depocentre had split into two, one to the north and the other in the south.

Top-Middle-Unit (upper *D. jurassicum*)

The Middle Unit isochron, Fig. 14(a), does not show one depocentre, but a pattern of lobate features originating from the Madeleine Trend high and running down the flanks. The Madeleine Trend and most of the Rankin Trend were now thinly covered by 50msecs or less of Middle Unit clean sandstones. The thin area to the northeast with less than 25msecs of Middle Unit may have been caused by erosion during Upper Unit/*P. iehiense* time. There is no evidence of syndepositional fault movement. The KV to Top-Middle-Unit isochron (Fig. 14b) shows a progression of the extension of the Madeleine Trend to the southwest, towards Cossack. In fact, the area near Cossack was as high as the Madeleine Trend. The depocentre was towards the north.

Figure 12(a). Time interval between seismic horizons Top-O-Mon (base Angel Formation) and MUC (Mid Jurassic Unconformity). Note that the thickest time interval is in the Kendrew Terrace, between the Madeleine Trend and the Rankin Trend.

Figure 12(b). Time interval between seismic horizons KV (Valanginian Unconformity) and Top-O-Mon (base Angel Formation). Note that the Kendrew Terrace is still a low after deposition of the Dingo Claystone (Top Dingo Claystone is seismic horizon Top-O-Mon).

(a) Map of time interval between seismic horizons Top-O-Mon (base Angel Formation) and MUC (Mid Jurassic Unconformity).

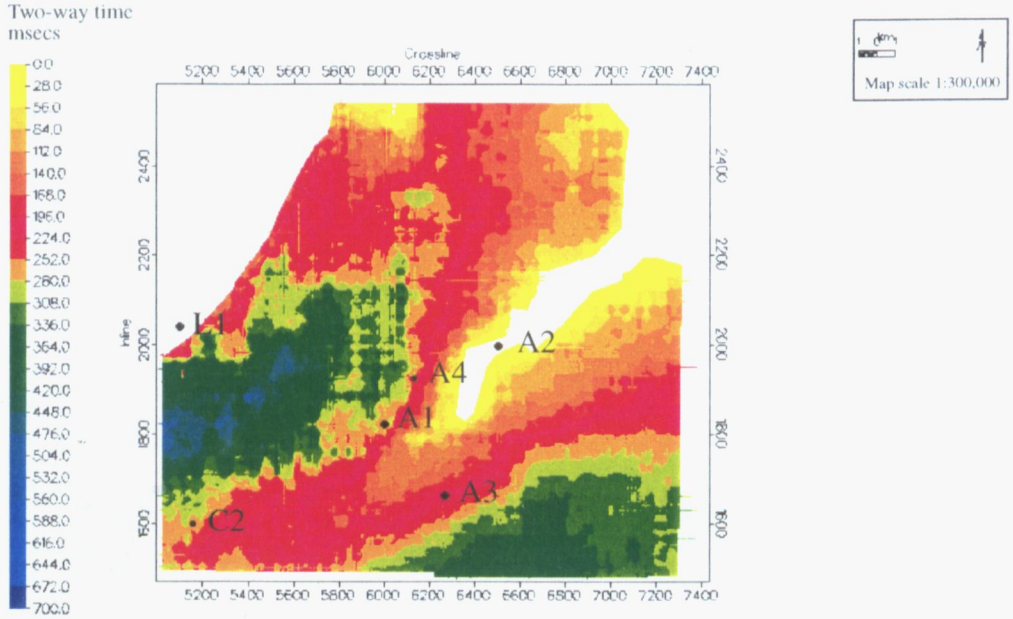

(b) Map of time interval between seismic horizons KV (Valanginian Unconformity) and Top-O-Mon (base Angel Formation).

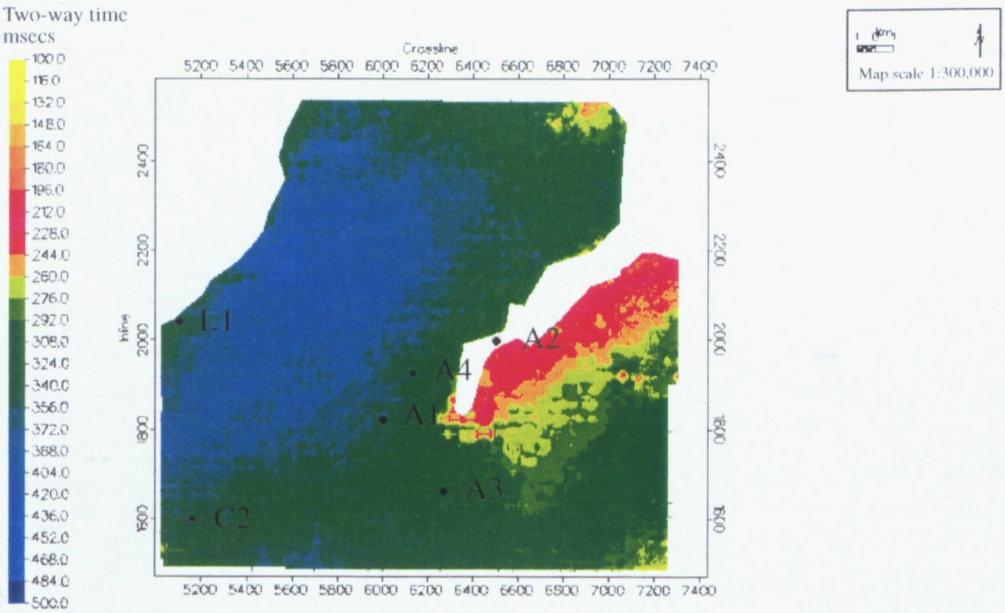

Figure 13(a). Time thickness of the Lower Unit of the Angel Formation (Top-Lower-Unit to Top-O-Mon). Note that the thickest time interval is in the Kendrew Terrace. The linear trends are intepreted to be syndepositional faults, and are discussed in Chapter 5.

Figure 13(b). Time interval between seismic horizons KV (Valanginian Unconformity) and Top-Lower-Unit. Note that after deposition of the Lower Unit, the Madeleine Trend is high, and the Kendrew Terrace is still low.

(a) Map of time thickness of Lower Unit, Angel Formation.

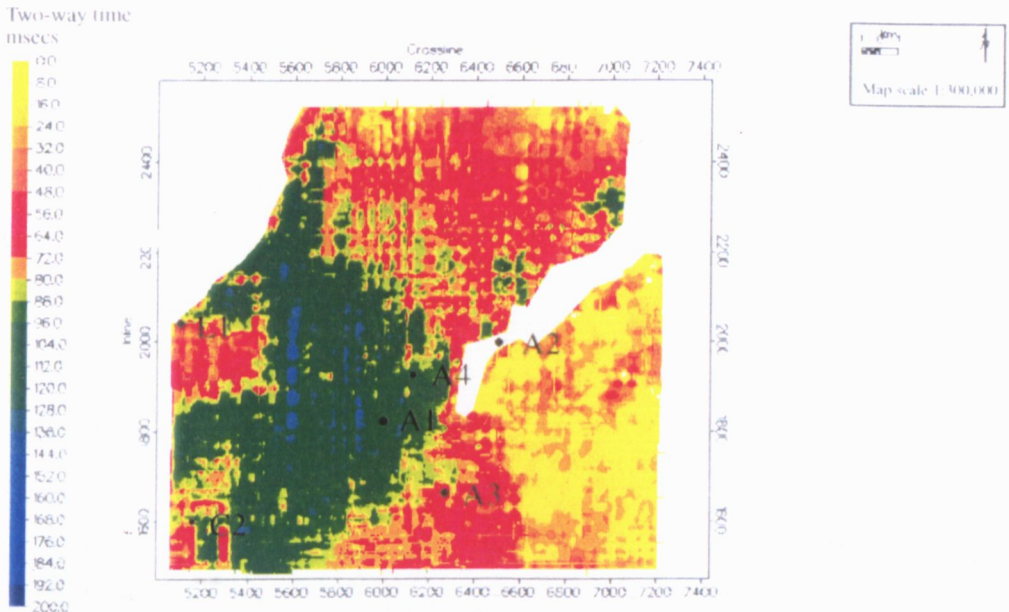

(b) Map of time interval between seismic horizon KV (Valanginian Unconformity) and Top-Lower-Unit, Angel Formation.

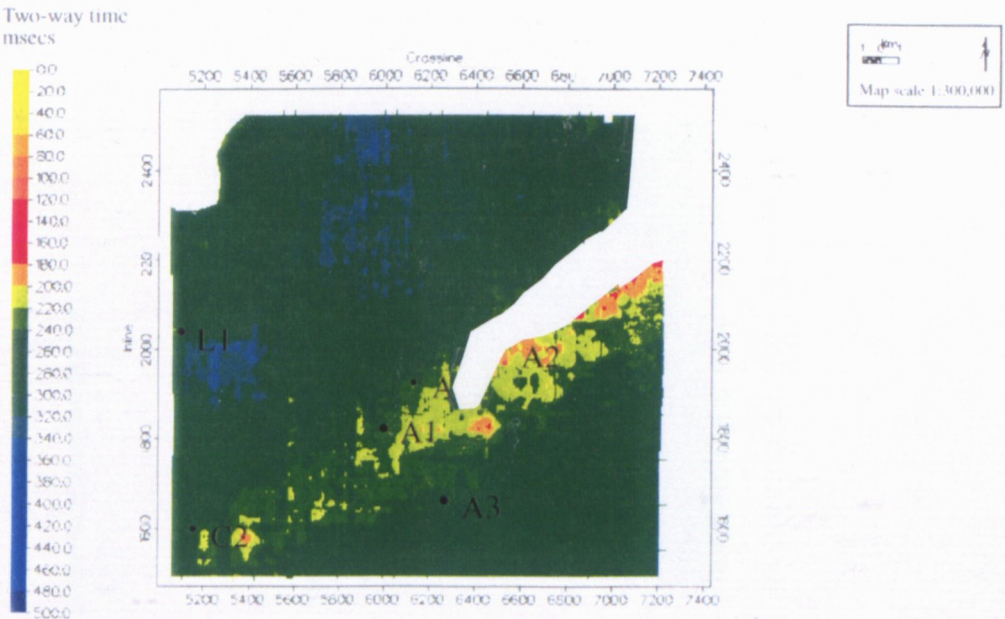

Figure 14(a). Time thickness of the Middle Unit of the Angel Formation (Top-Middle-Unit to Top-Lower-Unit). Note that the thickest time interval is in the Kendrew Terrace and the thinnest is along the Madeleine Trend and the Rankin Trend.

Figure 14(b). Time interval between seismic horizons KV (Valanginian Unconformity) and Top-Middle-Unit. Note that the thickest time interval is to the north of the study area, and the thinnest is along the Madeleine Trend, north of Angel-2 and near Cossack-2.

(a) Map of time thickness of Middle Unit, Angel Formation.

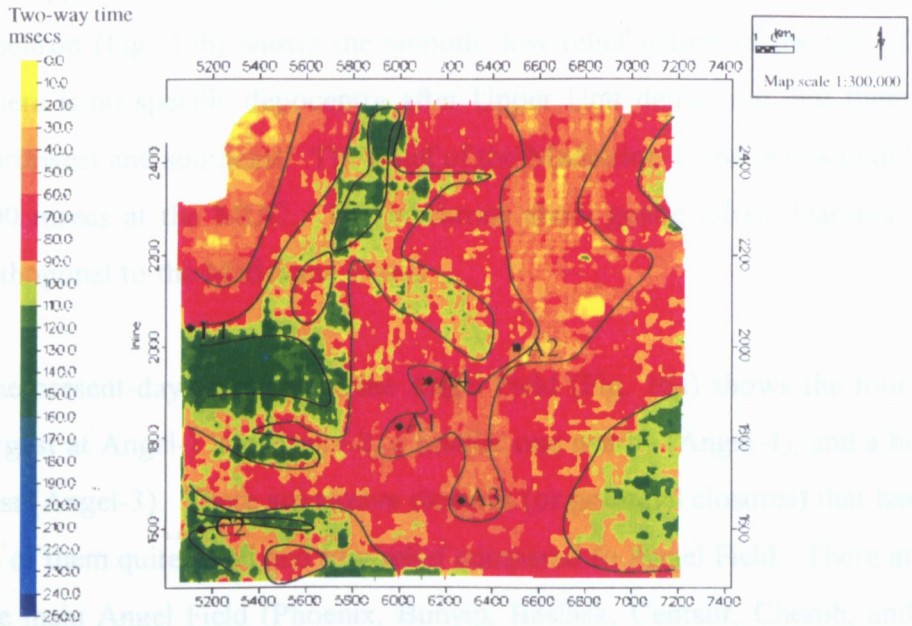

(b) Map of time thickness between seismic horizon KV (Valanginian Unconformity) and Top-Middle-Unit.

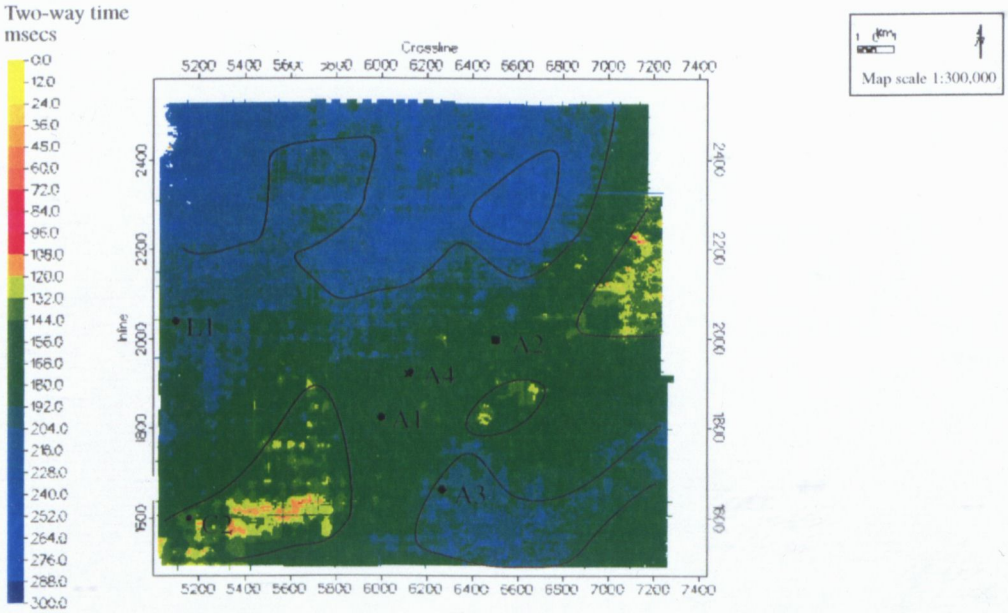

Top-Upper-Unit (top Angel Formation)

The Upper Unit Isochron (Fig. 15a) shows an overall increase in thickness from south to north of the study area. The Upper Unit covers the whole of the study area, in contrast to the Lower and Middle Units, which onlap the Madeleine Trend. There may have been some erosion of the Upper Unit, caused by the Early Cretaceous tectonic event. The KV to Top-Upper-Unit isochron (Fig. 15b) shows the smooth, low-relief nature of the top of the Angel Formation. There is no specific depocentre after Upper Unit deposition, but there is a gentle dip to the northwest and southeast. The relief of the Madeleine Trend is less than 50msecs, reduced from 600 msecs at the MUC. The isochrons show gentle lobate features running approximately orthogonal to the Madeleine Trend.

The present-day structure of the Angel Field (Fig. 16a) shows the four culminations: the two largest at Angel-1 and Angel-2, a smaller one nearby (Angel-4), and a broad flat closure to the east (Angel-3). There are twelve closures (or potential closures) that have not been drilled yet, all of them quite small and low-relief compared to Angel Field. There are six north and east of the main Angel Field (Phoenix, Bunyip, Basilisk, Centaur, Cherub, and Kraken), two east of Lambert-1 (Wyvern and Unicorn) , two north of Lambert-1 (Snark and Sphinx), and one between Angel and Cossack (Dragon), shown in Figure 16(c).

Figure 15(a). Time interval of the Upper Unit of the Angel Formation. Note that the thickest time interval lies in the north of the study area.

Figure 15(b). Time interval between seismic horizons KV (Valanginian Unconformity) and Top-Upper-Unit. Note the low relief of the Top-Upper-Unit along the Madeleine Trend.

(a) Map of time thickness of Upper Unit, Angel Formation.

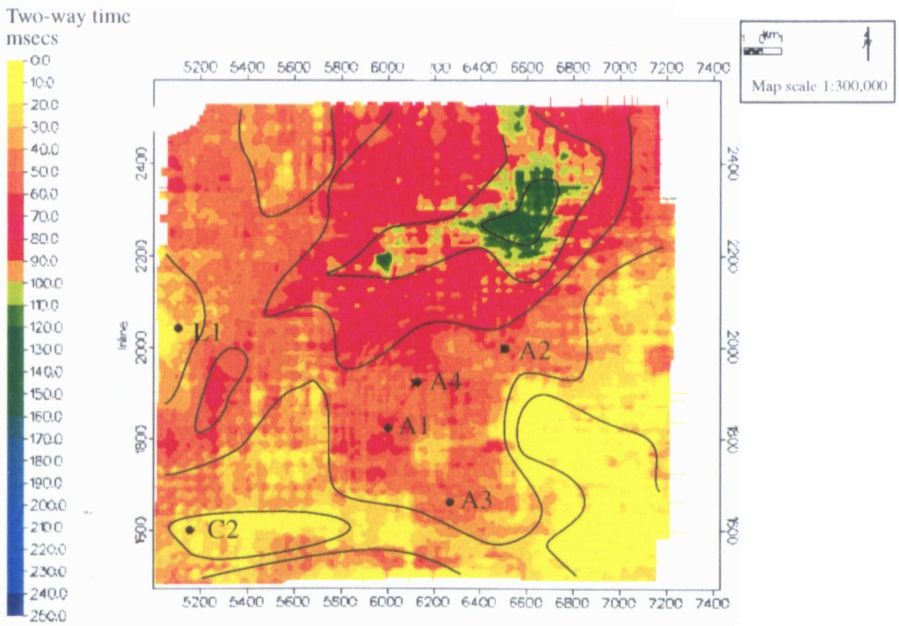

(b) Map of time interval between seismic horizon KV (Valanginian Unconformity) and Top-Upper-Unit.

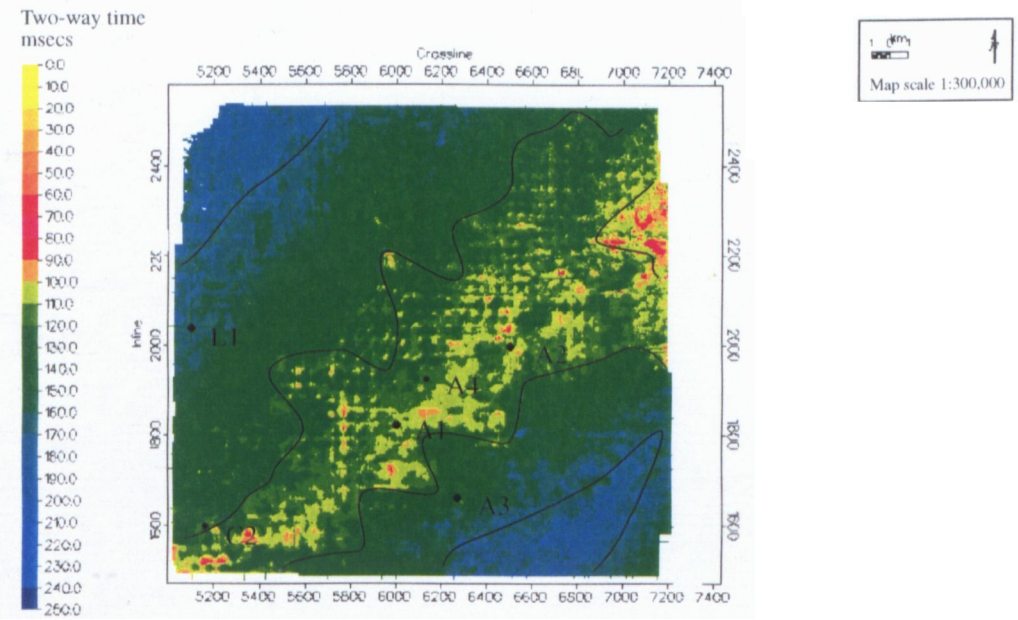

Figure 16(a). Time structure of Top-Upper-Unit (top Angel Formation), the top of the reservoir in the study area.

Two-way time in msec

1675
1698
1721
1744
1767
1790
1813
1836
1859
1882
1905
1928
1951
1974
1997
2020
2043
2066
2089
2112
2135
2158
2181
2204
2227
2250

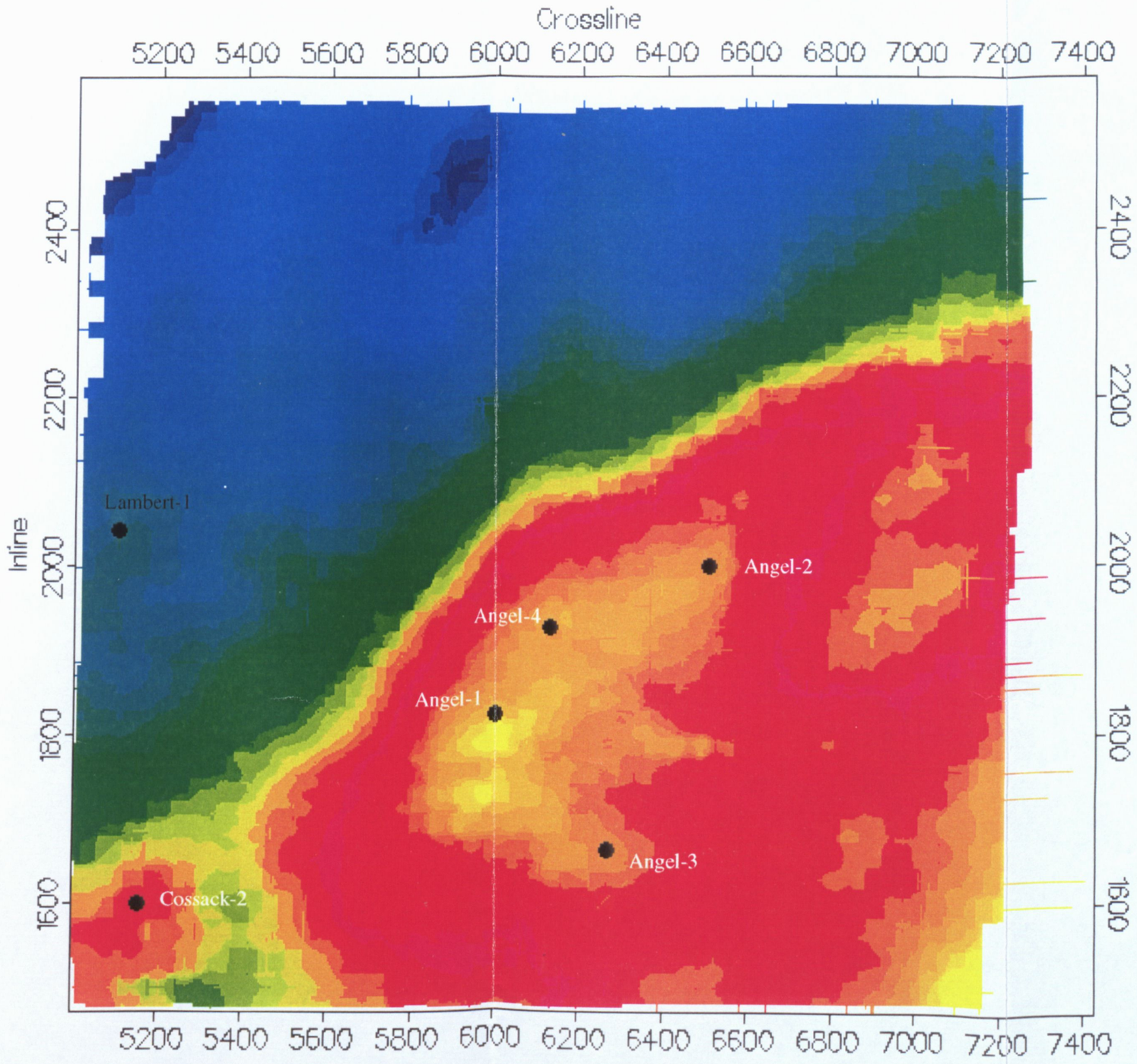

1 0 1 2 3 4 5 km

N

Scale 1: 222,200

Figure 16(b). Time thickness of Forestier Claystone.

(b) Map of time thickness of the Forestier Claystone.

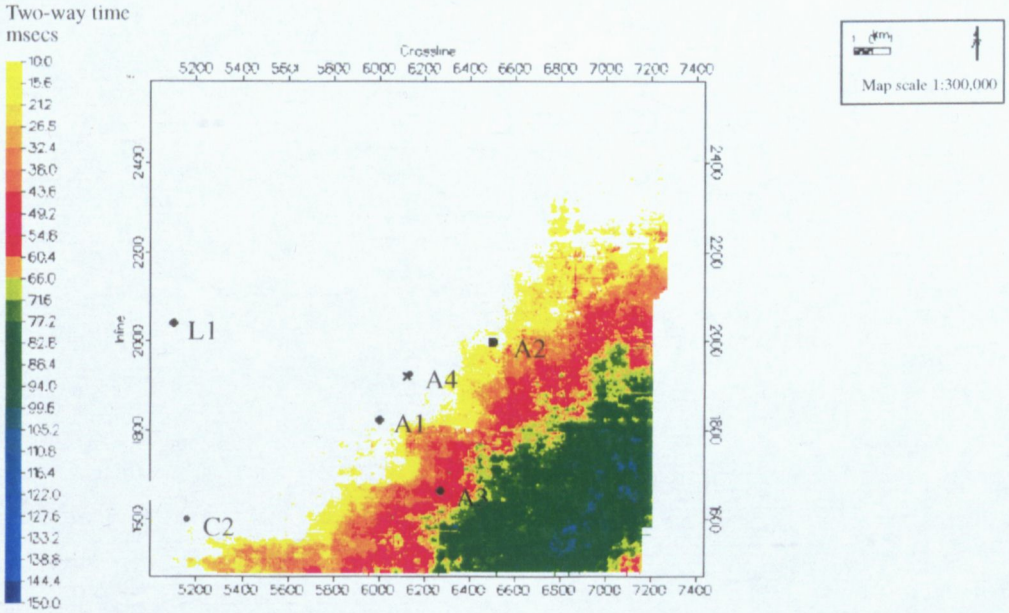

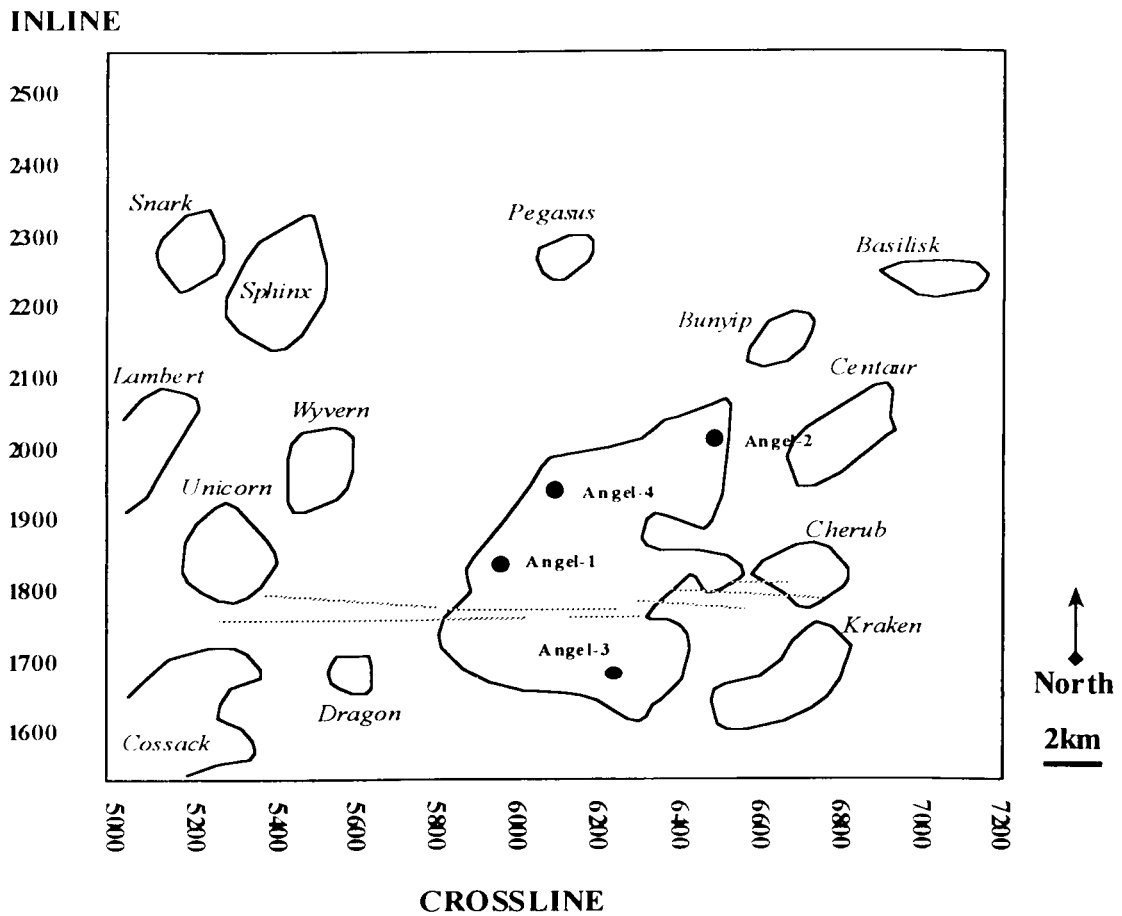

Figure 16(c). Study area showing outlines of time closures at top Angel Formation level.

Top-FC (Forestier Claystone)

The isochron of the Forestier Claystone (Fig. 16b) shows that it thins as it onlaps onto the Angel Formation on the Madeleine Trend. The only well to encounter it is Angel-3, where it is approximately 50msecs thick. It is interpreted to occur only in the Lewis Trough, and is not present in the Kendrew Terrace.

KV (Valanginian Unconformity)

The time map of the KV horizon (Fig. 17a) shows essentially the same structural elements as the Top-Upper-Unit map, as the two horizons are almost conformable. The KV amplitude map (Fig. 17b) shows broad SW-NE trending bands, probably due to variations in subcropping Barrow Group shales and/or supercropping Muderong shales.

Figure 17(a). Time structure to seismic horizon KV (Valanginian Unconformity). Note that the features are very similar to the Top-Upper-Unit time map (Fig. 16a), showing that the two horizons are approximately conformable.

Figure 17(b). Amplitude of seismic horizon KV (Valanginian Unconformity), showing NE-SW trending bands probably due to variations in subcropping Barrow Group shales and/or supercropping Muderong Shales.

(a) Map of time to seismic horizon KV (Valanginian Unconformity).

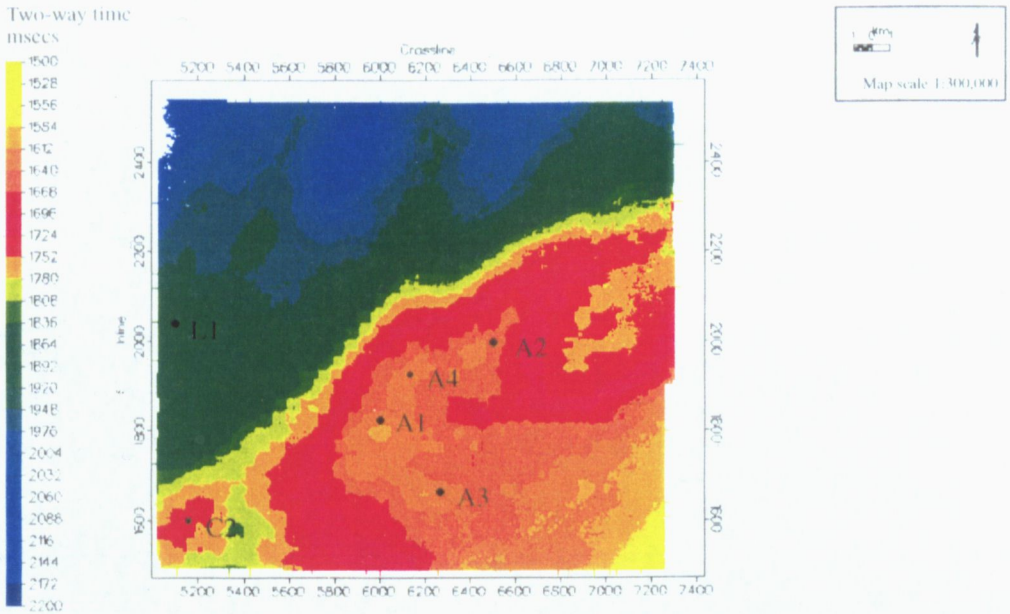

(b) Map of amplitude of seismic horizon KV (Valanginian Unconformity).

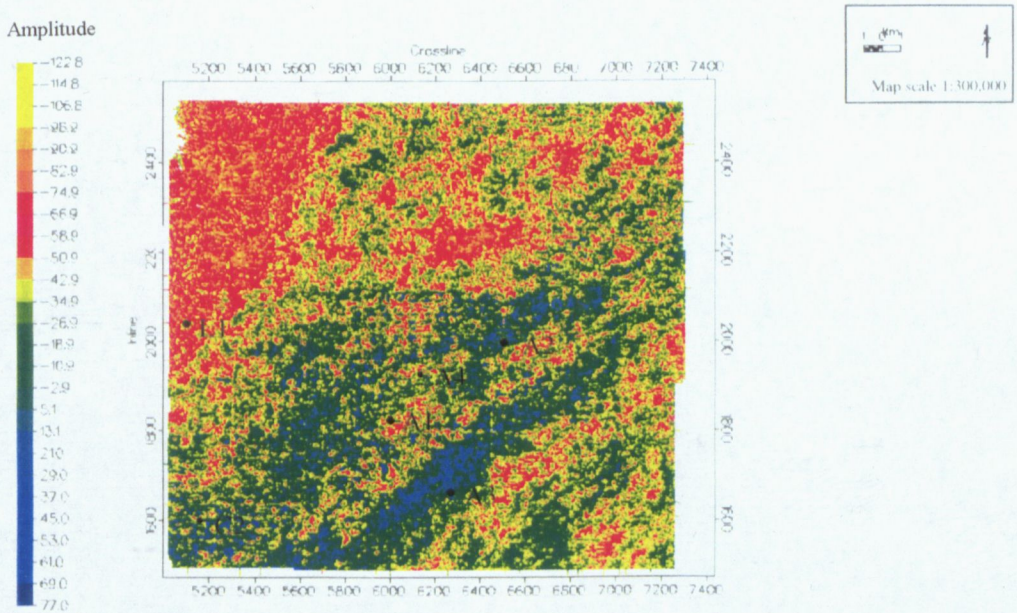

KA (Near top Aptian Unconformity)

The time map of the KA horizon (Fig. 18a) shows the same overall structure as the KV and Top-Upper-Unit maps, indicating that these horizons are approximately conformable, and that no significant tectonic movement occurred in the intervening period. The KA to KV isochron (Fig. 18b) is very smooth and featureless, with a gradual increase in thickness to the east. The amplitude map of KA (Fig. 19a) shows a banded pattern of variation, probably due to subcropping Muderong Shales.

Figure 18(a). Time structure of seismic horizon KA (Aptian Unconformity). Note that the features are very similar to the Top-Upper-Unit (Fig. 16a) and the KV (Fig. 17a) time map, showing that no significant tectonic movement occurred in the intervening period.

Figure 18(b). Time thickness between seismic horizon KA (Aptian Unconformity) and KV (Valanginian Unconformity). Note that the time thickness map is smooth and featureless.

(a) Map of time to seismic horizon KA (near top Aptian Unconformity).

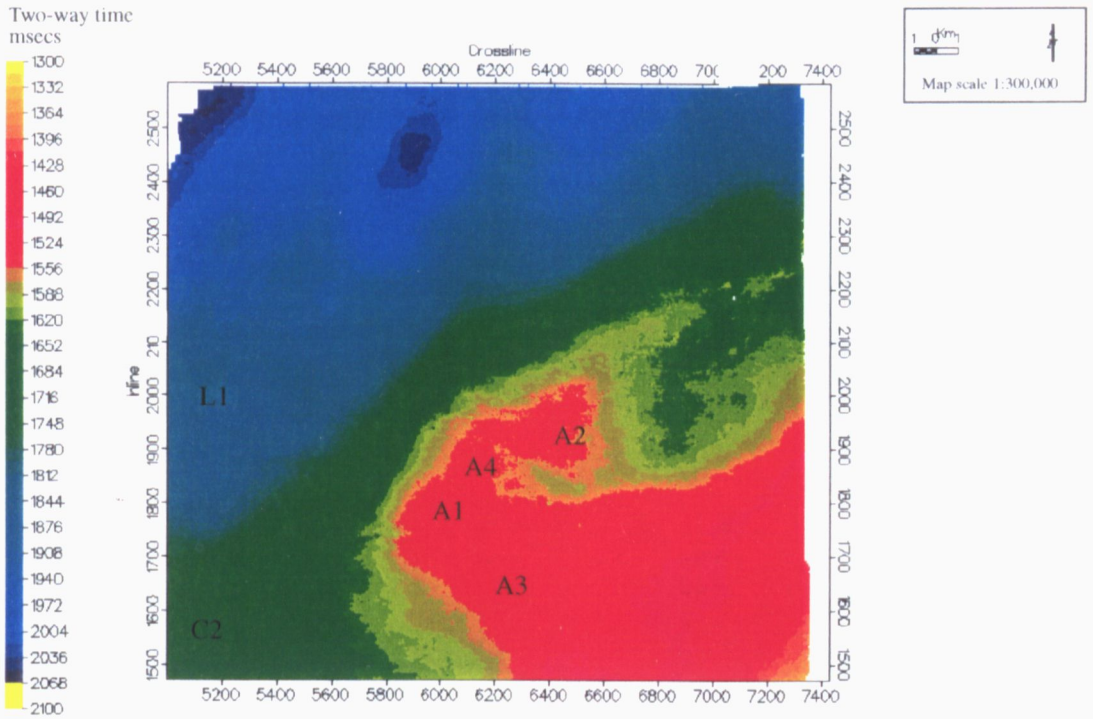

(b) Map of time thickness between seismic horizon KA (near top Aptian Unconformity) and KV (Valanginian Unconformity).

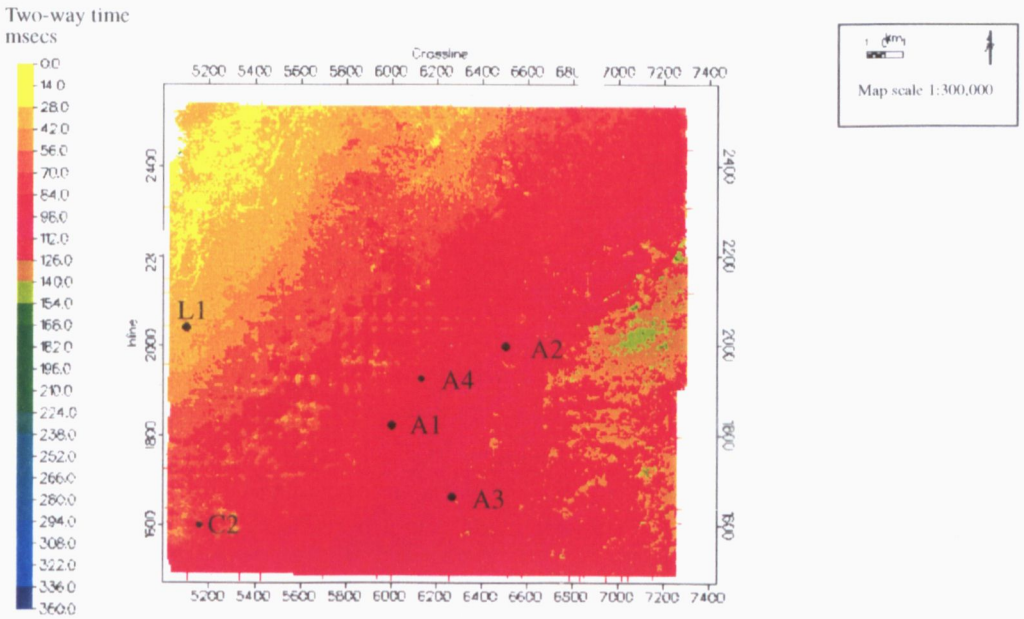

Figure 19(a). Amplitude map of seismic horizon KA (Aptian Unconformity). Note the variations in amplitude.

Figure 19(b). Azimuth map of seismic horizon KA (Aptian Unconformity).

(a) Amplitude of seismic horizon KA (Aptian Unconformity)

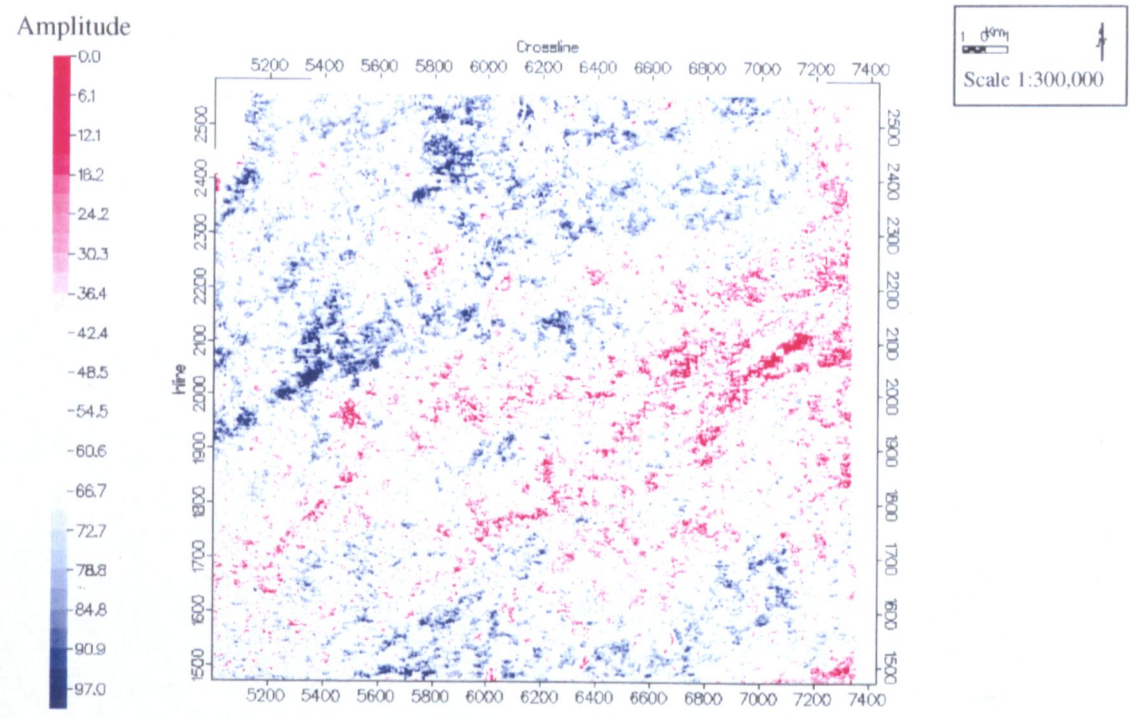

(b) Azimuth of seismic horizon KA (Aptian Unconformity).

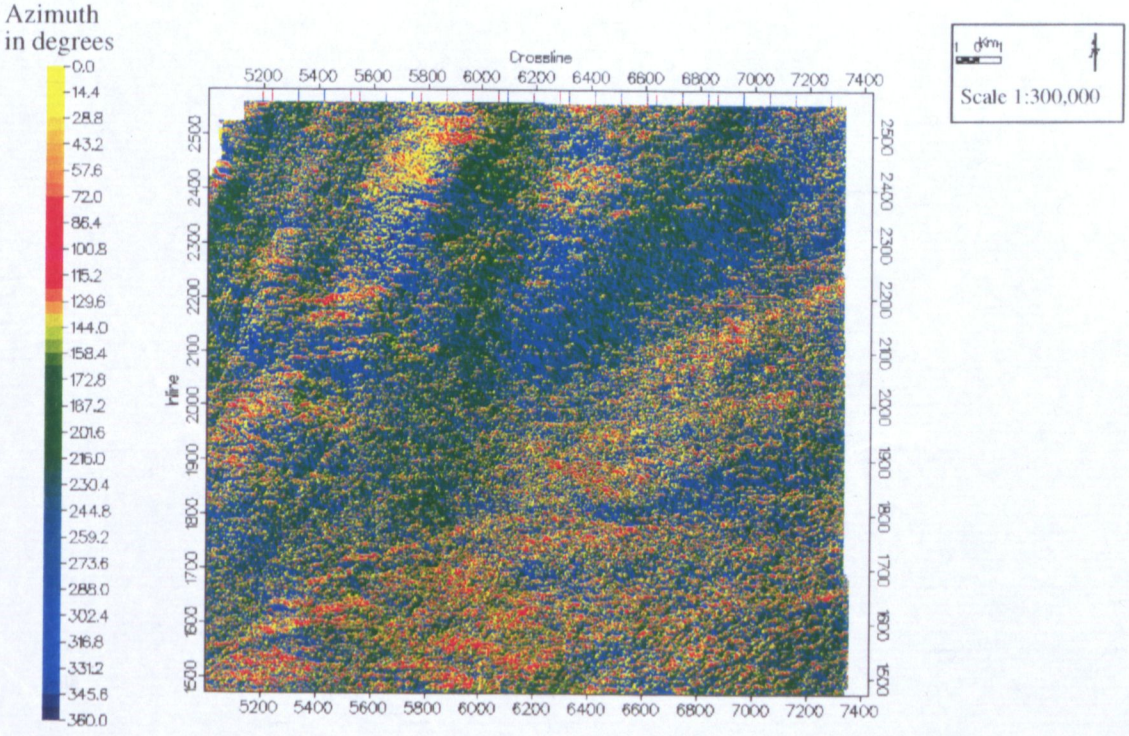

Permo-Carboniferous to Early Jurassic

The Dampier Sub-basin formed by Permo-Carboniferous extension of around 400%. This extension is thought to have occurred by pure shear in the lower crust, during which the crust thinned by two-thirds (Stagg and Colwell, 1994). A gravity model that matches a measured profile across the Dampier Sub-basin is shown in Figure 20(a). Crustal thinning is inferred to be present underneath the Lewis Trough (Hill, 1994). The model invoked is that of Lister et al. (1991), which contains a major low-angle detachment fault with a ramp-flat-ramp geometry, and a syncline overlying the thinnest crust (Fig. 20(b)). The elements of deformation that are produced in a sandbox model with a ramp-flat-ramp detachment fault geometry and 30% extension (Lemon and Mahmood, 1995) are shown in Figure 20(c). The geometry of the faults and folds is very similar to the model of Lister et al. (1991), especially the formation of a central syncline, and pronounced roll-over in the rotated block next to the footwall. The normal faults die out with depth towards the detachment fault.

There is little discussion in the literature of the geometry of the Permo-Carboniferous extensional faults. Lemon and Mahmood (1994) studied the Mermaid Fault, a normal fault with a complex detachment geometry at the southeastern margin of the Dampier Sub-basin. A comparison of the sandbox model discussed above with the Dampier Sub-basin cross-section presented by Hill (1994), shows that the structural features are consistent with the presence of a crustal detachment fault that starts near the Lambert Shelf and dips west towards the Rankin Trend, with the convex-up part of the fault lying underneath the Rosemary/Legendre Trend, as shown in Figure 20(d). The Rankin Trend and Exmouth Plateau are the translational block and the Kendrew Terrace is the lower rollover and crestal collapse graben.

The Lewis Trough is the hanging wall syncline, and the Rosemary/Legendre Trend is a high produced by the local compression that occurs above the flat part of the fault (shown in Fig 20(c) by a reverse fault). The rotated block is clearly visible between the Rosemary/Legendre Trend and the Lambert Shelf. This part of the detachment fault (in the rotated block) was abandoned during the Permian, as indicated by the lack of Triassic to Jurassic sediments. The later extensional movement during the Late Triassic and Early Jurassic was focussed along the Rosemary/Legendre Trend faults. The large subsidence of the Lewis Trough during the Triassic thermal sag caused the Madeleine Trend area to rotate towards the centre of the

trough as it subsided. Due to space constraints within the Kendrew Terrace, this rotation caused the Madeleine Trend to be uplifted, or squeezed up, as shown in Figure 21. In other words, subsidence of the Lewis Trough caused uplift of the Madeleine Trend.

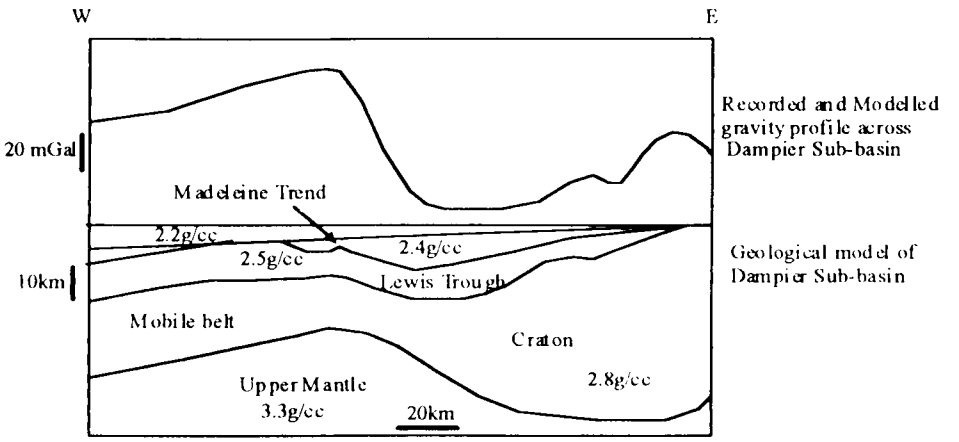

Figure 20(a). Gravity model across the Dampier Sub-basin, after Hill (1994).

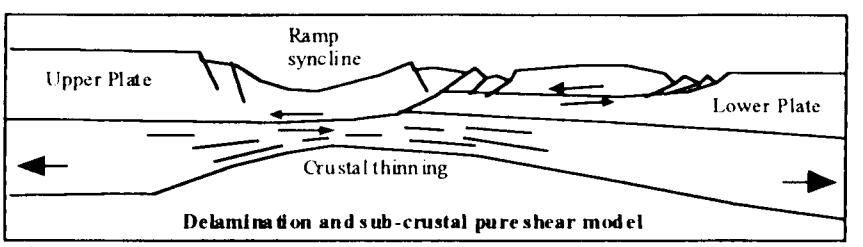

Figure 20(b). Detachment model for extension, after Lister et al. (1991).

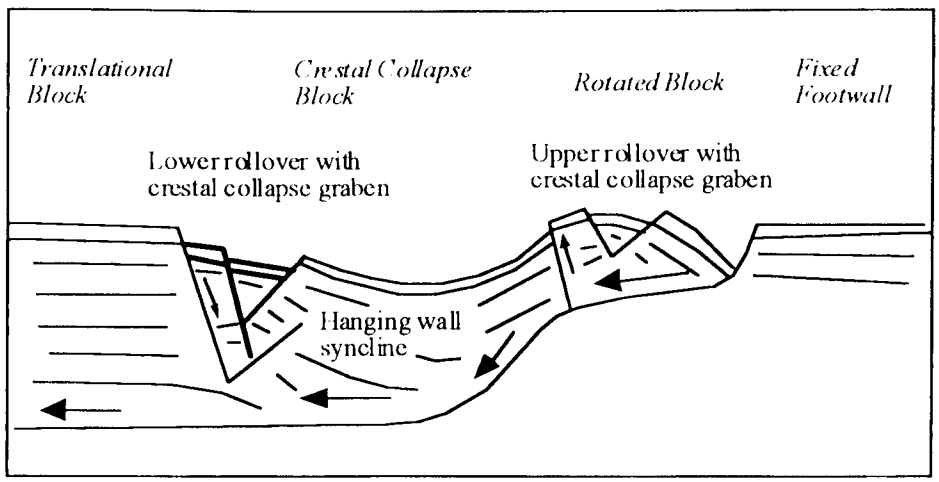

Figure 20(c). Generalised elements of deformation on a ramp-flat-ramp detachment fault, after Lemon and Mahmood (1995).

Figure 20(d). Section across the Dampier Sub-basin and conjectured ramp-flat-ramp detachment fault. Section from Hill (1994).

Figure 21(a). Crestal collapse graben formed during extension along detachment fault (Permian).

Figure 21(b). Further subsidence in the Lewis Trough squeezed the Madeleine Trend up (Late Triassic to Early Jurassic).

(d) Section across the Dampier Sub-basin and conjectured ramp-flat-ramp detachment fault. Section from Hill (1994).

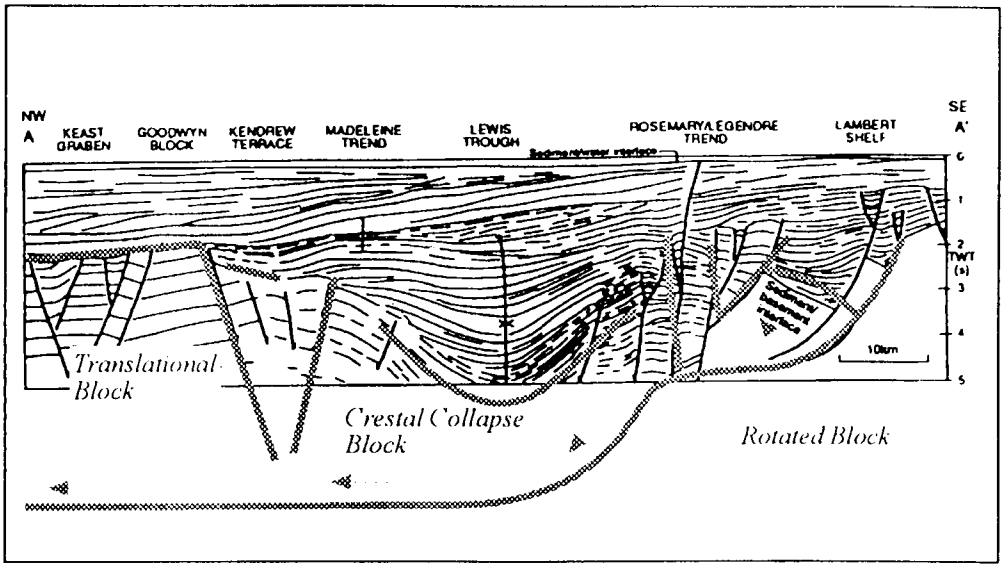

(a) Crestal collapse graben formed during extension along detachment fault (Permian)

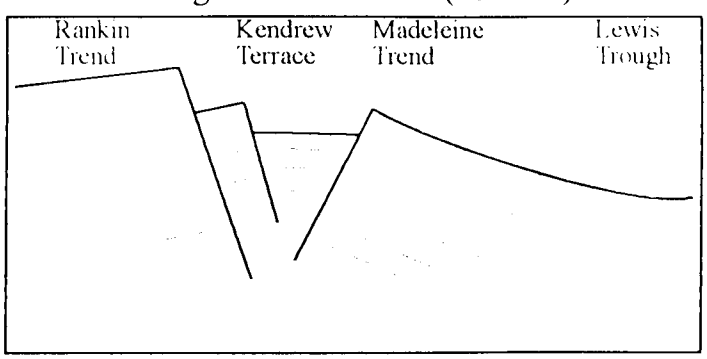

(b) Further subsidence in the Lewis Trough squeezed the Madeleine Trend up (Late Triassic to Early Jurassic)

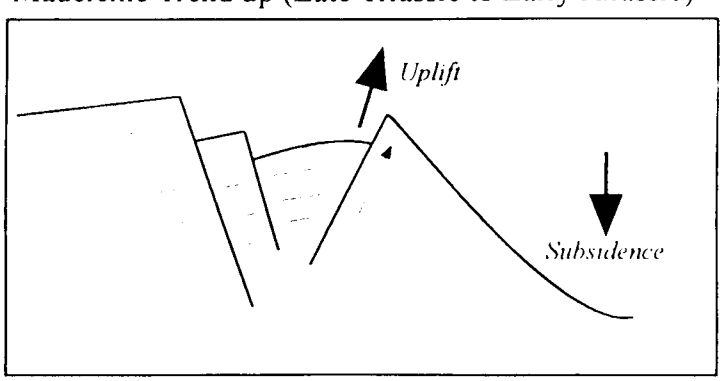

Middle to Late Jurassic

In the Middle to Late Jurassic (Callovian to Oxfordian), relative uplift was followed by rapid subsidence, which formed a regional unconformity with over 600 msecs two-way time of topographic relief in the study area (the 'Main Unconformity', or seismic horizon MUC). In the study area, the extension also resulted in movement on the normal faults in the Kendrew Terrace, the deepening of the Kendrew Terrace graben, and also probably further uplift of the Madeleine Trend.

Late Jurassic

The Late Jurassic (Tithonian) WNW extension caused extension and left-lateral movement on the Rosemary Fault System, at the eastern margin of the Lewis Trough (Miller, 1995). This mild, synsedimentary movement caused the formation of minor NE-SW trending normal faults, and anticlines trending E-W at confining bends of the Rosemary Fault. Since the tectonic event affected the Rosemary Fault System and the Rankin Trend (Newman, 1994), it seems likely that it affected the Madeleine Trend as well. The extension occurred during deposition of the Angel Formation, so synsedimentary tectonic movement may be expressed as changes in time thickness of the units of the Angel Formation. Figure 22 is the time thickness map of the Lower Unit with the Rankin and Madeleine Fault marked. The thickening of the unit adjacent to the faults may be due to normal movement on the faults, from the WNW extension. The WNW orientation of the extension will also cause a component of left-lateral movement along the Madeleine Fault. The time thickness map indicates the possibility of the formation of an antithetic right-lateral strike-slip fault oriented NNW and a reverse fault oriented approximately WNW, which are the types and orientations of faults predicted to occur in left-lateral movement. There is no obvious evidence of syndepositional faulting in the Middle and Upper Units, which tentatively dates the movement to the lower *D. jurassicum* palynological zone.

Figure 22. Time thickness of the Lower Unit, with interpreted syndepositional faults and orientation of the Tithonian tectonic event.

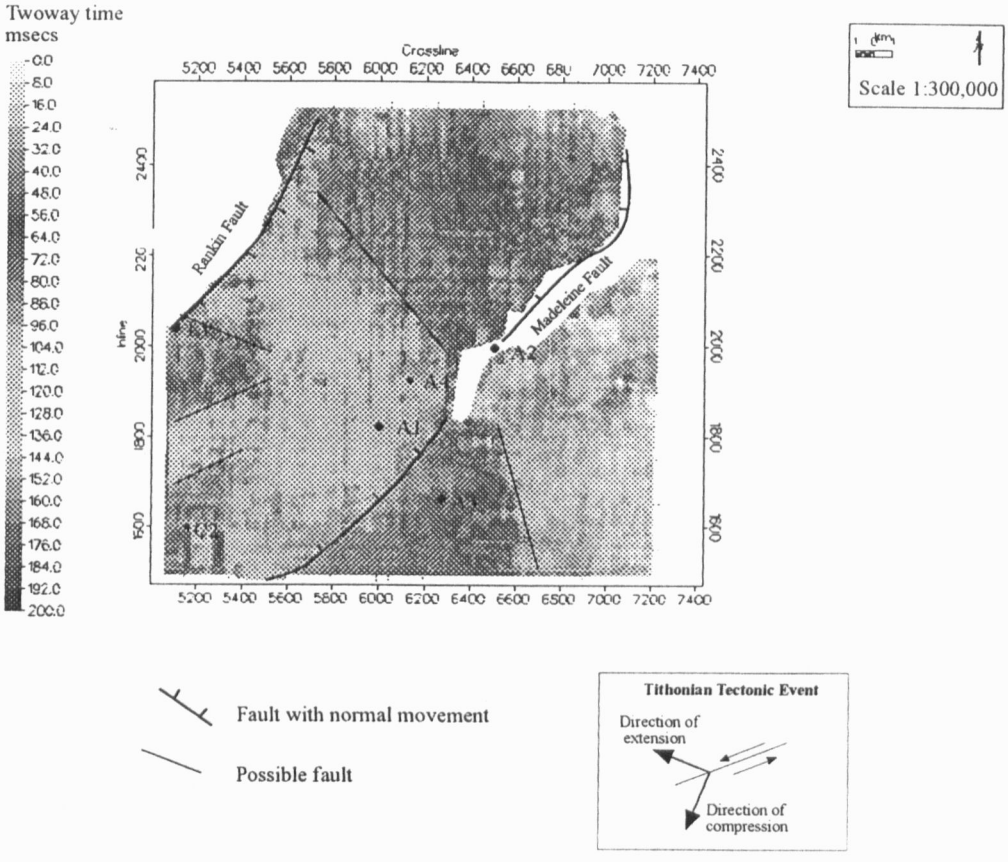
Twoway time
msecs
0.0
8.0
16.0
24.0
32.0
40.0
48.0
56.0
64.0
72.0
80.0
88.0
96.0
104.0
112.0
120.0
128.0
136.0
144.0
152.0
160.0
168.0
176.0
184.0
192.0
200.0
Crossline
5200 5400 5600 5800 6000 6200 6400 6600 6800 7000 7200 7400
Inline
1600 1800 2000 2200 2400
Rankin Fault
Madeleine Fault
A1
A2
A3
A4
A5
A6
Scale 1:300,000
Fault with normal movement
Possible fault
Tithonian Tectonic Event
Direction of extension
Direction of compression

Miocene

The Regional Stress Field

The compressional event which began in the Miocene and is continuing in the present day, has an approximately E-W maximum compressional stress vector in the North West Shelf (Denham and Windsor, 1991; Etheridge et al., 1991; Hillis, 1991; Hillis and Williams 1993, Tan et al., 1994, Coblentz et al., 1995). This has been determined from borehole breakouts, earthquake focal mechanisms, and near-surface measurements. The precise direction of maximum compressive stress can be determined from studies of borehole breakout (Hillis, 1991), and this technique has been used in Angel-2 and Angel-4, showing that the maximum compressional stress vector is oriented at 75-85 degrees, or approximately ENE, in the Angel Field (Woodside, 1990a).

Effect on the Madeleine Fault

The effect of ENE-WSW compression on the NE-SW Madeleine Fault is to cause right-lateral strike-slip movement along the fault, and also to cause an element of compression, or transpression. It is the new faults caused by this reactivation that cut the reservoir section in the Angel Field, and will therefore be studied in detail.

The orientation and style of structures that can be formed by lateral movement along a fault can be predicted by the strain ellipse of Harding (1974). The formation and development of these structures are discussed in detail by Tschalenko (1970). Applying this strain ellipse to the Madeleine Fault gives the predicted orientation of faults and folds that may be developed, if the fault pattern in the Angel Field has indeed been caused by right-lateral transpression, and can be compared with the observed structures.

Small strike-slip displacement at depth results in small discontinuous *en echelon* folds with four-way closure above the main fault (Harding, 1974; Christie-Blick and Biddle, 1985). These *en echelon* folds are the main potential hydrocarbon traps that form along a strike-slip fault (Harding, 1974), and are predicted here to occur with their crests aligned approximately NNE-SSW. Woodside (1988) observed that the orientations of the structures on the Madeleine Trend (eg Angel, Wanaea, Cossack, Dampier, Withnell) indicate right-lateral movement.

Several sets of faults are formed during strike-slip movement, including sets of conjugate vertical strike-slip faults, at angles of 30-35 degrees either side of the direction of maximum compression. These faults are called synthetic and antithetic shears, or Reidel and antiReidel

shears (Christie-Blick and Biddle, 1985). Normal faults, usually open, form orthogonal to the vector of extension, and reverse faults form orthogonal to the vector of compression (Harding, 1974).

Characteristics of Strike-Slip Faults

Strike-slip faults are linear to curvilinear in map view, and consist of a narrow subvertical principal fault zone at depth, topped with arrays of upward-diverging faults ('flower structures') (Christie-Blick and Biddle, 1985). They can be identified on a map view by:

1. features that are shifted or cut,
2. narrow, long bands of en echelon features,
3. parallel open normal faults in anticlines, and
4. faults with changing sense of throw.

They can be identified on vertical sections by:

1. flower structures - both positive (reverse faults) and negative (normal faults),
2. sub-vertical parallel fault planes with varying sense of throw and complex inner structure, and
3. 'Pop-up' blocks squeezed into the fault plane

(AAPG, 1988).

Fault Interpretation on the KA Horizon (Nr Top Aptian Unconformity)

Faults were picked on the KA horizon using artificial illumination of the horizon, and these are shown in Fig 23(a). This horizon was chosen as it was a strong continuous reflection which is close to the top of the reservoir (approximately 200msecs above). The faults picked using artificial illumination are of good quality, due to the strength of the reflection. The fault pattern in the reservoir should be similar to the fault pattern mapped from the KA horizon, as the two horizons are close. The aim of this is not to pick the exact faults at the reservoir level from the KA horizon, but to map the faults at the KA horizon, examine the fault pattern, and test if the fault pattern is consistent with E-W compression and consequent right-lateral reactivation of the Madeleine Fault. A 3D visualisation of the KA horizon, covering the southernmost two-thirds of the study area, is shown in Figure 24; note that the faulting is concentrated along the Madeleine Trend.

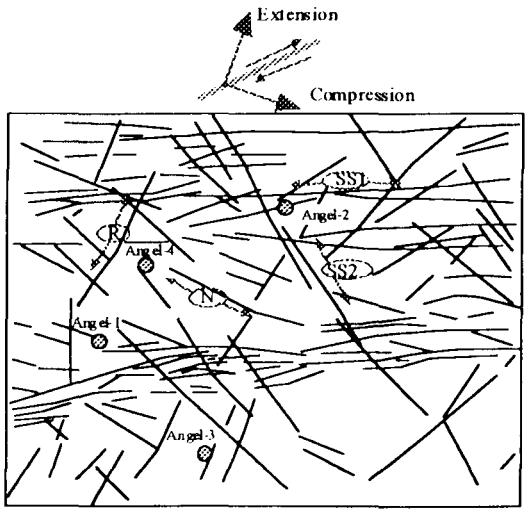

(a) Interpreted faults on seismic horizon KA, together with direction of extension and compression inferred from this fault pattern. The four sets of faults are: N = NW-SE normal faults, R = NNE-SSW reverse faults, SS1 = E-W strike-slip faults, and SS2 = NNW-SSE strike-slip faults.

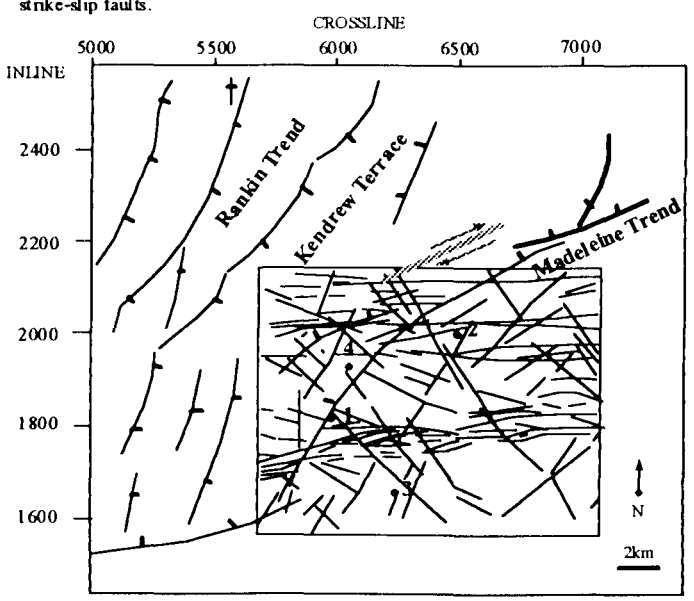

(b) Faults on time slice at 2600 msec, overlain by interpreted faults on seismic horizon KA from (a). Note that the inferred strike-slip movement (grey line) from (a) is parallel with with the Madeleine Trend (thick black lines).

Figure 23. Interpreted faults on seismic horizon KA, and comparison of inferred orientation of strike-slip movement to the orientation of the Madeleine Trend faults.

Figure 24. 3D visualisation of seismic horizon KA, showing the fault pattern on that horizon, and the concentration of faults along the Madeleine Trend.

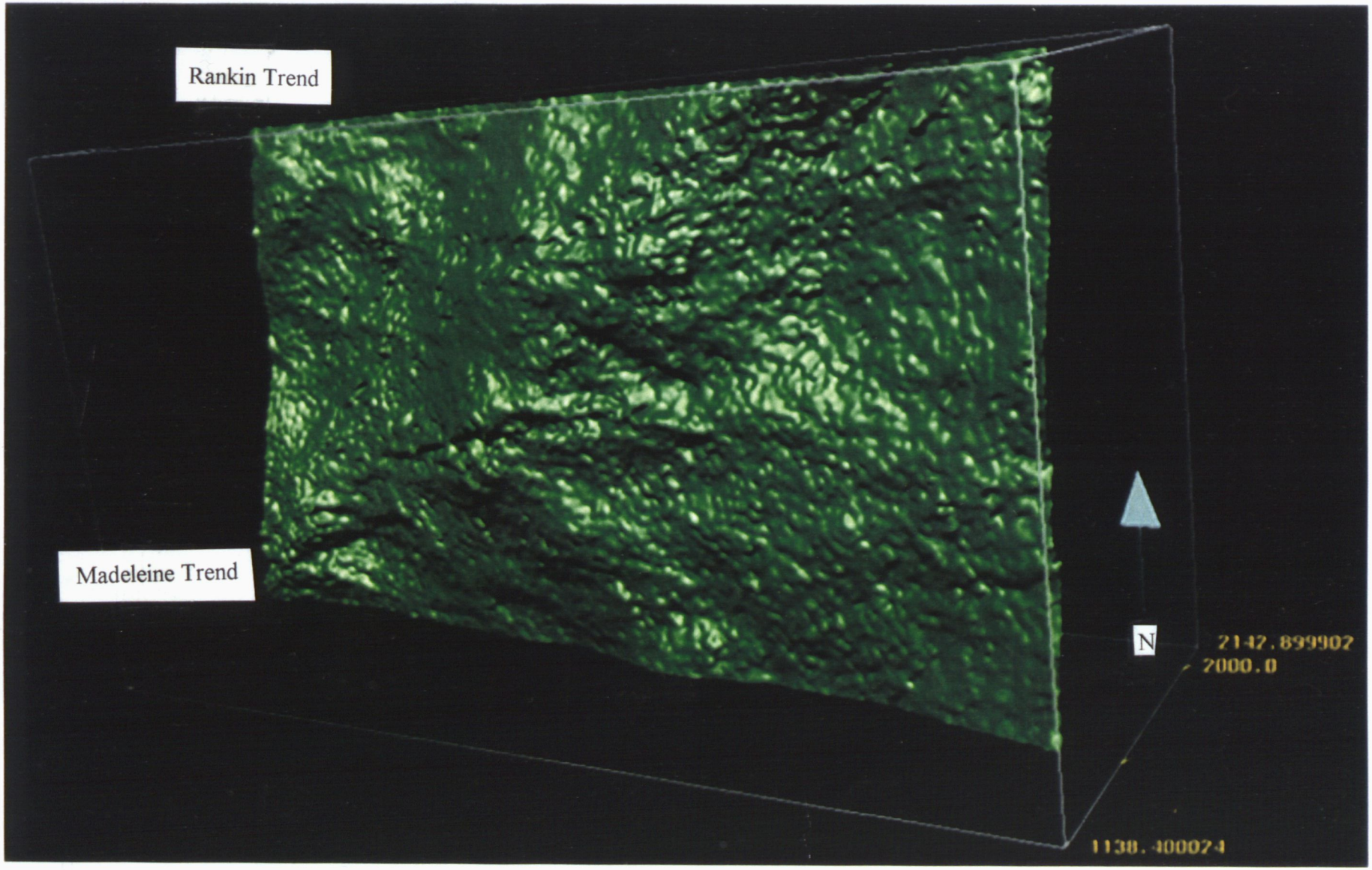
Rankin Trend
Madeleine Trend
N
2142.899902
2000.0
1138.400024

Figure 25(a) and (b). Selected seismic lines showing the main EW strike-slip fault zone.

(a) Crossline 5998, showing the main strike-slip zone (marked by a white arrow).

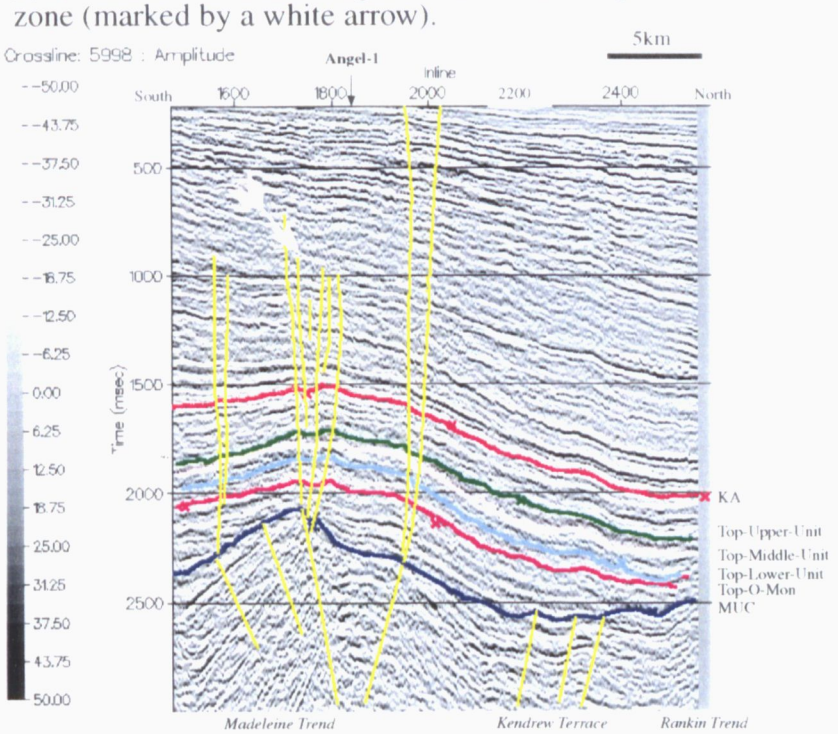

(a) Crossline 6636, showing the main strike-slip zone (marked by a white arrow).

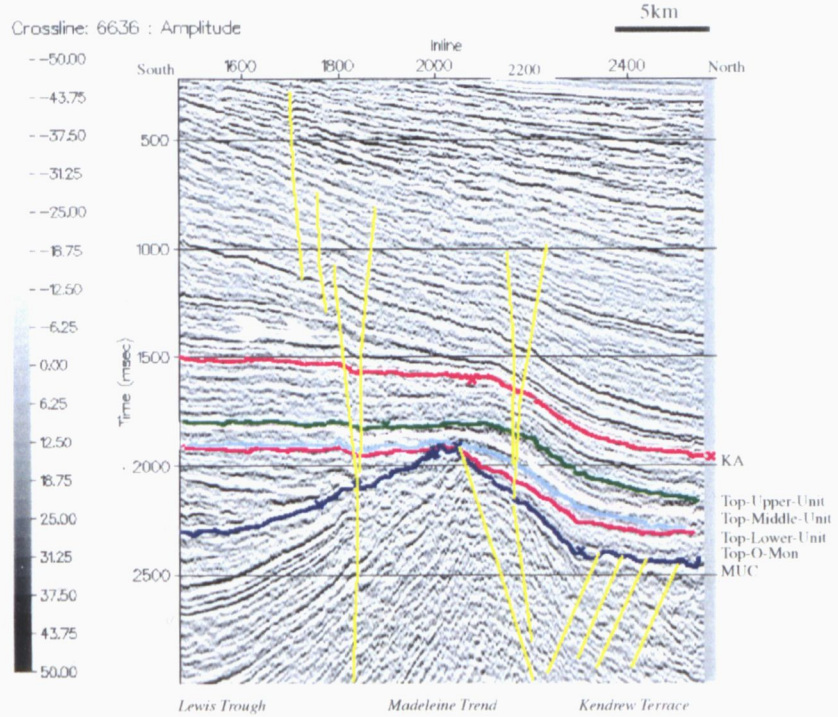

Figure 25(c). 3D visualisation of the KA and MUC seismic horizons, looking towards the east, showing the main strike-slip fault zone running EW across KA.

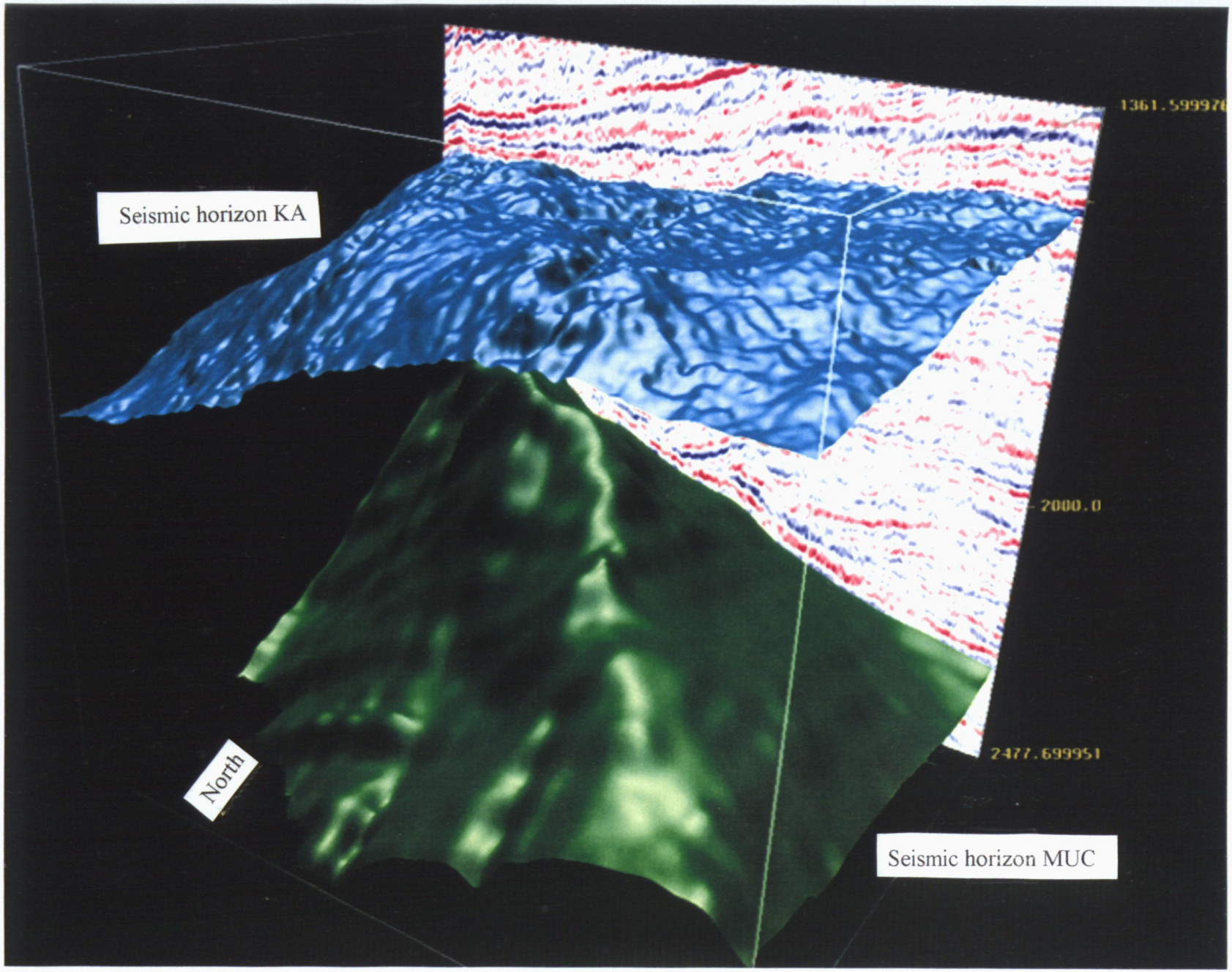
Seismic horizon KA
1361.599976
2000.0
2477.699951
North
Seismic horizon MUC

There are four sets of faults visible. The most prominent are strike-slip faults, oriented E-W, with an especially faulted zone just south of Angel-1. It is a long narrow zone (about 1 km wide) with subvertical parallel fault boundaries, and a complex inner structure (Fig 25). The fault zone is clearly seen in a 3D visualisation of the KA and MUC seismic horizons (Fig. 25c). The E-W strike-slip faults are more prominent than the NNW-SSE strike-slip faults, and this may be due to the effect of the structural grain of the W-WSW Pinjarra Orogeny, and/or the nearby WSW Cossigny Fault.

The NNE-SSW reverse faults have small but definite reverse movement, and in one area have produced a small closure (Wyvern) on the western flanks of the field (Fig 26a). The NW-SE normal faults are most prominent on the crest of the field, and have up to 25 msecs of throw (Fig 26b). An oriented core was cut in Angel-4, and an analysis of the fractures in the core showed that the only natural open fractures were those oriented NW-SE (Woodside, 1990b), the orientation of the normal faults, as predicted by the strain ellipse (Harding, 1974). Also visible is roll-over of the sediments on the northern side of the Madeleine Fault (Fig. 25a), indicating compression and reverse movement on the Madeleine Fault.

When the orientation of the strike-slip movement which was predicted from the interpreted fault pattern on the horizon KA (Fig. 23a) is compared to the orientation of the Madeleine Fault (Fig 23b), it can be seen that the predicted and actual orientations are very similar. It is concluded that the present-day fault pattern that exists in the reservoir in the Angel Field has been caused by Miocene reactivation of the Madeleine Fault.

Implications for Fluid Movement and Reservoir Development

It is known that faults can act as both conduit and barrier to fluid flow during their history (Knipe, 1987), but the present-day behaviour of the faults in the reservoir of the Angel Field will most probably be controlled by the present-day stress regime. The fact that the NW-SE-trending normal faults are the only faults in the Angel Field that are likely to be open and capable of transmitting fluids or gases will have an impact on the probable pattern of reservoir drainage when the field is brought on line. In particular, it is quite probable that the major E-W fault zone south of Angel-1 forms a significant barrier to fluid flow, and divides the field into two sections that will have to be developed separately.

Figure 26(a). Crossline 5552 showing the closure formed by a reverse fault (marked by a white arrow).

Figure 26(b). Crossline 6400 showing the normal faults at the crest of the field (marked by a white arrow).

(a) Crossline 5552, showing the closure formed by a reverse fault (marked by white arrow).

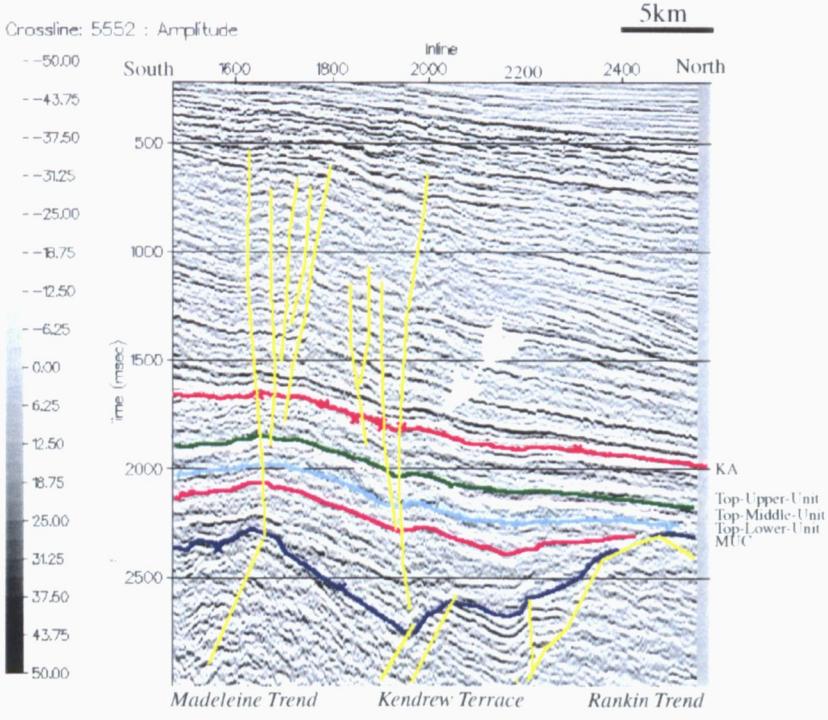

(b) Crossline 6400, showing the normal faults at the crest of the field (marked by white arrow)

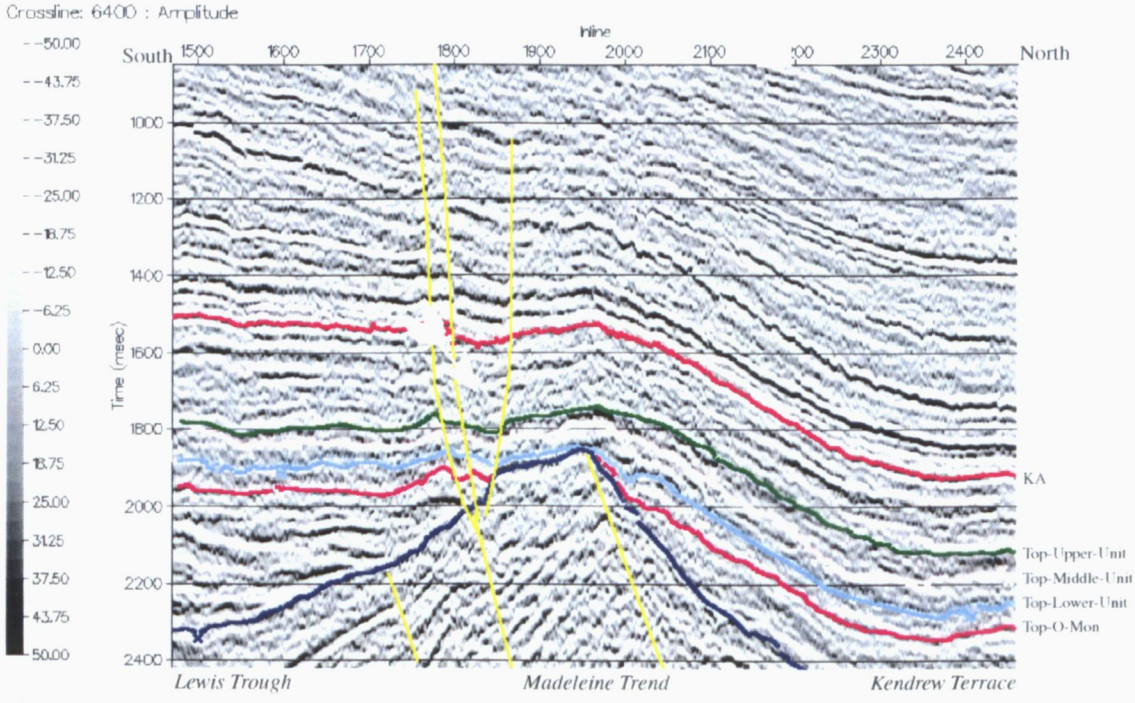

6. SEISMIC ATTRIBUTE MAPPING OF ANGEL FORMATION UNITS

After mapping the time thickness of each unit in the Angel Formation, the next step was to examine the internal seismic character of each unit, using a method developed here, to give clues to the direction of sediment transport and distribution of sediment types. This was integrated with the amplitude and isochron maps and knowledge of the depositional environment to produce a model for each unit.

Seismic Mapping of Sediment Transport Direction

The method used to map the direction of sediment transport was firstly to make a tracing of every 100th inline and every 200th crossline after flattening on the KA horizon to remove the effects of later deformation. This process yielded data on a 2.5 km square grid. Next the pattern of the reflections within each unit was analysed and classified into four categories:

1. dipping to the east or west for inlines,
2. dipping to the north or south for crosslines,
3. parallel, or
4. less than one cycle thick.

It was found that instantaneous phase displays were useful for picking the weaker reflections. A tracing of inline 2200 is shown in Figure 27 as an example. Two maps were prepared for each unit, one using crosslines and the other the inlines. These two were then combined to produce a map with an arrow at every grid point, showing the internal dip direction in 45 degree increments. The Middle Unit is shown as an example (Fig. 28). The arrows indicate the approximate direction of dip of the internal reflections of each unit and hence the local direction of sediment transport.

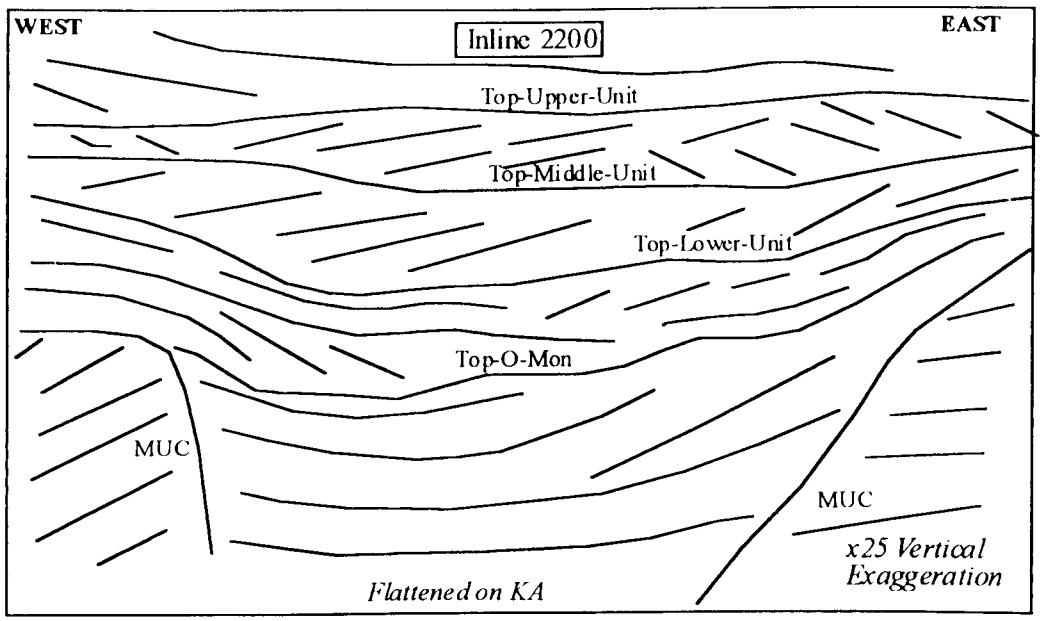

Figure 27. Tracing of inline 2200 showing units of the Angel Formation and their internal seismic character.

These maps were interpreted by drawing long arrows in order to clearly visualise the sediment transport direction in each unit (Fig. 29). Also shown are the sediment movement directions from Miller (1995) which were derived from a regional 2D grid, and the dipmeter rosettes from Angel-1. It can be seen that they both agree very well with the sediment transport patterns found here. There is quite a lot of noise in the seismic data at the Angel Formation level, but it is expressed mostly as events with high dips that crosscut the real reflections. Care was taken to exclude these events in interpreting the reflection patterns in each unit. As another quality check, several lines were chosen at random, the reflection pattern analysis was repeated, and the results compared to the original analysis. Both analyses gave almost identical results.

Lower Unit

Most of the sediment is sourced from the southwest, moves north and west into the Kendrew Terrace depocentre, and onlaps onto the Madeleine Trend (Fig. 29a). A small amount is sourced from the Rankin Trend. The amplitude map of Top-O-Mon (Fig. 30b) does not show any variation in amplitude that can be attributed to the sediment transport direction or sediment type. It appears that the Lower Unit has smoothly and homogeneously filled up the basin with sediment sourced from the southwest.

Figure 28. Pattern of reflections within the Middle Unit, initial interpretation from crosslines and inlines.

(a) Middle Unit, interpretation along crosslines

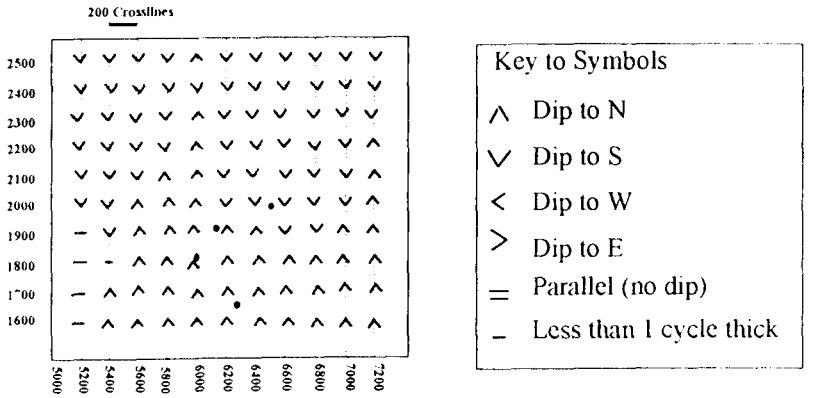

(b) Middle Unit, interpretation along inlines.

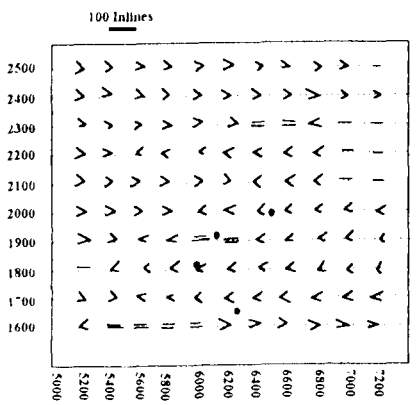

(c) Middle Unit, arrows combining crosslines and inlines.

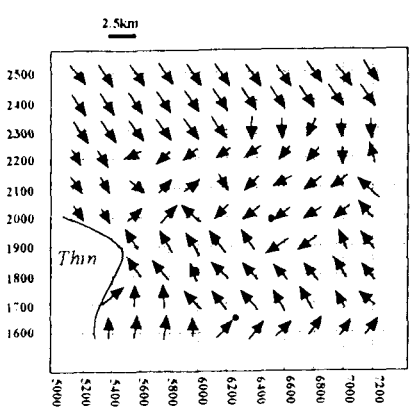

Figure 29. Sediment transport direction within the units of the Angel Formation.

(a) Lower Unit

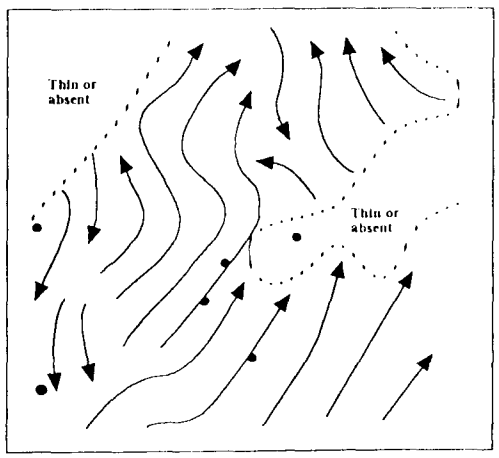

(b) Middle Unit

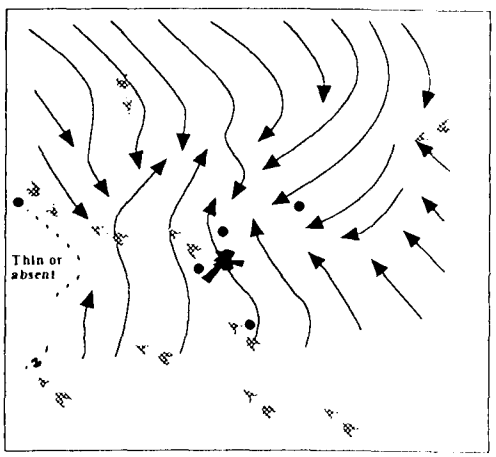

(c) Upper Unit

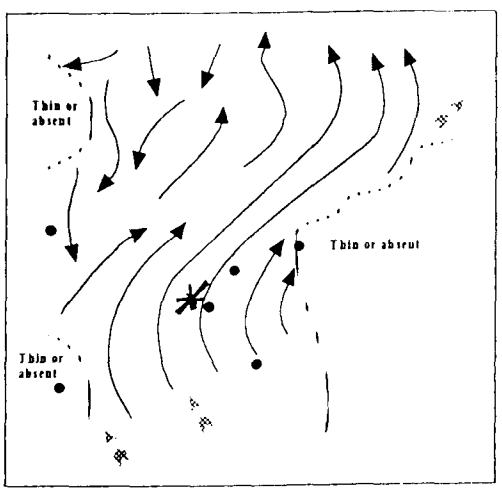

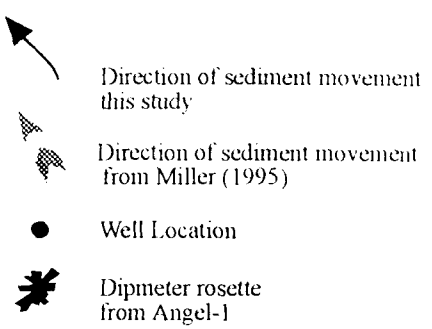

Middle Unit

The sediment transport direction map for the Middle Unit (Fig. 29b) tells a different story. There is approximately the same amount of sediment sourced from the south and from the north. The sediment from the south onlaps onto the Madeleine Trend, and swings around its southern end heading for the northern depocentre in the Kendrew Terrace. The sediment from the north is deflected towards the southwest by the Madeleine Trend. The Angel-1 dipmeter rosette shows the influence of both sediment sources. The area of strong negative amplitudes in the southeast of the study area (amplitude map of Top-Lower-Unit, Fig. 31) corresponds almost exactly with the area covered by the sediment sourced from the south. This implies that the sediment here differs in acoustic impedance (and therefore probably also in type) from the sediment sourced from the north. The internal striations in this area suggests that there was downlap or onlap.

In the amplitude map of Top-Middle-Unit (Fig. 32) the areas of medium to strong positive amplitudes correspond to Middle Unit depocentres (as defined by the Middle Unit isochron, Fig. 14a). The area of strong negative amplitudes south of Angel-1 corresponds to the intersection of the GWC with the Top-Middle-Unit horizon, and is believed to be a hydrocarbon effect. The area of strong negative amplitudes to the northeast of Angel-2 is caused by the dolomite-cemented zone. These two zones are discussed further in Chapter 8.

Upper Unit

The sediment transport direction in the Upper Unit is dominantly from the southeast (Fig.29c). It swings around the Madeleine Trend to run northeast to the depocentre to the north of the study area. A small amount of sediment is sourced from the northwest, most probably from the Rankin Trend. The amplitude of the Top-Upper-Unit horizon (Fig.33) has been affected by so many factors such as presence of gas or dolomite cement that it does not show any features attributable to the sediment transport direction.

Heavy mineral studies and sediment provenance

DiBona and Scott (1990) studied the trace heavy mineral composition of six wells in the Dampier Sub-basin. They found that Angel-3 (the only Angel well studied) had a unique heavy mineral suite, containing up to 35% hornblende in places. Hornblende is unstable and is easily decomposed during erosion, suggesting a local source with minimal reworking. They divided the Upper Jurassic section in Angel-3 into seven units. When these units are compared to the

units used in this study (Fig. 34) it can be seen that the Lower Unit corresponds to AN1, a low-hornblende unit with no correlation to any other wells used in the study. The Middle Unit corresponds to AN2, AN3, and AN4, high-hornblende units with no correlation with other wells and a high confidence in a separate source. The Upper Unit corresponds to AN5, AN6, and AN7, low-hornblende units with good correlations to similar units in all other wells (Calypso-1, Forestier-1, Samson-1, Talisman-1 and Rosemary-1).

Figure 30. Amplitude of seismic horizon Top-O-Mon (base of the Angel Formation).

(a) Amplitude of seismic horizon Top-Lower-Unit (mid *D. jurassicum*, top of the Lower Unit of the Angel Formation).

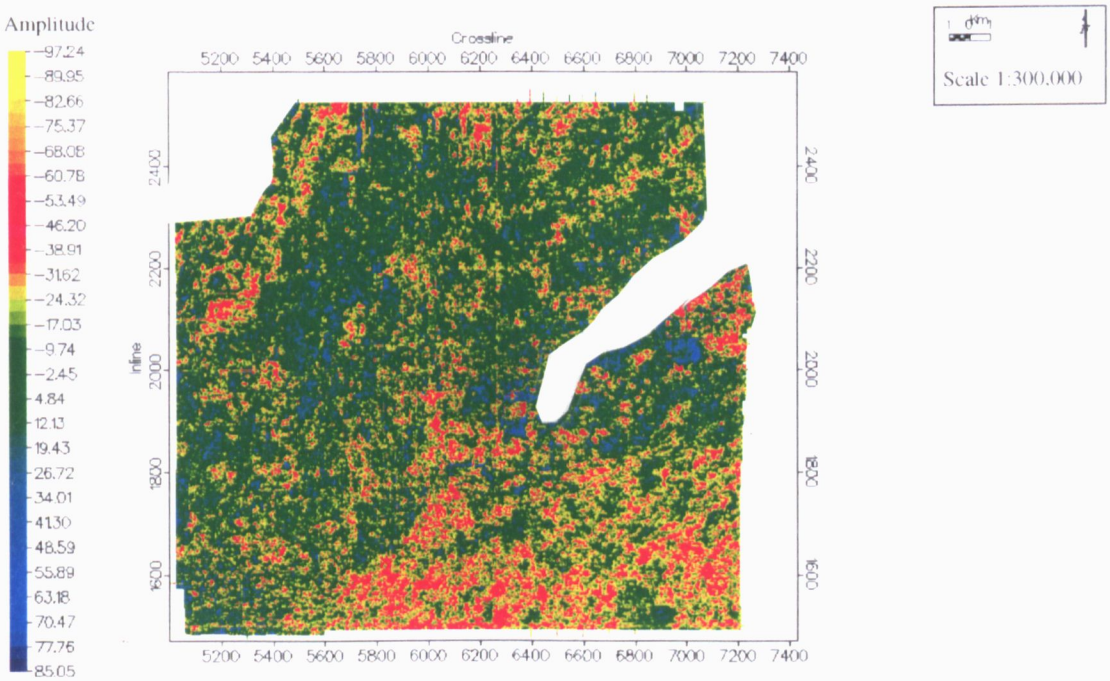

(b) Amplitude of seismic horizon Top-Lower-Unit (mid *D. jurassicum*, top of the Lower Unit of the Angel Formation), with direction of sediment movement within unit (arrows).

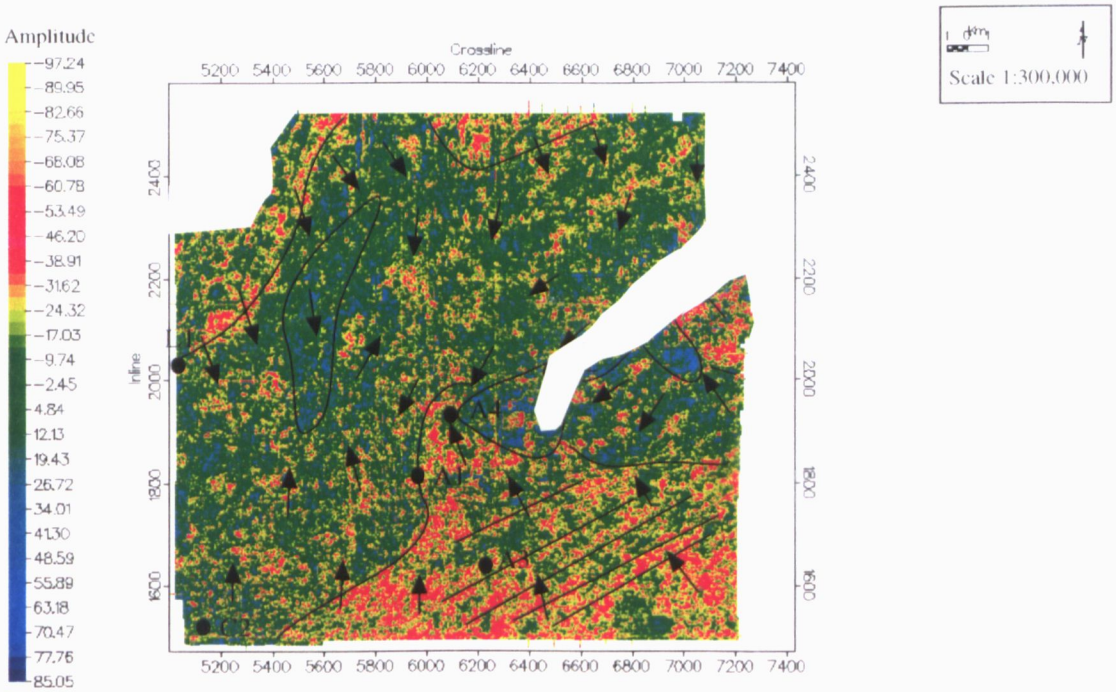

Figure 31. Amplitude of seismic horizon Top-Lower-Unit (top of the Lower Unit of the Angel Formation).

(a) Amplitude of seismic horizon KV (intra-Valanginian Unconformity)

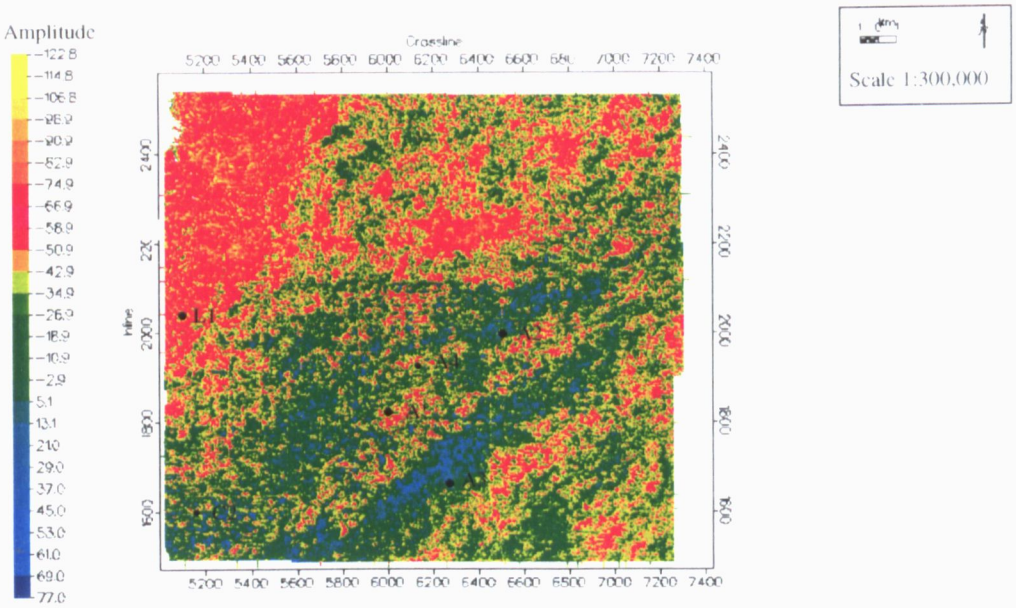

(b) Amplitude of seismic horizon Top-O-Mon (Top *O. montgomeryi*, base of the Angel Formation)

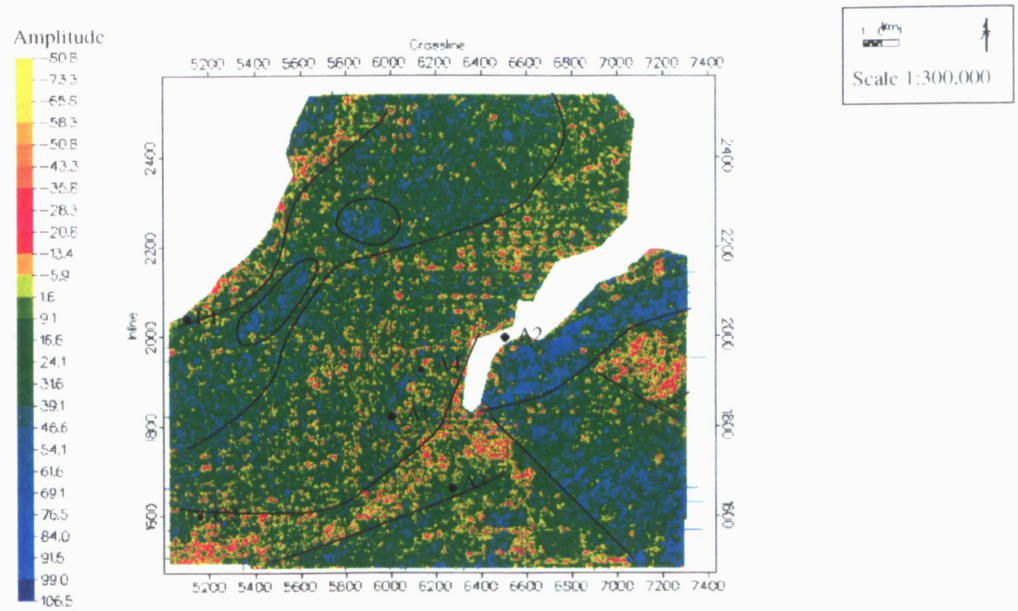

Figure 32. Amplitude of seismic horizon Top-Middle-Unit (top of the Middle Unit of the Angel Formation).

(a) Amplitude of seismic horizon Top-Middle-Unit (top *D. jurassicum*, top of the Middle Unit of the Angel Formation).

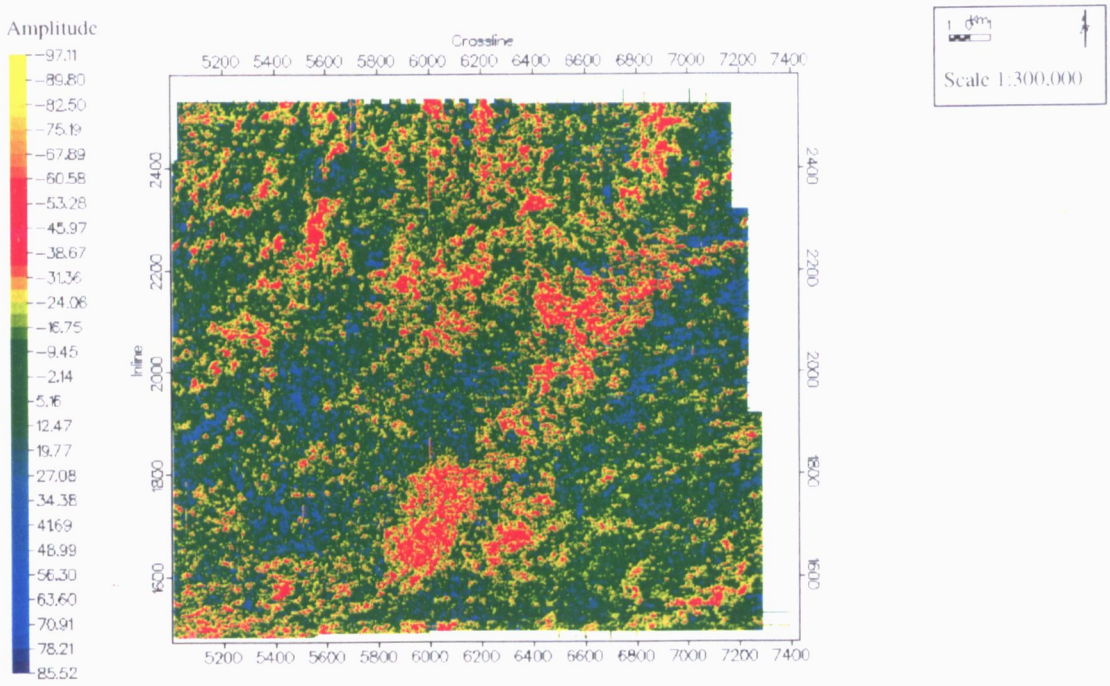

(b) Amplitude of seismic horizon Top-Middle-Unit (top *D. jurassicum*, top of the Middle Unit of the Angel Formation). Showing effect of dolomite cement in the north, and of gas in the south.

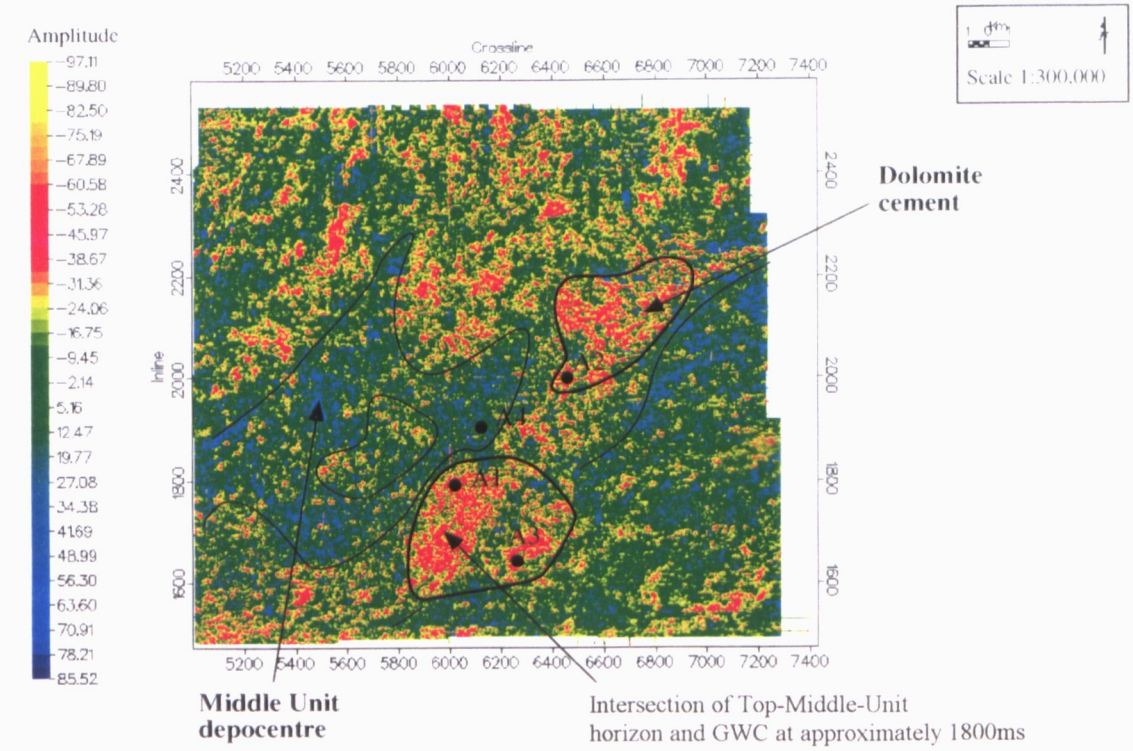

Figure 33. Amplitude of seismic horizon Top-Upper-Unit (top of the Angel Formation).

(a) Amplitude of seismic horizon Top-Upper-Unit (top of Angel Formation).

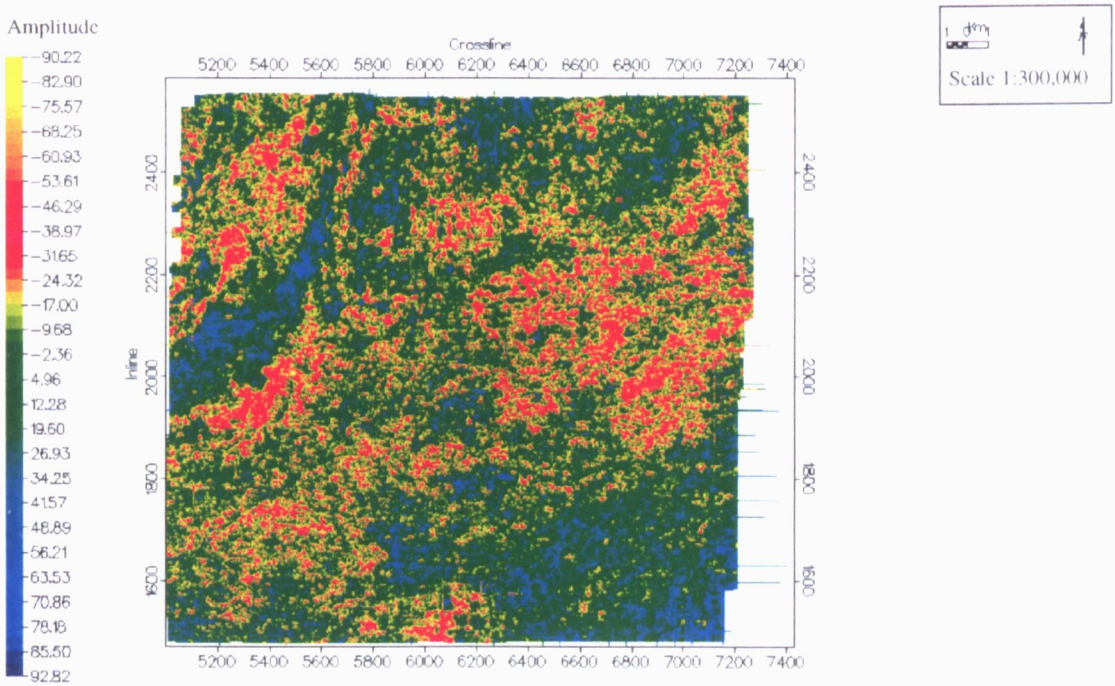

b) Amplitude of seismic horizon Top-Upper-Unit (top of Angel Formation), showing outline of known fields (black lines), time closures (white lines) and outline of dolomite-cemented zone (grey line).

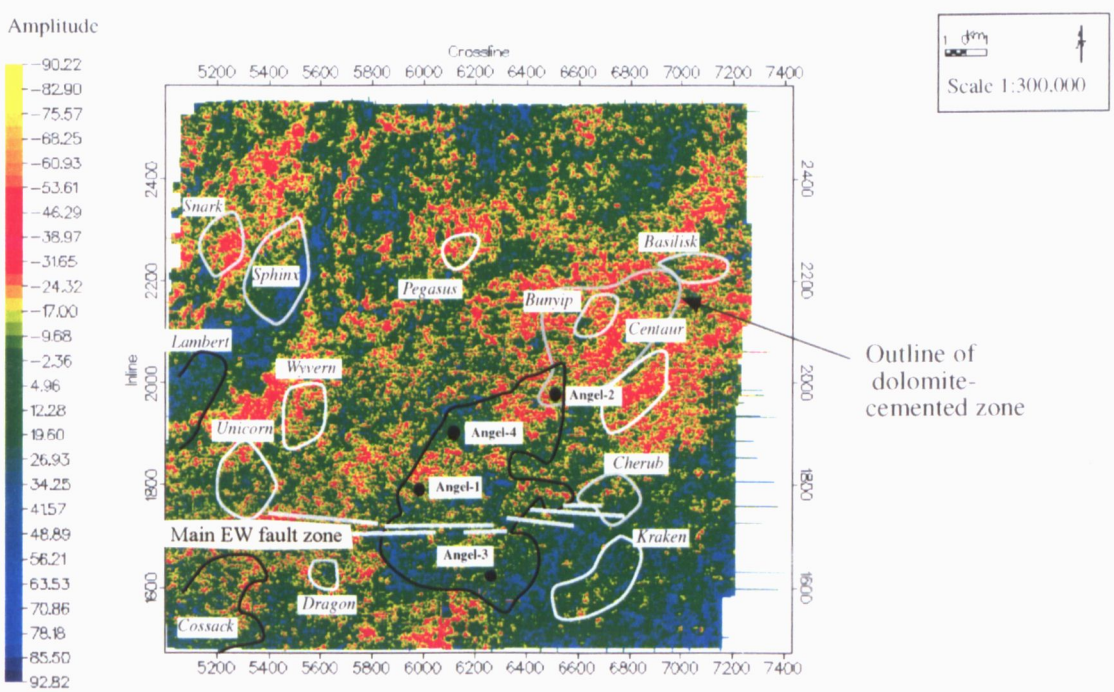

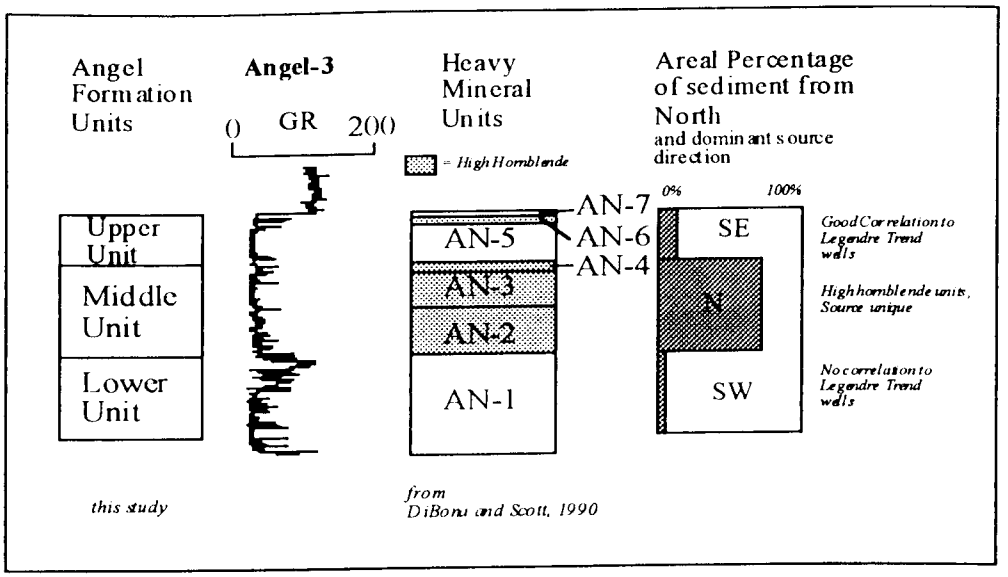

Figure 34. Angel Formation units defined by heavy mineral suite (DiBona and Scott, 1990) compared to units used in this study.

When this is compared to the sediment transport direction maps for each unit, it is clear that the Lower Unit, in which most of the sediment is sourced from the southwest, can not be correlated from any well used in this study (all of which lie to the east, on the Legendre Trend). This implies a possible distinct source from the southwest, from along the Kendrew Terrace, and maybe itself sourced from the sediments coming off the Rankin Trend. The Middle Unit, in which most of the sediment is sourced from the north, corresponds to the high-hornblende units. This suggests that the source for the Middle Unit was proximal to the north. It is known that sandstones of the Angel Formation are present in the Beagle Sub-basin, and were sourced from local areas of uplift such as the DeGrey Nose, the Lambert Shelf, and emergent intrabasin fault blocks (Blevin et al., 1994). The relative drop in sealevel during the deposition of this unit may have exposed the local areas of uplift to the north, therefore increasing the potential sediment input from those areas. It is possible that this sediment moved towards the south, into the Dampier Sub-basin. The Upper Unit, in which most of the sediment is sourced from the southeast, has been correlated to several wells along the Legendre Trend, suggesting that this is the source of the sediment. This is summarised in Figure 34.

Hocking (1992) suggested that the Tithonian sandstone in the Dampier Sub-basin had a multiple-feeder source from the Legendre Trend plus a separate point or canyon source in the

Angel area. Miller (1995) mapped a slope apron along the eastern margin of the Lewis Trough, with multiple source axes on the Legendre Trend, and a possible sediment source axis in the north. It is not in doubt that for most of the Callovian to Tithonian the major sediment source was the Legendre Trend area, but this study has looked at the *D. jurassicum* to *K. wisemaniae* sandstone in more detail than previous work, and has come to slightly different conclusions about the sediment provenance for this interval. The Legendre Trend did not play a major role as a sediment source for most of this interval. Rather, the Kendrew Terrace and the area to the north acted as major inputs for the Lower and Middle Units. It is only in the thin Upper Unit that the Legendre Trend became the main sediment source.

7.PETROPHYSICS

Data Available

The following logs were run over the reservoir section in all wells: gamma ray, sonic, density, neutron, and resistivity. The log data available are summarised in Table 7. The log data from Angel-1, 2 and 3, Lambert-1, and Cossack-2 were acquired from Wiltshire Geological Services. The data from Angel-4 were kindly donated by Woodside Offshore Petroleum Pty Ltd. Digital data for these wells were loaded into the Mincom package *GEOLOG*, which was used for all log analysis and display.

	Angel-1	**Angel-2**	**Angel-3**	**Angel-4**
Year Drilled	1971	1972	1973	1990
Gamma Ray	GR	GR	GR	GR
Sonic	DT	DT	DT	DT plus shear
Density	FDC	FDC	FDC	LDT
Neutron	SNP	SNP	CNL	CNL
Resistivity	LL7	LL9	LL9	LLD/LLS
Micro-resistivity	MLL/ML	MLL/ML	no	MSFL
Other	Induction, , SP, HDT, FIT	Induction, , SP, HDT, FIT	SP, HDT, FIT	SP, RFT, SHDT

Table 7. Summary of log data available over the reservoir section, and the tool used to record the log, for the four Angel wells.

Quality Control and Environmental Corrections

The original field records for each log were checked for quality of calibrations and field procedure. In Angel-3, the density and neutron logs in the interval 2837-3786m appear to be reading incorrectly: the neutron readings are 12 pu too high and the density readings are also 0.04 g/cc too high. The calibrations appear to be correct. This is below the zone of interest, so no further investigation was carried out.

Borehole environment corrections were applied, for factors such as borehole size, mud density, temperature, mudcake and so on, which were read from the log headers. The log data were

depth matched as required, using the deep resistivity log as the depth reference. The reservoir temperature in Angel-2 was estimated, using the Horner plot method, to be 105 degC. The reservoir temperature could not be estimated in Angel-1 or 3 because only one bottom hole temperature was recorded on the log header in the entire suite (100 degC). This is an indication of either broken thermometers (and no replacements) or sloppy operating technique on the part of the engineer. The bottom-hole temperature in Angel-4 was 100 degC. The borehole conditions were good in all wells, with no significant washouts or hole rugosity.

Petrophysical Evaluation

Porosity and Volume of Clay

Total porosity was calculated using the density log, corrected for hydrocarbons using the microresisitivity. The gas density used was 0.22 g/cc (Woodside, 1989). The matrix density used for Angel-1 and Angel-3 was 2.67 g/cc, and 2.65 g/cc for Angel-4. This difference is attributed to the different density tools used: the older FDC versus the newer LDT. Angel-2 contains significant amounts of dolomite, which results in a matrix density of up to 2.75 g/cc where the dolomite is present. These values were determined from resistivity-density crossplots, and differ only slightly from the values used by Woodside (1989, 1992). Where the dolomite cement was absent, the matrix density was 2.67 g/cc. The average porosity for all wells (in the upper 75m) except Angel-2 was 18% (Figs. 35 and 36). In Angel-2, the average porosity in the non-cemented section was 18% and over the gross cemented interval the average porosity was 8%. The volume of clay minerals in the rock, V_{CL}, was calculated from the GR log using $\frac{GR - GR_{min}}{GR_{max} - GR_{min}}$. The average V_{CL} for the Angel wells (1,2,3 and 4) was 8%, 6%, 17% and 13% respectively (Figs. 35 and 36).

Hydrocarbon Saturation

The hydrocarbon saturation was determined in Angel-4 using the Archie equation,

$$Sw = \sqrt[n]{\frac{FR_w}{R_t}},$$

and

$$F = \frac{1}{\Phi^m},$$

(13)

Figure 35. Histograms of porosity and V_{clay} for wells Angel-1, Angel-2, and Angel-3.

(a)

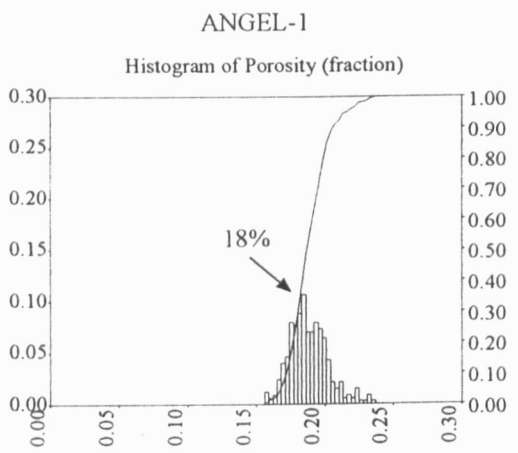
ANGEL-1
Histogram of Porosity (fraction)
18%

(b)

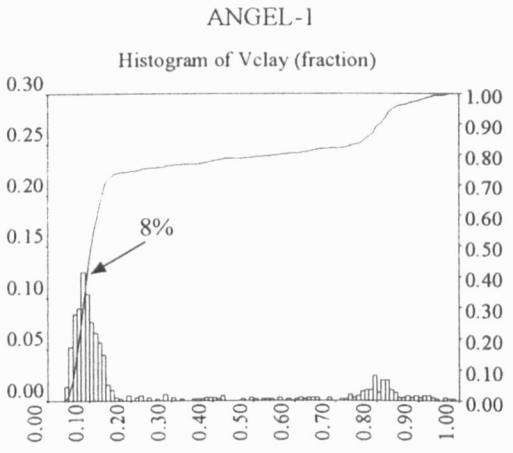
ANGEL-1
Histogram of Vclay (fraction)
8%

(c)

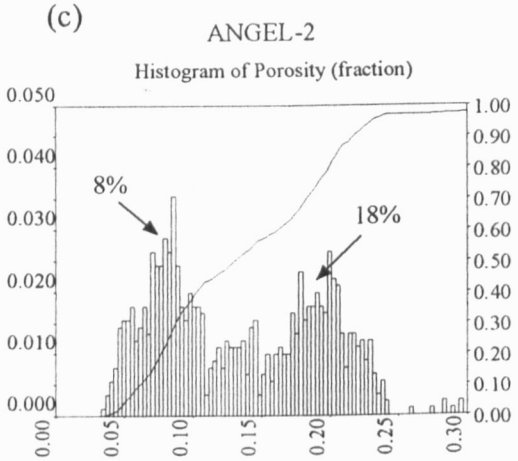
ANGEL-2
Histogram of Porosity (fraction)
8%
18%

(d)

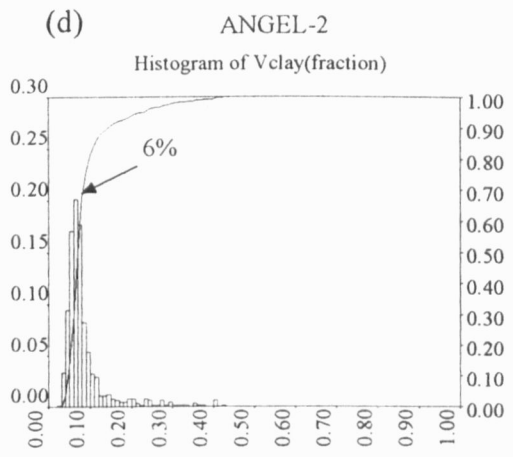
ANGEL-2
Histogram of Vclay(fraction)
6%

(e)

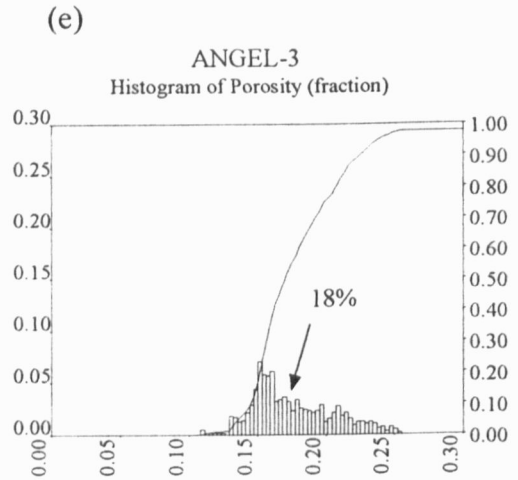
ANGEL-3
Histogram of Porosity (fraction)
18%

(f)

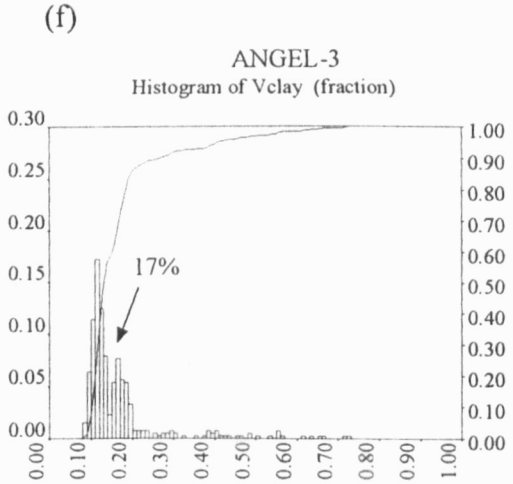
ANGEL-3
Histogram of Vclay (fraction)
17%

Figure 36. Histograms of porosity, density, water saturation and invaded zone water saturation for Angel-4.

(a)

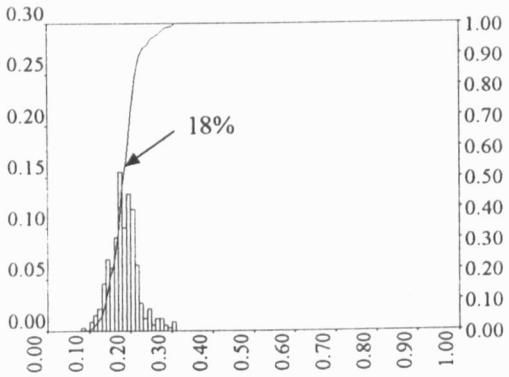
ANGEL-4
Histogram of Porosity (fraction)
18%
0.30
0.25
0.20
0.15
0.10
0.05
0.00
1.00
0.90
0.80
0.70
0.60
0.50
0.40
0.30
0.20
0.10
0.00
0.00
0.10
0.20
0.30
0.40
0.50
0.60
0.70
0.80
0.90
1.00

(b)

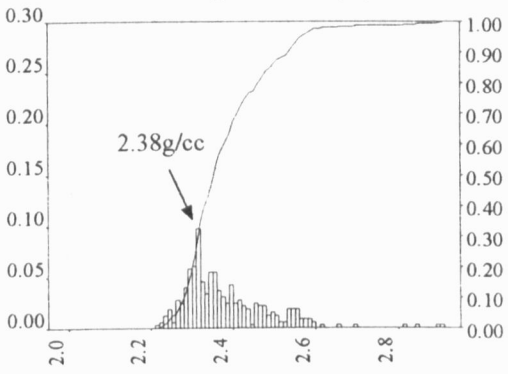
ANGEL-4
Histogram of density (g/cc)
2.38g/cc
0.30
0.25
0.20
0.15
0.10
0.05
0.00
1.00
0.90
0.80
0.70
0.60
0.50
0.40
0.30
0.20
0.10
0.00
2.0
2.2
2.4
2.6
2.8

(c)

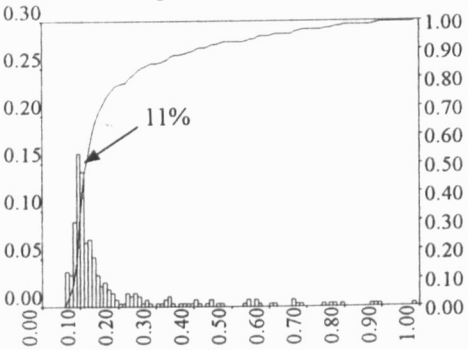
ANGEL-4
Histogram of Sw (fraction)
11%
0.30
0.25
0.20
0.15
0.10
0.05
0.00
1.00
0.90
0.80
0.70
0.60
0.50
0.40
0.30
0.20
0.10
0.00
0.00
0.10
0.20
0.30
0.40
0.50
0.60
0.70
0.80
0.90
1.00

(d)

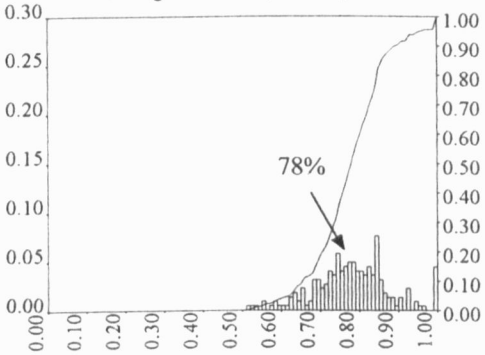
ANGEL-4
Histogram of Sxo (fraction)
78%
0.30
0.25
0.20
0.15
0.10
0.05
0.00
1.00
0.90
0.80
0.70
0.60
0.50
0.40
0.30
0.20
0.10
0.00
0.00
0.10
0.20
0.30
0.40
0.50
0.60
0.70
0.80
0.90
1.00

where S_w is water saturation, F is the formation factor, R_w is pore-water resistivity, R_t is true rock resistivity, and Φ is porosity. The reservoir sands are only very slightly shaly, therefore the correction for clay conductivity is minimal, as indicated from cation exchange capacity (CEC) measurements on core plugs from Angel-4 (Woodside, 1992). The cementation factor, m, and saturation exponent, n, are 1.73 and 1.81 respectively, and the formation water resistivity is 0.095 ohm-m at 100 degC, which corresponds to a water salinity of 24,000 ppm $NaCl_{eq}$ (Woodside, 1992). These values were determined from Angel-4 measurements, which used a dual laterolog resistivity tool, rather than the Laterolog 7 and 9 used in the earlier wells. These older tools are less focussed and more influenced by invasion, and it was considered that the results from the more modern tool would be more accurate.

A full set of modern resistivity logs was available for Angel-4, and the R_t was calculated from the LLD/LLS logs, corrected using the MSFL. The invasion diameter was calculated to be between 0.5 and 1m. The average water saturation in Angel-4 was found to be 11%, and the average residual water saturation was 78% (Fig. 36).

Shear and Compressional Slowness

The average compressional slowness of the gas-bearing interval of Angel-4 was 82 us/ft (12200ft/s or 3720m/s), and the average V_p/V_s ratio was 1.66 in the gas zone, and 1.79 in the water-wet zone. The V_p/V_s ratio was lowered by the presence of gas in the invaded zone. The residual gas is indicated by the value of S_{xo} being 78%, ie. in the invaded zone, the pore spaces contain 22% gas. Knowing the effect of gas on the P-wave velocity is crucial to AVO analysis, and this is discussed in the next section on Biot-Gassman modelling.

Summary

The logs from Angel-4 were used to determine physical parameters of the rocks for input into modelling, by a simple petrophysical analysis. Angel-4 was used in preference to the other wells, as it has a reasonably complete suite of modern logs. The petrophysical parameters were averaged over the top 75m of the reservoir. It is assumed that the rock properties of the Angel Formation in the reservoir interval do not vary much in the Angel wells, except in Angel-2. The errors induced by this process are likely to be minimal, due to the homogeneous nature of the reservoir rock in each well. The presence of the dolomite-cemented zones in Angel-2 completely changes the seismic response of the interval and makes this type of analysis minimally useful where the dolomite cement is present.

Modelling the effect of gas on rock properties

The elastic properties of a saturated rock may be expressed in terms of the properties of the solid skeleton of the rock and the fluid in the pore spaces, by the Biot-Gassman equations (Gassman, 1951; Thomsen, 1985), a modified low-frequency approximation of Biot's (1956) theory. The equations, in terms of compressional (V_p) and shear (V_s) velocities, are

$$V_p^2\rho = K_p + K_b + 4/3N,$$

$$V_s^2\rho = N,$$

and

$$K_p = \frac{1-\frac{K_b}{K_m}}{\frac{(1-\frac{K_b}{K_m})-\Phi}{K_m}+\frac{\Phi}{K_f}}, \tag{14}$$

where K_b is wetted bulk modulus, K_p is pore space modulus, K_m is solid matrix modulus, K_f is pore fluid modulus, N is shear modulus, ρ is bulk density, and Φ is porosity. K_b and N depend on the mineralogy of the rock, and depend strongly on porosity for a given rock. The bulk density ρ is given by

$$\rho = \Phi(\rho_w S_w + \rho_h(1-S_w)) + (1-\Phi)\rho_m \tag{15}$$

where ρ_w, ρ_h and ρ_m are the densities of water, hydrocarbon, and solid rock matrix respectively, S_w is water saturation and Φ is porosity. The effect on shear velocity of fluid composition is small as it only affects ρ. The effect on P-wave velocity of fluid composition is larger, as it affects the pore space modulus K_p.

The assumptions inherent in these equations are:

1. The pore spaces are connected,
2. The frequency of the sound wave is low (seismic rather than ultrasonic),
3. The solid is locally homogeneous and isotropic,
4. There are no cracks in the rock,

5. The relative movement between fluid and solid is very small compared to movement of the bulk rock, ie., fluid and solid move together, and
6. The fluid does not interact with the solid in any way that could change the shear modulus.

The effect of cracks is taken into account by the squirt theory (Dvorkin and Nur, 1993; Dvorkin et al., 1994). The Biot-Gassman equations are a first order approximation to the fluid saturation effects as a function of mineralogy and porosity in granular rocks (Thomsen, 1985; Murphy et al., 1993). The predictions of velocity from these equations work very well in clean quartz sandstones (Murphy et al., 1993). All terms in the Biot-Gassman may be measured or estimated from log or rock data, except the wetted bulk modulus K_b and shear modulus N. The moduli K_b and N may be estimated using an empirical relationship between the respective solid matrix moduli (K_m, N_m), and porosity, in the form

$$K_b = (1-\beta)K_m, \tag{16a}$$

and

$$N = (1-\beta)N_m \tag{16b}$$

Here β is the empirical Biot coefficient, where

$$\beta = 1-(1-\Phi)^{1-\frac{3}{\Phi}}, \tag{17}$$

(Krief et al., 1990) or

$$\beta = 0.022 + 2.666\Phi + 3.002\Phi^2 - 9.002\Phi^3, \tag{18}$$

(Murphy et al., 1993). Using one of these two equations, the Biot-Gassman equations can be written in a form where all inputs can be determined from logs, cores, or laboratory measurements:

$$V_p^2 = \frac{(1-\beta)}{\rho}(K_m + \frac{4}{3}N_m) + \frac{\beta^2}{\rho}[\frac{1}{\frac{(\beta-\Phi)}{K_m} + \frac{\Phi}{K_f}}] \quad ,$$

and

$$V_s^2 = (1-\beta)\frac{N_m}{\rho}. \qquad (19)$$

The effect of water saturation on the compressional and shear velocities was calculated by changing S_w, recalculating ρ and K_f (fluid modulus) and determining new values for V_p and V_s. The effect of porosity on the velocities was modelled by using equations (17) or (18) to calculate a new β and ρ, then using these for new values of V_p and V_s. The effect of clay percentage (actually any change in rock lithology) was modelled by recalculating the solid matrix moduli K_m and N_m, and the bulk density. Using this technique, it was possible to model the effect of changes in water saturation (for any hydrocarbon type), porosity and lithology on the compressional and shear velocities of the rock. This method is a first-order approximation only, and its limitations and assumptions outlined previously must be kept in mind, but it is widely used and gives good results in clean sandstones.

Angel-4: Fluid Substitution

An *EXCEL* spreadsheet was used for the Biot-Gassman modelling. The input for Angel-4 consists of the averaged rock properties that were calculated earlier in this section. The Krief et al. (1990) equation (17) was used for the Biot coefficient. The results are shown in Fig. 37. The Poisson's Ratio in the water-wet rock is almost 0.25, and it decreases quickly to 0.17 for water saturations below 95% (ie with 5% gas or more). This implies that a small gas saturation has an almost identical effect on the Poisson's Ratio as a high gas saturation, which is a perennial problem in AVO analysis (Castagna and Backus, 1993). Figure 37(a) shows that the *P*-wave velocity is around 12900 ft/sec (3930m/s) when the rock is water-wet, decreasing to 12200 ft/sec (3720m/s) at a water saturation of 80%, and then slowly increasing with increasing gas saturation to 12500ft/sec (3800m/s). The acoustic impedance is greatly affected by the presence of gas (Fig. 37c) and showed a significant drop at 95% water saturation. The presence of gas at saturations higher than 5% is predicted from this model to significantly

affect the rock properties of the Angel Formation reservoir, which should be visible in the seismic data. The probability of distinguishing an economic gas saturation from low-saturation 'fizz-water' is likely to be minimal.

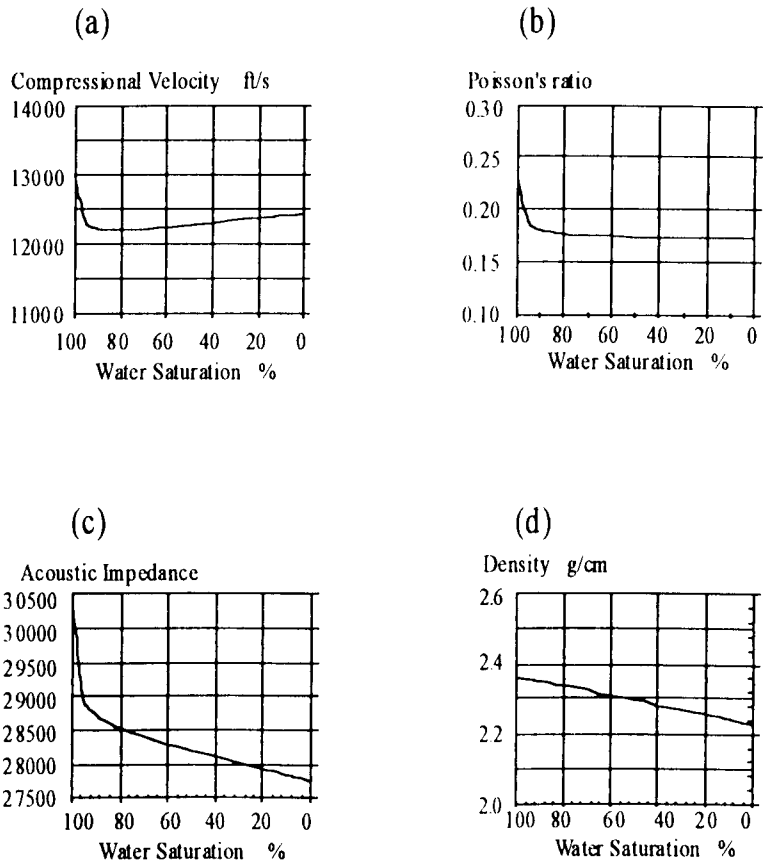

Figure 37. Biot-Gassman fluid replacement model of Angel Formation sandstone at Angel-4.

8. AMPLITUDE ANALYSIS OF THE STACKED 3D SEISMIC DATA

Analysis of the amplitudes in stacked 3D seismic data for information on lithology and fluid properties is an essential part of a detailed field study. The techniques commonly used are inversion to acoustic impedance and geostatistical modelling. The seismically-derived values of acoustic impedance are tested for correlation with log-derived properties such as porosity, lithology, and water saturation at well locations and the log properties are then extrapolated through the volume, guided by the seismically-derived acoustic impedance. Inversion requires good quality data and careful processing including preservation of relative amplitudes. Geostatistical modelling uses log data to predict small-scale structure in the reservoir. Commonly-used methods include kriging, stochastic modelling, and object-based generic units (Ariffin et al., 1995). Geostatistical modelling was not suitable for this study due to lack of well control. Computer software for inversion of a 3D volume was not available during this study, therefore other methods that were less dependent on computing power and well control were used to examine the amplitudes in the stacked 3D data.

Dolomite-cemented zones in the Angel Field

Diagenetic characteristics of the dolomite cement

In wells drilled to date, the Angel Formation is generally of good reservoir quality, with porosity of 14-20% and core permeability of 150-700mD, except in Angel-2, where the porosity is reduced to 5% or less and permeability to a few milliDarcies (Vincent and Tilbury, 1988) by pore-filling dolomite cement (Ryan-Grigor and Schulz-Rojahn, 1995). Petrographic investigations show that the dolomite cement occurs in irregular patches, locally completely cementing the rock, and has a poikilotopic texture. The dolomite cement occurs late in the diagenetic sequence of the Angel Formation (Fig. 8). The dolomite cement is observed to fill sub-vertical microfractures containing small angular to sub-angular quartz grains, and contains minor oil, suggesting that petroleum migration occurred synchronously with microfracture development and carbonate cementation. Carbon isotope values of the dolomite cement range from -14.1 to -15.5 per mil PDB, and oxygen isotope values range from -9.9 to -10.5 per mil PDB (Schulz-Rojahn et al., 1996).

Log character of the dolomite cement

The dolomite-cemented zones in Angel-2 produce marked increases in density and resistivity, and decreases in neutron porosity and sonic travel time (Fig. 38). In carbonate-cemented

intervals, bulk density can be as high as 2.6g/cc, compared to about 2.35g/cc in sandstones without significant cement. The sonic log reads around 260 μs/m (3850m/s) in uncemented zones, and this decreases to around 180-200 μs/m (5000-5550m/s) in cemented zones. The cement occurs in discrete zones that range from a few metres up to about 40m thick, separated by up to 20m of relatively clean, porous sandstone. The cumulative thickness of these cemented intervals, that occur both above and below the gas-water contact, is about 164m, or approximately 67 per cent of the *P. iehiense* and *D. jurassicum* zones intersected at Angel-2 (Ryan-Grigor and Schulz-Rojahn, 1995).

Seismic response of the dolomite cement

Figure 38 shows the acoustic impedance produced by the density and sonic logs in the upper Angel Formation at Angel-2. The wavelet in the 3D seismic data has a centre frequency of around 35Hz. The Dix interval velocity, calculated from the stacking velocity, at reservoir depth is around 3500m/s, with a resulting seismic wavelength of 100m. As the limit of resolution is approximately one-quarter of a wavelength, the acoustic impedance curve has been filtered the minimise the effect of beds thinner than 25m. When the filtered acoustic impedance curve is compared to the vertical extent of the cemented zones, it is apparent that each major cement interval has produced a separate, seismically visible change in acoustic impedance. The synthetic seismogram for Angel-2, provided a good match with the 3D seismic data. Close to the well location, seismic reflections correlate well with individual carbonate-cemented zones. However, these individual reflections can not be traced away from Angel-2, which may be due to a lack of lateral continuity of the cemented layers, or tuning effects related to the changes in thickness and vertical arrangement of the layers. Furthermore, the seismic data are affected by multiples which may also account for the fact that individual cemented layers can not be mapped away from the well location. Only the grossly cemented interval is mappable as a result of its high-amplitude seismic response. Areal delineation of this high-amplitude zone was accomplished by taking the root-mean-square of the amplitude in a 130msec interval below the top of the Angel Formation (the Top-Upper-Unit horizon). A map of this RMS amplitude (Fig. 39) suggests that the dolomite cement is confined to the north-eastern parts of the Angel Field. The amplitudes are strongest along the crest of the Madeleine Trend structure, and extend northwards well past the present-day gas-water contact. The area of high amplitudes in the southern part of the field near Angel-1 is attributed mostly to the presence of gas, and is discussed later.

Figure 38. The effect on the well logs of the dolomite-cemented zones in Angel-2, showing the smoothed acoustic impedance curve, and the match of the synthetic seismogram to the 3D seismic at the well location. Note the very high acoustic impedance produced by the dolomite-cemented zones.

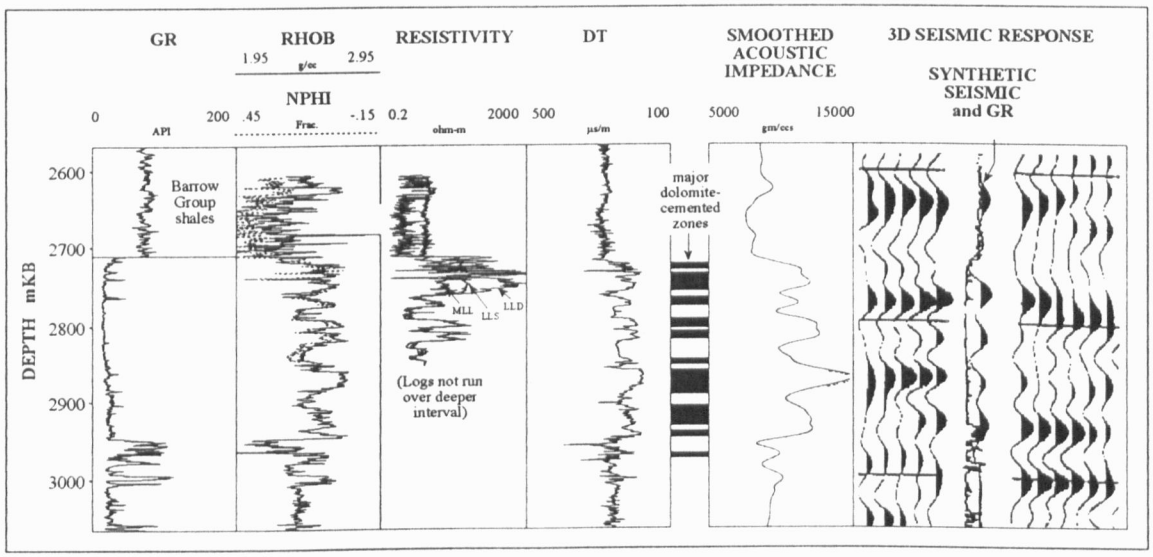
GR
RHOB
1.95 g/cc 2.95
NPHI
0 API 200 .45 Frac. -.15
RESISTIVITY
0.2 ohm-m 2000
DT
500 µs/m 100
SMOOTHED ACOUSTIC IMPEDANCE
5000 gm/ccs 15000
3D SEISMIC RESPONSE
SYNTHETIC SEISMIC and GR
DEPTH mKB
2600
2700
2800
2900
3000
Barrow Group shales
MLL
LLS
LLD
(Logs not run over deeper interval)
major dolomite-cemented zones

Figure 39. RMS amplitude in 130ms time window below the top of the Angel Formation (Top-Upper-Unit seismic horizon).

(a) RMS amplitude in 130msecs time window below Top-Upper-Unit horizon.

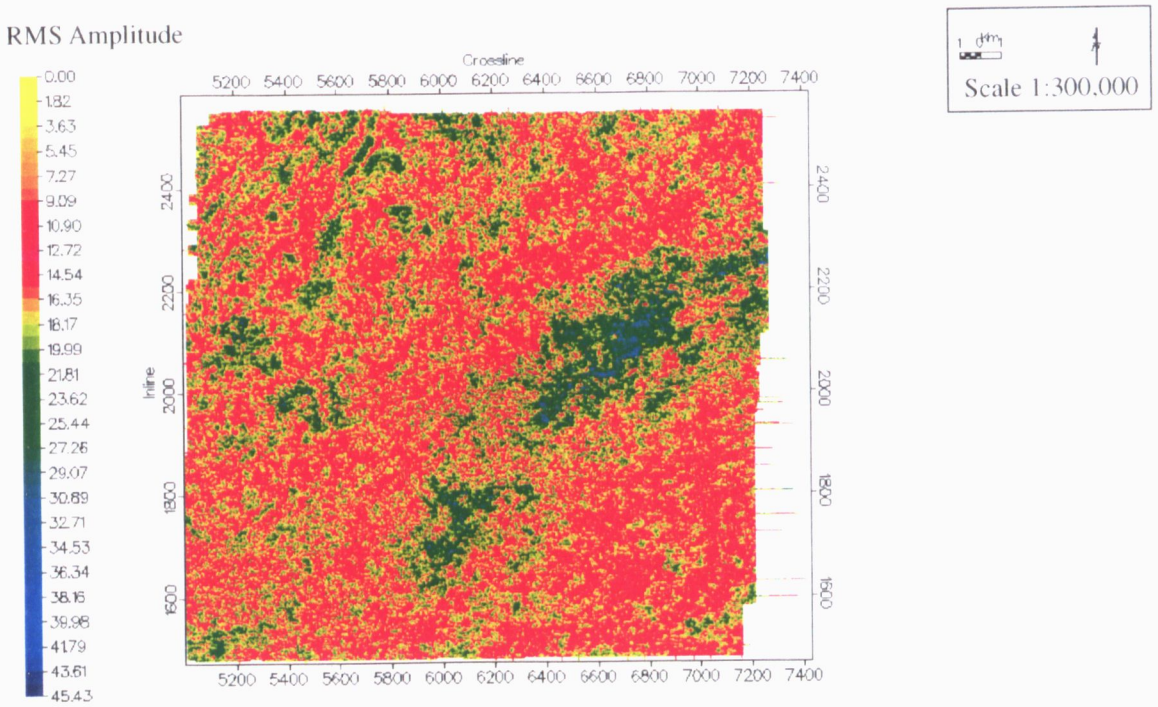

(b) RMS amplitude in 130msecs time window below Top-Upper-Unit horizon, showing outline of known fields (black lines), time closures (white lines) and outline of dolomite-cemented zone (grey line).

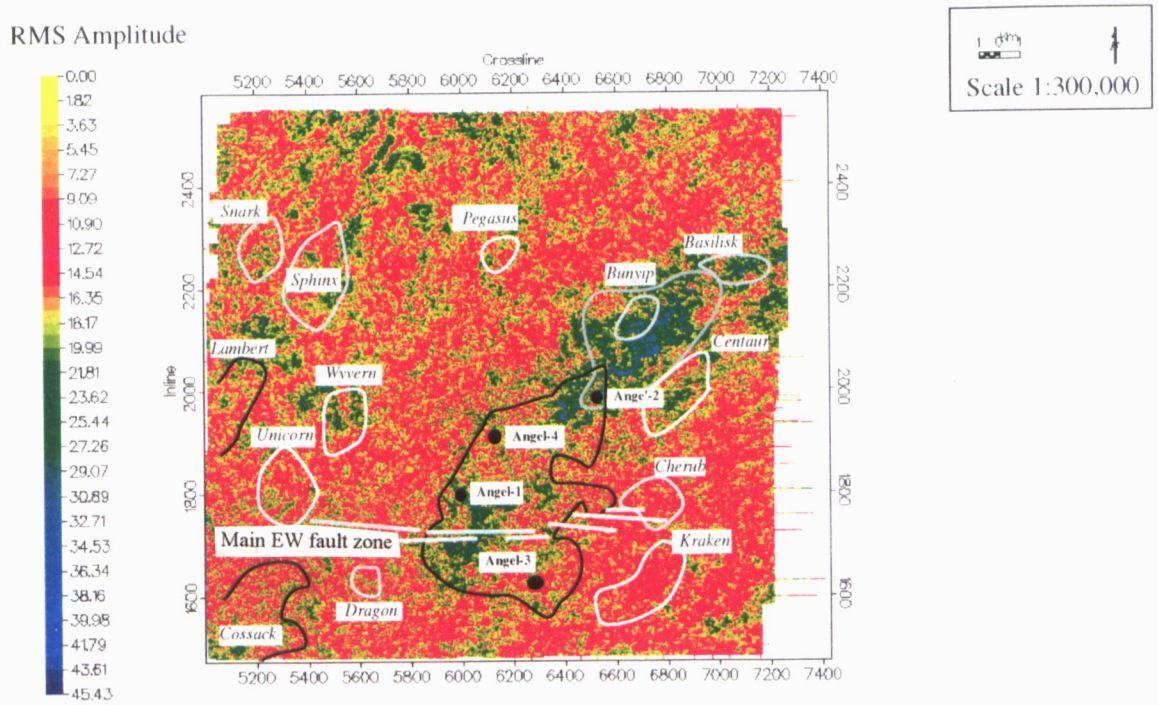

Evolution of structural closure relative to dolomite cement emplacement

Isochron maps produced for the interval between the top of the Angel Formation (Top-Upper-Unit horizon) and selected Tertiary horizons enabled identification of the timing of development of structural closure in the Angel Field. The Tertiary horizons were TE (Eocene), mid-Miocene (TME), and Late Miocene (TML2). They are all regional to global erosional or non-depositional events, and each is assumed to have had little or no relief at the time of its formation. The isochron maps (Fig. 40) indicate that no structural closure was available at reservoir level in the Angel Field until the late Miocene. A significant NNE-SSW trending ridge first developed during the Eocene in response to differential compaction over the Madeleine Trend. From the Mid-Miocene onwards, the incipient drape structure began to gently tilt towards the north and west and relief increased. By the late Miocene, the northerly tilt and continued differential compaction had produced a closure at reservoir level, coinciding with the present-day occurrence of the high-amplitude zone thought to reflect major carbonate cementation. From the Late Miocene onward, the continued northwest tilt of the structural trend shifted the closure towards the south until its present-day position was attained.

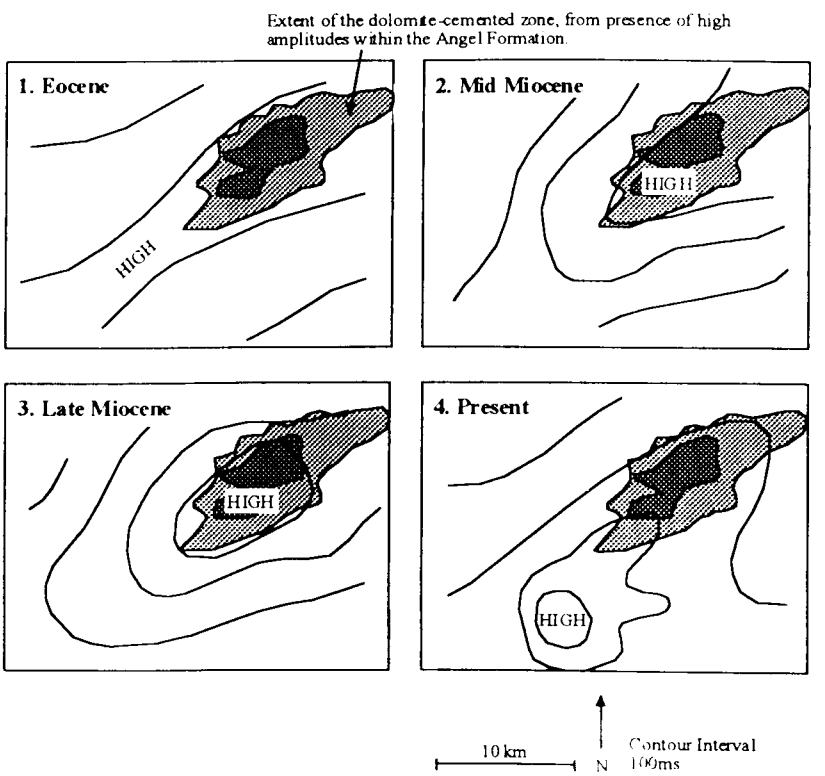

Figure 40. Time interval between the top of the Angel formation (Top-Upper-Unit) and selected Tertiary horizons, to identify timing of development of structural closure in the Angel Field.

Origin and emplacement of dolomite cement

Several preliminary models for the origin and emplacement of the dolomite are discussed in Ryan-Grigor and Schulz-Rojahn (1995), and compared using the available seismic, petrophysical and petrographic evidence. Schulz-Rojahn et al. (1996) present additional evidence (isotope analysis, scanning electron microscope imaging, and back-scattered electron imaging) from both the Angel Field, and the Gidgealpa Field in the Cooper Basin, and discuss in detail the most probable model for the origin and emplacement of the dolomite. This model is outlined here, and shown in Figure 41.

The timing of the emplacement of the dolomite cement in the Angel Field is thought to be Late Miocene, after the development of structural closure, and during the Miocene-to-Present tectonic activity and hydrocarbon migration (Ryan-Grigor and Schulz-Rojahn, 1995; Schulz-Rojahn et al., 1996), and occurred at a temperature of around 90-100 degC. During the Miocene, hydrocarbon migration from underlying Triassic to Middle Jurassic source rocks was focussed along faults (Parry and Smith, 1988) and is believed to have been accompanied by deep basinal fluids charged with carbon dioxide. The migrating carbon dioxide entered the Angel Formation either directly from the underlying source rocks, or along Miocene-age faults. The Angel Formation pore-water contained pH-buffering agents such as organic acid anions, and mixing of these buffering agents with the carbon dioxide triggered carbonate cement precipitation. Organic acid anions are produced during early oil generation, and the lower, shale-rich Angel Formation became early mature for oil generation in the early Tertiary. It is assumed that the dolomite cement was emplaced at the crest of the structural closure. The position of the crest of the structure and the area of the high-amplitude reflections, interpreted to be the extent of the dolomite-cemented sandstone, coincide during the Late Miocene. This implies that the dolomite cement was precipitated during the Late Miocene (Schulz-Rojahn et al., 1996).

Figure 41. Model for origin and emplacement of dolomite cement in the Angel Field, compared with a similar occurrence in the Gidgealpa Field in the Permian Cooper Basin of South Australia. From Schulz-Rojahn et al. (1996).

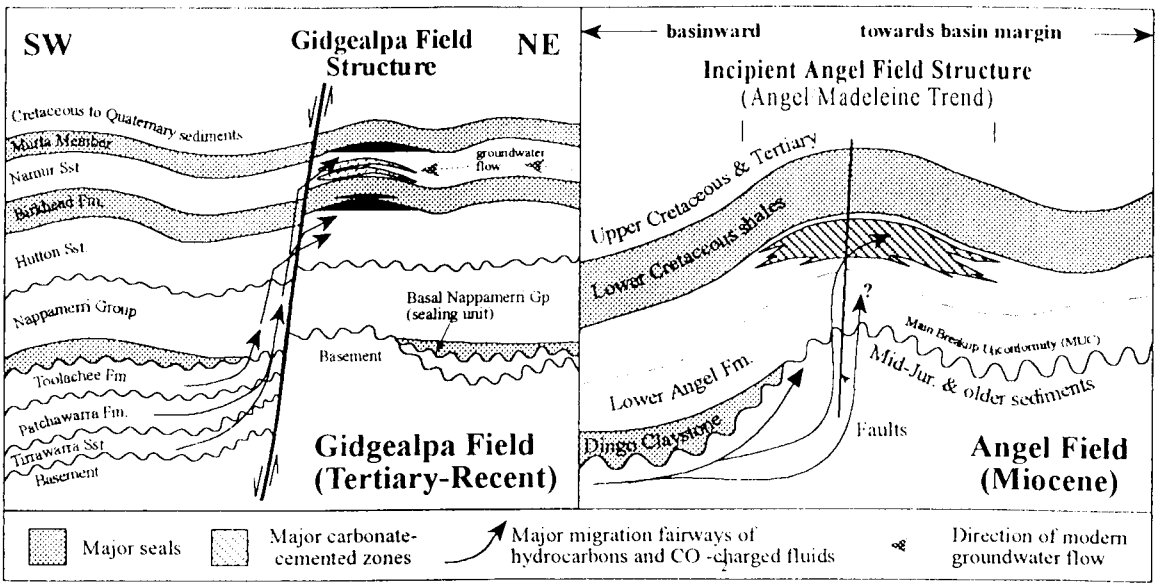
SW
Gidgealpa Field Structure
NE
Cretaceous to Quaternary sediments
Murta Member
Namur Sst
Birkhead Fm.
Hutton Sst
Nappamerri Group
Toolachee Fm
Patchawarra Fm.
Tirrawarra Sst
Basement
groundwater flow
Basal Nappamerri Gp (sealing unit)
Basement
Gidgealpa Field (Tertiary-Recent)
basinward
towards basin margin
Incipient Angel Field Structure
(Angel Madeleine Trend)
Upper Cretaceous & Tertiary
Lower Cretaceous shales
?
Main Breakup Unconformity (MBU)
Lower Angel Fm.
Mid-Jur. & older sediments
Dingo Claystone
Faults
Angel Field (Miocene)
Major seals
Major carbonate-cemented zones
Major migration fairways of hydrocarbons and CO -charged fluids
Direction of modern groundwater flow

Major dolomite cement is absent in the Wanaea-Cossack area to the southwest. This is hypothesised to be due to the presence of a thick blanket of Middle Jurassic shale, which is absent from the Angel area. The Mid-Jurassic shale could have prevented the migrating gas and carbon dioxide from entering the Wanaea-Cossack closures, precipitating dolomite cement, and replacing the oil with gas. The implication of this is that an undrilled prospect in the study area must be in an area where the Mid-Jurassic shale is thick enough to prevent gas migration, here assumed to be at least 50ms or approximately 100m thick, and be unbreached, for oil to be present. Table 8 lists the closures in the study area and the underlying presence of Mid Jurassic shale (Dingo Claystone), taken from the isochron map of the base of the Angel Formation (Top-O-Mon) to the Main Unconformity (MUC).

Closure	Thick Mid Jurassic Shale under closure?	Probable Hydrocarbon type
Angel[GAS]	no	gas
Basilisk	no	gas
Bunyip	no	gas
Centaur	maybe	gas?
Cherub	maybe	gas?
Cossack [OIL]	yes	oil
Dragon	yes	oil
Kraken	yes	gas spill from Angel?
Lambert [GAS]	no	gas
Pegasus	yes	oil
Phoenix	yes	oil
Snark	no	gas
Sphinx	no	gas
Unicorn	maybe	gas?
Wyvern	maybe	gas?

Table 8. Presence or absence of thick Mid Jurassic shales under closures, and probable hydrocarbon type. Known fields are marked with a superscript denoting their dominant hydrocarbon type.

High-amplitude zone in the south of the Angel Field

An examination of the map of RMS amplitude (Figure 39) shows an area of high RMS amplitude lies within the southern Angel Field. It is important for reserves calculations and development strategy to know whether this area of high RMS amplitude has been caused by the presence of dolomite cement in the sandstone or by some other phenomenon, such as the presence of gas. Well control does not give convincing proof that there is no dolomite cement, since Angel-1 lies on the northern edge of the zone, and does not penetrate the highest amplitudes.

Fluid substitution modelling in the previous chapter suggests that the presence of gas in the Angel Formation should decrease its acoustic impedance. The zero offset reflection coefficient at the top of the Angel Formation would be expected to go from moderately positive to around zero or weakly negative as a result of the pore fluid changing from water to gas. This could account for the amplitude changes observed in the southern part of the Angel Field (Figure 33). On this map, the negative amplitudes surrounding the field (reds and yellows) change to positive amplitudes (green and blue) across the line marking the approximate position of the GWC.

The reflection coefficient of the GWC is calculated to be approximately 0.05, which is not very strong, but should be visible. Close examination of the seismic data shows an almost flat reflection within the southern Angel Field. This reflection has been picked as the Top-Middle-Unit horizon. Figure 42 shows two examples of this reflection, on inline 1800 and crossline 6050. On both seismic lines, the amplitude of the Top-Middle-Unit is highest when the horizon enters the gas column, which is at approximately 1800ms, probably due to tuning between the reflections from the GWC and the Top-Middle-Unit. The amplitude map of the Top-Middle-Unit (Fig. 32) shows that the area of high amplitudes in the southern part of the Angel Field coincides with the intersection of the horizon with the gas-water contact at around 1800ms.

There may be a dolomite-cemented zone present within the Angel Formation in the southern part of the field. If there was a dolomite-cemented zone present close to or at the top of the

Angel Formation, it would probably be visible on the amplitude map of the Top-Upper-Unit (Figure 33) as an area of high negative amplitudes (red), as seen in the northern high-amplitude zone. Since this is not observed, it is hypothesised that any dolomite-cemented zone, if present, lies below the top of the Angel Formation. If dolomite-cemented layers similar to those at Angel-2 were present in this area, with *P*-wave velocities around 5000m/s and bulk densities of 2.6g/cc, they would create high amplitude reflections which would be prominent and highly visible in the seismic data, and would be very similar to the northern zone of high amplitudes. Since this is not the case (see Fig. 9a), any dolomite-cemented layer present must have a smaller percentage of dolomite than seen in Angel-2, which will result in a slower *P*-wave velocity, lower bulk density and lower amplitudes.

To test whether such a zone would be detectable in the seismic data, a series of synthetic seismograms were generated from the sonic and density logs of Angel-1. The logs were blocked over the reservoir interval and the presence of a gas column, which varied in thickness from 0m to 160m, was modelled by modifying the values of the sonic and density logs according to the Biot-Gassman fluid replacement modelling results in Chapter 7. The dolomite-cemented zone was modelled as a layer 30m thick, lying at the Top-Middle-Unit level, with a *P*-wave velocity of 4000m/s and a bulk density of 2.4g/cc, which does not change with the presence of gas. These parameters were chosen to characterise a dolomite-cemented layer, with a smaller percentage of dolomite than seen at Angel-2, as discussed previously, and represent a high-impedance layer with low porosity, where the presence of gas does not greatly affect the impedance. The Western Atlas program *QUIKLOG* was used to generate zero-offset synthetic seismograms, using a minimum-phase wavelet with a Ricker spectrum and a 35Hz centre frequency. Figure 43 (a) to (f) shows the resulting synthetic seismograms for Angel-1 with increasing thickness of gas, and (g) to (l) shows the results with the same gas column thickness, and the dolomite-cemented zone.

The synthetic seismograms show that the presence of gas in the Angel Formation lowers the reflectivity at the top of the sandstone so that it generates a much weaker event than the same sand with water in the pores. They show that the GWC and the dolomite-cemented layer both generate quite strong events that should be visible within the gas column on the 3D seismic data. They also show that there is an increase in the amplitude and number of the reflections within the interval with an increase in thickness of the gas column, in the presence of the dolomite-cemented zone. If the RMS amplitude is calculated in a time window as big as the estimated largest possible gas column below Top-Upper-Unit (130msecs) and this RMS

amplitude is then mapped, it may show if a dolomite-cemented zone is present. If there is a dolomite-cemented zone, the RMS amplitude will be higher when the gas column is thick, and taper off to reach a constant value at the edge of the gas. A similar effect would be expected for interbeds of lithologies other than dolomite within the reservoir which have impedances similar to or greater than that of the water-wet reservoir, and are of low porosity, so that the pore fluid has little effect on their impedance.

Thin bed tuning is very likely to affect this kind of analysis, especially around the edges of the field. The tuning may be constructive or destructive, depending on the arrangement of internal reflectors, the gas column, noise, the wavelet and many other factors. If tuning is present, it may be visible as a band of higher or lower values of amplitude around the edges of the field, depending on the impedance contrasts.

It can be seen that high RMS amplitudes also occur within the GWC, especially near Angel-1 where Top-Upper-Unit is highest and the gas column is thickest. This seems to point to the presence of a dolomite-cemented zone, as modelled. The increase in RMS amplitude could also possibly be due to multiples within the gas column, or lithological variations within the Upper Unit. From this examination of the seismic data, it seems that the presence of a dolomite-cemented layer, or some other high impedance heterogeneity, at or near Top-Middle-Unit level within the southern Angel Field is possible, and cannot be ruled out. The presence of a dolomite-cemented layer in the southern part of the Angel Field implies that dolomite cement was being at least partly precipitated during the time when the southern part of the field was structurally highest. The southern part of the Angel Field became the crest of the field sometime after the Late Miocene and before the Present (see Figure 40). Any dolomite-cemented layers in the southern part of the field may represent a small pulse of precipitation, probably occurring between the Pliocene and the Present, slightly later than the main phase of dolomite cementation, which is thought to have occurred during the Late Miocene.

Figure 42. Selected seismic sections showing prominent flat-lying reflections, possibly caused by the gas-water contact.

(a) Inline 1800 showing possible reflection from gas-water contact, marked by white arrow.

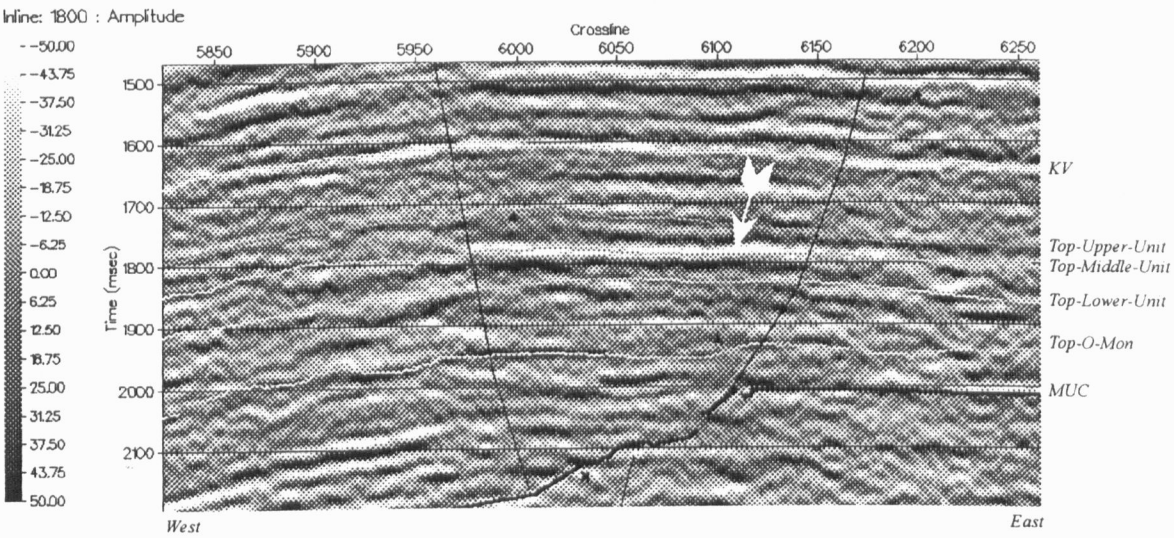

(b) Crossline 6050 showing possible reflection from gas-water contact, marked by white arrow.

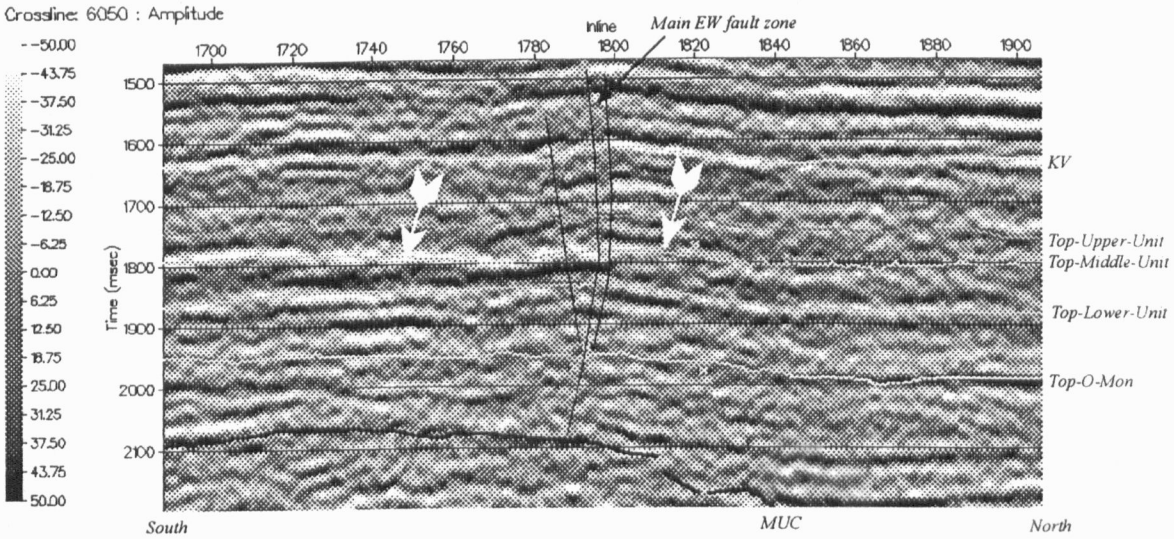

Figure 43. Series of synthetic seismograms to test if the presence of a dolomite-cemented layer is seismically visible, in the presence of a gas column of varying thickness.

Sketch of Acoustic Impedance Model

Increasing AI

No dolomite-cemented layer

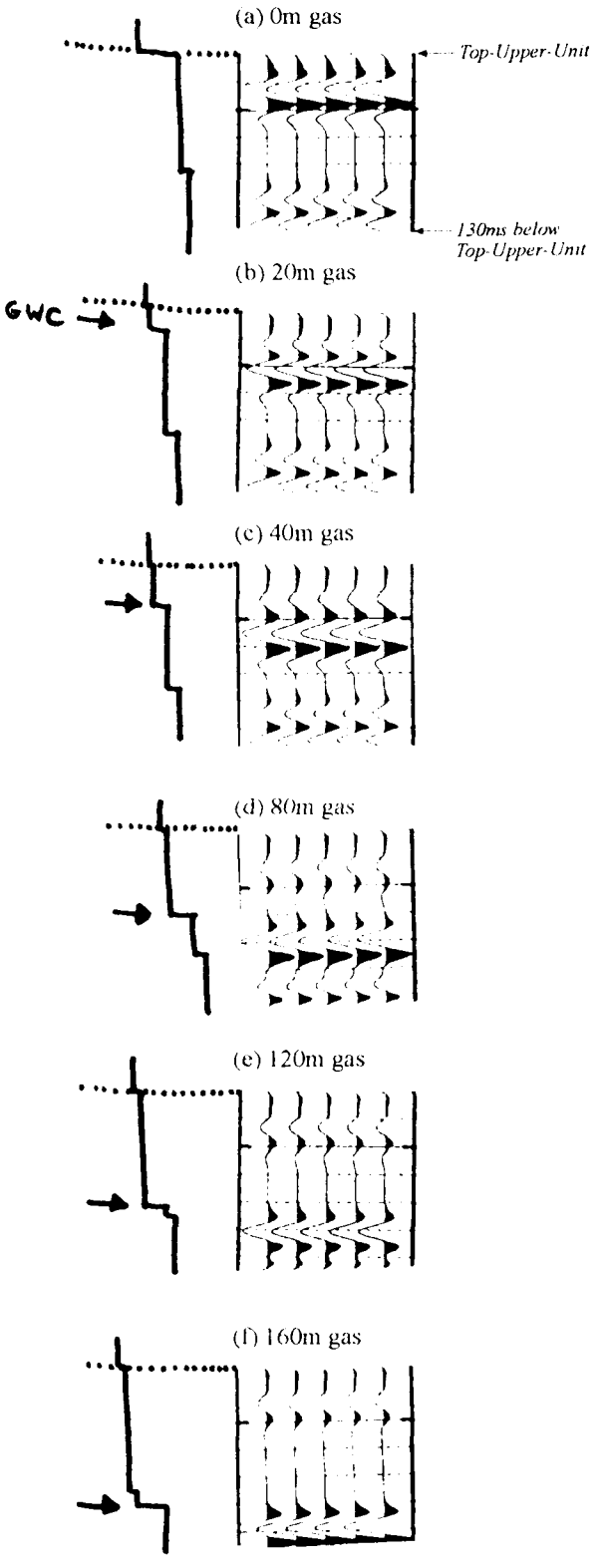

Dolomite-cemented layer at Top-Middle-Unit level
Cemented layer is 30m thick, 2.4g/cc, 4000m/s.

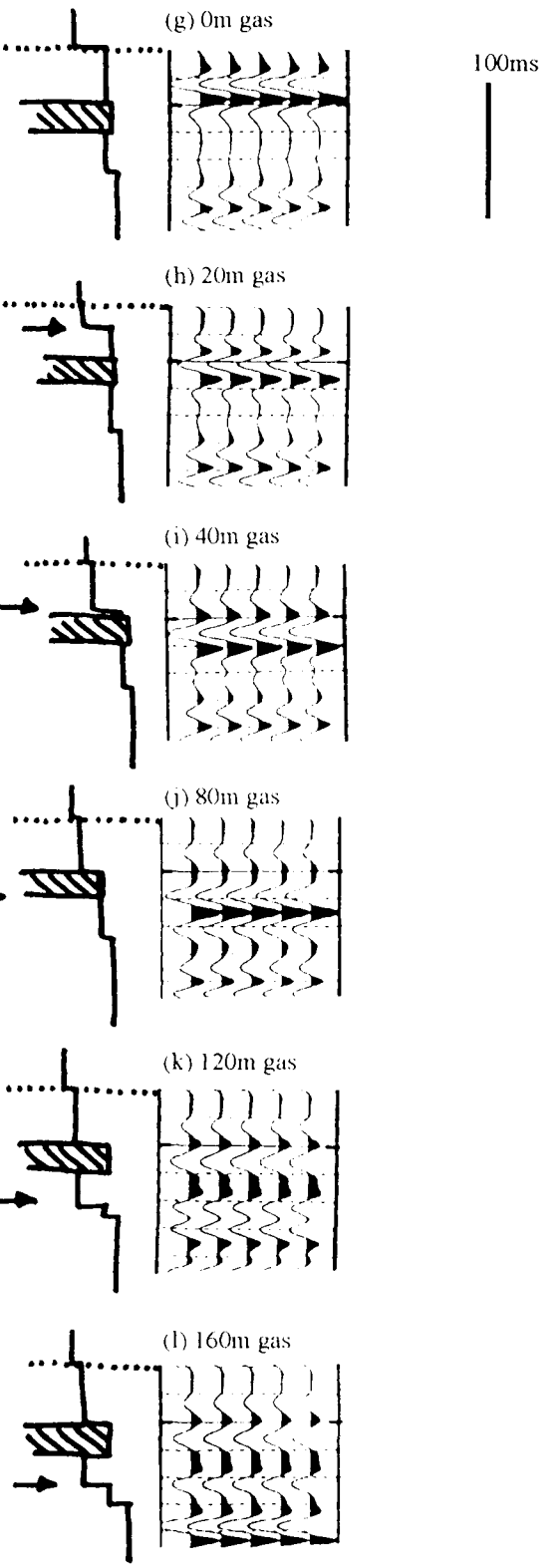

Seismic detection of fluid contacts

If the RMS amplitude also responds to gas, as previously conjectured, and the seismic time to the pinchout of the GWC against the base of the seal is reasonably constant, then a crossplot of RMS amplitude versus time to the top of the reservoir should show the seismic time of the GWC. This is because the RMS amplitude will be fairly constant below the GWC, and increase with decreasing time to the top of the reservoir above the GWC as the gross gas column increases. When this is done for the Angel Field, with the northern dolomite-cemented zone excluded, the predicted pattern is observed. The change in trend of RMS amplitude occurs at around 1785msecs (Fig 44). This can be interpreted as an estimate of the average time to the GWC in the area analysed. A crossplot for the northern dolomite-cemented zone only (Fig. 45) shows an overall increase of RMS amplitude with decreasing two-way time, but no definite inflection point marking the GWC, unlike Figure 44.

The GWC determined from wireline logs in Angel-1, 2 and 4 was found to be practically identical (2746mss), but the wireline GWC in Angel-3 was found to be 7 metres deeper, at 2753mss. It was then assumed that the Angel-3 logs were off depth and they were corrected, assuming a common GWC in all four wells. However, the driller's depth for the core that was cut in Angel-3 agreed with the original logged depth, not with the corrected depth (Woodside, 1992). The original logged depth will be used here, which implies a 7 metre difference in GWC between Angel-3 in the south of the field, and the other three wells.

Figure 44. RMS amplitude versus time to Top-Upper-Unit crossplot, covering Angel Field area and excluding the northern dolomite-cemented zone. Note the increase in RMS amplitude starting at 1785ms.

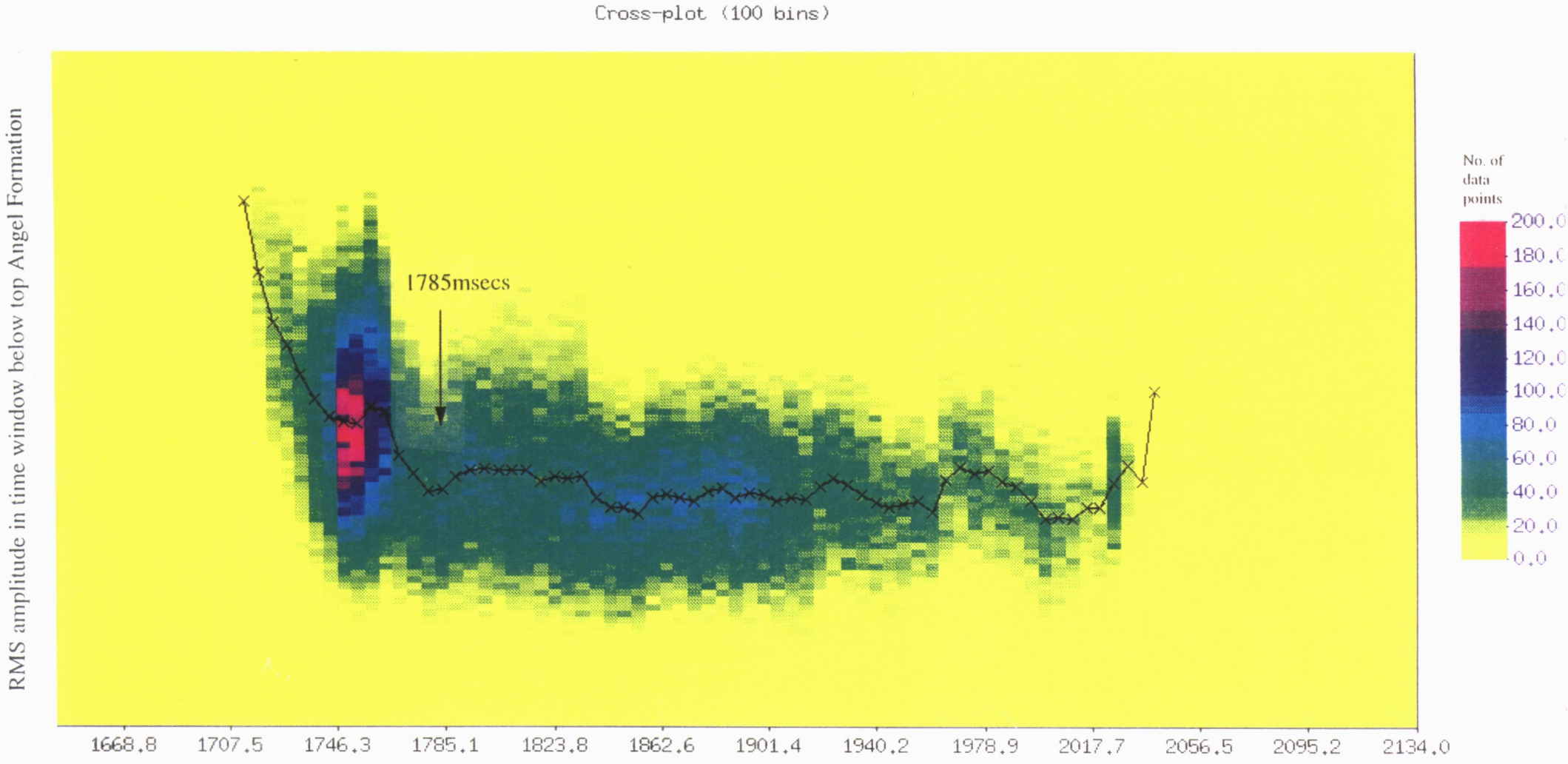

Excluding dolomite-cemented zone

Figure 45. RMS amplitude versus time to Top-Upper-Unit crossplot, covering the northern dolomite-cemented zone only. Note the lack of a definite inflection point at 1785ms.

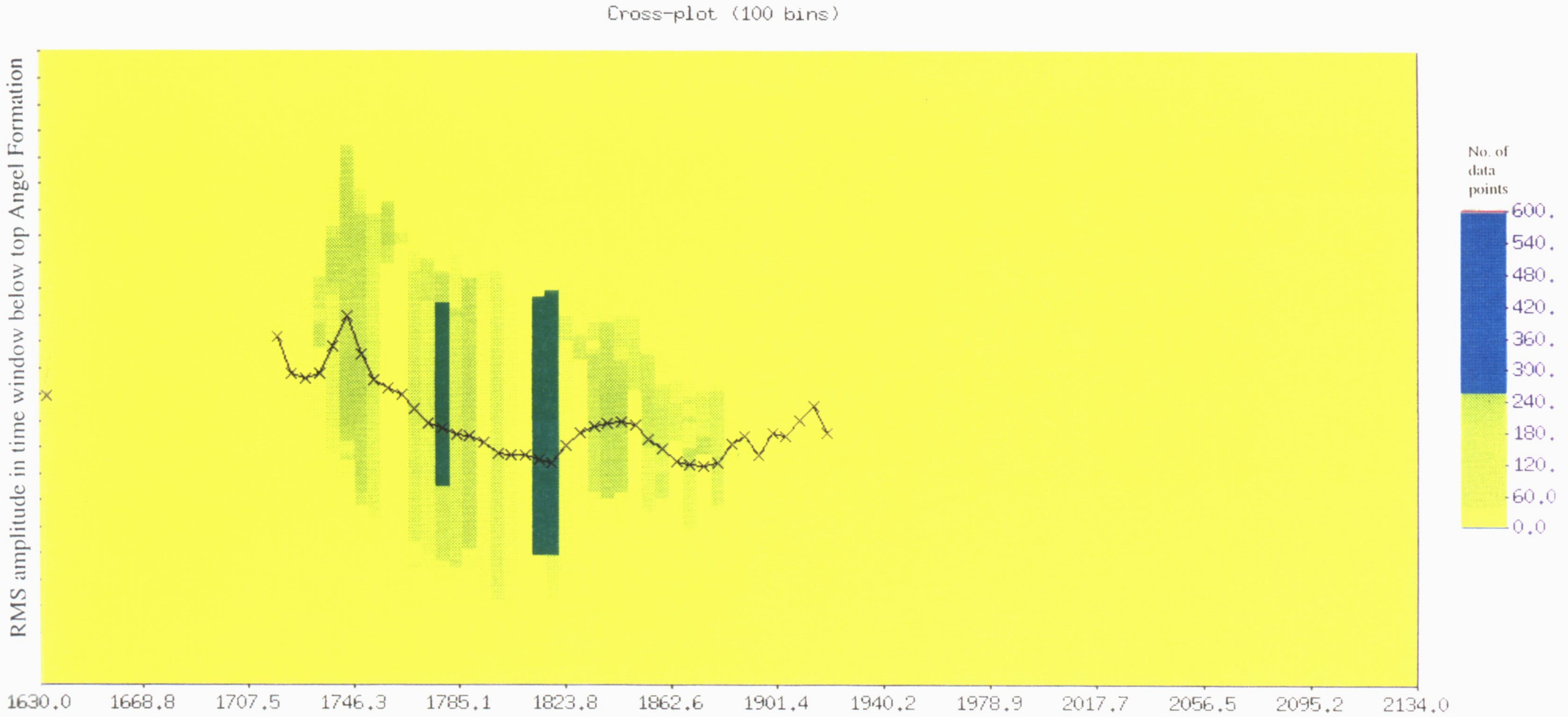

Dolomite-cemented zone only

Angel-3 also contains unequivocal oil indications, with log analysis indicating an oil leg 31 metres thick with Sw ranging from 0.75 to 0.45, and live oil in cuttings (Fig. 46). Unfortunately technical problems did not allow a DST in this oil zone. None of the other wells contain this oil leg, although they all contain traces of residual oil. Putting this evidence together with the fact that there is a 1km wide fault zone running through the field between Angel-3 and the other wells and it seems very likely that this fault zone is acting as a barrier, and that the Angel Field consists of two pools with different hydrocarbon-water contacts and an oil leg in the southern part. Crossline 6050 (Fig. 42b) runs across the main EW fault zone from north to south, and shows a possible increase in time of the Top-Middle-Unit horizon to the south of the main EW fault zone. In this area, the Top-Middle-Unit reflection is probably a composite from the horizon itself and the hydrocarbon-water contact, so the change in time may be due to a change in the hydrocarbon-water contact.

With this in mind, two RMS amplitude versus two-way time of Top-Upper-Unit crossplots were made, one covering the field south of the fault zone, and the other covering the north (again excluding the major dolomite-cemented zone), to see if the different GWCs could be detected (Fig. 47). The scatter in the data in Figure 47 is similar to that in Figures 44 and 45. The 'seismic GWC' from the northern field is 1778 msecs. The depth of this 'seismic GWC', determined from the time-depth curve of the checkshot survey in Angel-4 (in the northern field) is 2748mss. This is only 2 metres deeper than the value from the wireline logs (2746mss). The 'seismic GWC' from the southern field is 1797 msecs (Fig 47b). The depth of the 'seismic GWC', determined from the time-depth curve of the checkshot survey in Angel-3 is 2779mss. The wireline GOC is 2753mss, and the wireline OWC is 2777mss. The 'seismic GWC' is only 2m below the wireline OWC, compared with 26m below the wireline GOC.

These results, although apparently extremely accurate, are probably only so close by chance, and possibly by the cancellation of random errors due to the large areas included in each crossplot (approximately 5km by 10km, or 40,000 data points). A larger area implies more data points and better statistics, and a more accurate determineation of the GWC. A larger area also implies more chance of significant changes in GWC time due to velocity variations or different GWCs, which in turn implies more scatter in the plot and a less accurate determination of the GWC. However, taking the plots in Figure 47 at face value, it would seem difficult to pick the seismic GWC much shallower than 1797 msecs in the southern part of the field, nor much deeper than 1778 msec in the northern part of the field, suggesting

different contacts. There is a large scatter in the data, as seen in Figures 44 and 45, and there is scope to interpret the contacts at different places. For example there could be an apparent contact at around 1750ms in Figure 47(b), at a change in slope. An implicit assumption in this method is that the GWC or OWC occurrs at a constant two-way time in the area covered in the crossplots. If this is the case, it seems possible that the RMS amplitude is responding to the oil present in the southern field, and this technique has helped to find a GWC and possibly an OWC, directly from the seismic data. Light oil with a high gas-oil ratio, such as from Wanaea or Cossack Oil Fields (Woodside, 1989b, 1990e), will have almost the same effect on the acoustic impedance of a rock as gas (Clark, 1993). Wanaea and Cossack Oil Fields lie approximately 10km directly downdip from Angel Field, and are full to spill point in the Angel Formation. If some oil escaped, it could have formed an oil leg in the southern Angel Field as seen today.

Figure 46. Oil indications in Angel-3. From Woodside (1989).

Angel-3 Oil Indications

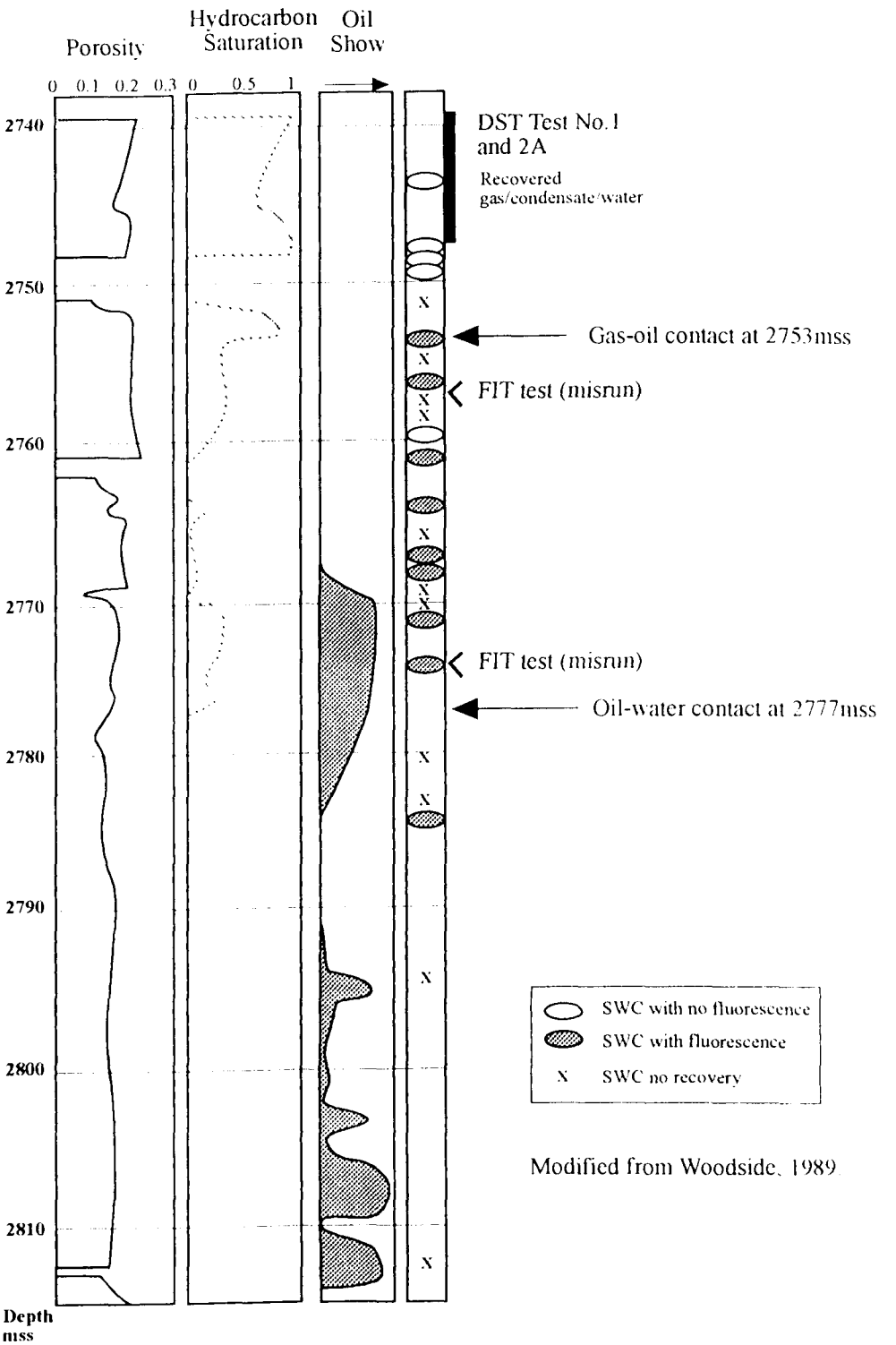

Modified from Woodside, 1989

Figure 47. RMS amplitude versus time to Top-Upper-Unit crossplots, north and south of the main EW fault zone, showing interpreted hydrocarbon-water contacts.

(a) Crossplot of two-way time to top of reservoir versus RMS amplitude in time window below top of reservoir, southern part of Angel Field. Oil-water contact at 1797msecs.

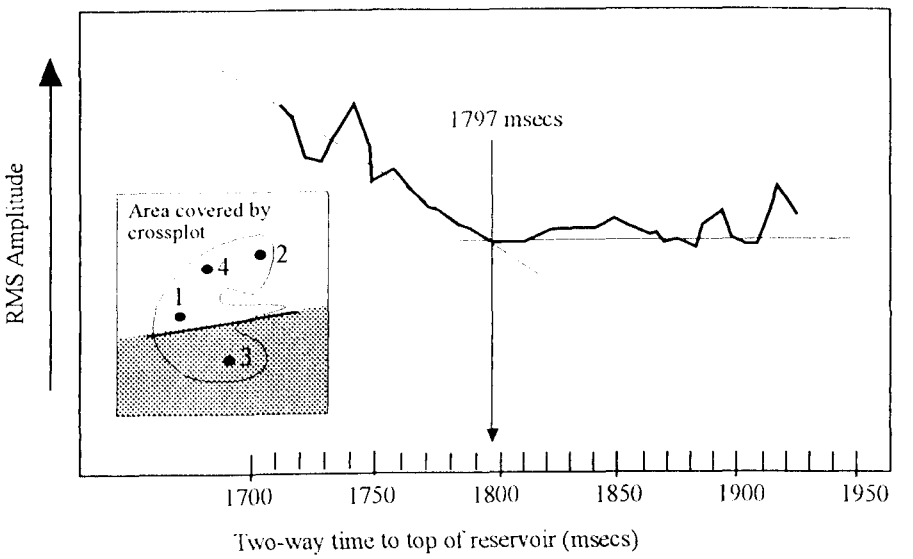

(b) Crossplot of two-way time to top of reservoir versus RMS amplitude in time window below top of reservoir, northern part of Angel Field excluding dolomite-cemented zone. Gas-water contact at 1778msecs.

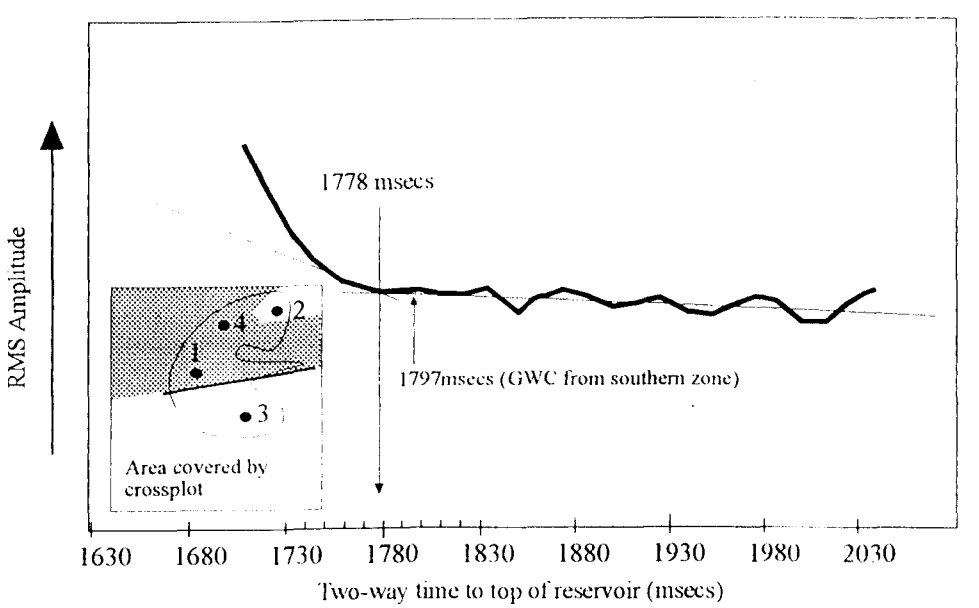

9. AMPLITUDE VARIATION WITH OFFSET

Introduction

The concept and application of amplitude variation with offset (AVO) analysis were introduced into petroleum exploration by Ostrander (1984) in these words:

'The P-wave reflection coefficient at an interface separating two media is known to vary with angle of incidence. The manner in which it varies is strongly affected by the relative values of Poisson's Ratio of the two media. For moderate angles of incidence, the relative change in reflection coefficient is particularly significant when Poisson's Ratio differs greatly between the two media.

Theory and laboratory measurements indicate that gas sands tend to exhibit abnormally low Poisson's Ratios. Embedding a low velocity gas sand into sediments having 'normal' Poisson's Ratios should result in an increase in reflected P-wave energy with angle of incidence. This phenomenon has been observed on conventional seismic data recorded over known gas sands.'

Some examples of recent AVO analysis are:

Gulf Coast/Gulf of Mexico	(Ross and Beale, 1994; Hall et al., 1995; Ross, 1995; Castagna and Smith, 1994; Rutherford and Williams, 1989; Allen and Peddy, 1993; Allen et al, 1993),
North Sea	(Reilly, 1994; Landro et al., 1995; Landro et al., 1992; Barnett et al., 1995),
Texas	(Burnett, 1990),
South Africa	(Fatti et al., 1994; van den Berg et al., 1992; Buland et al., 1995),
Italy	(Mazzotti and Mirri, 1991),
Canada	(Lu and Lines, 1995; Nazar and Lawton, 1993; Coulombe et al., 1992),
Saudi Arabia	(Chiburis, 1984, 1987, 1993),
Indonesia	(Chacko, 1989; Santoso et al., 1995),
Venezuela	(Regueiro et al., 1993),

Australia

Gippsland Basin	(Spence et al., 1992),
Otway Basin	(Lovibond and Rauch, 1995), and
Cooper-Eromanga Basin	(Pinchin and Mitchell, 1991).

Most AVO analysis has been for gas detection in sandstone reservoirs, in Tertiary sediments in the Gulf Coast. Some recent examples of AVO analysis for other purposes are:

Gas detection in carbonates	(Chiburis, 1984; Ho et al., 1992; Harvey, 1993; Lu and Lines, 1995; Santoso et al., 1995; Couloumbe et al., 1992),
Oil detection in carbonates	(Chiburis 1984, 1987),
Oil detection in clastics	(Hwang and Lellis, 1988),
Porosity detection	(Chacko, 1989; Harvey, 1993; Landro et al., 1995; Lovibond and Rauch, 1995; Lu and Lines, 1995),
Lithology discrimination	(van den Berg et al., 1992; Mazzotti et al., 1994; Buland et al., 1995),
Detection of fractured zones	(Ho et al., 1992),
EOR monitoring	(Tsingas and Kanasewich, 1991),
Constraining tomographic inversion	(Mair et al., 1995)
Gold exploration	(van den Berg et al., 1992),
Thickness of a thin layer	(Nazar and Lawton, 1993), and
Velocity of the seabottom	(Amundsen and Reitan, 1994).

The Zoeppritz Equations and Approximations

A series of complex equations, derived by Zoeppritz in 1919, show that the amplitudes of the waves reflected and transmitted at an interface between two media depend on the angle of incidence and the elastic properties of the two media. Koefoed (1956) showed that the P-wave reflection coefficient can vary considerably with the angle of incidence when the Poisson's Ratio (σ) of the two media are very different. The equations have been simplified by Bortfield (1961), Richards and Frasier (1976), Aki and Richards (1980), Shuey (1985), Gelfand et al. (1986), Smith and Gidlow (1987), and Mallick (1993). The Aki-Richards-Frasier

approximation sets the equations in terms of changes in bulk density and *P*- and *S*-wave velocity across the interface

$$R(\theta) \approx a\frac{\Delta V_p}{V_p} + b\frac{\Delta \rho}{\rho} + c\frac{\Delta V_s}{V_s}, \tag{1}$$

where

$$a = \frac{1}{2} + \tan^2 \theta,$$

$$b = \frac{1}{2} - \frac{2V_s^2}{V_p^2}\sin^2 \theta,$$

$$c = -\frac{4V_s^2}{V_p^2}\sin^2 \theta,$$

V_p, V_s, and ρ are average values, ΔV_p, ΔV_s, and Δρ the difference between the lower and upper layers, and θ is the average of the incident and reflection angles (Figure 48).

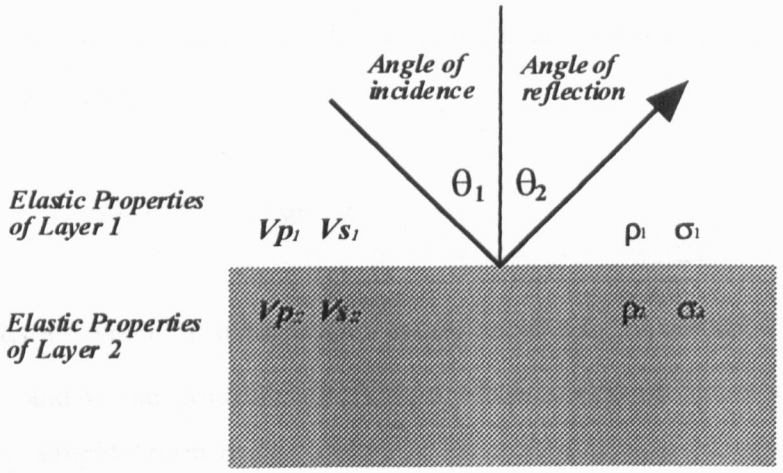

Figure 48. **Interface between two media, with incident wave, and elastic properties of each layer.**

Aki and Richards (1980) also give the exact expressions for all the reflection and transmission coefficients generated at an interface between two elastic media. Shuey (1985) recast the Aki and Richards (1980) approximation in terms of V_p, ρ and σ:

$$R(\theta) \approx R_p + \{A_0 R_p + \frac{\Delta\sigma}{(1-\sigma)^2}\}\sin\theta_1 + \frac{1}{2}\frac{\Delta V_p}{V_p}(\tan^2\theta_1 - \sin^2\theta_1),$$

(2)

where θ_1 is the angle of incidence, and

$$R_p = \frac{\rho_2 V_{p2} - \rho_1 V_{p1}}{\rho_2 V_{p2} + \rho_1 V_{p1}},$$

$$A_0 = B_0 - 2(1 + B_0)(\frac{1-2\sigma}{1-\sigma}),$$

$$B_0 = \frac{\frac{\Delta V_p}{V_p}}{\frac{\Delta V_p}{V_p} + \frac{\Delta\rho}{\rho}}.$$

The first term is the normal incidence *P*-wave reflection coefficient and dominates the response for small angles of incidence. The second term is important at intermediate angles of incidence out to approximately 30°, and the third term becomes dominant as the critical angle is approached. Incident angles are commonly restricted to less than 30°, in exploration practice. Under these circumstances, $\tan^2\theta_1 - \sin^2\theta_1$ is much smaller than $\sin^2\theta_1$, and the third term can be ignored, giving:

$$R(\theta_1) \approx I + G\sin^2\theta_1.$$

(3)

This equation yields a straight line on an amplitude versus $\sin^2\theta$ crossplot, where I is the intercept and G the gradient. A further simplification of Shuey's simplification of Aki and Richards' simplification of the Zoeppritz equations was by Hilterman (1989, 1990) who set Poisson's ratio at 0.33 (V_p/V_s=2) and used the first two terms, to give

$$R(\theta_1) \approx R_p + (\frac{9}{4}\Delta\sigma - R_p)\sin^2\theta_1,$$

(4)

or alternatively, an estimation of the change in σ, Δσ, may be made using the expression

$$\Delta\sigma \approx \frac{4}{9}(I + G).$$

(5)

The assumption of a constant Poisson's ratio has the potential to cause large errors in the estimation of the change in Poisson's Ratio (Mallick, 1993).

Gelfand et al. (1986) rearranged the Aki and Richards (1980) approximation, by also assuming that V_p/V_s is 2, and ignoring the third term, to give

$$R(\theta) \approx \frac{1}{2}[\frac{\Delta V_p}{V_p} + \frac{\Delta \rho}{\rho} +] + [\frac{1}{2}\frac{\Delta V_p}{V_p} - \frac{\Delta V_s}{V_s} - \frac{1}{2}\frac{\Delta \rho}{\rho}]\sin^2\theta, \tag{6a}$$

which can be rewritten as

$$R(\theta) \approx R_p + (R_p - 2R_s)\sin^2\theta \tag{6b}$$

where R_s is the S-wave reflection coefficient.

Another method of simplifying the Aki and Richards (1980) approximation is the Fluid Factor method of Smith and Gidlow (1987). They removed the dependence on density by using the Gardner et al. (1974) equation

$$\rho \sim V_p^{0.25}. \tag{7}$$

Substituting this into the Aki and Richards equation results in the reflection coefficient as a weighted sum of the P- and S-wave velocity variations only. The linear relationship between V_p and V_s in water-wet sands and shales found by Castagna et al. (1985) is used to define a background trend of V_p/V_s. The Fluid Factor calculation then defines where V_p/V_s differs from the background, potentially highlighting locations where V_p has been reduced by gas.

Mallick (1993) recasts the Zoeppritz equations in terms of the fluid-fluid reflection coefficient at the interface, R_f, and the ratio of the change in shear modulus to the average bulk density $\Delta\mu/\rho$:

$$R(p) \approx R_f(p) - \frac{2\Delta\mu}{\rho}p^2 + [\frac{\Delta\mu}{\rho}]^2 V_{p1}V_{s2}p^2, \tag{8}$$

where p is the ray parameter, μ is the shear modulus, V_{p1} is the P-wave velocity in the upper layer, and V_{s2} the S-wave velocity in the lower layer. These simplifications illustrate that at small angles, the AVO response is dominated by P-wave impedance contrasts, and at larger angles by contrasts in Poisson's Ratio.

AVO Inversion

AVO analysis is considered by some workers (eg Ursin and Tjaaland, 1992) to be a special case of seismic inversion, rather than a direct hydrocarbon indicator. Inversion of the Zoeppritz equations is non-unique, as many combinations of rock properties can result in the same change in amplitude with offset. The parameters that can be found in AVO inversion are the ratios of the bulk density, P-wave velocity, and Poisson's Ratio (or V_p/V_s) in the upper and lower media, when the input is the P-wave amplitudes as a function of angle of incidence, as in a CMP gather. In practise, only one or two parameters can be estimated, although this can be improved by using longer offsets and including converted waves (Drufuca and Mazzotti, 1995; Ursin and Tjaaland, 1992), and also by using as much *a priori* information as possible (Martinez and McMechan, 1991; Dahl and Ursin, 1992). Some examples of AVO inversion are provided by Piggott et al. (1990) who used AVO inversion to detect porosity in a carbonate reservoir, Hampson (1991) who demonstrated a Monte Carlo technique, and Sen and Stoffa (1992) who used a genetic algorithm.

The AVO inversion approach is complicated by various factors such as the limited bandwidth of seismic data, variable wavelets, limited offsets or angles, overburden effects, multiples and so on (Drufuca and Mazzotti, 1995). Velocity error, in terms of residual NMO, can also cause significant errors in AVO inversion (Spagnolini, 1994; Tura and Hanitzsch, 1995). Another approach that has been used is to model the amplitude variation with offset as a Taylor series expansion polynomial in the offset coordinate, thus avoiding the conversion from offset to angle. The polynomial coefficients are found by the least-squares method (Ursin and Dahl, 1992; Ursin and Ekren, 1995). Since the AVO inversion approach depends so critically on good data quality, it was not used in this study.

Factors affecting seismic amplitudes

One of the critical assumptions of AVO analysis is that the offset-dependent reflectivity can be recovered from the recorded seismic amplitudes. The aim when processing the raw data is to preserve the component of the amplitude due to reflectivity while removing unwanted events and amplitude components and minimising processing artifacts. A multitude of factors have the potential to affect recorded seismic amplitudes, many of which are listed in Table 9. The factors have been divided into four groups: signal, potential signal, noise without offset dependence, and noise with offset dependence. The signal is the variation in amplitude with offset or angle from the interface of interest, and the potential signal is usually treated as unwanted noise, but may in some circumstances contain useful information. The factors have also been classified as intrinsic (inelastic attenuation for example), acquisition (eg. source and receiver directivity), or processing factors (eg. NMO stretch). These factors will be discussed in terms of their effect on the AVO response, both relative and absolute.

GROUP	FACTOR	TYPE
1. Signal		
a.	Change in RC with offset from one interface	I
2. Potential Signal		
a.	Mode conversions	I
b.	Tuning caused by NMO convergence	I
c.	Composite reflections from multiple interfaces	I
3. Noise with no offset dependence		
a.	Random noise	I
b.	Instrument effects	A
4. Noise with offset dependence		
a.	Multiples	I
b.	Other coherent noise	I
c.	Spherical spreading	I
d.	Inelastic attenuation	I
e.	Anisotropy	I
f.	Transmission losses	I
g.	Overburden effects	I
h.	Structural effects	I
i.	Statics	I
j.	Fresnel zone	I
k.	Source and receiver directivity	A
l.	Irregular source strength	A
m.	Receiver sensitivity	A
n.	NMO correction	P
o.	Trace equalisation and mute	P
p.	Prestack Migration/DMO	P
q.	AGC	P
r.	Offset to angle conversion	P

Table 9. Some of the factors that have the potential to affect recorded seismic amplitudes. The factors have been classified by type: I=intrinsic, such as inelastic attenuation; A=acquisition, such as receiver directivity; and P=processing, such as NMO.

AVO Processing - Relative or Absolute?

In the vast majority of cases, even after the most careful and painstaking pre-processing and corrections, the AVO response seen in the seismic data does not match the theoretical or expected AVO response. This implies that the corrections applied are not accurate, or that not all the multitude of factors have been compensated for. There are two approaches to this which are different in AVO 'philosophy' but both basically involve a calibration step. The first approach is to design an empirical correction that is applied to the corrected gathers to change the observed AVO response to what is theoretically expected. This approach has been followed by Duren (1992), Rutherford (1993), and Ross and Beale (1994). The relative AVO response is not changed, although the absolute AVO reponse is (Figure 49). The second approach concentrates on identifying changes in AVO, and is not so concerned about factors affecting the amplitude that are relatively constant along a line or in a survey. In effect, the second approach is more concerned with 'anomaly hunting' in a particular area.

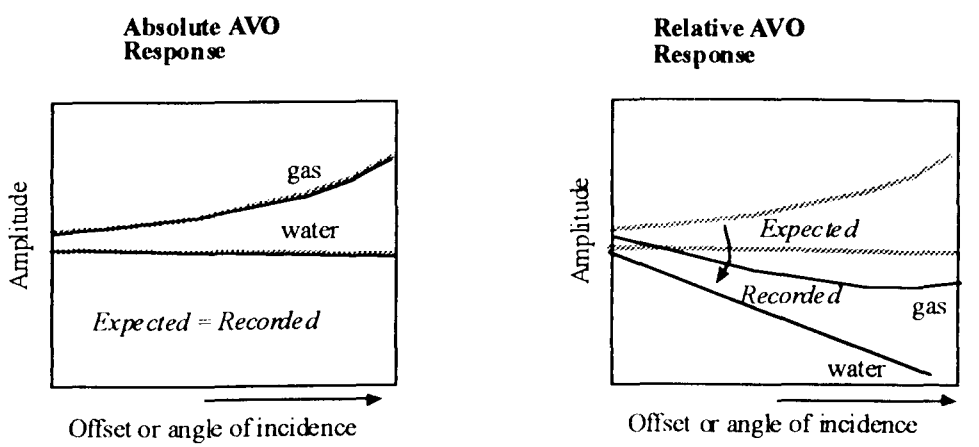

Figure 49. Diagram showing concept of absolute and relative AVO response. The absolute AVO response has been recovered when the seismic data matches the expected AVO response (calculated from rock properties) in absolute amplitude. Relative AVO response is where the recorded amplitudes in the seismic data do not match the expected values, but the separation in the AVO response between gas and water has been preserved.

2a. Mode conversions

Mode-converted waves (*P*-S_v reflections) from horizons above the target event have been found to have quite large amplitudes, especially at far offsets and when originating from interfaces with large velocity contrasts (Hron et al., 1986). Mode-converted waves interfere with the *P*-wave reflections from the target horizon at medium to far offsets (Spence et al., 1992; Snyder and Wrolstad, 1992; Martinez, 1993) and manifest as undulations in the AVO response (Ross, 1993). It has also been suggested that the locally-converted shear wave in a

thinly layered rock can have a significant effect on the AVO response of the target horizon (Simmons and Backus, 1994). Removal of mode-converted waves in the prestack domain is difficult due to their non-linear and non-hyperbolic nature. Analysis of mode-converted waves can add valuable information such as estimation of transverse isotropy parameters δ and η (Tsvankin and Thomsen, 1995) and estimation of the amount of shear-wave splitting (Turner and Hearn, 1995). Mode-converted waves from overlying horizons will affect the absolute AVO response, but may have a minimal effect on the relative AVO response. The locally-converted shear wave has the potential to affect the relative and absolute AVO response.

2b. Tuning caused by NMO convergence

Offset-dependent tuning is caused by interference of wavelets from closely-spaced interfaces with slightly different NMO curves. At far offsets, the NMO curves converge, if velocity increases with depth, and the resultant wavelet interference may cause large changes in AVO response (Swan, 1991). The effect is reduced if NMO correction is applied before AVO analysis, but this introduces the problem of NMO stretch, which is discussed in section **4n**. Nazar and Lawton (1993) have found offset-dependent tuning of the *P-P* and *P-S*$_v$ waves a useful tool for determining thickness of a thin conglomerate layer. The effect on the absolute and relative AVO response is very difficult to determine, but it is likely to have an effect on both.

2c. Composite reflections from multiple interfaces

Interfaces in real rocks are often much more complex than a simple planar layer. The interface may be a continuous gradation or have fine-scale layering, or a combination of both. This may cause large amplitude anomalies (Kindelan et al., 1989), depending on the type of layering and its thickness compared to the seismic wavelength. The total AVO response of a thin bed is a combination of the AVO response due to the angles of incidence at the reflecting interfaces, and interference effects (ie thin-bed tuning). Mazzotti et al. (1994) have found that for a thinly-bedded target, the AVO response is strongly dependent on the nature of the convolving wavelet and the effect of differential interference. The resulting AVO response will be complex and very difficult to decompose into the contributing factors. Thin-bed tuning affects a thin high-velocity layer more than a thin low-velocity layer (Juhlin and Young, 1993). Composite reflections have the potential to affect the relative and absolute AVO response.

3a. Random noise

Individual traces have a lower signal-to-noise ratio than stacked traces, and in AVO analysis, which uses pre-stack data, the noise-reducing power of CMP stacking is not available.

However, if the structural dip is low and the geology does not change dramatically in a short distance, adjacent gathers along a line may be stacked to form 'super gathers', which will have a higher signal-to-noise ratio than single gathers (Ostrander, 1984). If gathers have sufficient traces, for instance 80 or 120, stacking of adjacent traces within a gather (with differential NMO applied for the stacking) may also help to reduce the noise. Random noise should not greatly affect the relative or the absolute AVO response.

3b. Instrument effects

Instrument effects are usually treated by deconvolution before stack, to give the data the desired phase and wavelet shape. Some examples are: prestack signature deconvolution (Duren, 1992), field wavelet designature (Martinez, 1992), instrument deconvolution (Hong et al., 1993), and minimum phase recovery (Mazzotti and Ravagnan, 1995). Instrument effects are expected to be minimal.

4a. Multiples

F-k demultiple is commonly used to remove long-period multiples (Yu, 1985; Ramsden et al., 1988) although it usually attenuates the primaries at short offsets (Fatti et al., 1994). Predictive deconvolution and tau-p filtering are also used to attenuate long-period and interbed multiples (Castagna, 1993). Multiples with a small difference in moveout from the primaries (less than 1 cycle, most interbed multiples) cause interference in the data that is very difficult to remove, and are the 'single most important data quality issue for marine AVO' (Castagna, 1993). Interbed multiples have the potential to cause a decrease of amplitude with offset (Martinez, 1993), while pegleg multiples have been observed to cause an increase in amplitude with offset caused by interference at far offsets (Kemp and Gallagher, 1995). Multiples are not expected to greatly affect the relative AVO response, if it is assumed that the overburden which is generating the multiples is reasonably constant over the area of interest.

4b. Other coherent noise

Coherent noise that has been generated by the source, such as ground roll in land data and guided waves in marine data, can usually be suppressed by appropriate velocity filtering. Diffractions (eg. generated from terminations at fault planes) have the potential to be a significant source of error in faulted areas. Diffractions can be minimised by prestack migration. Sideswipe may be a problem in AVO analysis in areas with complex structure and steep dips. There is not much that can be done at present if there is a lot of sideswipe energy in the data (Ross,1993) except apply full 3D prestack migration which is expensive and time-consuming.

4c. Spherical spreading

Wave propagation effects in general produce an overall decrease in the amplitude with offset. These include spherical spreading, transmission losses, inelastic attenuation, and interbed multiples (Martinez, 1993). For a true offset-dependent spherical spreading correction, a detailed velocity-depth model is needed. Since this is usually not known, an approximation using stacking velocity is used (Ursin, 1990). Spherical spreading will have a strong effect on absolute AVO response, causing an overall decrease in amplitude with offset, but a minimal effect on the relative AVO response.

4d. Inelastic attenuation

Inelastic attenuation of the signal through the overburden changes the AVO response due to time and offset-dependent amplitude decay and phase changes due to dispersion. Correction for the inelastic attenuation of the overburden requires estimation of the parameter Q, which is inherently difficult and very sensitive to noise (White, 1992; Mazzotti and Ravagnan, 1995). The effect on the relative AVO response is minor (Mazzotti and Ravagnan, 1995) although the effect on the absolute AVO response is major (Martinez, 1993). For a reasonably constant overburden, the effect should be reasonably constant.

4e. Anisotropy

Most sedimentary rocks, especially shales, are anisotropic, that is the velocity of *P*- and *S*-wave propagation depends on the direction of propagation. Many sedimentary rocks may be described, to a good approximation, as being transversely isotropic (TI) with a symmetry axis oriented perpendicular to the bedding plane. This anisotropy may be due to a preferred grain orientation of anisotropic minerals, for instance clay mineral platelets in shales (Sayers, 1993, 1994). It may also be caused by the fact that a finely-layered rock, made up of isotropic layers, is equivalent to a TI medium at low (seismic) frequencies (Backus, 1962; Schoenberg, 1994). Many rocks also contain sets of cracks or fractures. A rock of this type, with TI plus fractures, will display azimuthal anisotropy as well. Detection of the orientation of the azimuthal anisotropy, using AVO, can indicate the orientation of the open fractures (Sayers, 1995). Azimuthal anisotropy will not be further discussed here. Failure to account for anisotropy in seismic processing may lead to errors in:

- velocity analysis (Tsvankin and Thomsen, 1994; Alkalifah and Tsvankin, 1994),
- NMO (Tsvankin, 1995a, 1995b),

- migration (prestack and poststack)(Alkalifah and Larner, 1994; Jaramillo and Larner, 1995; Uzcategui and Mujica, 1995),
- time-to-depth conversion (Banik, 1987; Juhlin and Windhofer, 1992), and
- AVO analysis (Samec and Blangy, 1992; Kim et al., 1993, Blangy, 1994; Rueger and Tsvankin, 1995).

Energy is not distributed evenly along an anisotropic wavefront, but focussed in the areas of the wavefront with the tightest curvature (Tsvankin, 1995c). This focussing effect will also affect AVO analysis, particularly when the anisotropy of the target horizon is variable within the area being studied.

Thomsen (1986) introduced three parameters, ε, γ, and δ, defined as combinations of the elastic moduli to characterise TI. Of these parameters, it is δ which principally controls the effect of TI on AVO behavior at small to moderate angles of incidence (Banik, 1987, Wright, 1987; Blangy, 1994), and is the most difficult to measure. Banik (1987) related the *P-P* reflection amplitude to the angle of incidence θ_1 and the parameter δ, for small angles of incidence and weak TI:

$$R_a(\theta_1) = R(\theta_1) + \frac{\Delta\delta}{2}\sin^2\theta_1. \qquad (9)$$

In this equation, $R_a(\theta_1)$ is the *P-P* reflection amplitude for angle of incidence θ_1 at the interface between two transversely isotropic media, $R(\theta_1)$ is the *P-P* reflection amplitude in the absence of anisotropy, and $\Delta\delta = \delta_2 - \delta_1$, where δ_1 and δ_2 are the values of δ on the upper and lower sides of the interface respectively. Equation (9) shows that the effect of TI on the reflection coefficients depends only on the change in δ across an interface, and not on the actual values of δ, for small offsets and weak TI.

The effect of TI on Rutherford and Williams' (1989) AVO model has been studied by Kim et al. (1993), and Blangy (1994). After considering the shales in the database of Thomsen (1986), Kim et al. (1993) assumed a range of -0.2 to 0.6 for the δ values of shale. They concluded that δ is therefore typically positive in shales. The value of δ for the underlying sandstone was set at zero. Their values for $\Delta\delta$ were thus mostly negative, and the effect of this was to make the gradient of the AVO response more negative, amplifying the AVO effect.

Published measurements (Thomsen, 1986; Vernik and Nur, 1992, Leaney, 1994) on TI materials show that there is a useful empirical correlation between *Vp/Vs* and δ (Ryan-Grigor, 1996). The relationship between δ and *Vp/Vs* can be simplified by assuming a linear relationship between C_{13}/C_{44} and *Vp/Vs*. The anellipticity parameter η also shows a useful empirical correlation with *Vp/Vs*. The correlations imply that knowledge of *Vp/Vs* is sufficient to make an estimate of the anellipticity of the *P*- and *S*- wavefronts in a rock, regardless of the lithology. In this way the effect of TI on the AVO response of a particular interface may be estimated, in the absence of any more accurate data. The empirical relationships indicate that rocks tend to become more anelliptic with increasing *Vp/Vs*. Rocks with *Vp/Vs* smaller than about 1.8 tend to have zero to small positive values of δ, while rocks with *Vp/Vs* larger than around 2 tend to have zero to medium negative δ values. Most previous work has assumed a positive value of δ in shales, but this is not necessarily true. If in fact the δ of a shale is negative (*Vp/Vs* is around 2 or higher), and the shale overlies a sandstone, the positive change in δ across the interface could cause a false negative AVO gas indicator. If shale with *Vp/Vs* less than 1.8, as measured in organic-rich and over-pressured shales, overlies a water-filled sandstone, this could cause a false positive AVO gas indicator. However, if the effect of TI can be estimated, then the chances of success for AVO analysis in correctly predicting the presence of hydrocarbons can be increased. The effect on relative AVO is likely to be minimal.

4f. Transmission losses

Stratification of the overburden is responsible for transmission losses as the wave passes through the overlying layers on its way to and from the target horizon. In particular, highly reflective interfaces such as the waterbottom and hard streaks have the potential to greatly affect the AVO response at the target horizon (Gassaway, 1984). This will change the absolute AVO response but given that the overburden is reasonably constant over an area, should have a minimal effect on the relative AVO response.

4g. Overburden effects

Overburden effects include variable velocity layers, shallow gas, gas leakage and seafloor carbonate mounds. These cannot be assumed to be constant over an area such as a field, and have the potential to cause large errors (Yu et al., 1985). Overburden effects can be compensated for by ray-based elastic prestack depth migration. Another approach is to use an adjacent horizon, known or assumed to have a laterally consistent AVO response, as a reference to normalise the target horizon, and thus compensate for all overburden effects, as

described by Chiburis (1984, 1987). Leakage of gas from a reservoir into the overburden may cause partial gas saturation and high attenuation, and an anomalous AVO response (Sengupta and Rendleman, 1991). The effect of 'pods' of anomalous material within the overburden, which cause variable absorption and changes in travel time, is visible (Fig. 50) in a midpoint-offset display of amplitude or two-way time as V-shapes or chevrons of varying angle with their apex at zero offset (Kjartansson, 1980).

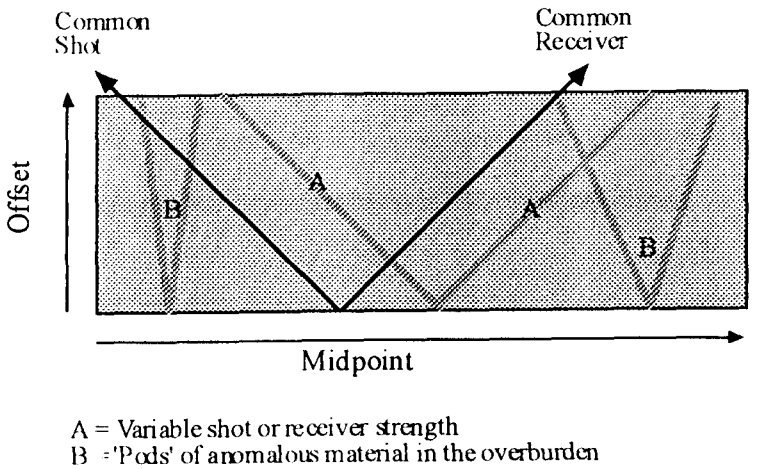

Figure 50. A diagram of a midpoint-offset display of amplitude or two-way time, showing the effect of 'pods' of anomalous material within the overburden (B) and variable source and receiver strength (A), which cause variable absorption and changes in travel time, visible as V-shapes or chevrons of varying angle with their apex at zero offset.

4h. Structural effects

Non-planar interfaces can change the AVO response. Interfaces with curvature much larger than the wavelength will focus and defocus the incident energy, causing a decrease in amplitude along the crest of an anticline, and an increase in a syncline (Castagna, 1993). The curvature effect decreases with offset for an anticline, which will make the gradient more positive, and increase with offset for a syncline, which will also tend to make the gradient more positive. The relative size of these effects compared to other factors is not known. The effect of curved layers can be compensated for by applying 'true amplitude' prestack migration, which while probably not true amplitude in the strictest sense, may be considered to be amplitude-preserving. Surfaces with periodic or random curvatures smaller than the incident seismic wavelength have the potential to produce large changes in the amplitudes (Kindelan et al., 1989). Ross (1992) presented a case study where an anomalous AVO response occurred close to the edge of a salt structure, due to refraction of a substantial portion of the upgoing

energy into the diapir and not out to the surface. The assumption of no dip used in most AVO analysis may introduce errors where dip is significant. These include errors in the calculation of angle of incidence and incorrect NMO velocities (Resnick et al., 1987).

4i. Statics

Accurate surface-consistent static corrections are very important for land AVO analysis (Mazzotti and Mirri, 1991) but statics can also affect marine data, especially for thin bed targets (Treadgold et al., 1990).

4j. Fresnel zone

The amplitude of the reflection observed on any particular trace depends on the weighted average of the reflection coefficient within the Fresnel Zone. Thus there is the potential for a narrow target to be missed, and for an AVO gas response seen in gathers (without prestack migration) to be downdip of the actual gas-water contact (Allen and Peddy, 1993). This scenario will be the same if the explorer is looking for gas, oil, porosity, or fractured zones with AVO analysis. Prestack migration will increase the lateral resolution, and reduce the potential error.

4k. Source and receiver directivity

The energy generated from a seismic source does not propagate with the same strength in all directions, but is usually focussed downwards by using an array of air guns in marine surveys, and vibrator arrays and moveup in Vibroseis land surveys. An array tends to attenuate energy moving in near horizontal directions. The effect of a particular array of sources or receivers on the recorded signal may be calculated from the spacing and weighting of the individual elements in the array (Sheriff and Geldart, 1982). Gassaway et al. (1987) and Mazzotti and Ravagnan (1995) point out that the receiver array attenuation can play a major role in controlling the AVO response, by acting as a lowpass filter at the far offsets. If the same array (source and receiver) is used throughout a survey, the effect on the relative AVO response will be small, although the effect on the absolute AVO response may be large.

4l. and 4m. Irregular source strength and receiver sensitivity

Surface-consistent amplitude correction may be applied to correct for amplitude variations caused by irregular source strength and receiver sensitivity (Yu, 1985). In marine surveys, variation in source strength is usually caused by failure of guns in the source array (Yu, 1985), which will cause a variation in source signature as well. For land surveys, the variation in source strength and signature will be much larger than for marine surveys, due to variable coupling effects, near-surface geology (irregular weathered layer, watertable, sand dunes) and

so on (Chiburis, 1993). The effect of variable receiver or shot strength on the amplitude of a particular horizon is visible in a midpoint-offset display as amplitude bands, corresponding to the common-receiver or common-shot directions (Fig. X). This has been noted by Kjartansson (1980) and Mair et al. (1995).

4n. NMO correction

The conventional method of extracting amplitudes along a horizon is to attempt to perfectly NMO-correct the gather, and then extract the amplitude along a constant time. It must be noted here that all real reflections are non-hyperbolic to some degree, which implies that NMO is never perfect. The distortion in the wavelet shape at far offsets due to the NMO, while not changing the peak wavelet amplitude, causes different points on the wavelet and hence different amplitudes to be in line after NMO is applied. NMO stretch in a Ricker wavelet can cause the far offset amplitude, measured in this manner, to be only 61% of its actual peak value, even when the velocity field is correct (Swan, 1991). Using static shifts to align the event will eliminate NMO stretch, but will not reduce offset-dependent tuning. If the NMO is not perfect, perhaps due to statics, incorrect velocity analysis, or non-hyperbolic moveout curves, the amplitudes that will be picked will also be incorrect. NMO problems can be reduced if the amplitude is measured in a time window after NMO (Mazzotti, 1990), or alternatively if the event is picked on the gathers without NMO correction.

4o. Trace equalisation and mute

Trace equalisation consists of multiplying each sample of a trace by a scalar so that some measure of the average amplitude of each trace (usually root-mean-squared or average absolute amplitude) is constant from trace to trace. Application of whole-trace equalisation has the effect of changing the amplitudes of the whole trace, but it preserves relative changes in amplitude between traces, as shown by Yu (1985). The effect of whole-trace equalisation will be reasonably constant if the mute applied to the gathers is also reasonably constant. A change in the mute pattern will cause a change in the trace scaling factors, and possibly cause a change in AVO response.

4p. Prestack Migration/DMO

It is becoming more common to include prestack time or depth migration in the AVO processing stream, especially in structurally complex areas. These algorithms are computationally intensive and it is questionable whether they are really 'true amplitude'. The advantages of prestack migration are that it places all reflections in their correct position, collapses diffractions, increases the signal-to-noise ratio, reduces dip-related problems, and

corrects for spherical divergence. Widmaier et al. (1995) provide an example of prestack time migration in AVO processing. They use a ray-based amplitude-preserving Kirchoff migration, applied in the common-offset domain, and corrected for thin layering in the overburden.

4q. AGC

Automatic gain control (AGC) or short-window equalisation has the potential to greatly change the AVO response in the data (relative and absolute), and should be avoided in the processing stream whenever possible (Yu, 1985; Castagna et al., 1985; Ahmed, 1991; Castagna, 1993). The effect of the AGC on the AVO response will be minimised if, within the time window of the AGC, there is no event that is radically different in AVO response from the background, except possibly the target horizon, and if the AGC time window around the target horizon does not enter a muted zone at far offsets (Allen and Peddy, 1993).

4r. Offset to angle conversion

The traces in CMP gathers are sorted in terms of offset, and to apply Zoeppritz' equations or any of the simplications requires the data in terms of angle of incidence, so that conversion between offset and angle of incidence is required. The conversion depends on the velocity structure and is variable with two-way time and offset. One method, used when analysing gathers at a well location, is to generate a layered velocity model from the logs, and then raytrace through this model. The velocity layers are usually assumed to be homogeneous and isotropic. If they have a vertical velocity gradient, errors will be introduced, of the order of 10% in AVO intercept and gradient for commonly observed values of velocity gradient (Xu et al., 1993). Another method is that described by Walden (1991), which uses Snell's law and the Dix equation to give angle of incidence in terms of offset, interval velocity of the layer above, and time at zero offset. The advantage of this is that it may be used away from well data, if the interval velocity of the layer above is known to be reasonably constant, for instance in a regional shale. A method which avoids this problem entirely is to apply DMO or prestack migration.

East Dampier 3D Survey Processing

The prestack processing of the data used in this study will be discussed, with reference to the possible effects of each algorithm on the relative and absolute AVO reponse. The data used were the binned gathers along fourteen selected inlines of the 3D survey, which had been kept for further velocity analysis. The gathers have had f-k velocity filtering and demultiple, predictive deconvolution, and adjacent trace sum applied to them. Table 10 shows the complete processing stream applied to the gathers. It was not possible to obtain binned raw gathers, since they had not been generated during processing.

1.	Filter	4-125Hz, convert to zero phase
2.	Resample	2 to 4 msecs
3.	Amplitude recovery	6dB/sec from 0-4sec
4.	Pre-decon mute	
5.	Velocity filtering	Shot domain, +/- 7ms/trace 100% cosine tapering
6.	Adjacent trace sum	2 on 1 with differential NMO
7.	Velocity filtering	Receiver domain, +/- 14ms/trace, 100% cosine tapering
8.	Predictive deconvolution	
9.	f-k demultiple	Cutoff velocity 100000m/s, 25% attenuation
10.	Tidal statics	calculated from tide tables
11.	3D binned gather	100% overlapping bins

Table 10. The processing stream applied to the seismic data (binned gathers) used in this study.

Most of the processing stream is aimed at removing multiples. Multiples are a known major problem in the North West Shelf (Ramsden et al., 1988), caused by the thick Tertiary carbonate wedge that overlies the target horizon. The hard waterbottom reduces the energy that reaches the target horizon, and causes very strong waterbottom and pegleg multiples. Strong intrabed multiples are generated within the carbonate wedge, with a long period and a moveout velocity very similar to the primaries. F-k demultiple is commonly used in the North West Shelf, combined with inner trace muting and predictive deconvolution, and has been

found to be most successful in the parts of the Carnarvon Basin with shallower waterdepth (Ramsden et al., 1988) such as the study area.

The zero-phase filter applied at the start of the processing stream did not work as predicted, and the data therefore are not zero phase. No data-dependent scaling processes are explicitly noted in the processing stream. Such scalers are sometimes built into software modules such as f-k filtering and deconvolution, and therefore are not mentioned in processing reports or side labels. In the absence of any information to the contrary, it was assumed that any such scalers used relatively long windows, and have not caused large variations in relative AVO response at the target level. In places, the far mute has been increased, probably due to excessive noise on the far offsets. This has not affected the AVO interpretation, as these far offsets, larger than around 3000m, were not used in the AVO analysis. None of the other processes applied to the binned gathers should have greatly changed the relative AVO response.

Discussion

It is very probable that there are mode converted waves in the data, produced by the strong reflectors in the overburden. These will tend to appear on the mid to far traces as events which cut across the primary reflections, causing undulations in the amplitude tracked along the primaries. Interference caused by multiples will manifest similarly. Side-swipe should not be a significant issue in this data set, since the structure at the target horizon is very flat-lying. Diffractions may be present, since there is significant faulting in places at the target horizon, and the data have not been migrated. Variation in the overburden may cause changes in inelastic attenuation, lateral and vertical velocity gradients and so on, which will affect the AVO response at the target horizon.

Gas leakage from the reservoir has the potential to cause large errors, but there is no evidence of gas leakage into overlying horizons (no dimming of amplitudes or time delays) and no evidence of gas leakage to surface (Heggie et al., 1991). Structural effects such as lensing and the effects of dip are not expected to be significant since the dip of the target horizon in the study area is everywhere less than 3^0. The lateral resolution of the binned gathers will be defined by the Fresnel zone, since they have not been migrated. The radius of the Fresnel zone at the target horizon is approximately 400-450m. The problems caused by NMO stretch have been avoided by picking the amplitudes on uncorrected gathers, as discussed in the next

section, but this introduces possible errors caused by tuning from NMO convergence of reflectors near the target horizon.

The response of the airgun array was calculated and the combination of the close array spacing, the small number of elements, and the near-vertical raypaths through the water result in an array response which basically does not attenuate the frequencies in the signal. The response of the receiver array (Fig. 51a) was calculated and it can be seen that the total array response, being the combined effect of the source and receiver arrays, starts to attenuate the signal by 3dB or more at a horizontal wavenumber of 0.018 m^{-1} (Fig. 51b). Figure 51(c) shows the total array response in terms of angle of incidence for selected frequencies. It can be seen that the lower frequencies, especially those below 30 Hz, are not significantly affected for angles of incidence less than around 35°. The 60 Hz component however is significantly attenuated at smaller angles of incidence, showing that the array response is acting as a lowpass filter at the far offsets, as expected. The absolute AVO response will be affected but the relative AVO response will not, as the source and receiver array configurations are constant over the entire survey.

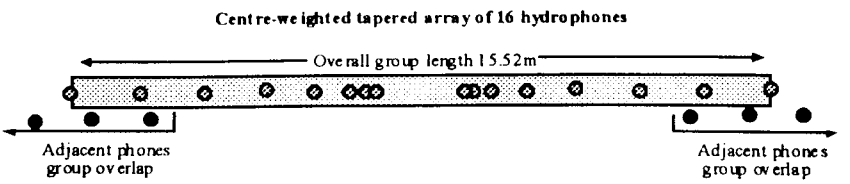

Figure 51(a). Configuration of individual hydrophone group.

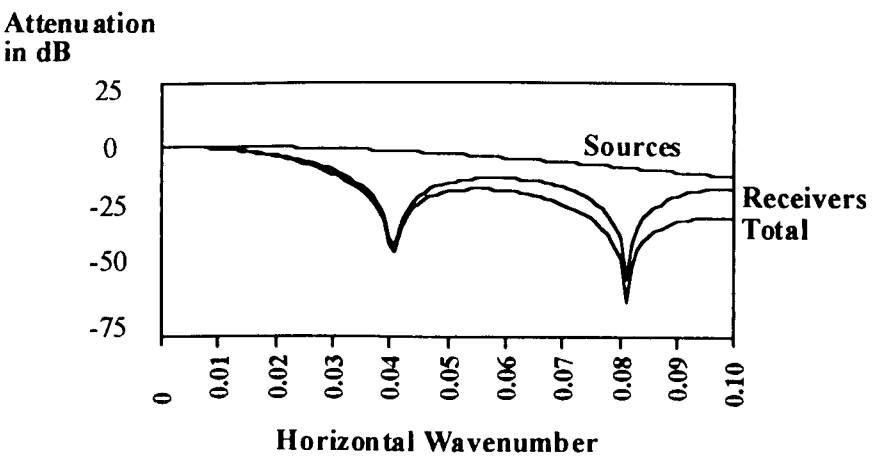

Figure 51(b). Array response for source and receiver arrays, in terms of horizontal wavenumber and attentuation in decibels (dB).

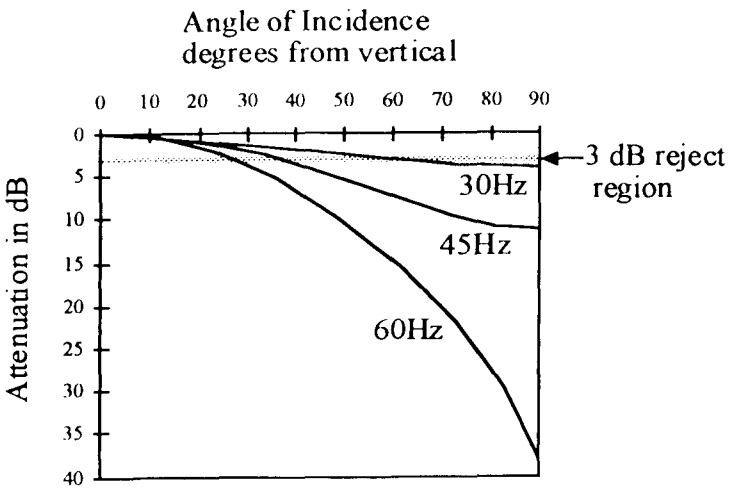

Figure 51(c). Total array response for selected frequencies, in terms of angle of incidence at sources/receivers from vertical and attenuation in dB.

The maximum effective offset at the target horizon, taking into account the far offset mute and noise on the far offsets, is around 2000m, which corresponds to an angle of incidence at the target horizon of 20°, and an angle of emergence into the receivers of 10°. This implies that the effect of the source and receivers on the recorded signal, from Figure 51(c), will be minimal.

The effect of anisotropy (δ) on the AVO response was determined from the empirical relationship between V_p/V_s and δ (Ryan-Grigor, 1996). A value for V_p/V_s of 1.9 in the overlying shale implies a δ that is near zero (0.02), and V_p/V_s of 1.7 in the sandstone implies δ is also near zero, around 0.04. The effect on the AVO response depends on $(\Delta\delta/2)\sin^2\theta_1$, which reaches 0.003 at 20° angle of incidence, the maximum angle used in this study, and will therefore be minimal.

10. AVO INTERPRETATION

AVO Intercept and Gradient

The processing sequence applied to the gathers used in this study has been discussed, along with its probable effect on the absolute and relative AVO response. The processing sequence does not appear to have any elements which would seriously damage relative AVO effects although it clearly is not designed to retrieve the absolute AVO response from the data. The next step is to pick the amplitudes at the target horizon, convert the offsets to angles, and calculate intercept and gradient.

Amplitudes

The gathers were loaded into the 3D seismic interpretation program AIS-3D as a 3D volume in midpoint-offset-time space. The target horizon was directly picked from the gathers, using common-offset sections, common-midpoint sections, and time slices to aid the picking. The gathers were not corrected for NMO, to avoid the problems with NMO described previously. Prestack migration was not an option. Several authors have used the amplitude envelope within a time window, rather than the exact amplitude at a particular time sample, as it is independent of phase and compensates for small errors in picking the horizon. Mazzotti and Ravagnan (1995) used the envelope maximum within a time window, while Hall et al. (1995) used the trace envelope, a low-frequency rectified version of the original trace. The window approach was used, because the horizon was picked manually (the automatic tracker did not perform very well with single-fold data) and the phase of the data is not well constrained. The maximum negative amplitude within a 60msec time window was extracted beneath the pick, which corresponds to an increase in acoustic impedance with depth. The average amplitude within the time window was also extracted, as were measurements using smaller and larger time windows, but all gave very similar results. Figure 52 shows the time picks and amplitude maps for the target horizon for inlines 1600, 1700, 1740, and 2120. Both raw and smoothed amplitude data are displayed. The raw data was used for AVO analysis, and the smoothed amplitude data is shown to better illustrate the amplitude trends.

Offset to angle

In order to convert the offsets to angles, the method of Walden (1991) was used. A constant velocity was assumed for the overlying shale. Also, a flat layered velocity model was constructed from the Angel-4 sonic log, and raytracing was done using the Western Atlas programs MIMIC and QUIKCDP (Fig. 53). The raypaths are almost straight, due to the high-

Figure 52. Time, amplitude, and smoothed amplitude of the Top-Upper-Unit horizon, on prestack gathers 2120, 1740, 1700, and 1600.

(a) Two-way time map of Top-Upper-Unit

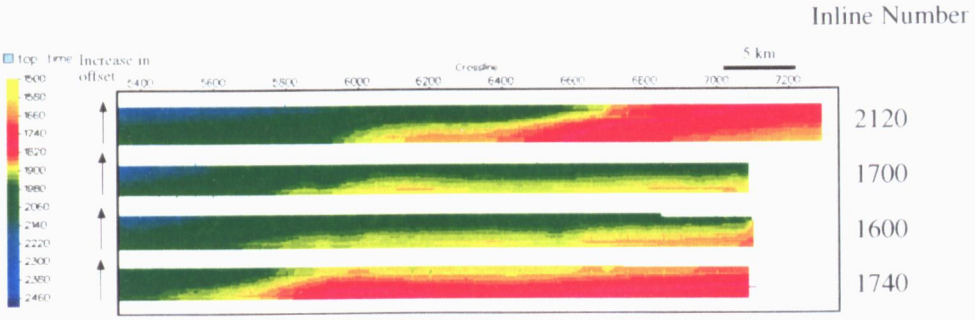

(b) Average Amplitude in 60msec time window below Top-Upper-Unit

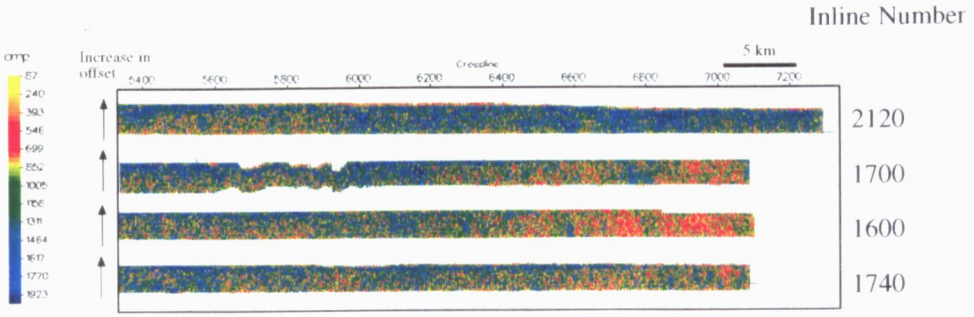

(c) As above, smoothed

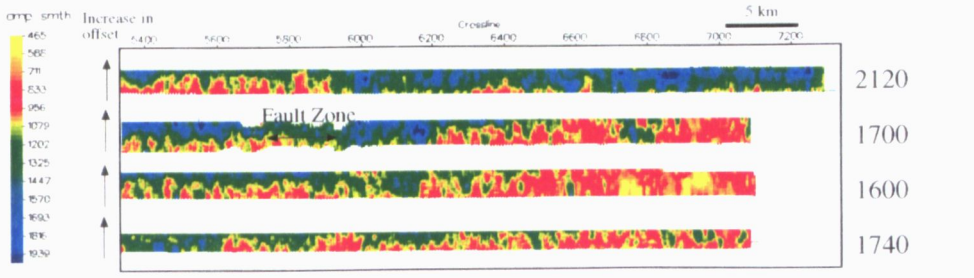

Figure 53. Flat layered model from sonic and density logs of Angel-4, with raytracing of shot gather using acquisition geometry, showing angle of incidence at the target horizon and at the receivers.

(a) Angle of incidence of rays at target horizon and angle of emergence of rays into receivers, from raytracing through flat layered model below.

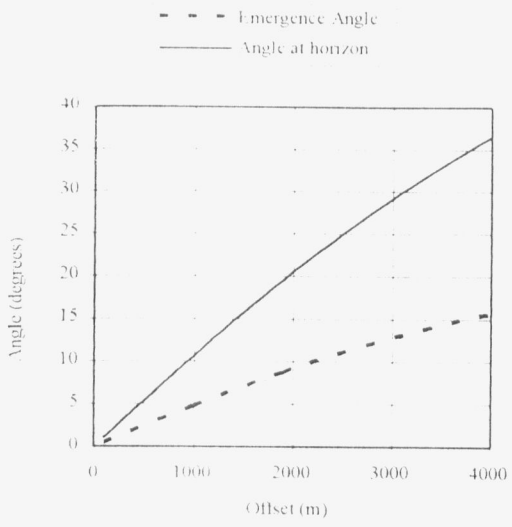

(b) Flat layered model from sonic and density logs of Angel-4, with raytracing of single shot gather using acquisition geometry, showing raypaths to target horizon (top Angel Formation) only.

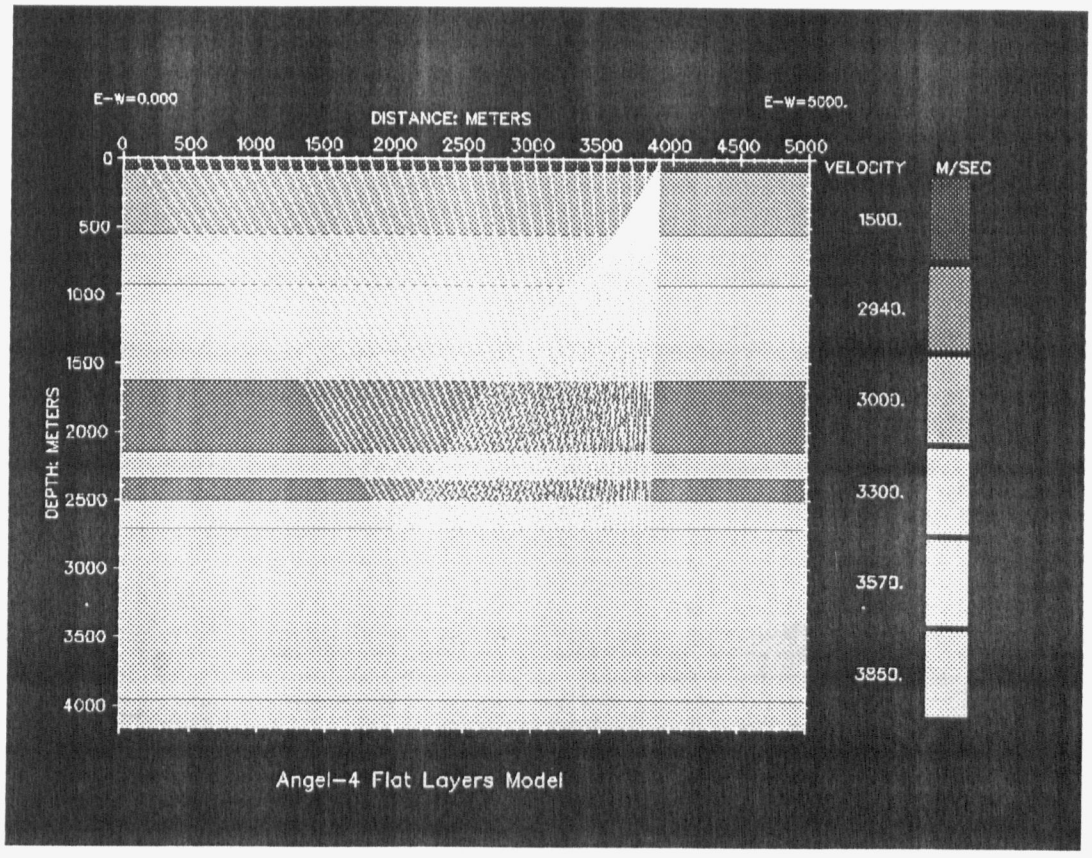

velocity Tertiary sediments. The near traces have angles of incidence on the target horizon of a few degrees, while the far offsets have angles around 30°. This is in accordance with the angles of incidence calculated using Walden's method.

Intercept and Gradient

An essential part of the AVO analysis is to derive values of intercept and gradient. In this study, Shuey's (1985) approximation will be used, as it does not assume any particular value for V_p/V_s or Poisson's Ratio. It is restricted to angles of incidence less than 30°, but this does not greatly constrain the input data, as the gathers do not contain angles higher than 20° with useful data at the level of the target horizon, due to the far offset mute, and noise on the far offsets. The method of Walden (1991) is used for the straight-line fit between amplitude and $\sin^2\theta$. This method is robust and handles noisy data and outliers very well. The first estimate is given by regression by medians, which is refined using maximum likelihood regression to provide a best fit. The runs test statistic parameter is also calculated. This measures the validity of the fit, by examining runs of positive and negative residuals to check for systematic error. If the absolute value of the runs test statistic is less than three, the fit is acceptable, ie the residuals are randomly positive and negative. Intercept and gradient were calculated for all midpoints along fourteen inlines: 1600, 1662 (nearest Angel-3), 1700, 1740, 1820 (Angel-1), 1924 (Angel-4), 2000 (Angel-2), 2120, 2140, 2180, 2238, 2287, 2320, and 2347. Approximately 12,600 gathers were processed in total. The intercept and gradient, together with the mean error and runs test statistic, were calculated for each gather (crossline number) along inlines 1662, 1820, 1924, and 2000. The data are quite noisy but the trends in the intercept and gradient are clear. Figure 55 shows three gathers on inline 1700, at crosslines 5800, 6200, and 7000. Crossline 5800 lies in the Angel Field, close to the main E-W fault zone, just south of Angel-1; crossline 6200 is also within the Angel Field, south of Angel-3; and crossline 7000 lies on the eastern flank of the Angel Field, within the Lewis Trough. Figure 56 shows the amplitude extracted from the target horizon plotted against $\sin^2$ (angle of incidence), for these three gathers, and the line of best fit calculated from the method of Walden (1991), together with the runs test statistic and the mean error of the fit.

Standard Methods of AVO analysis

Rutherford and Williams (1989) classified the AVO responses of a shale overlying a gas sand into three groups. Class I has a large positive intercept and a negative gradient (with all amplitude values positive). Class II has an intercept close to zero, a negative gradient, and possibly a polarity reversal (amplitude values change from positive to negative at some offset). Class III has a large negative intercept and a negative gradient (all amplitude values negative). The classic gas response in the low-impedance sands of the Gulf Coast is Class III, a large intercept and a large negative gradient. The AVO gas indicator used is the AVO product, the product of the intercept and gradient, which in these cases gives a large positive number. The AVO product does not pick up gas sands of Class I or II (Castagna and Smith, 1994).

Figure 54(a). Raw intercept and gradient along inline 1662, with the runs test statistic and the mean error. A runs test statistic between 3 and -3 is an acceptable fit.

Inline 1662

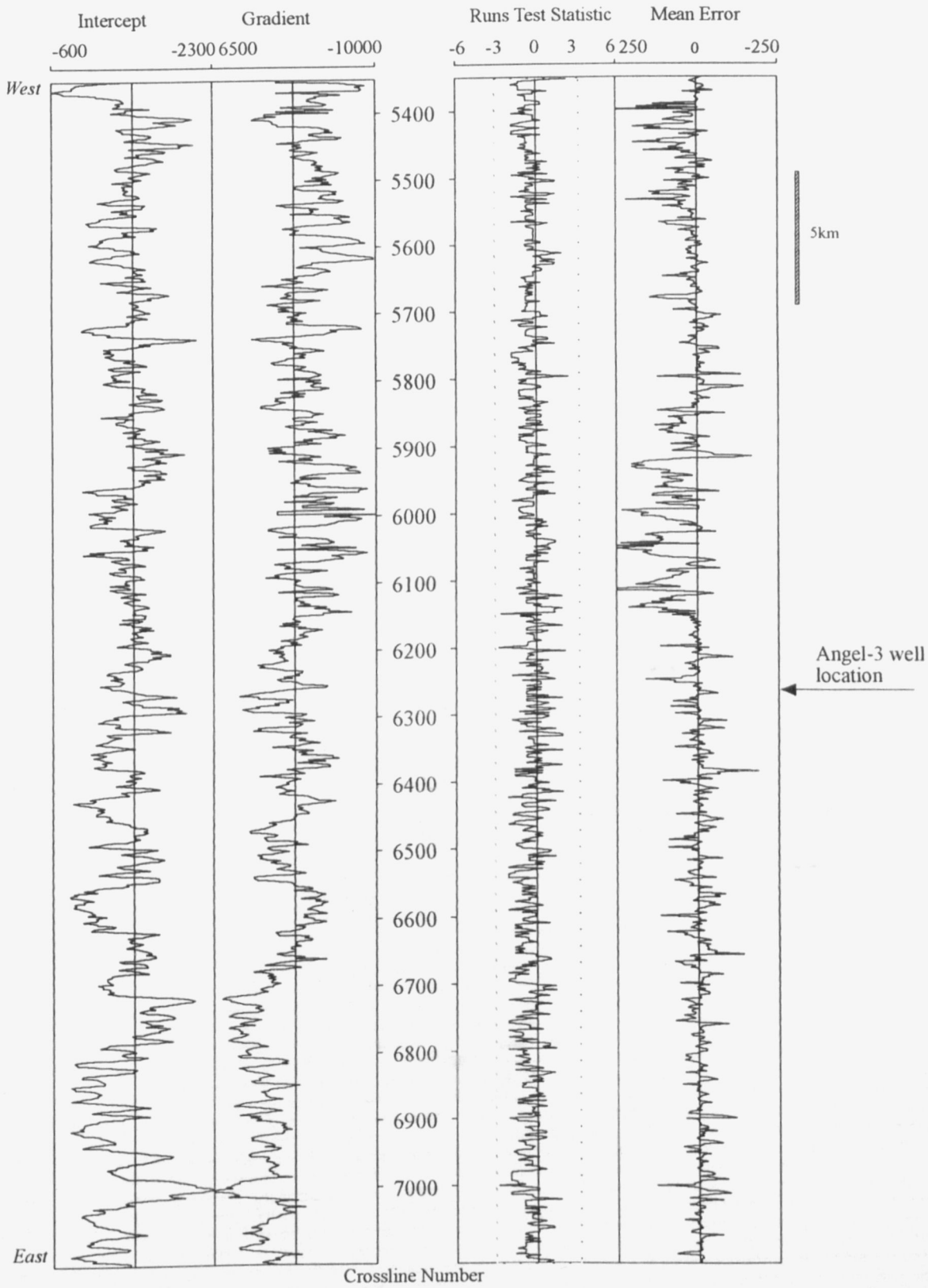
Intercept
Gradient
Runs Test Statistic
Mean Error
-600
-2300 6500
-10000
-6 -3 0 3 6 250 0 -250
West
East
5400
5500
5600
5700
5800
5900
6000
6100
6200
6300
6400
6500
6600
6700
6800
6900
7000
5km
Angel-3 well location
Crossline Number

Figure 54(b). Raw intercept and gradient along inline 1820, with the runs test statistic and the mean error. A runs test statistic between 3 and -3 is an acceptable fit.

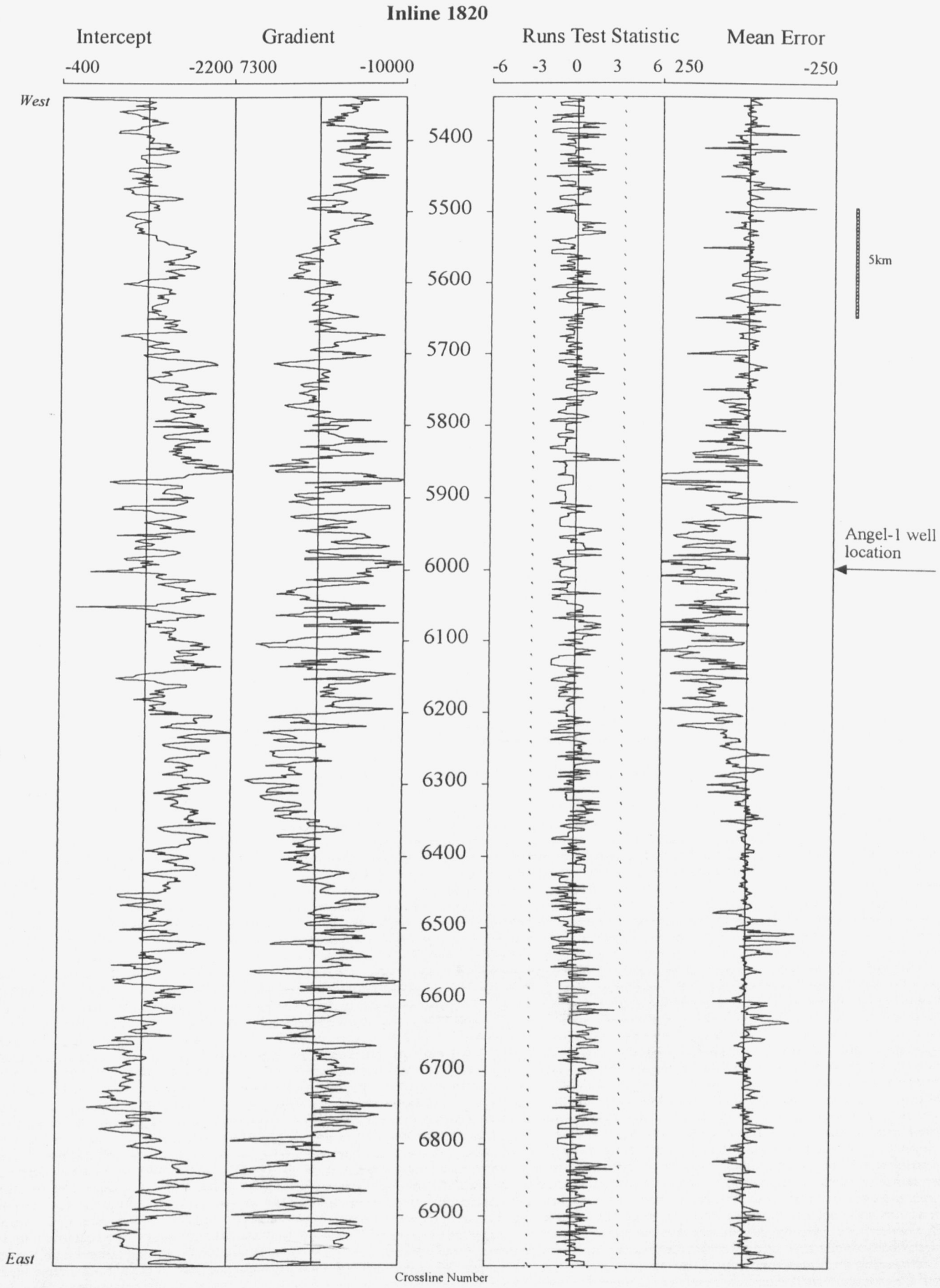
Inline 1820
Intercept
Gradient
Runs Test Statistic
Mean Error
-400
-2200
7300
-10000
-6
-3
0
3
6
250
-250
West
East
5400
5500
5600
5700
5800
5900
6000
6100
6200
6300
6400
6500
6600
6700
6800
6900
5km
Angel-1 well location
Crossline Number

Figure 54(c). Raw intercept and gradient along inline 1924, with the runs test statistic and the mean error. A runs test statistic between 3 and -3 is an acceptable fit.

Inline 1924

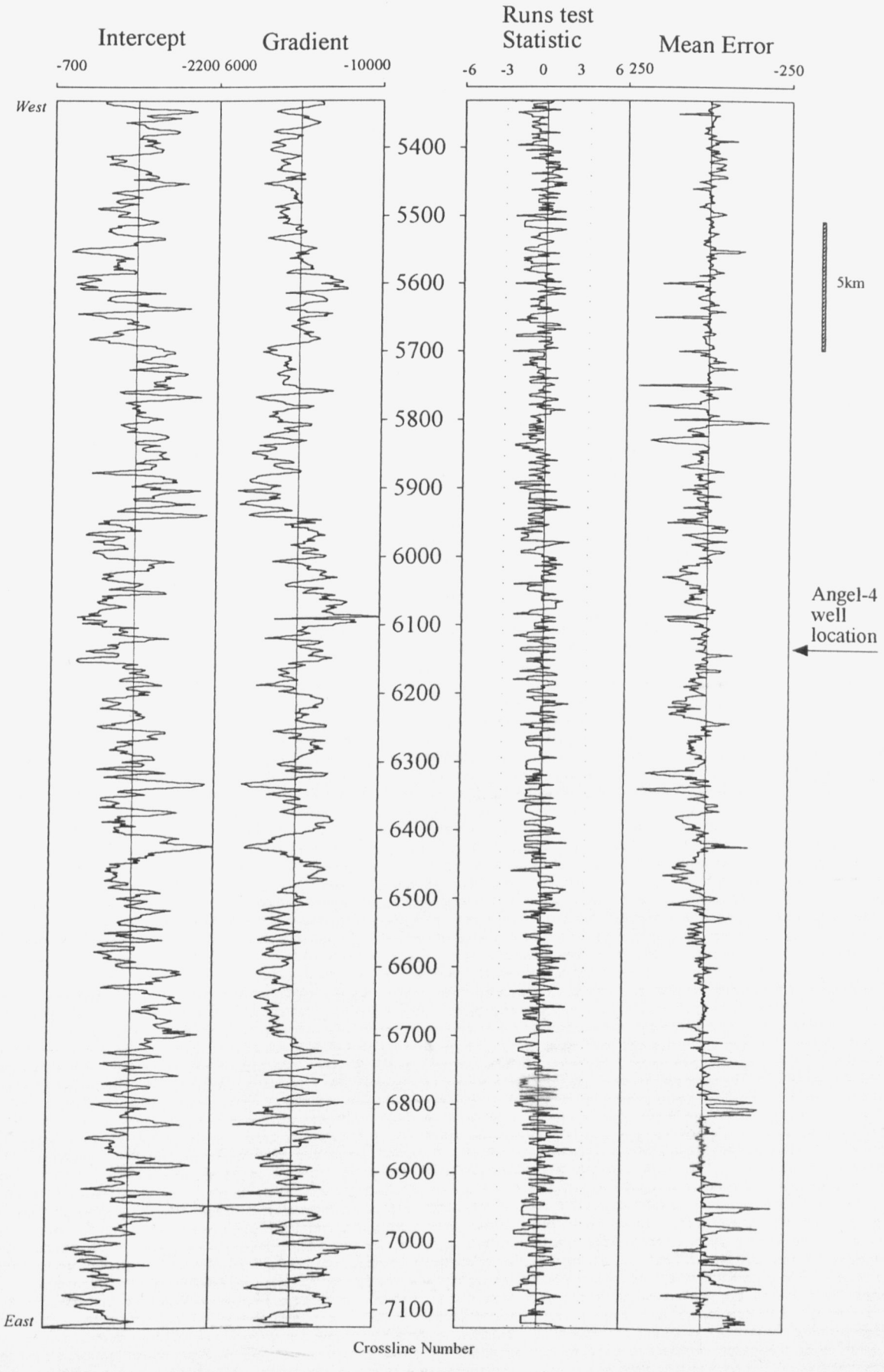
Intercept
Gradient
Runs test Statistic
Mean Error
-700
-2200 6000
-10000
-6 -3 0 3 6 250
-250
West
East
5400
5500
5600
5700
5800
5900
6000
6100
6200
6300
6400
6500
6600
6700
6800
6900
7000
7100
5km
Angel-4 well location
Crossline Number

Figure 54(d). Raw intercept and gradient along inline 2000, with the runs test statistic and the mean error. A runs test statistic between 3 and -3 is an acceptable fit.

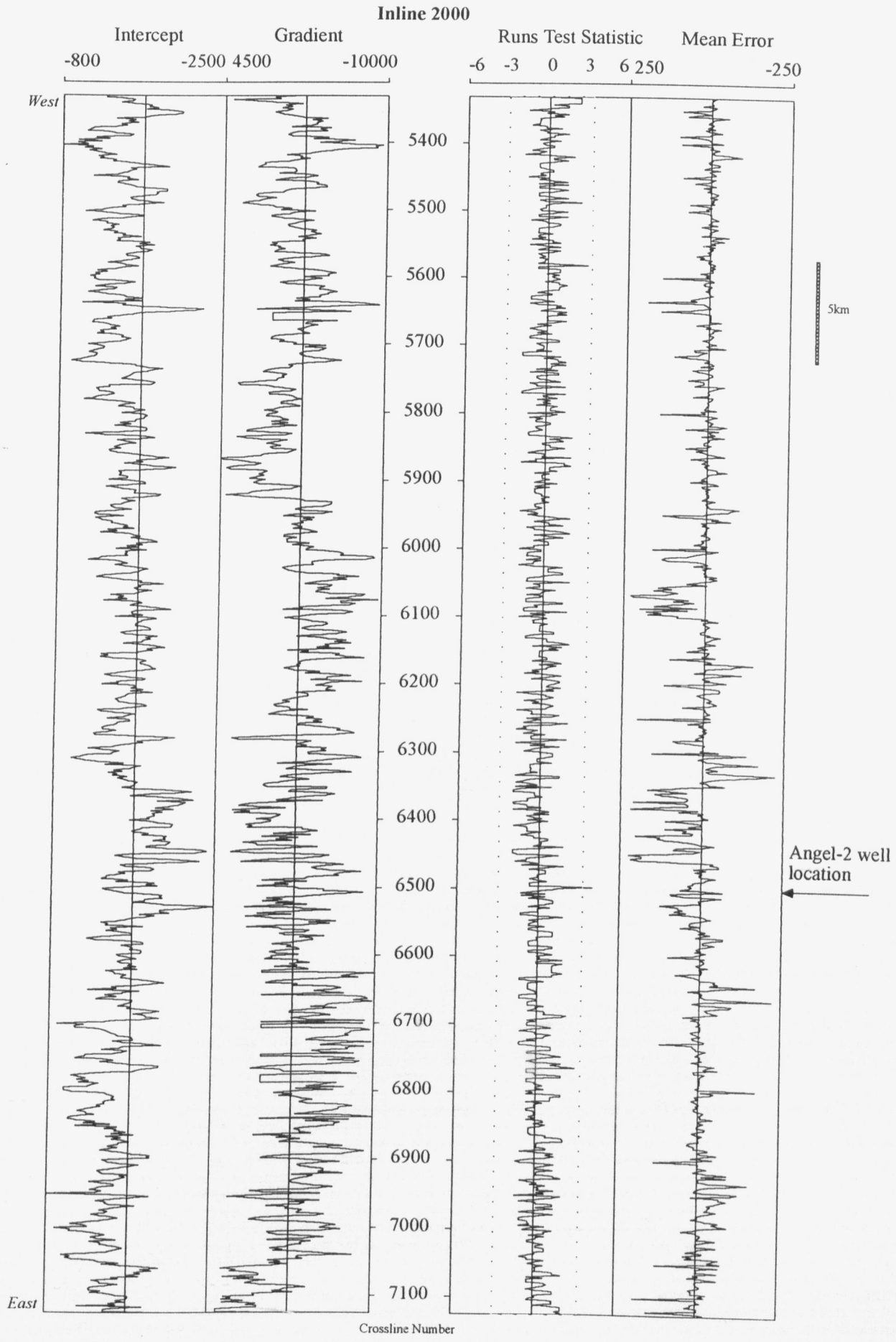
Inline 2000
Intercept
Gradient
Runs Test Statistic
Mean Error
-800
-2500
4500
-10000
-6
-3
0
3
6
250
-250
West
East
5400
5500
5600
5700
5800
5900
6000
6100
6200
6300
6400
6500
6600
6700
6800
6900
7000
7100
5km
Angel-2 well location
Crossline Number

Figure 55. Selected gathers along inline 1700. Crossline 5800 is near the main EW fault zone, at the crest of the field and has the lowest signal-to-noise ratio. Crossline 6200 is near Angel-3 on the southeastern edge of the field, and has a medium signal-to-noise ratio. Crossline 7000 lies on the eastern edge of the study area, and has a high signal-to-noise ratio. Note that there is no strong visual change of amplitude with offset at target zone.

Inline 1700
Crossline 5800

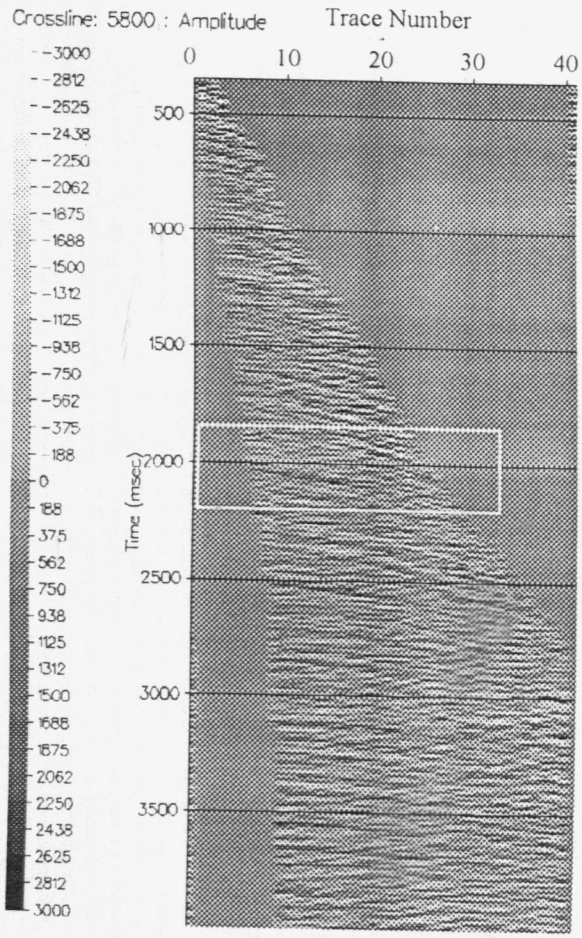

Near main E-W fault zone, on crest of field
Lowest signal-to-noise ratio

Inline 1700
Crossline 6200

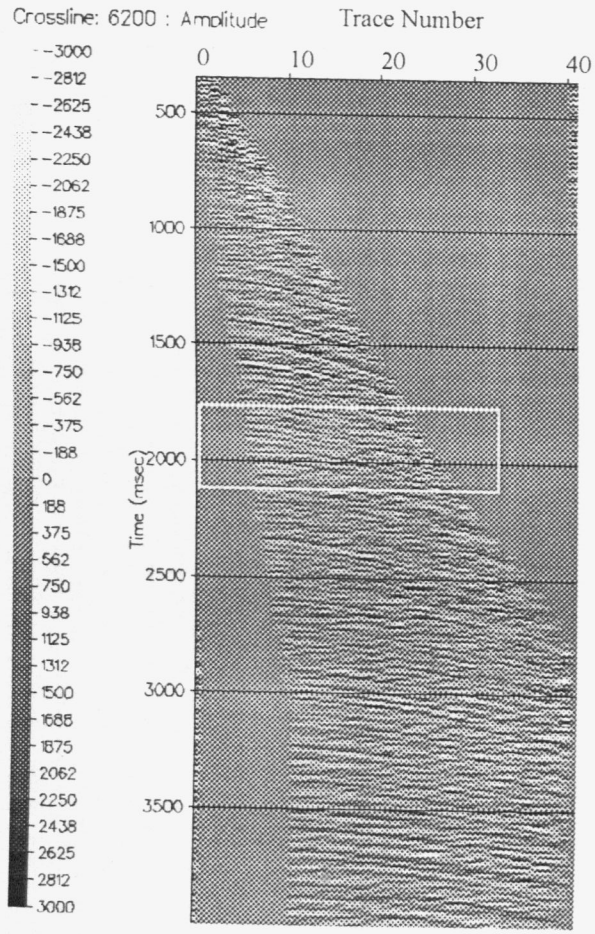

Near Angel-3, edge of field,
medium signal-to-noise ratio

Inline 1700
Crossline 7000

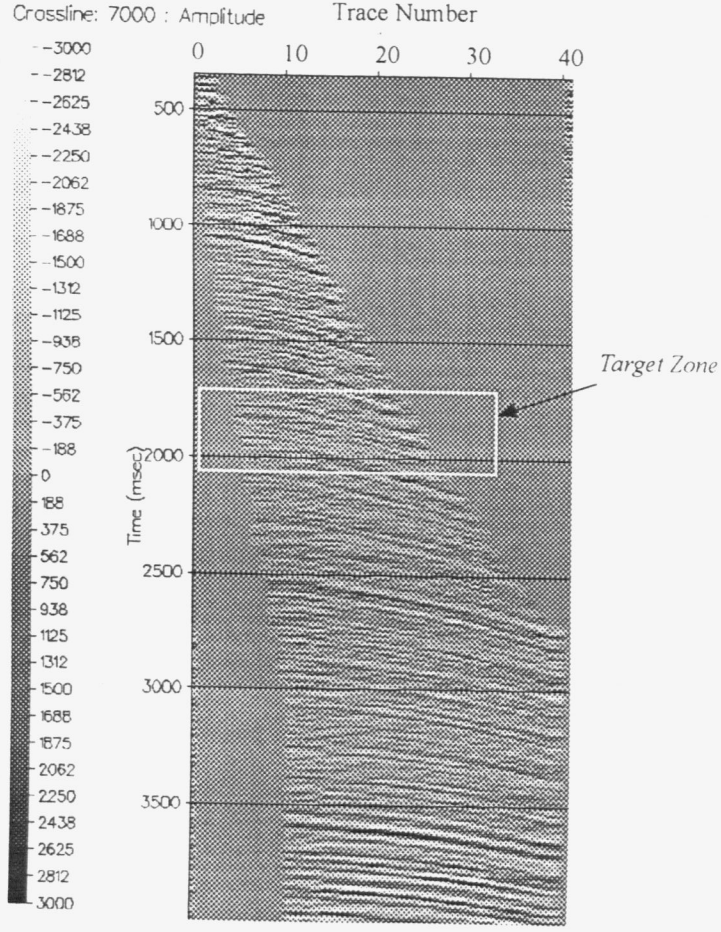

On eastern flank of Angel Field,
highest signal-to-noise ratio

Figure 56. Amplitude versus sine squared (angle of incidence) plots for the three selected gathers along inline 1700.

(a) Inline 1700, crossline 5800.

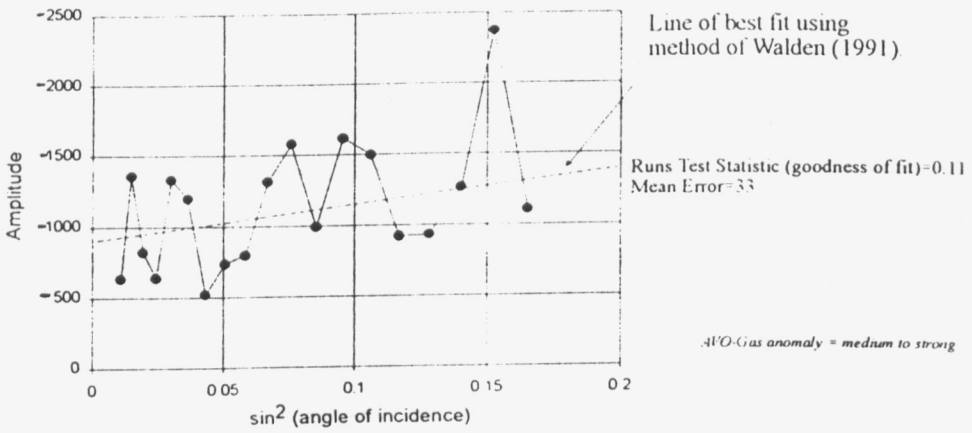

(b) Inline 1700, crossline 6200.

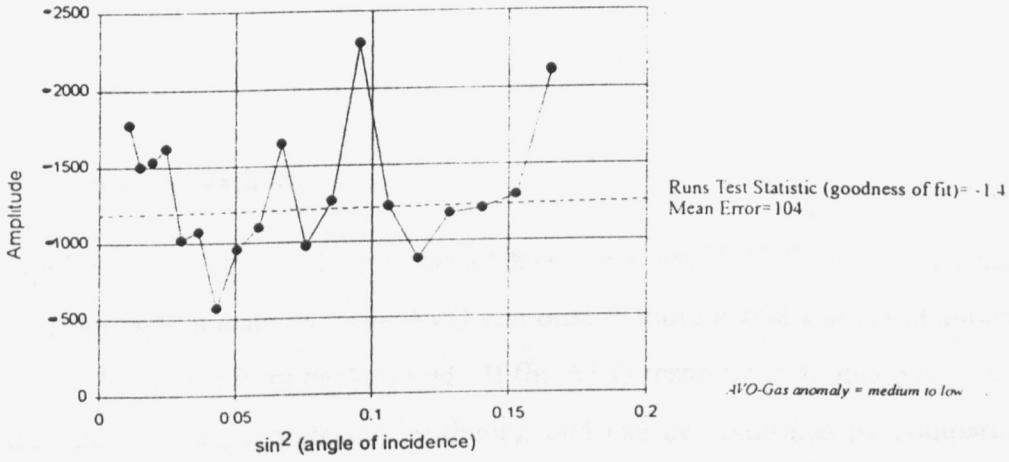

(c) Inline 1700, crossline 7000.

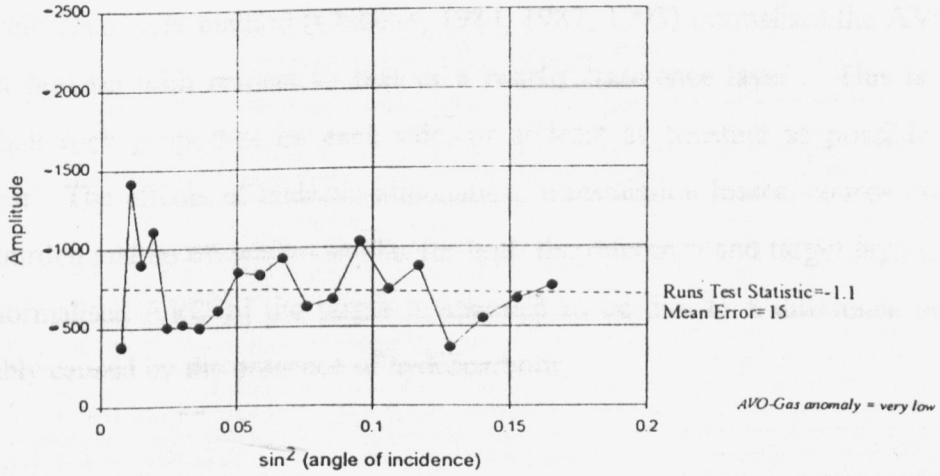

There are significant differences in AVO behaviour between the traditional low-impedance gas sand targets of the Gulf Coast, and targets where the sandstone is of similar or higher impedance relative to the surrounding shales, as in the Angel Field, for which the AVO response is Class I or II. In low-impedance sands, which have a high porosity (30-35%), the presence of gas has a large effect on V_P. The AVO intercept and the amplitude in the stacked data are both strong gas indicators (Peddy and Sengupta, 1995). In high-impedance sands, with lower porosity, the change in V_p due to gas is smaller, and the intercept may be much smaller, and either positive or negative, and therefore not a strong gas indicator by itself. In the low-impedance sands, there is a large difference between the σ of gas sands (0.10-0.15) and water sands (0.30-0.35) (Peddy and Sengupta, 1995), which results in a high gradient. In high-impedance sands, the water-wet σ is lower (0.20-0.25 in the Angel Field), and this makes the difference in σ between gas and no gas 0.05-0.15, compared to 0.15-0.25 for the low-impedance sands. Therefore, in high-impedance sands, the gradient alone is not a strong gas indicator. The product of intercept and gradient for high-impedance sands will often be negative or close to zero.

Anomaly-hunting methods

The target horizon in the study area has a Class I or Class II AVO response, which requires a different approach in analysis. The AVO response is more subtle and AVO anomalies are the target - the deviations from background. If the AVO response is anomalous, is in accordance with the relative change predicted by theory, and can be confirmed by comparing the AVO anomaly with other evidence such as structural extent, then an AVO anomaly may be a useful hydrocarbon indicator.

The reference-layer method (Chiburis, 1984, 1987, 1993) normalises the AVO response of the target horizon with respect to that of a nearby 'reference layer'. This is an interface with constant rock properties on each side, or at least as constant as possible over the area of interest. The effects of inelastic attenuation, transmission losses, source and receiver arrays, overburden and so on will be similar for both the reference and target layers, so any change in the normalised AVO of the target is assumed to be due to a difference in the target layer, possibly caused by the presence of hydrocarbons.

Castagna et al. (1985) and Krief et al. (1990) found that there is a linear correlation between V_p^2 and V_s^2 in water-wet sands and shales. The hydrocarbon-bearing rocks plotted away from the linear correlation of the water-wet rocks. The Castagna et al. (1985) correlation was utilised by Smith and Gidlow (1987) to define their Fluid Factor, which is another anomaly-hunting technique, described in a previous section. Castagna (1991) suggested that AVO analysis incorporate a crossplot between R_p and R_s, the P-wave and S-wave reflection coefficient series, derived using the approximation of Hilterman (1990).

The relationship between P-wave velocity and density (Gardner et al., 1974), when combined with the linear relationship between V_p^2 and V_s^2 (Castagna et al., 1985), can be expressed in terms of AVO intercept I and gradient G (Foster et al., 1993). The equation predicts that the AVO water or background trend will be linear and pass through the origin of an intercept versus gradient crossplot, at an anticlockwise angle from the vertical of approximately 32° for log data and 16° for seismic data. This has been observed by Foster et al. (1993) in many wells. Hydrocarbon bearing rocks will plot at the edges of the main cloud of data points or away from the background trend. It must be kept in mind that an anomalous point could also be generated by any rock layer that is different from the background eg salt, coal, carbonates, igneous intrusions or overpressured shales. It has also been noted (Reilly, 1994) that the AVO response of high-impedance unconformity surfaces in the North Sea is very similar to that of the gas sands. However, this crossplot method does not assume that the presence of hydrocarbon always produces a large positive gradient, as much current AVO analysis does, and is therefore more robust and applicable to a wider range of geological settings.

Verm and Hilterman (1995) follow a similar method, but they crossplot intercept against PR. This parameter is given by

$$PR = \frac{\sigma_2 - \sigma_1}{(1 - \frac{\sigma_1 + \sigma_2}{2})^2}, \tag{10}$$

where σ_1 is Poisson's Ratio of the upper layer and σ_2 is Poisson's Ratio of the lower layer, found by a linear inversion of the AVO response using the form

$$R(\theta)=I\cos^2\theta+PR\sin^2\theta, \tag{11}$$

as suggested by Hilterman (1989). In this equation, I is the intercept. The values of intercept and PR are calculated for an entire section, and crossplotted. The reflectors caused by lithologic boundaries form separate clouds, and the crossplot shows the 'depositional model expressed on the seismic section'. Figure 57 is a sketch of the resulting crossplot. The linear relationship between intercept and gradient noted by Foster et al. (1993) is visible, as well as the separation of the gas points from the background trend.

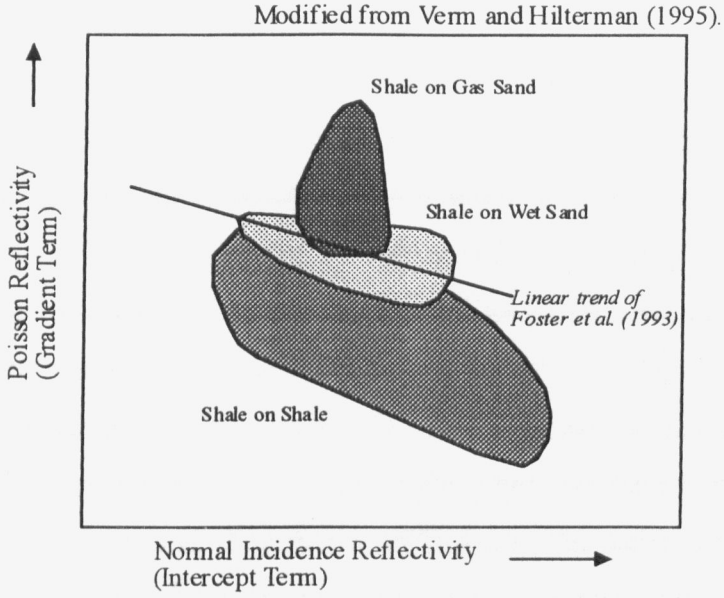

Figure 57. AVO analysis crossplot of Vern and Hilterman (1995).

Castagna and Smith (1994) suggest that R_p-R_s is a gas indicator in clastics that will work for Class I, II, and III AVO responses. The equation can be calculated from

$$R_p - R_s \approx \frac{I+G}{2}, \tag{12}$$

and assumes that V_p/V_s is equal to 2. R_p-R_s tends to be near zero in water-wet sands, is always more negative in gas sands, and works best when there is a strong gas effect on V_p. This implies that R_p-R_s will work best for Class III responses, and where V_p/V_s is close to 2.

Method used in this study

Since the data is a set of intercept/gradient pairs along a particular horizon, the reference layer method of Chiburis (1984, 1987, 1993) seemed appropriate. Unfortunately, in the study area there was no suitable reference horizon. The nearby strong KA (Aptian Unconformity) and

KV (Intra-Valanginian Unconformity) reflectors both had variable amplitude, as shown in their amplitude maps (Figs 19a and 17b), implying variable rock properties over the study area. Any reflections above this were within the Tertiary carbonate wedge, and since it is the carbonate wedge itself that produced most of the wave propagation effects, these reflectors were not suitable. Immediately below the target horizon is the Main Unconformity, which has an extremely variable character in the stacked data and about 600msec relief in the study area, so it also was not suitable.

The R_p-R_s method of Castagna and Smith (1994) was applied to the data. This involved simply taking the average of the intercept and gradient pairs along each inline and contouring the values, to get a map of R_p-R_s over the study area (Figure 58). The assumption with this method is that V_p/V_s is close to 2. Full-waveform sonic logs were run at Angel-4, and found that in the overlying shale the V_p/V_s was 1.9 and in the reservoir sandstone it was 1.8. When the method was expressed in terms of an intercept versus gradient crossplot, the lines of equal $(I+G)/2$, which is a scaled version of R_p-R_s, cut across the cloud of data points, indicating that the probable gas points lie at the top of the cloud, and have higher gradients (Figure 59). The crossplot of Verm and Hilterman (1995) shows the same pattern (Fig. 57), where the gas points lie at the end of the cloud of data points with the highest gradient, which is equivalent to higher values of parameter PR. An examination of Figure 59 indicates that the addition of gas to the sandstone decreases the impedance contrast with the overlying shale, which reduces the intercept, and causes an increase in gradient.

Gas Indicator mapping from AVO

The map of R_p-R_s (Fig. 58) shows discrete areas where the AVO analysis predicts the presence of gas. When this is superimposed on the time closures on the Top-Upper-Unit (the top of the reservoir) all of the AVO anomalies except one correspond to areas of time closure, and therefore to known or probable structural traps. The AVO gas response, as calculated by the R_p-R_s method, shows anomalies that are in accordance with the relative change predicted by theory (R_p-R_s becomes more negative in the presence of gas), and the anomalies correspond reasonably well in shape and extent with the time closures at top reservoir

Figure 58. Map of gas indicator R_p-R_s (Castagna and Smith (1994) generated from R_p-R_s values for the Top-Upper-Unit of the Angel Formation, extracted along each of the fourteen inlines used in this study, after contouring and smoothing. The most positive values are coloured blue and are least likely to be gas, and the most negative values are coloured red and are most likely to contain gas.

(a) Map of gas indicator R_p-R_S.

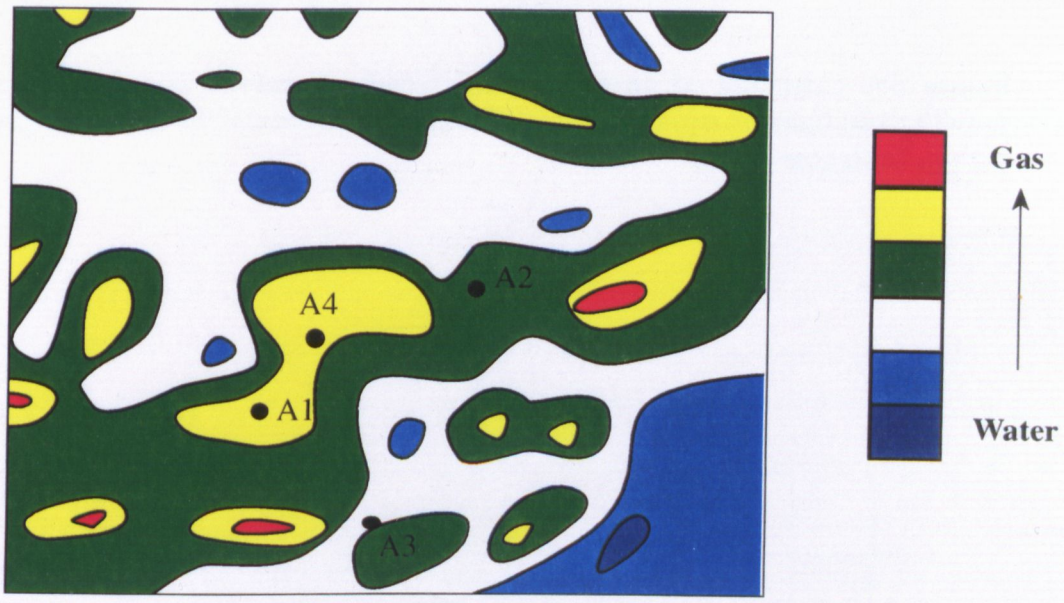

(b) Map of gas indicator R_p-R_S with fields (solid line), time closures at top Angel Formation level (dotted line), and major E-W fault zone south of Angel-1.

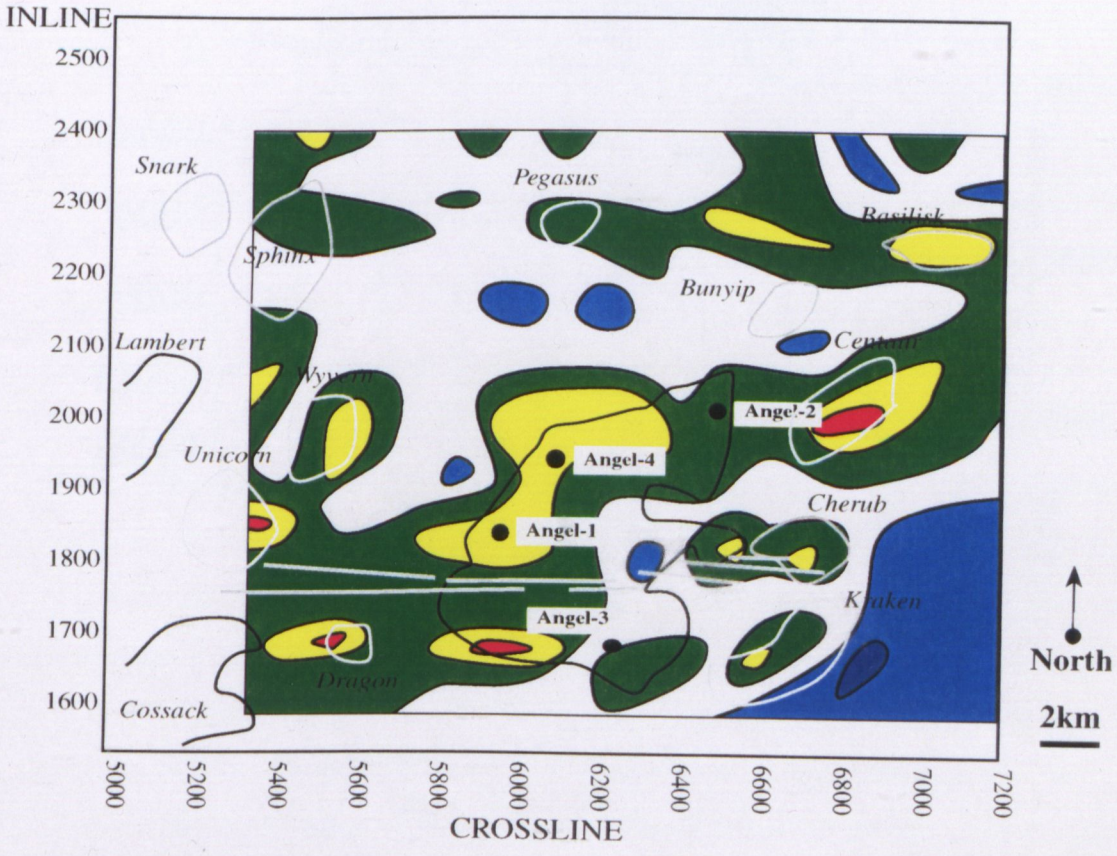

Figure 59. Crossplot of Intercept and Gradient values calculated from inline 1924, showing the lines of equal values of (Intercept+Gradient)/2 which is a scaled version of the gas indicator R_p-R_s.

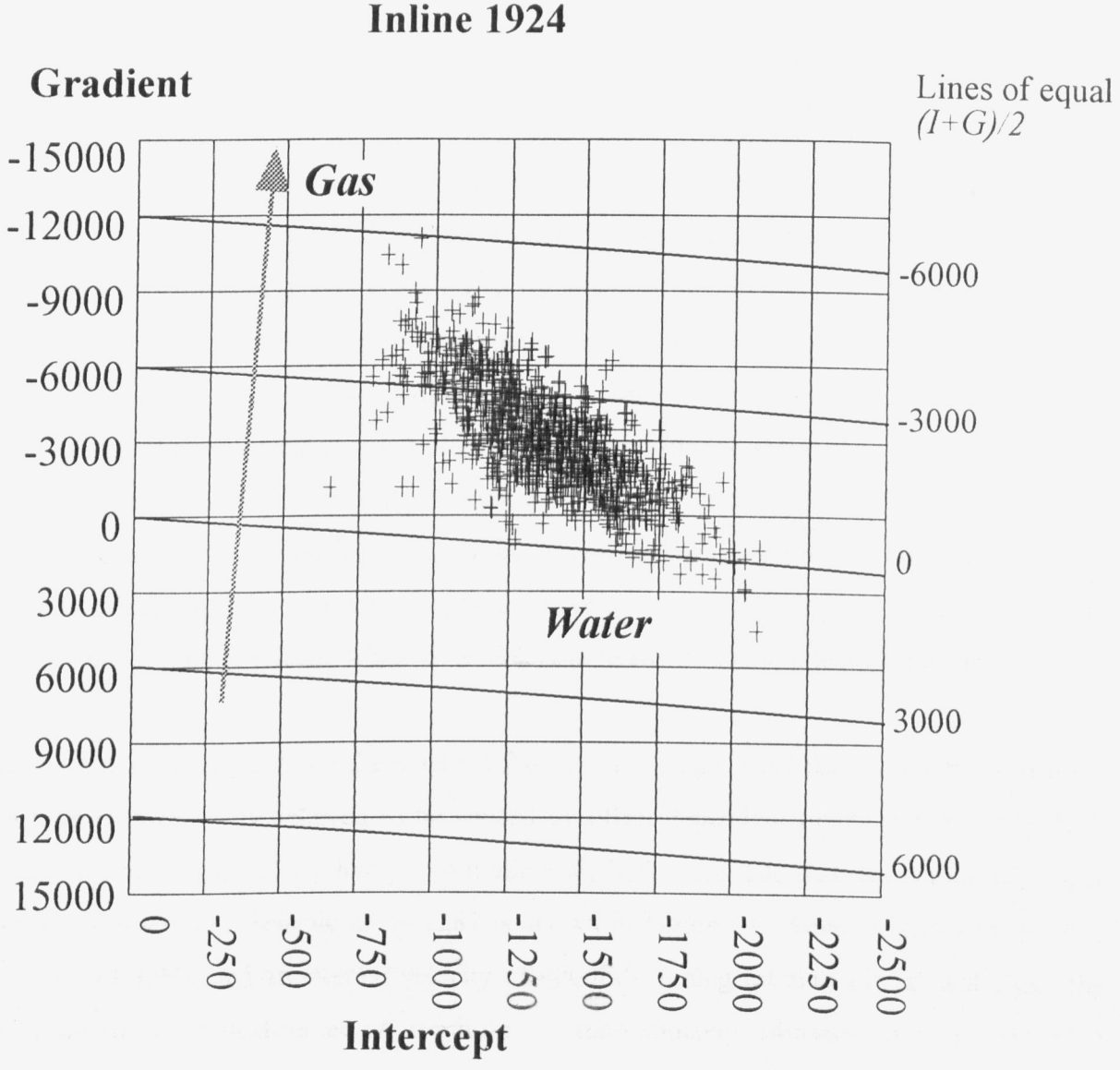
Inline 1924
Gradient
Lines of equal
(I+G)/2
-15000
-12000
-9000
-6000
-3000
0
3000
6000
9000
12000
15000
Gas
Water
-6000
-3000
0
3000
6000
0
-250
-500
-750
-1000
-1250
-1500
-1750
-2000
-2250
-2500
Intercept

level. The usefulness of this method is that it is derived directly from the seismic data with few assumptions, and indicates if there is in fact a detectable AVO effect present, before any detailed work is done to extract more quantitative information.

The Angel Field itself has a medium to strong AVO anomaly, except near Angel-2. The closure to the north of the Angel Field (Bunyip) does not show an AVO anomaly. The absence of the AVO anomaly near Angel-2 and in Bunyip is probably due to the presence of the dolomite-cemented layers. To investigate this, the sonic and density logs from Angel-2 over the dolomite-cemented interval were firstly blocked by hand into 11 layers. These layers were then input into *VESPA*, a Western Atlas program that computes synthetic shot gathers, using the visco-elastic wave equation. The synthetics were generated with primaries and mode conversions only (ie no multiples or surface waves). The effect of gas was simulated by reducing V_p and density using Biot-Gassman fluid replacement modelling (Chapter 7). The synthetic shot gathers (Fig. 60) showed that the effect of the presence of gas is overwhelmed by the reflections from the dolomite-cemented zones, and this was probably why the closure to the north of Angel and the area around Angel-2 does not show an AVO anomaly. It is probable that Bunyip contains gas, because the next closure to the north (Basilisk), which is outside of the dolomite-cemented zone, does show an AVO anomaly. The effect of gas on the AVO response in the presence of the dolomite-cemented zones cannot be calculated using a simple two-layer model. The dolomitic layers have a strong and complex effect on the AVO response due to tuning effects, which over-rides the relatively subtle effect of the gas.

There is one AVO anomaly on the northern flanks of the Angel Field that does not correspond to a time closure. It is believed to be caused by offset-dependent tuning between the Top-Upper-Unit reflection and a reflection of moderately high amplitude that lies within the Upper Unit of the reservoir. Seismic inline 2287 is shown in Figure 61. Given a dominant seismic frequency of 35Hz, and an interval velocity of 4000m/s, tuning (at zero-offset) will affect the amplitude of the reflectors at an isochron of approximately 14msecs (one quarter of a wavelength). Offset-dependent tuning, ie tuning of the NMO curves of each reflector, will occur at around this same time thickness. When the time thickness between the internal reflector and Top-Upper-Unit is plotted along the inline and compared with the extent of the gas anomaly, as in Figure 62, it can be seen that the extent of the gas anomaly closely matches the area where the isochron is 14msecs or less.

Figure 60. Synthetic shot gathers generated from the sonic and density logs of Angel-2, using the viscoelastic wave equation, primary events and mode conversions only, no multiples or surface waves. Note the minimal difference in the seismic response between the two models (gas and no gas).

(a) Angel-2 VESPA model, water wet. Wavelet used has Ricker frequency spectrum, dominant frequency of 35Hz. Plot scaled as true amplitude, no equalisation applied within trace or between traces.

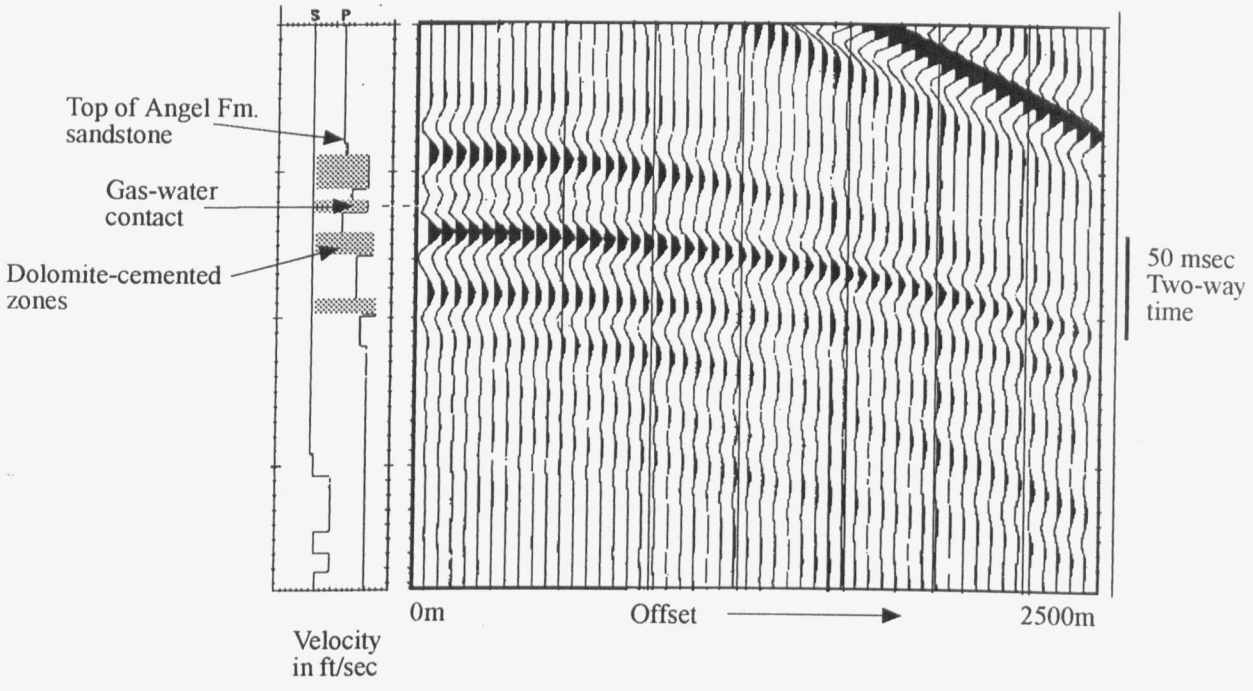

(b) Angel-2 VESPA model, gas at 90% saturation (Sw=10%). Wavelet and scaling as above.

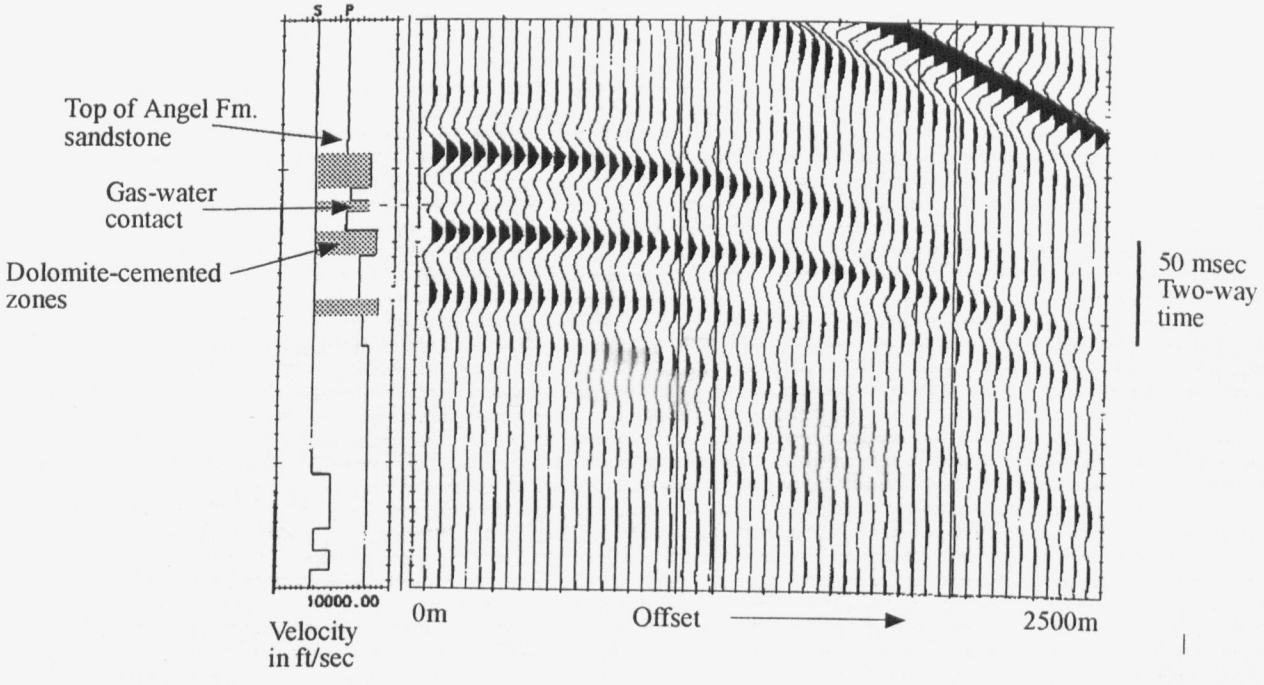

Figure 61. Inline 2287, showing the intra-Upper Unit reflection believed to have caused a false gas indication due to tuning between the intra-Upper Unit reflection and Top-Upper-Unit.

(a) Inline 2287, no interpretation.

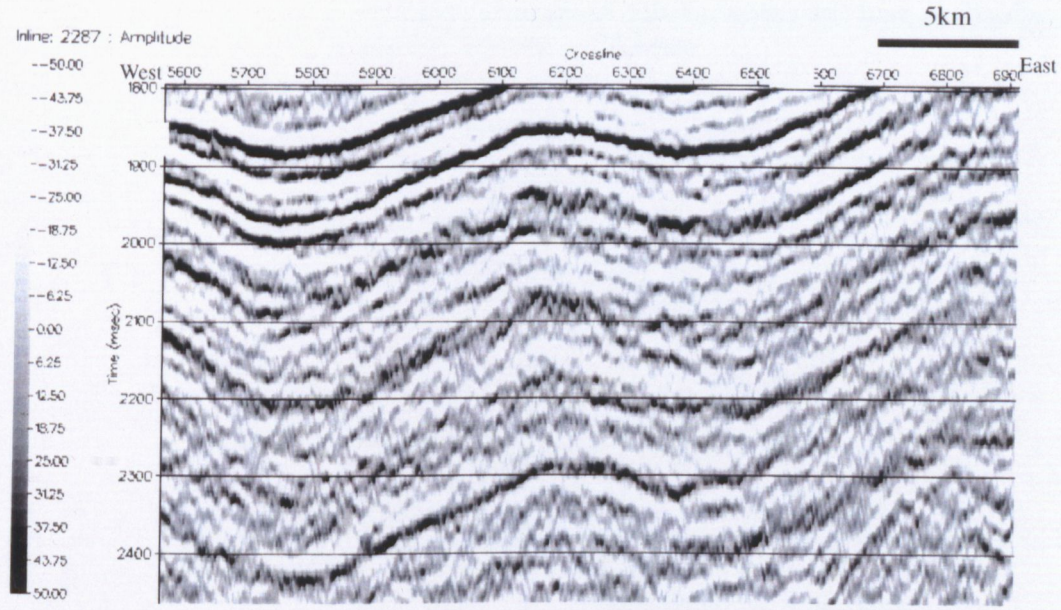

(b) Inline 2287, with interpreted horizons, showing intra-Upper Unit reflector.

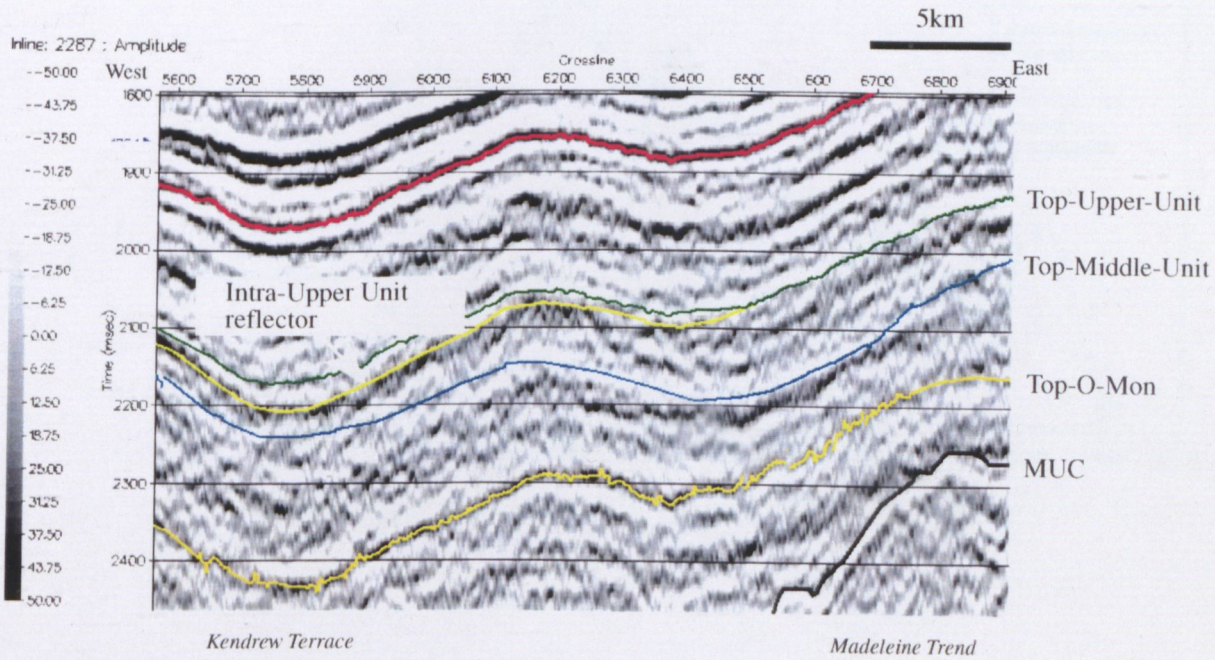

Figure 62. Model of effect of tuning on time thickness and amplitude of a thin bed, compared to time thickness between the intra-Upper-Unit reflection and the Top-Upper-Unit reflection, and the extent of the R_p-R_s anomaly.

(a) Sketch showing changes in amplitude and apparent time thickness as a bed decreases in thickness.

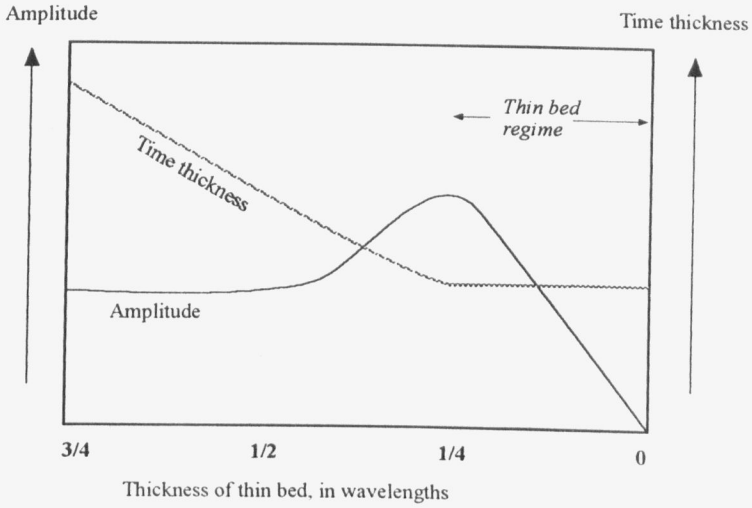

(b) Time thickness between Top-Upper-Unit and intra-Upper-Unit horizons. Dotted line is smoothed time thickness.

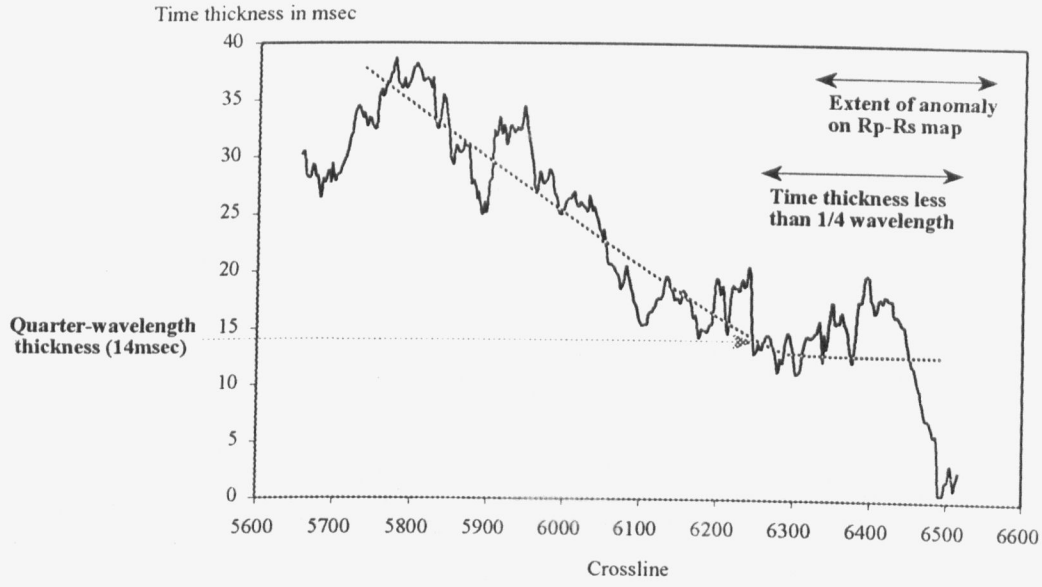

There is a slight difference between the position and extent of the AVO anomalies and the corresponding time closures. This can be explained by the fact that the AVO anomalies are derived from noisy data which has been heavily smoothed and errors in their position and size are not unexpected. The smearing of the prestack data over the Fresnel Zone, possible distortions in the time closures due to velocity variations and/or the comparison between locations derived from unmigrated prestack data with those from migrated poststack data may also produce minor contributions to the mismatch.

11. INTEGRATION OF AVO INTERPRETATION AND PETROPHYSICS

Introduction

The AVO gas indicator map presented in the previous section was generated from the seismic data, and no particular assumptions were made about the rock properties, except that V_p/V_s=2. In order to examine the intercept and gradient data for information on porosity and V_{clay} of the reservoir sandstone, some calibrations from the well data must be made. The log analysis, described in Chapter 7, concentrated on Angel-4, the most recent well, which has a reasonably complete suite of modern logs. The petrophysical work had the main aim of determining physical properties, such as density and *P*-wave velocity of the reservoir rock, for use in AVO modelling. The analysis concentrated on the uppermost 50m of the Angel Formation, as it is this portion of the rock which generates the seismic reflection which has been mapped as top of the Angel Formation (Top-Upper-Unit).

The petrophysical parameters derived from the log analysis, such as water saturation and porosity, were input into a Biot-Gassman Fluid Replacement model. This allowed the prediction of compressional and shear velocities for various water saturations and hydrocarbon types. In this section, further modelling is described which investigated the effect of variation in porosity, V_{clay}, and the properties of the overlying Barrow Group shale, on the compressional and shear velocities. The AVO response was then calculated, and the results displayed as Intercept-Gradient crossplots.

Angel-4: Porosity and Hydrocarbon Type

The effect of variations in porosity and hydrocarbon type was modelled for Angel-4, using an *EXCEL* spreadsheet based on the Simon Petroleum Technology *CRSPLT* program. The porosity was varied 3% up and down from the original 18%, while assuming the clay volume to be constant. The hydrocarbons were: dead oil, three oils with increasing gas/oil ratios (GOR), and methane. The physical properties of the hydrocarbons were assumed to be the default values supplied with *CRSPLT*. The water saturation for all hydrocarbon types was 11%, as seen in Angel-4. The properties of the overlying shale were also input (*P*-wave velocity 11200 ft/s (3410m/s), bulk density 2.48g/cc, and Poisson's Ratio of 0.28). The spreadsheet then calculated the AVO response that would be generated for each case (each porosity and each hydrocarbon type) using a simple two-layer model and Shuey's approximation. The resulting values were plotted on an Intercept-Gradient crossplot. The results from Angel-4 are shown in Figure 63(a). It can be seen that for a given porosity, the

presence of hydrocarbons with increasing GOR causes a small increase of Gradient and a negative shift of the Intercept. The effect of a decrease in porosity, for a given hydrocarbon type, is to cause an increase in the Gradient and a positive shift in the Intercept.

Angel-4: Clay Volume and Overlying Shale

The effect of a variable clay volume, and a constant porosity, were evaluated in the same manner as described above, and Figure 63 (b) shows the resulting AVO response. An increase in V_{clay} had a similar effect to an increase in porosity: a decrease in the Gradient and a more negative Intercept. The rock properties of the overlying Barrow Group shale also had an effect on the AVO response, as shown in Figure 64. The effect of *P*-wave velocity, Poisson's Ratio and density of the shale were evaluated separately. The properties of the underlying sandstone remained constant. Each variable had a slightly different effect on the AVO response, when considered in terms of the Intercept-Gradient crossplot. A decrease in *P*-wave velocity, with no change in density or Poisson's Ratio, caused an increase in Gradient and almost no change in Intercept (Fig. 64a). An increase in Poisson's Ratio of the overlying shale has a very similar effect, seen in Figure 64(b). The effect of a decrease in density however is very different; the Intercept was much more positive and the Gradient increased slightly (Fig. 64c). The overlying Barrow Group shale in Angel-1 and Angel-2 had a density around 2.2-2.3g/cc, compared to around 2.4-2.5g/cc in the other wells. The *P*-wave velocity of the shale is almost constant in all wells, but there is no information on the variation of the Poisson's Ratio. The decrease in density was equivalent, in AVO effect, to a decrease in porosity (in the constant V_{clay} model) or a decrease in V_{clay} (in the constant porosity model). This can be seen by comparing Figure 64(c) with Figure 63.

Application to seismic data

The Intercept-Gradient crossplots produced from the Biot-Gassman modelling, for variable porosity and V_{clay} (Fig. 63) were 'calibrated' to the seismic data. This was done by overlaying the points that correspond to Angel-4 (from the Biot-Gassman plot and the seismic plot), as shown in Figure 65. The points on the seismic data from inline 1924, around the Angel-4 well location are marked on Figure 65 by a grey oval. It is overlain by the point from the Biot-Gassman plot corresponding to 18% porosity and methane at Sw=11%, representing Angel-4 (from Fig. 63). The Biot-Gassman plot was then rotated so that the lines of equal hydrocarbon type are close to parallel to the orientation of the lines of equal R_p-R_s , the gas indicator used in this study (Figure 59). This rotation is analogous that observed by Foster et al.

Figure 63. Intercept versus Gradient crossplots, evaluating the effect of variable porosity and V_{clay}, with various hydrocarbons in the pore spaces on the AVO response of the Angel Formation at Angel-4.

(a)

Angel-4

Constant Vclay, variable Porosity

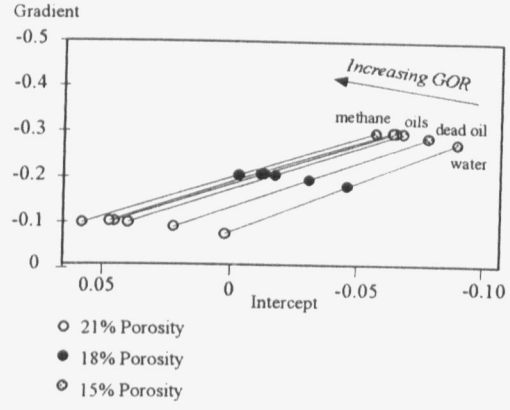

(b)

Constant Porosity, variable Vclay

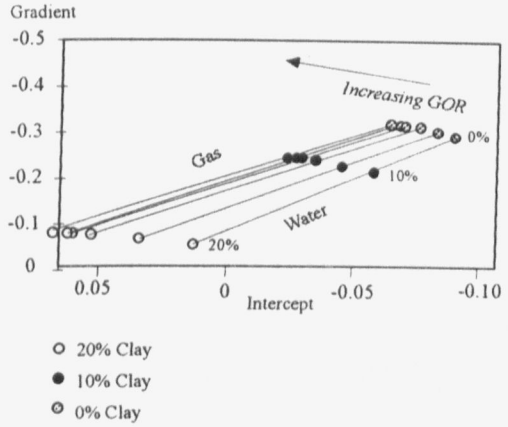

Figure 64. Intercept versus Gradient crossplots, evaluating the effect of variation of the overlying shale on the AVO response of the Angel Formation at Angel-4.

(a)

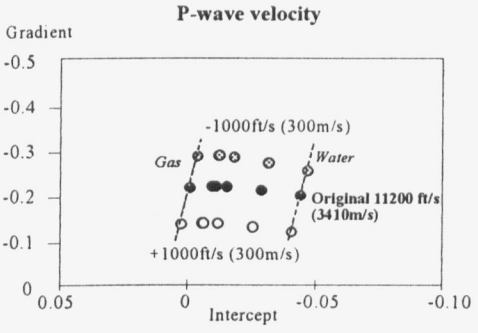
P-wave velocity
Gradient
-0.5
-0.4
-0.3
-0.2
-0.1
0
-1000ft/s (300m/s)
Gas
Water
Original 11200 ft/s
(3410m/s)
+1000ft/s (300m/s)
0.05
0
Intercept
-0.05
-0.10

(b)

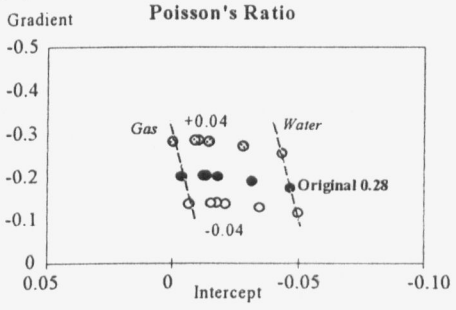
Gradient
Poisson's Ratio
-0.5
-0.4
-0.3
-0.2
-0.1
0
Gas
+0.04
Water
Original 0.28
-0.04
0.05
0
Intercept
-0.05
-0.10

(c)

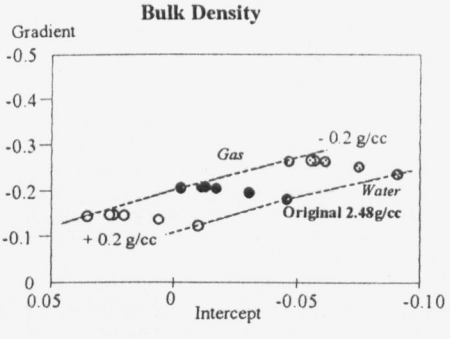
Bulk Density
Gradient
-0.5
-0.4
-0.3
-0.2
-0.1
0
Gas
- 0.2 g/cc
Water
Original 2.48g/cc
+ 0.2 g/cc
0.05
0
Intercept
-0.05
-0.10

Figure 65. Intercept versus Gradient crossplot of the data from inline 1924, showing the data points from the Angel-4 well location on inline 1924 (marked by the grey oval). This is overlain by the Intercept versus Gradient crossplot from Figure 63(a), that has been calibrated to the seismic data by scaling and rotation.

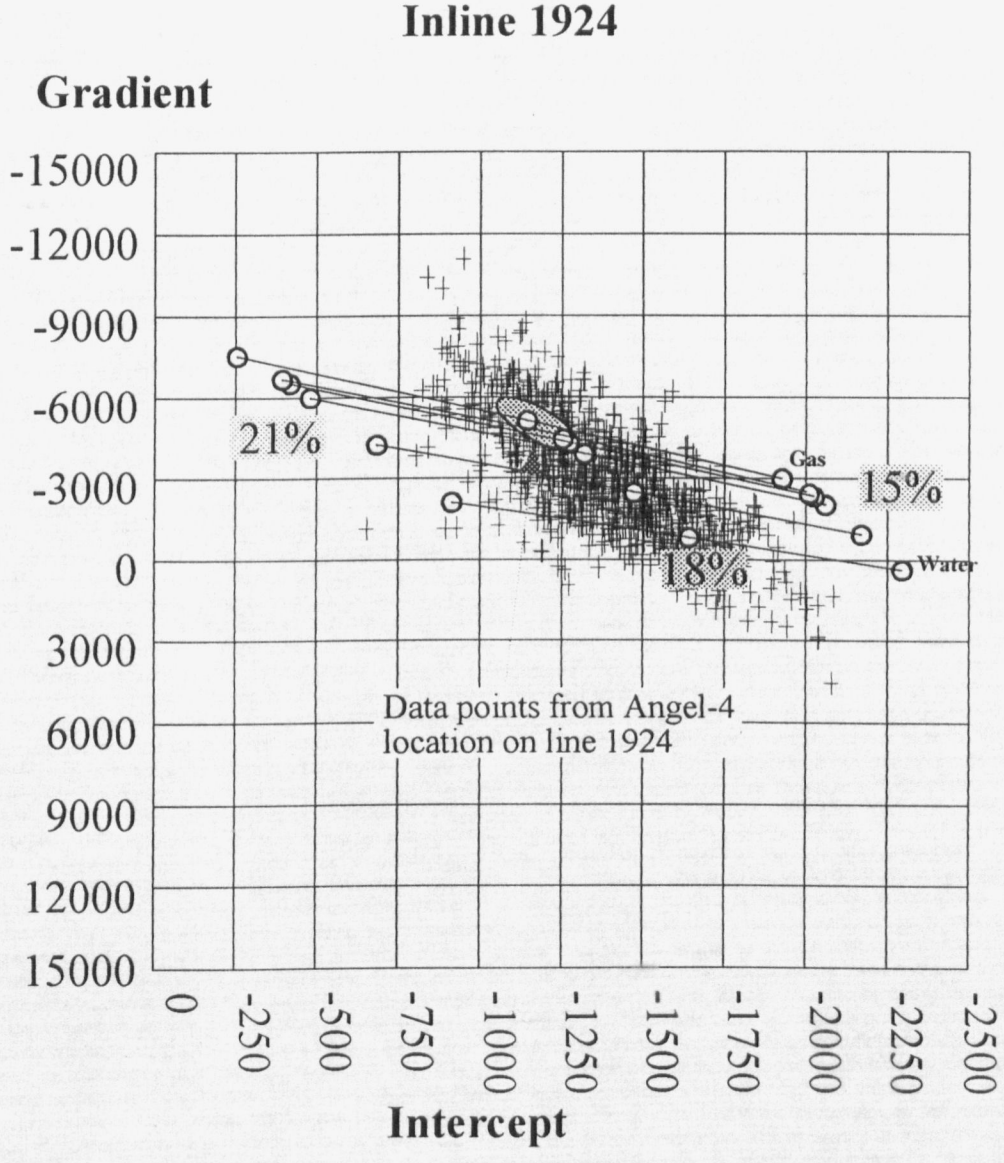
Inline 1924
Gradient
-15000
-12000
-9000
-6000
-3000
0
3000
6000
9000
12000
15000
21%
Gas
15%
18%
Water
Data points from Angel-4
location on line 1924
0
-250
-500
-750
-1000
-1250
-1500
-1750
-2000
-2250
-2500
Intercept

(1993), where there is a difference in trend angle between AVO from seismic data and AVO calculated from models based on log data, attributed to transmission losses in the seismic data during propagation through the overburden. After the rotation, the orientation of the points of equal porosity was close to parallel to the seismic data cloud. The final step was to scale the Biot-Gassman plot in size (keeping the aspect ratio constant) so that the water point lies approximately at the other end of the cloud. This new method is empirical and is considered to be at best semi-quantitative. More well control in the Angel Field would have resulted in a more accurate calibration, using several wells to scale and rotate the Biot-Gassman plot.

Extraction of AVO-Porosity and AVO-Vclay

Values of AVO-derived porosity (AVO-porosity) and V_{clay} (AVO-V_{clay}) were derived from the seismic data, using the empirical calibration described above. The AVO-porosity was extracted, assuming that V_{clay} is constant, and vice versa for AVO-V_{clay}, for each of the fourteen inlines for which binned gathers were available, and the values were contoured over the study area. The AVO-porosity and AVO-V_{clay} maps are essentially the same map with different contour values, due to the similarity in the AVO response to variations in porosity and V_{clay}, as discussed in the previous section. The raw unsmoothed data were from each inline were input into the contouring and mapping package SURFER, and contoured and smoothed. The data were also contoured by hand as quality control to the mapping package, and the resulting maps were very similar.

Figure 66 shows the computer-contoured map of AVO-porosity. There are two regions of lower porosity visible, with values down to 15%, near Angel-1 and Angel-2, and the southeast corner near Angel-3 has porosities over 20%. When the AVO-porosity values predicted at the well locations is compared to the log values, it can be seen that there are discrepancies of 3-4%, summarised in Table 11. The assumption of constant V_{clay} and variable porosity that was used in the generation of this map, does not appear to be valid. Testing the maps of AVO parameters using such a small number of wells, which are all clustered in one area, is not the optimum method. More wells evenly spread over the study area would give more confidence in the empirical calibration and the maps of AVO attributes. There are two variables (Intercept and Gradient) and three unknowns (porosity, V_{clay}, and presence of gas) in this method, therefore there is a fundamental ambiguity in the results. An independent third variable is needed to resolve the effects on the AVO response of variation in porosity and volume of clay.

Figure 66. Map of AVO-derived porosity, generated from the fourteen inlines used in the study using the empirical calibration to the Biot-Gassman fluid replacement model for Angel-4, and then contoured and smoothed over the study area. The calibration assumes a constant V_{clay} of 13%.

(a) Map of AVO-derived porosity.

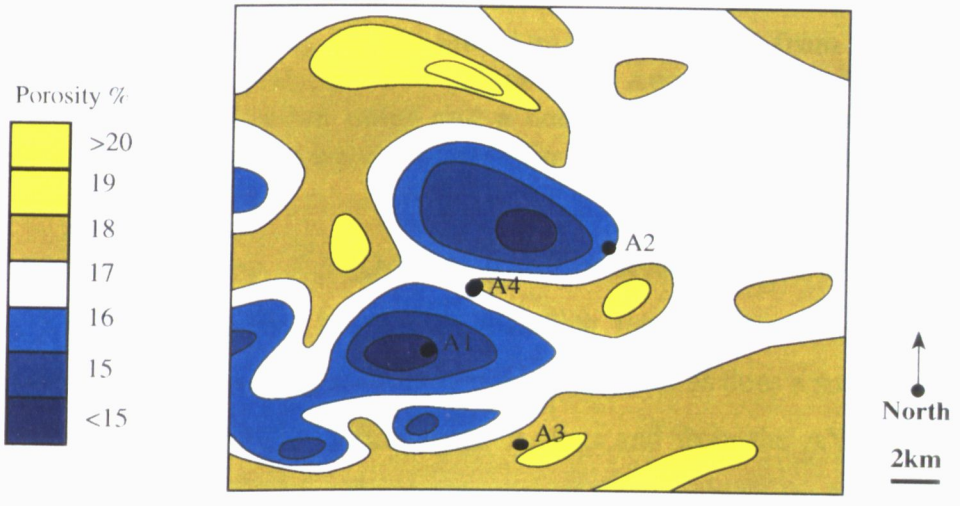

(b) Map of AVO-derived porosity with fields (solid line), time closures at top Angel Formation level (dotted line), and the major E-W fault zone south of Angel-1.

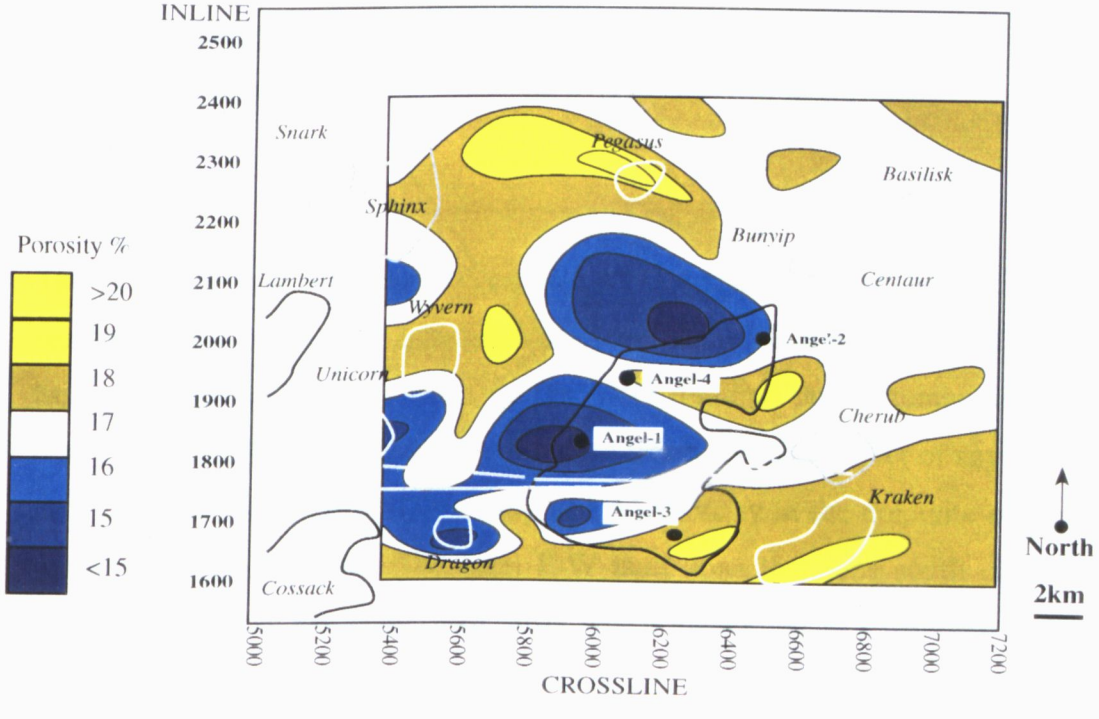

Well	Porosity %			V_{clay} %		
	Logs	AVO	AVO corr	Logs	AVO	AVO corr
Angel-1	18	<15	18	8	<5	10
Angel-2	12	16	-	6	5	-
Angel-3	18	18	-	17	15-20	-
Angel-4	(18)	(18)	-	(13)	10-15	-

Table 11. Porosity and V_{clay} for the four Angel wells, values from log analysis compared to values from AVO analysis. The values from Angel-4 are in brackets because they were used as the calibration point and a comparison is not valid. The Angel-1 AVO porosity and V_{clay} have also been corrected for overlying low-density shales.

Figure 67 shows the map of AVO-V_{clay}. It can be seen that there is a region of lower V_{clay} running SW-NE across the study area, including the area around Angel-1 and -2. The southeastern corner shows higher V_{clay} values, up to 25%, as does a small area in the north. A comparison between the V_{clay} values from the logs and from the AVO shows that they are quite close, except at Angel-1. The assumption of constant porosity and variable V_{clay} used in the generation of this map appears to be more satisfactory, in terms of matching the AVO analysis results to the well control. A change in V_{clay} results in a change in porosity in real rocks, as opposed to these simple models where it has no effect. The areas on the AVO-V_{clay} map with higher values will in all probability have a lower porosity (as well as permeability), so this map may be thought of as indicating overall reservoir quality.

Discussion

The effect of V_{clay} and porosity on the AVO response in the presence of the dolomite-cemented zones cannot be calculated using the Biot-Gassman models. The dolomitic layers have a strong and complex effect on the AVO response due to tuning and constructive and destructive interference, which over-rides the relatively subtle effect of any changes in porosity or V_{clay}. The values of AVO-porosity and AVO-Vclay in the dolomite-cemented zone were therefore not meaningful. The main E-W fault zone that runs south of Angel-1 caused a relative decrease in amplitude with offset which manifested as a decrease in R_p-R_s, and as an increase in the AVO-porosity and AVO-V_{clay}. The decrease in amplitude with offset is probably due to increased noise in the faulted area, caused by diffractions, multiples and so on, and a consequent decrease in energy in the primary reflection.

The overlying shale at Angel-1 had an anomalously low density, and the effect of this low density on the AVO response (from the Biot-Gassman model) was to increase the Intercept,

Figure 67. Map of AVO-derived volume of clay, V_{clay}, generated from the fourteen inlines used in the study using the empirical calibration to the Biot-Gassman fluid replacement model for Angel-4, and then contoured and smoothed over the study area. The calibration assumes a constant porosity of 18%.

(a) Map of AVO-derived Vclay.

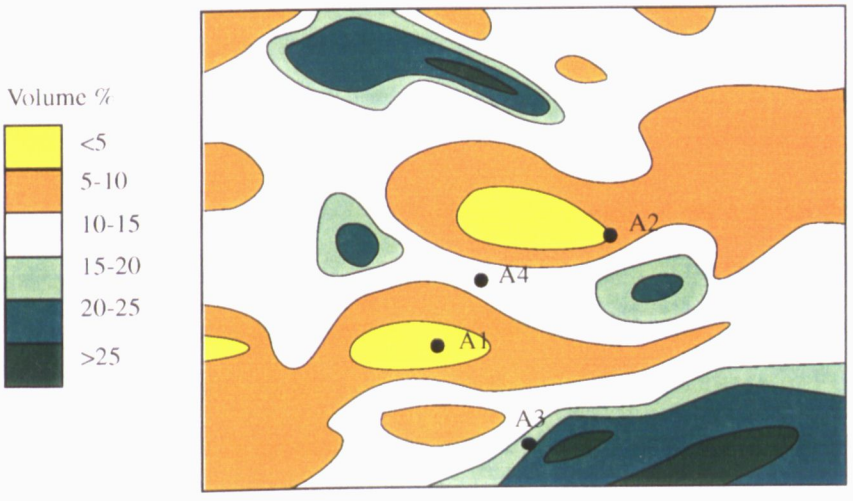

(b) Map of AVO-derived Vclay with fields (solid line), time closures at top Angel Formation level (dotted line), and the major E-W fault zone south of Angel-1.

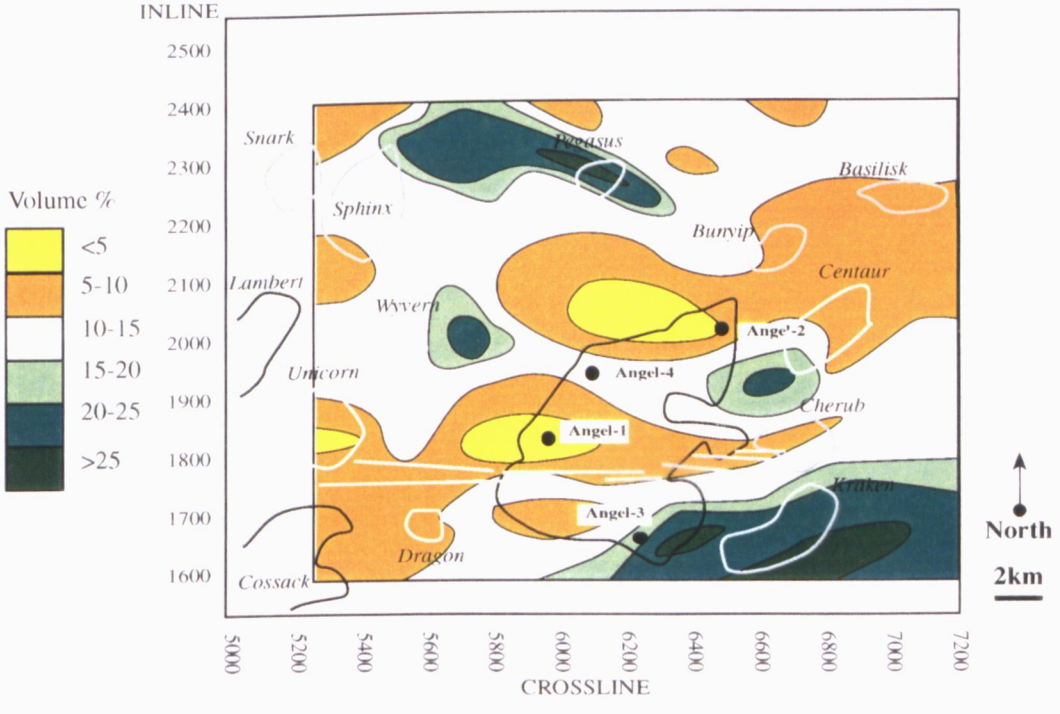

and slightly increase the Gradient. The AVO porosity and V_{clay} are lower at Angel-1 than indicated by the logs (Table 11). The correction to the AVO reponse for the 0.2g/cc decrease in density shifted the AVO-porosity from 15% to 18%, and the AVO-V_{clay} from 3% to 10%, which are closer to the log values. The areal extent of the low-density shale is not known, so the correction was not applied to the maps. It is likely that the low-density shales occur on the crest of the field, which coincides with the area of low AVO-V_{clay} and AVO-porosity around Angel-1.

An increase in Poisson's Ratio in the overlying shale can cause a false positive gas indicator, and an apparent decrease in AVO-porosity and AVO-V_{clay}. The closures in the study area that fit these criteria are Unicorn, Centaur, Basilisk and Cherub. It will be very difficult to distinguish the false positives from real gas, especially if the increase in Poisson's Ratio occurs over a structural high. It is apparent that the physical properties of the overlying shale play a very important part in controlling the AVO response in the study area, and probably in many other areas, and any error estimate must take the potential effects of the shale into account. An assumption that the shale is constant in its physical properties has the potential to cause considerable errors, and possibly the drilling of unsuccessful wells.

Table 12 lists the known and potential closures in the study area, and the AVO-derived information on presence of gas and V_{clay}.

Closure	Gas Indicator	AVO-V_{clay}
Angel^{GAS}	Med-Strong	0-15
Basilisk	Med	5-10
Bunyip	None	n/a
Centaur	Strong	5-20
Cherub	Med	5-15
Dragon	Weak-Med	5-10
Kraken	Med	15-25
Pegasus	Med	15-25+
Sphinx	Weak-Med	10-15
Unicorn	Strong	0-10
Wyvern	Med	10-15

Table 12. AVO parameters: strength of gas anomaly and V_{clay} for Angel Field, together with other potential closures in the study area. n/a indicates that the closure is within the dolomite-cemented zone, and no useful AVO information was available.

12. INTEGRATED MODEL FOR THE ANGEL FM. UPPER UNIT

A model for the Upper Unit, in terms of reservoir quality and environment of deposition, was developed by integrating all of the information that has been gathered in this study. The stacked 3D seismic data gave information about the palaeo-topography, the pattern of sediment movement, and the source area, as well as the fault pattern in the reservoir. The AVO analysis of the prestack data gave information about the presence of gas, and a semi-quantitative measure of reservoir quality (V_{clay}). The Upper Unit is the major reservoir rock in this area, as it is the topmost unit in the Angel Formation, and directly underlies the regional seal. The Middle Unit also contains a portion of the gas in the Angel Field, but no information is available from AVO analysis.

Reservoir Quality

Figure 68 combines several maps previously produced to give an overall view of the Upper Unit. The white area in the southeastern corner is where the Upper Unit is very thin, or absent, and the white area northeast of Angel-2 is the dolomite-cemented area where AVO analysis is not useful. The lowest AVO-V_{clay}, and therefore the best reservoir quality, is shown in light grey. It can be seen that the best reservoir quality lies along the Madeleine Trend, which runs SW-NE across the study area, and also along the Rankin Trend in the northwest corner of the study area. The Madeleine Trend marks an increase in slope where the low-angle shelf that runs between the Lewis Trough and the Madeleine Trend steepens into the Kendrew Terrace. It was not a distinct structural high at the time of deposition of the Upper Unit, although there was probably some subtle topography. The sediment was sourced from the Legendre Trend (in the southeast), and the sediment then moved around the southern end of the Madeleine Trend, south of Angel-2, and then northwards to the depocentre. The better-quality reservoir sand lies along the main sediment movement path, which is towards the northeast, parallel to the northern side of the Madeleine Trend.

Presence of Gas

The trapping of gas in the Upper Unit depends on the occurrence of structural closures. Eleven time closures at Upper Unit level have been studied using both the pre- and post-stack 3D seismic data. Ten of these show an AVO gas anomaly, and the other (Bunyip) lies within the dolomite-cemented zone. There is one anomaly that does not occur within a time closure, on the northern flank of the Angel Field, and this can be explained by offset-dependent tuning from an intra-formation reflector. Most of the time closures are small and low-relief when compared to the Angel Field. The three largest and highest-relief closures are discussed below, together with a possible eastwards extension of the Angel Field.

The Basilisk closure is predicted to contain clean Upper Unit sandstone (5-10% V_{clay}), which will probably be relatively thin, due to its position at the northern edge of the Madeleine Trend. The underlying Middle Unit will also probably be clean but thin. There are probably no major dolomite-cemented intervals as seen in Angel-2, but the rock may contain a small percentage of dolomite. Basilisk probably contains gas, since it exhibits a moderately strong AVO gas anomaly, and has no layer of Mid Jurassic claystone to seal off the migrating gas from the underlying Mid Jurassic and Triassic rocks.

Bunyip is predicted to contain clean sandstone, similar to that of Basilisk. Major dolomite-cemented zones are present, which if they are similar to those seen at Angel-2, are around 165m thick in total, and reduce the porosity from around 17% to 5% or less. No gas anomaly is visible, due to the effect of the dolomite-cemented zones. There is probably gas present, due to the proximity to the Angel Field.

Cherub is more an extension to the Angel Field than a separate closure. The Upper Unit is very thin to absent. The AVO maps indicate a sandstone with between 5-15% V_{clay}. Cherub has a moderately strong AVO gas anomaly, and probably contains gas, due to its proximity to the Angel Field.

Sphinx is on the edge of the Rankin Trend, in a similar position to Lambert Field. A sandstone of 10-15% Vclay is predicted. The AVO gas anomaly is weak, which may indicate the presence of oil, or may be due to some other factor such as tuning. However, the underlying Dingo Claystone is absent, which is more indicative of any hydrocarbons present being gas. In contrast, Lambert Field overlies a thick sequence of Dingo Claystone.

Figure 68. Overall reservoir quality map of the Upper Unit of the Angel Formation, combining the information from analysis of prestack and stacked 3D seismic data. The best reservoir quality is along the northern side of the Madeleine Trend, and also in the northwest of the study area, near the Rankin Trend.

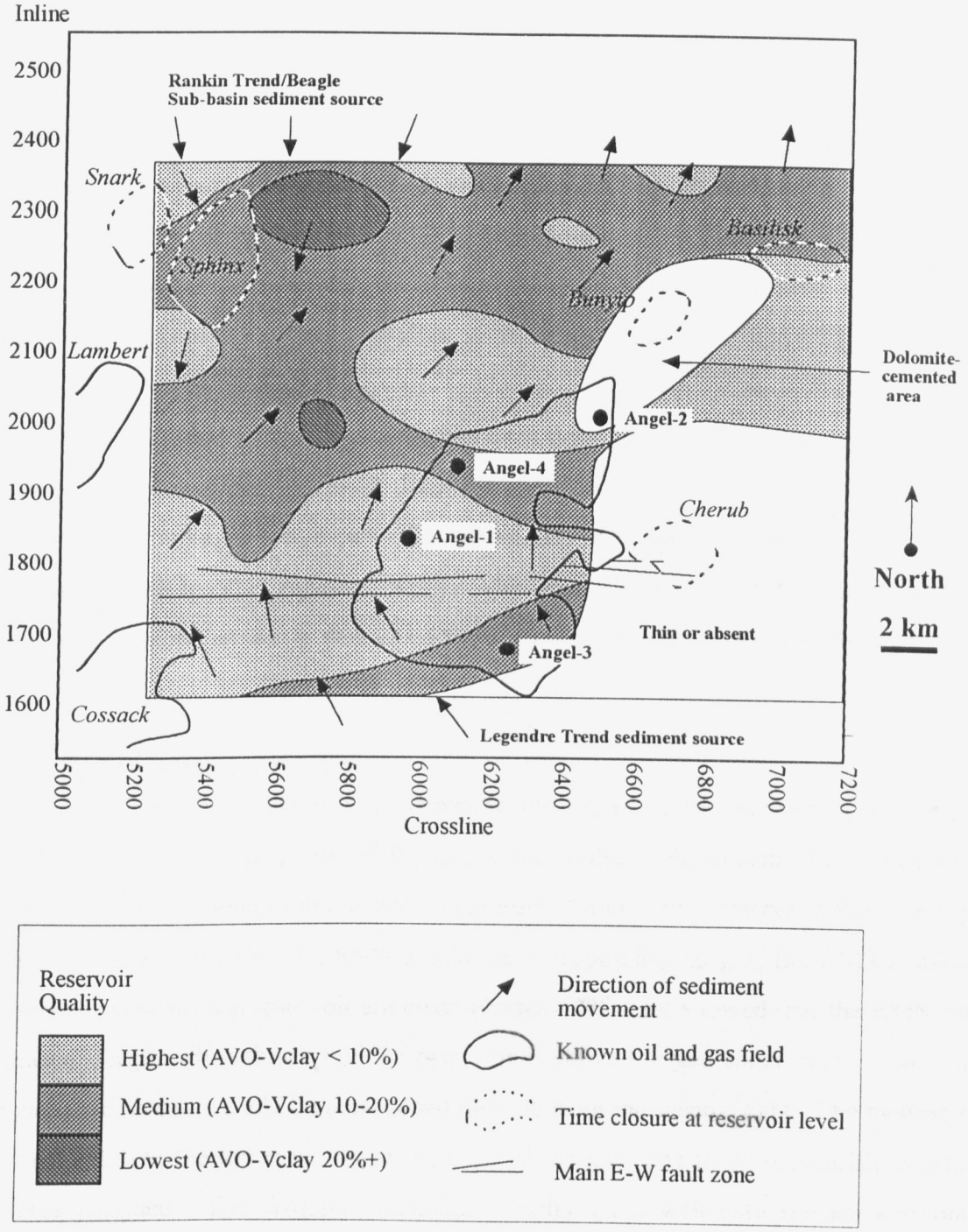
Inline
2500
2400
2300
2200
2100
2000
1900
1800
1700
1600
Rankin Trend/Beagle
Sub-basin sediment source
Snark
Sphinx
Lambert
Basilisk
Bunyip
Dolomite-
cemented
area
Angel-2
Angel-4
Angel-1
Cherub
Thin or absent
Angel-3
Cossack
Legendre Trend sediment source
North
2 km
5000
5200
5400
5600
5800
6000
6200
6400
6600
6800
7000
7200
Crossline

Reservoir
Quality
Highest (AVO-Vclay < 10%)
Medium (AVO-Vclay 10-20%)
Lowest (AVO-Vclay 20%+)
Direction of sediment
movement
Known oil and gas field
Time closure at reservoir level
Main E-W fault zone

AVO Analysis

One of the assumptions of AVO analysis is that the offset-dependent reflectivity can be recovered from the recorded seismic amplitudes. A multitude of factors have the potential to affect the recorded seismic amplitudes. An extensive literature survey has identified 23 of these factors, although there are no doubt others. It was not possible to rank the factors in terms of the magnitude of their effect on AVO response, as this appears to depend very much on the type of survey, the source used, the geological setting, and so on. For example, the AVO response recorded in a land survey in a desert, using Vibroseis sources, and with a shallow, thin target horizon will have very different controlling factors from the response recorded in a marine survey using airguns, with a deep target horizon in a highly-faulted area.

Most of the AVO work in the literature has been done in the Gulf Coast region, and it is only recently that more work has been done on older, deeper rocks, and in varying geological terrains. The simple, although powerful, techniques that work very well in the Gulf Coast do not work so well in other regions. Newer AVO analysis techniques, such as Intercept versus Gradient crossplots, are being developed to fully utilise the data from these regions.

Direct Hydrocarbon Indicators

A new technique was developed for mapping the extent of the gas within the Angel Field, which showed the two-way time of the gas-water contact independent of any well data. The method looks for anomalies in the RMS amplitude within a time interval below the top of the reservoir. As a check that the RMS amplitude is responding to gas, the RMS amplitude and two-way time of the top reservoir are cross-plotted. This plot showed that the RMS amplitude increased sharply when the top of the reservoir is above the gas-water contact, and therefore the gas-water contact could be determined directly from the seismic data. The method requires the travel time to the top reservoir at the edge of the gas zone to be reasonably constant over the area analysed. The crossplot technique results agree well with the known contacts in Angel Field, and in particular appear to confirm the presence of different contacts in the north and south of the field, as suggested by the well data. There is evidence that the method responds to an oil-water contact in the south of the field, where there is a small oil leg below the gas.

It has been suggested by several authors (eg Clark, 1993) that light oils with a high GOR have an effect on seismic data that is very close to that of gas. Modelling of the effect of oil on seismic data should include the effect of dissolved gas. There is great scope for future work in re-examining seismic data (preferably 3D) over known oil fields, even those in rocks generally assumed to be too old for direct hydrocarbon indicators. The RMS-time crossplot method may be easily applied to many fields. It may not work in some geological situations, but it is simple and requires no special data processing. One possible application is to monitor the changes in hydrocarbon-water contacts during production, if repeated seismic surveys are run over the field.

The Miocene Compressional Event

The importance of the Miocene-to-Present compressional event in both forming hydrocarbon traps and triggering hydrocarbon migration is known from several basins along the North West Shelf and in the Timor Sea, and has been confirmed in this study. During the Miocene, probably the Late Miocene, the structural trap and the faults in the reservoir of Angel Field formed, the hydrocarbon migration occurred, and the dolomite cement was precipitated. The behaviour of the faults (as fluid conduits or seals) in the reservoir of the Angel Field will most probably be controlled by the present-day stress regime. The fact that the NW-SE-trending normal faults are the only faults in the Angel Field that are likely to be open and capable of transmitting fluids or gases will have an impact on the probable pattern of reservoir drainage. It has been suggested by some workers (Yielding et al., 1992) that the pattern of faults in rock is fractal, that is the fault pattern seen on a map is the same at all scales, from regional to microscopic. They suggest that examining the faults in a particular area, from a combination of 3D seismic mapping and core data, can give information on the fractal dimension of the fault pattern, and the characteristics of the fault population in that area. This in turn can be used as additional input into a reservoir model, for instance to investigate the effects of the fault pattern on fluid flow in the reservoir.

The Late Triassic to Early Jurassic tectonic event

Opinion is divided as to whether the Late Triassic to Early Jurassic tectonic event was E-W extensional and N-S compressional or vice versa. The difference hinges on whether the Lewis Trough is interpreted to have formed by compression or extension. This study has shown that E-W extension along a westwards dipping detachment fault followed by subsidence is consistent with the observed structures and faults in the sub-basin, and explains some

previously cryptic features, such as the nature of the Madeleine Trend, and the reason for the extreme angle of the Madeleine Fault. It was suggested by Stagg (pers. comm. in Miller, 1995) that the Dampier Sub-basin, together with the Beagle Sub-basin, is the upper plate portion of of a failed rift, and the Barrow Sub-basin to the south is the lower plate portion of the rift, and that these are separated by a Palaeozoic N-S transfer zone. This model suggests that the Madeleine Trend is the eastern edge of a crestal collapse graben (the Kendrew Terrace), which has been rotated and pushed up by the subsiding Lewis Trough. It is usually stated that the Rankin Fault, that forms the eastern edge of the Rankin Trend, is a crustal detachment (eg Stagg and Colwell, 1994; Etheridge and O'Brien, 1994). This study suggests that in the Dampier Sub-basin, it is not a crustal detachment, but the western edge of the crestal collapse graben. A comparative study of the Dampier, Barrow, and Beagle Sub-basins would help to clarify the form of the detachment fault, as would sandbox modelling.

The nature of the intra-Angel Formation horizons

The various schools of thought on seismic stratigraphy (eg Vail et al., 1977; Galloway, 1994) all require and assume that seismic reflections are time-synchronous. With this assumption, 'each seismic sequence represents a depositional sequence with its own particular regional distribution, stratal geometry, thickness pattern and geological history' (Mitchum and Vail, 1977). Evidence for or against this is sparse in the literature. The intra-Angel Formation horizons were found to be close to time-synchronous in this study, except for the base of the Upper Unit. The Upper Unit is time-transgressive on the scale of this study but time-synchronous within plus or minus half a cycle, the acceptable error given by Vail et al. (1977). The Upper Unit is possibly a lithostratigraphic unit, which may be time-transgressive. Several previous studies have sub-divided the Angel Formation, but these subdivisions were not felt to be suitable, as they were based mostly on regional 2D seismic lines, and a pre-conceived stratigraphic framework.

14. CONCLUSIONS

AVO analysis

AVO analysis using intercept-gradient crossplots was a useful and robust method, especially when empirically calibrated to the well control via Biot-Gassman fluid replacement modelling, a new approach developed in this study. AVO analysis gave a good gas indicator, and a semi-quantitative reservoir quality indicator. Confidence in the AVO gas anomalies is increased by the fact that they are in accordance with the relative change predicted by theory, and by the similarity between the areal extent of the anomalies and the time closures at top reservoir level. The one closure that does not show an anomaly is Bunyip, which lies within the dolomite-cemented zone. However, visco-elastic 1D modelling predicts that the gas effect will not be visible in the presence of the dolomite-cemented layers. The gas anomaly with no closure that lies on the northern flank of the Angel Field can be attributed to offset-dependent tuning between the top reservoir reflection and an internal reflection of high amplitude within the Upper Unit of the reservoir. The properties of the overlying shale had a significant effect on the AVO response, and have the potential to cause false positive gas anomalies. It must also be kept in mind that a low gas saturation will cause an AVO anomaly that is indistinguishable from an anomaly caused by high gas saturation.

Dolomite cemented Zones

The presence and extent of gas, and the two-way time of the hydrocarbon-water contacts were determined by analysis of the amplitudes of the stacked 3D seismic data. The extent of the dolomite-cemented zones of the Angel Formation were mapped from the 3D seismic. The major dolomite cement occurs only in the northern part of the field, in a roughly oval-shaped area along the crest of the Madeleine Trend. The Angel Field structural closure formed late in the Tertiary, mostly probably post-Eocene. The dolomite cement formed in the Miocene, synchronous with hydrocarbon migration into the structure. The dolomite is believed to have precipitated in a reaction between carbon dioxide associated with hydrocarbon migration, and organic acid anions in the Angel Formation pore-water. The organic acid anions were produced as the lower, shale-rich Angel Formation and Dingo Claystone entered the early oil generation window in the Tertiary. The cumulative thickness of the dolomite-cemented zones is 164m at Angel-2. The estimated volume of dolomite cement is approximately 1 cubic kilometre. The dolomite cement could compartmentalise the northern part of the Angel Field into many separate flow zones, with risk of bypassed hydrocarbons.

Tectonics and Faulting

It is hypothesised that the Dampier Sub-basin is underlain by a low-angle detachment fault which dips towards the west, and has a ramp-flat-ramp geometry. The fault starts at the Lambert Shelf, and the convex-up part of the fault lies underneath the Rosemary/Legendre Trend. The Lewis Trough was formed by extension and subsidence. It is not necessary to invoke major compressional tectonic events to explain its formation. Subsidence of the Lewis Trough during the Triassic and Early Jurassic caused rotation and uplift of the Madeleine Trend. Mid Jurassic extension caused further development of the Madeleine Trend and the Kendrew Terrace graben. Late Jurassic WNW extension caused mild synsedimentary left-lateral movement on the Madeleine Fault during the deposition of the Middle Unit of the Angel Formation. Miocene-to-Present E-W compression caused right-lateral strike-slip movement along the Madeleine Fault, and the formation of the faults that cut the reservoir interval. The fault orientations are (1) E-W strike-slip faults, with a major fault zone approximately 1km wide running just south of Angel-1, (2) NNW-SSE strike-slip faults, (3) NNE-SSW reverse faults, and NW-SE normal faults. The behaviour of the faults in the reservoir (in terms of seal or conduit) will be controlled by the present-day stress regime. The NW-SE normal faults are likely to be open to fluid flow, and the others to be closed. The main E-W fault zone is acting as a seal; there are different hydrocarbon-water contacts on the north and the south sides of the fault zone.

The Angel Formation

The Angel Formation has been sub-divided into three units - Upper, Middle and Lower. The horizons that separate these layers are very close to time-synchronous in the study area, implying that each unit was a separate depositional sequence with a particular geological history. Each of the three units was sourced from a different area, in contrast to the usual assumption that the Legendre Trend was the major sediment source, with some minor input from the north. The Lower Unit was sourced from the south-west, probably from the Rankin Trend via the Kendrew Terrace. The Middle Unit was sourced from the north as well as the south, and the two sediments have slightly different acoustic impedances. The northern source is probably local areas of uplift such as the DeGrey Nose and the uplifted fault blocks of the Beagle Sub-basin. The Upper Unit is sourced mostly from the southeast, probably from the Legendre Trend, with a small amount coming from the Rankin Trend. The Madeleine Trend was a positive structure throughout the Middle to Upper Jurassic, and the Angel Formation onlapped onto it, finally covering it during deposition of the Middle Unit.

Angel Formation Upper Unit

The best reservoir quality (cleanest sandstone and highest porosity) in the Upper Unit occurs along the Madeleine Trend, and the worst quality within the Kendrew Terrace, to the north-west of the Angel Field. The dolomite cement in the Angel Formation drastically reduces porosity, and therefore also reservoir quality, in the northern portion of the field. The presence of gas in the Upper Unit depends on the occurrence of structural closures, or the presence of stratigraphic traps. Eleven time closures at Upper Unit level were studied using both the pre- and post-stack 3D seismic data. Ten of these showed an AVO gas anomaly, and the other (Bunyip) was within the dolomite-cemented zone. The one gas anomaly that did not occur within a time closure, on the northern flank of the Angel Field, was caused by offset-dependent tuning between an intra-formation reflection and that from the top of the reservoir.

The Basilisk closure is predicted to contain gas in clean sandstone (5-10% V_{clay}) with no major dolomite-cemented intervals. The Bunyip closure is predicted to contain gas in clean sandstone, but with major dolomite-cemented zones, which, if they are similar to those seen at Angel-2, will have reduced the reservoir quality to almost nil. No gas anomaly was visible, due to the effect of the dolomite-cemented zones. In Cherub closure, gas in a sandstone with between 5-15% $V_{clay.}$ is predicted. The Sphinx closure is predicted to contain sandstone of 10-15% $V_{clay.}$ The AVO gas anomaly is weak, which may indicate the presence of oil.

Methods used in this study

This was an integrated multi-disciplinary study of a particular gas field, the Angel Field of the North West Shelf, offshore Western Australia. The approach used here of utilising all available data has generated many new ideas on the tectonic history of the basin, the age and method of formation of the dolomite cement, and the source of the sediment in the reservoir unit. It has focussed on the use of 3D seismic data, specifically the integrated analysis of the pre-stack gathers and the stacked data to delineate the reservoir quality, and developed a new method that empirically calibrates the well control to the seismic data. There is great scope for studies of this type to be done on many existing fields, both oil and gas, now that 3D seismic surveys of increasing quality and resolution are being routinely acquired over old acreage as basins become mature for petroleum exploration, and emphasis is shifting to efficiency of development of known fields.

15. REFERENCES

AAPG Course Notes - Continental Wrench Tectonics and Hydrocarbon Habitat, 1988.

ARIFFIN, T., SOLOMON, G., UJANG, S., BEE, M., JENKINS, S., CORBETT, C., DORN, G., WITHERS, R., OZDEMUR, H., and PEARSE, C., 1995, Seismic tools for reservoir management. Oilfield Review, 7(4), 4-17.

AGSO North West Shelf Study Group, 1994, Deep reflections on the North West Shelf: Changing perceptions of basin formation. In: Purcell, P. G., and Purcell, R. R. (Eds), The sedimentary basins of Western Australia. Proceedings of the PESA Symposium, Perth, 1994, 64-76.

AHMED, H., 1991, Reconnaissance AVO on surface seismic data. SEG Research workshop on Lithology-relating elastic properties to lithology at all scales, St Louis, 1991.

AKI, K., and RICHARDS, P.G., 1980, Quantitative seismology, theory and methods, volume 1. Freeman.

ALKALIFAH, T.A., and LARNER, K., 1994, Migration error in transversely-isotropic media. Geophysics, 59, 1405-1418.

ALKALIFAH, T. A., and TSVANKIN, I., 1995, Velocity analysis for transversely isotropic media: 64th Ann. Internat. Mtg., Soc. Expl. Geophys., Expanded Abstracts, 1000-1003.

ALLEN, J.L., and PEDDY, C.P., 1993, Amplitude variation with offset: Gulf Coast case studies. SEG.

ALLEN, J.L., PEDDY, C.P., and FASNACHT, T.L., 1993, Some AVO failures and what (we think) we have learned. The Leading Edge, March 1993, 162-167.

AMUNDSEN, L., and REITAN, A., 1994, AVO estimation of waterbottom P- and S-wave velocities from the particle velocity field. Journal of Seismic Exploration, 3, 231-243.

APTHORPE, M., 1988, Cainozoic depositional history of the North West Shelf region. In: Purcell, P.G. and Purcell, R.R. (Eds.), The North West Shelf, Australia. Proceedings of the PESA Symposium, Perth, 55-84.

BAILLIE, P.W., POWELL, C.McA., LI, Z.X., and RYALL, A.M., 1994, Tectonic framework of Western Australia's Neoproterozoic to Recent sedimentary basins. In: Purcell, P. G., and Purcell, R. R. (Eds), The sedimentary basins of Western Australia. Proceedings of the PESA Symposium, Perth, 1994, 45-62.

BACKUS, G.E., 1962, Long wave elastic anisotropy produced by horizontal layering. Journal of Geophysical Research, 67, 4427-4440.

BANIK, N. C., 1987, An effective anisotropy parameter in transversely isotropic media: Geophysics, **52**, 1654-1664.

BARBER, P., 1994, Sequence stratigraphy and petroleum potential of Upper Jurassic - Lower Cretaceous depositional systems in the Dampier Sub-basin, North West Shelf, Australia. In:

Purcell, P. G., and Purcell, R. R. (Eds), The sedimentary basins of Western Australia. Proceedings of the PESA Symposium, Perth, 1994, 525-542.

BARNETT, R.F., MARGESSON, R.W., and D'ANGELO, R.M., 1995, Use of rock properties and AVO in the Everest Field development, UKCS. Petroleum Geoscience, 1, 311-317.

BINT, A. N., and HELBY, R., 1988, Upper Triassic palynofacies and environmental interpretations for the Rankin Trend, Northern Carnervon Basin, W.A. In: Purcell, P. G., and Purcell, R. R. (Eds), The sedimentary basins of Western Australia. Proceedings of the PESA Symposium, Perth, 1994, 591-598.

BINT, A. N., and MARSHALL, N. G., 1994, High resolution palynostratigraphy of the Tithonian Angel Formation in the Wanaea and Cossack Oil Fields, Dampier Sub-basin. In: Purcell, P. G., and R. R., (Eds.), The sedimentary basins of Western Australia: Proceedings of the PESA Symposium, Perth, 1994, 543-553.

BIOT, M.A., 1956, The theory of propagation of elastic waves in a fluid-saturated solid.I.Lower frequency range. Journal of the Acoustical Society of America, 28, 179-191.

BLANGY, J. P., 1994, AVO in transversely isotropic media - An overview: Geophysics, **59**, 775-781.

BLEVIN, J. E., STEPHENSON, A. E., and WEST, B. G., 1994, Mesozoic structural development of the Beagle Sub-basin-Implications for the Petroleum Potential of the Northern Carnarvon Basin. In: Purcell, P. G., and R. R., (Eds.), The sedimentary basins of Western Australia: Proceedings of the PESA Symposium, Perth, 1994, 479-495.

BORTFIELD, R., 1961, Approximation to the reflection and transmission coefficients of plane longitudinal and transverse waves. Geophysical Prospecting, 9, 485-502.

BULAND, A., LANDRO, M., SOLLIE, R., ANDERSEN, M., and DAHL, T., 1995, Lithology identification by AVO inversion. SEG International Exposition and 65th Annual Meeting, Houston, 1995.

BRADSHAW, M. T., BRADSHAW, J, MURRAY, A. P., NEEDHAM, D. J., SPENCER, L., SUMMONS, R. E., WILMOT, J., and WINN, S., 1994, Petroleum systems in West Australian Basins. In: Purcell, P. G., and R. R., (Eds.), The sedimentary basins of Western Australia: Proceedings of the PESA Symposium, Perth, 1994, 93-117.

BRADSHAW, M.T., YEATES, A.N., BEYNON, R.M., BRAKEL, A.T., LANGFORD, R.P., TOTTERDELL, J.M., and YEUNG, M., 1988—Palaeogeographic Evolution of the North West Shelf Region. In: Purcell, P.G. and Purcell, R.R. (Eds.), The North West Shelf, Australia. Proceedings of the PESA Symposium, Perth, 29-54.

BRIKKE, I, 1982, Geochemical interpretation of some oils and condensates from the Dampier Sub-basin of Western Australia, APEA Journal, 22, 179-187.

BURNETT, R.C., 1990, Seismic amplitude anomalies and AVO analyses at Mestena Grande Field, Jim Hogg Co., Texas. Geophysics, 55, 1015-1025.

CASTAGNA, J. P., BATZLE, M. L., and EASTWOOD, R. L., 1985, Relationships between compressional-wave and shear-wave velocities in clastic silicate rocks: Geophysics, **50**, 571-581.

CASTAGNA, J.P., 1991, Seismic lithology overview. SEG 61st Annual International Meeting Expanded Abstracts.

CASTAGNA, J.P., 1993, AVO Analysis - Tutorial and review. In: Castagna, J.P. and Backus, M.M. (Eds), Offset-dependent reflectivity, theory and practise of AVO analysis. SEG.

CASTAGNA, J.P. and BACKUS, M.M. (Eds), Offset-dependent reflectivity, theory and practise of AVO analysis. SEG.

CASTAGNA, J.P., and SMITH, S.W., 1994, Comparison of AVO indicators: A modelling study. Geophysics, 59, 1849-1855.

CHACKO, S., 1989, Porosity identification using amplitude variations with offset: examples from South Sumatra. Geophysics, 54, 942-951.

CHIBURIS, E.F., 1984, Analysis of amplitude versus offset to detect gas-oil contacts in the Arabic Gulf. SEG 54th Annual International Meeting Expanded Abstracts, 669-670.

CHIBURIS, E.F., 1987, Studies of amplitude versus offset in Saudi Arabia. SEG 57th Annual International Meeting Expanded Abstracts, 614-616.

CHIBURIS, E.F., 1993, AVO applications in Saudi Arabia. in Castagna, J.P., and Backus, M.M. (eds), Offset-dependent reflectivity-theory and practice of AVO analysis. SEG, 211-229.

CHRISTIE-BLICK, N., and BIDDLE, K. T.,1985, Deformation and basin formation along strike-slip faults, in Biddle, K. T., and Christie-Blick, N., eds., Strike-slip deformation, basin formation and sedimentation. SEPM Special Publication 37, 1-34.

CLARK, V. A., 1993, Effect of oil under in-situ conditions on the seismic properties of rocks. Geophysics, 57(7), 894-901.

COBLENTZ, D. D., SANDIFORD, M., RICHARDSON, R. M., ZHOU, S., and HILLIS, R., 1995, The origins of the intraplate stress field in continental Australia. Earth and Planetary Sciences Letters, in press.

COCKBAIN A. E., 1989, The North West Shelf. APEA Journal, 29, 529-545.

COULOUMBE, C.A., STEWART, R.R., and JONES, M.J., 1992, Elastic wave AVO using borehole seismic data. SEG 62nd Annual International Meeting Expanded Abstracts.

DAHL,T., and URSIN, B., 1992, Non-linear AVO inversion for a stack of anelastic layers. Geophysical Prospecting, 40, 243-265.

DENHAM, D., and WINDSOR, C. R., 1991, The crustal stress pattern in the Australian continent. Exploration Geophysics, 22, 101-106.

DiBONA, P., and SCOTT, J., 1990, Heavy mineral study of the Late Jurassic and Early Cretaceous section from fifteen wells within the Barrow-Dampier Sub-basins, North-West Shelf, W.A. WA Centre for Petroleum Exploration, Curtin University, Unpublished Report.

Di TORO, G. A. E., 1994, The reservoir geology of the Wanaea and Cossack Oil Fields. in Purcell, P. G., and R. R., (Eds.), The sedimentary basins of Western Australia: Proceedings of the PESA Symposium, Perth, 1994, 557-572.

DRUFUCA, G., and MAZZOTTI, A., 1995, Ambiguities in AVO inversion of reflections from a gas-sand. Geophysics, 60, 134-141.

DUREN, D.E., 1992, Range-equation weights for AVO. Geophysics, 57, 1203-1208.

DVORKIN, J., HOLEN-HOEKSMA, R., and NUR, A., 1994, The squirt flow mechanism: macroscopic description. Geophysics, 59, 428-438.

DVORKIN, J., and NUR, A., 1993, Dynamic poroelasticity: A unified model with the squirt and Biot mechanisms. Geophysics, 58, 524-533.

ETHERIDGE, M. A., and O'BRIEN, G., 1994, Structural and tectonic evolution of the Western Australian margin basin system. PESA Journal, 45-63.

ETHERIDGE, M., MCQUEEN, H., and LAMBECK, K., 1991, The role of intraplate stress in Tertiary (and Mesozoic) deformation of the Australian continent and its margins: a key factor in petroleum trap formation. Exploration Geophysics, 22, 123-128.

EXON, N. F., and von RAD, U., 1994, The Mesozoic and Cainozoic sequences of the Northwest Australian Margin, as revealed by ODP core drilling and related studies. In: Purcell, P. G., and R. R., (Eds.), The sedimentary basins of Western Australia: Proceedings of the PESA Symposium, Perth, 1994, 181-199.

FATTI, J.L., SMITH, G.C., VAIL, P.J., STRAUSS, P.J, and LEVITT, P.R., 1994, Detection of gas in sandstone reservoirs using AVO analysis: a 3D case history using the Geostack technique. Geophysics, 59, 1362-1376.

FOSTER, D.J., SMITH, S.W., DEY-SARKAR, S., and SWAN, H.W., 1993, A closer look at hydrocarbon indicators. SEG 63rd Annual International Meeting Expanded Abstracts.

GALLOWAY, W.E., 1994, Siliciclastic systems and sequences in hydrocarbon exploration and production. NCPGG, Adelaide University, Unpublished inhouse course notes.

GARDNER, G., GARDNER, L., and GREGORY, A, 1974, Formation velocity and density-the diagnostic basics for formation traps. Geophysics, 39, 770-780.

GASSAWAY, G.S., 1984, Effects of shallow reflectors on amplitude versus offset (seismic lithology) analysis. SEG 54th Annual International Meeting Expanded Abstracts, 665-669.

GASSAWAY, G.S., BROWN, R.A., and BENNETT, L.E., 1987, Pitfalls in seismic amplitude versus offset analysis: case histories. Exploration Geophysics, 18, 65-70.

GASSMAN, F., 1951, Elastic waves through a packing of spheres. Geophysics, 16, 673-685.

GELFAND, V., NG, P., NGUYEN, H., and LARNER, K., 1986, Seismic lithologic modelling of amplitude versus offset data. SEG 56th Annual International Meeting Expanded Abstracts.

HALL, D.J., ADAMICK, J.A., SKOYLES, D., DEWILDT, J., and ERICKSON, J., 1995, AVO as an exploration tool: Gulf of Mexico case studies and examples. The Leading Edge, August 1995, 863-869.

HAMPSON, D., 1991, AVO inversion, theory and practice. The Leading Edge, 11(6), 39-42.

HARDING, T. P.,1974, Petroleum traps associated with wrench faults. AAPG Bulletin, 58(7), 1290-1304.

HARVEY, P.J., 1993, Porosity identification using amplitude variations with offset in Jurassic carbonate, offshore Nova Scotia. The Leading Edge, March 1993, 180-184.

HEGGIE, D., O'BRIEN, G., BICKFORD, G., BISHOP, J., and HARTMAN, B., 1991, Direct hydrocarbon detection in bottom-waters of the Australian continental margin:Application to offshore hydrocarbon exploration. PESA Journal, 75-90.

HELBY, R., MORGAN, R., and PARTRIDGE, A.D., 1987, Mesozoic zonation. In P.A. Jell, (ed), Studies in Australian Mesozoic palynology. Associatio of Australian Palynologists, Sydney, 71-94.

HILL, G., 1994, The role of the pre-rift structure in the architecture of the Dampier Basin area, North West Shelf, Australia. APEA Journal, 34, 602-613.

HILLIS, R.R., 1991, Australia-Banda Arc collision and in-situ stress in the Vulcan Sub-basin (Timor Sea) as revealed by borehole breakout data. Exploration Geophysics, 22, 189-194.

HILLIS, R.R., and WILLIAMS, A.F., 1993, The contemporary stress field of the Barrow-Dampier Sub-basin and its implications for horizontal drilling. Exploration Geophysics, 24, 567-576.

HILTERMAN, F., 1989, Is AVO the seismic signature of rock proerties? SEG 59th Annual International Meeting Expanded Abstracts.

HILTERMAN, F., 1990, Is AVO the seismic signature of lithology? A case history of Ship Shoal-South Addition. The Leading Edge, 9(6), 15-22.

HO, S.M., LEE, S.S., and PURNELL, G.W., 1992, Comparison of P-wave AVO techniques for locating zones of fractured dolomite within non-reservoir limestone. SEG 62nd Annual International Meeting Expanded Abstracts.

HOCKING, R.M., 1985, Revised stratigraphic nomenclature in the Carnarvon Basin. Western Australia Geological Survey, 1985/1, 985-986.

HOCKING, R.M., 1988, Regional geology of the Northern Carnarvon Basin. In: Purcell, P.G., and Purcell, R.R. (Eds), The North West Shelf, Australia. Proceedings of the PESA Symposium, Perth, 97-114.

HOCKING, R.M., 1992, Jurassic deposition in the Southern and Central North West Shelf. Geological Survey of Western Australia, 1992/7.

HONG, M.R., CASTAGNA, J.P., and SICKING, C.J., 1993, A model-based analysis of AVO in the Sacramento Valley. in Castagna, J.P., and Backus, M.M. (eds), Offset-dependent reflectivity-theory and practice of AVO analysis. SEG, 230-237.

HRON, F., MAY, B.T., COVEY, J.D., and DALEY, P.F., 1986, Synthetic seismic sections for acoustic, elastic, anisotropic and vertically inhomogeneous layered media. Geophysics, 51, 710-735.

HWANG, L.F. and LELLIS, P.J., 1988, Bright spots related to high GOR oil reservoir in Green Canyon. SEG 58th Annual International Meeting Expanded Abstracts.

INGRAM, B., and MORGAN, R., 1988, The development and status of the Mesozoic palynostratigraphy of the North West Shelf, Australia. In: Purcell, P.G., and Purcell, R.R. (Eds), The North West Shelf, Australia. Proceedings of the PESA Symposium, Perth, 581-590.

JARAMILLO, H., and LARNER, K., 1995, Prestack migration error in transversely isotropic media: 65th Ann. Internat. Mtg., Soc. Expl. Geophys., Expanded Abstracts, 1204-1207.

JUHLIN, C., and YOUNG, R., 1993, Implications of thin layers for amplitude variation with offset (AVO) studies. Geophysics, 58, 1200-1204.

JUHLIN, C., and WINDHOFER, M., 1992, Anisotropy and misties in seismic data: a modelling study. Exploration Geophysics, 23, 167-171.

KEMP, A.C., and GALLAGHER, J.W., 1995, Seismic lithology and fluid analysis on a seismic workstation. SEG 65th Annual International Meeting, AVO/Inversion Workshop, Houston, 1995.

KIM, K. Y., WROLSTAD K. H., and AMINAZADEH F., 1993, Effects of transverse isotropy on *P*-wave AVO for gas sands: Geophysics, **58**, 883-888.

KINDELAN, M., SERIANI, G., and SGUAZZERO, P., 1989, Elastic modelling and its application to amplitude versus angle interpretation. Geophysical Prospecting, 37, 3-30.

KJARTANSSON, E., 1980, Attenuation of seismic waves in rocks and applications in energy exploration. Stanford University, PhD Thesis, unpublished.

KNIPE, R.J., 1987, The influence of fault zone processes and diagenesis on fluid flow. In: Horbury, A.D., and Robinson, A.G. (Eds), Diagenesis and basin development, AAPG Studies in Geology, 36, 135-151.

KOEFOED, O., 1956, On the effect of Poisson's Ratio of rock strata on the reflection coefficients of plane waves. Geophysical Prospecting, 4, 381-387.

KOPSEN, E, 1994, Northern Carnarvon Basin hydrocarbon distribution and future petroleum potential. In: Purcell, P. G., and R. R., (Eds.), The sedimentary basins of Western Australia: Proceedings of the PESA Symposium, Perth, 1994, 127-139.

KOPSEN, E., and McGANN, G., 1985, A review of the hydrocarbon habitat of the Eastern and Central Barrow-Dampier Sub-basins, Western Australia. APEA Journal, 25, 154-176.

KRIEF, M., GARAT, J., STEFFINGWERFF, J., and VENTRE, J., 1990, A petrophysical interpretation using the velocities of P- and S-waves (full-waveform sonic). The Log Analyst, Nov-Dec 1990, 355-369.

LANDRO, M., BULAND, A., and D'ANGELO, R., 1995, Target-oriented AVO inversion of data from Valhall and Hod Fields. The Leading Edge, August 1995, 855-861.

LANDRO, M., HELGESEN, J., CHAPEL, F., and PICART, I., 1992, Target-oriented AVO inversion of North Sea data. SEG 62nd Annual International Meeting Expanded Abstracts.

LANGE, J.N., and ALMOGHRABI, H.A., 1988, Lithology discrimination for thin layers using wavelet signal parameters. Geophysics, 53, 1512-1519.

LEANEY, W. S., 1994, AVO and anisotropy from logs and walkaways: Expl. Geophys., **24**, 623-630.

LEMON, N.M., and MAHMOOD, T., 1994, Two and three dimensional analogue modelling of extensional faulting with application to the North West Shelf, WA. APEA Journal, 34(1), 555-565.

LEMON, N.M., and MAHMOOD, T., 1995, Atlas of 3D analogue modelling of extensional fault systems plus field applications. National Centre for Petroleum Geology and Geophysics, University of Adelaide, 111pp.

LISTER, G.S., ETHERIDGE, M.A., and SYMONDS, P.A., 1991, Detachment models for the formation of passive continental margins. Tectonics, 10, 1038-1064.

LOVIBOND, R., and RAUCH, M., 1995, AVO as an exploration tool in the Penola Trough, Otway Basin. Exploration Geophysics, 26, 448-455.

LU, H-X.L., and LINES, L., 1995, AVO and Devonian reef exploration: difficulties and possibilities. The Leading Edge, August 1995, 879-881.

MAIR, D., BERESFORD, G., and CAROLL, S., 1995, Using variations in amplitude with offset and midpoint to constrain tomographic inversion. Exploration Geophysics, 26, 444-447.

MALLICK, S., 1993, A simple approximation to the P-wave reflection coefficient and its implication in the inversion of amplitude variation with offset data. Geophysics, 58, 544-552.

MARTINEZ, R.D., 1992, Constrained seismic data processing sequence for AVO analysis including a case history. SEG 62nd Annual International Meeting Expanded Abstracts.

MARTINEZ, R.D., 1993, Wave propagation effects on amplitude variation with offset measurements: a modelling study. Geophysics, 58, 534-543.

MARTINEZ, R.D., and McMECHAN, G.A., 1991, Tau-p seismic data for viscoelastic media, part 1: modelling. Geophysical Prospecting, 39, 141-156.

MAZZOTTI, A., 1990, Prestack amplitude analysis methodology and application to seismic bright spots in the Po Valley, Italy. Geophysics, 55, 157-166.

MAZZOTTI, A., 1991, Amplitude, phase and frequency versus offset applications. Geophysical Prospecting, 39, 863-886.

MAZZOTTI, A., MELIS, A.M., RAVAGNAN, G., and BERNASCONI, G., 1994, AVO signatures of actual and synthetic reflections from different petrophysical targets. Geophysical Prospecting, 42, 463-476.

MAZZOTTI, A., and MIRRI, S., 1991, An experience in seismic amplitude processing. First Break, 9(2), 65-73.

MAZZOTTI, A., and RAVAGNAN, G., 1995, Impact of processing on the amplitude versus offset response of a marine seismic data set. Geophysical Prospecting, 43, 263-281.

MILLER, L., 1995, The sedimentary architecture of postrift depositional systems, Dampier Sub-basin, North West Shelf. Unpublished PhD Thesis, University of Adelaide.

MITCHUM, R.M., and VAIL, P.R., 1977, Seismic stratigraphy and global changes of sealevel, Part 7: Seismic stratigraphic interpretation procedure, in Payton, C.E., (ed.), Seismic Stratigraphy-applications to hydrocarbon exploration. AAPG Memoir 26, 135-143.

MURPHY, W., REISCHER, A., and HSU, K., 1993, Modulus decomposition of compressional and shear velocities in sand bodies. Geophysics, 58, 227-239.

NAZAR, B.D., and LAWTON, D.C., 1993, AVO analysis of a thin conglomerate deposit. Journal of Seismic Exploration, 2, 333-348.

NEWMAN, S., 1994, Clues to the structural history of the Rankin Trend from 3-D seismic data. In: Purcell, P.G., and Purcell, R.R. (Eds), The sedimentary basins of Western Australia. Proceedings of the PESA Symposium, Perth, 497-507.

OSTRANDER, W.J., 1984, Plane-wave reflection coefficients for gas sands at non-normal angles of incidence. Geophysics, 49, 1637-1648.

PARRY, J.C., and SMITH, D.N., 1988, The Barrow and Exmouth Sub-basins. In: Purcell, P.G. and Purcell, R.R. (Eds), The North West Shelf, Australia. Proceedings of the PESA Symposium, Perth, 1988, 129-145.

PEDDY, C.P., and SENGUPTA, M.K., 1995, AVO Analysis of high-impedance reservoirs. SEG International Exposition and 65th Annual Meeting, Houston, 1995.

PICKERING, K. T., HISCOTT, R. N., and HEIN, F. J., 1990, Deep Marine Environments: Clastic sedimentation and tectonics. Unwin Hymer, London.

PIGGOTT, J.D., SHRESTHA, R.K., and WARWICK, R.A., 1990, Direct determination of carbonate reservoir porosity and pressure from AVO inversion. SEG 60th Annual International Meeting Expanded Abstracts.

PINCHIN, J., and MITCHELL, A.B., 1991, Seismic AVO analysis of Permian gas sand at Kerna Field, Cooper Basin. Exploration Geophysics, 22, 305-308.

POWELL, D.E., 1976, The geological evolution of the continental margin off Northwest Australia. APEA Journal, 16, 13-23.

RAFIPOUR, B., and HERRIN, E., 1986, Phase offset indicator (POI): a study of phase shift versus offset and fluid content. Geophysics, 51-679-688.

RAMSDEN, C.R.T., HOBSON, M.R., and COOPER, R., 1988, The geophysicist's bane: multiple suppression on the North West Shelf. In: Purcell, P.G. and Purcell, R.R. (Eds.), The North West Shelf, Australia. Proceedings of the PESA Symposium, Perth, 55-84.

REGUEIRO, J.S., 1993, AVO analysis in low- and high-porosity gas sand reservoirs. in Castagna, J.P., and Backus, M.M. (eds), Offset-dependent reflectivity-theory and practice of AVO analysis. SEG, 238-249.

REILLY, J.M., 1994, Wireline shear and AVO modelling:applications to AVO investigations of the Tertiary, UK Central North Sea. Geophysics, 59, 1249-1260.

RESNICK, J.R., NG, P., and LARNER, K., 1987, Amplitude versus offset analysis in the presence of dip. SEG 57th Annual International Meeting Expanded Abstracts.

RICHARDS, P.G., and FRASIER, C.W., 1976, Scattering of elastic waves from depth-dependent inhomogeneities. Geophysics, 41, 441-458.

ROSS, C.P., 1992, Incomplete AVO near salt structures. Geophysics, 57, 543-553.

ROSS, C.P., 1993, AVO in the presence of coherent noise. The Leading Edge, March 1993, 196-201.

ROSS, C.P., 1995, Improved mature field development with 3D/AVO technology. First Break, 13(4), 139-145.

ROSS, C.P., and BEALE, P.L., 1994, Seismic offset balancing. Geophysics, 59, 93-101.

ROSS, M. I., and VAIL, P. R., 1994, Sequence stratigraphy of the Lower Neocomian Barrow Delta, Exmouth Plateau, Northwestern Australia. In: Purcell, P. G., and Purcell, R.R. (Eds), The sedimentary basins of Western Australia. Proceedings of the Petroleum Exploration Society of Australia Symposium, Perth, 1994, 435-455.

RUEGER, A., and TSVANKIN, I., 1995, Azimuthal variation of AVO response for fractured reservoirs. SEG International Exposition and 65th Annual Meeting, Houston, 1995.

RUTHERFORD, S.R., 1993, Noise-discriminating, statistical-amplitude compensation for AVO analysis. Geophysical, 58, 1831-1839.

RUTHERFORD, S.R., and WILLIAMS, R.H., 1989, Amplitude-versus-offset variations in gas sands. Geophysics, 54, 680-688.

RYAN-GRIGOR, S., 1996, Empirical relationships between transverse isotropy parameters and Vp/Vs: implications for AVO, Geophysics, in review.

RYAN-GRIGOR, S., and GRIFFITHS, C., 1996, An Early Cretaceous source rock in the Kendrew Terrace?, The APEA Journal, 36, in press.

RYAN-GRIGOR, S., and SCHULZ-ROJAHN, J.P., 1995, Seismic delineation of structure-controlled carbonate cement and potential economic implications, Angel Field, North West Shelf. The APEA Journal, 35, 280-295.

SAMEC, P., and BLANGY, J.P., 1992, Viscoelastic attenuation, anisotropy and AVO. Geophysics, 57, 441-450.

SANTOSO, D., HENDRAJAYA, L., WATKINS, J.S., ALAM, S., and MUNADI, S., 1995, Estimation of Parigi reservoir characteristics using seismic attributes, AVO analysis, and AVO inversion. SEG International Exposition and 65th Annual Meeting, Houston, 1995.

SAYERS, C.M., 1993, Anelliptic approximations for shales. Journal of Seismic Exploration, 2, 319-331.

SAYERS, C.M., 1994, The elastic anisotropy of shales. Journal of Geophysical Research, 99, 767-774.

SAYERS, C. M., 1995, Simplified anisotropy parameters for transversely isotropic sedimentary rocks: Geophysics, **60**, in press

SCHOENBERG, M., 1994, Transversely isotropic media equivalent to thin isotropic layers. Geophysical Prospecting, 42, 885-915.

SCHULZ-ROJAHN, J.P., RYAN-GRIGOR, S., and ANDERSON, A., 1996, The role of ascending CO_2-charged fluids along petroleum conduits: crestal, late-stage carbonate cements in clastic reservoirs of the Angel Field and Gidgealpa Field, Australia. SEPM Special Volume on Carbonate Cements in Clastic Reservoirs, in press.

SEN, J.K., and STOFFA, P.L., 1992, Genetic inversion of AVO. The Leading Edge, 11(1), 27-29.

SENGUPTA, M.K., and RENDLEMAN, C.A., 1991, Case study: the importance of gas leakage in interpreting amplitude versus offset (AVO) analysis. Geophysics, 56, 1886-1895.

SHERIFF, R.E., and GELDART, L.P., 1982, Exploration Seismology, Cambridge University Press.

SHUEY, R.T., 1985, A simplification of the Zoeppritz equations. Geophysics, 50, 609-614.

SIMMONS, J.L., and BACKUS, M., 1994, AVO modelling and the locally converted shear wave. Geophysics, 59, 1237-1248.

SMITH, G.C., and GIDLOW, P.M., 1987, Weighted stacking for rock property estimation and detection of gas. Geophysical Prospecting, 35, 993-1014.

SNYDER, A.G., and WROLSTAD, K.H., 1992, Direct detection using AVO, Central Graben, North Sea. Geophysics, 57, 313-325.

SPAGNOLINI, U., 1994, Compound events decomposition and the interaction between AVO and velocity information. Geophysical Prospecting, 42, 241-259.

SPENCE, K.W., ECCLESTONE, M.W., and YOUNG, I.M., 1992, A seismic amplitude versus offset study in the Sole area, Gippsland Basin. The APEA Journal, 265-273.

STAGG, M.J., and COLWELL, J.B., 1994—The structural foundations of the Northern Carnarvon Basin. In Purcell, P. G., and Purcell, R.R. (Eds), The sedimentary basins of Western Australia. Proceedings of the PESA Symposium, Perth, 1994, 349-364.

STEIN, A., 1994, Rankin Platform, Western Australia: Structural Development and exploration potential. In Purcell, P. G., and Purcell, R.R. (Eds), The sedimentary basins of Western Australia. Proceedings of the PESA Symposium, Perth, 1994, 349-364.

STRAHILEVITZ, R., and GARDNER, G.H.F., 1995, Fracture detection using P-wave AVO. SEG International Exposition and 65th Annual Meeting, Houston, 1995.

SWAN, H.W., 1991, Amplitude versus offset measurement errors in a finely layered medium. Geophysics, 56, 41-49.

TADEPALLI, S.V., McDONALD, J.A., SEKHARAN, K.K., and TATHAM, R.H., 1995, 3D AVO physical modelling experiment over a simulated fracture medium. SEG International Exposition and 65th Annual Meeting, Houston, 1995.

TAN, C. P., WILLOUGHBY, D. R., HILLIS, R.R., ZHOU, S., MILHAUS, H. B., and AOKI, T., 1994, Wellbore instability in the North West Shelf of Australia. APEA Journal, 34, 3-18.

THOMPSON, N.B, HOCKING, R.M., COLLINS, L.B., VOON, J.W.K., and MIDDLETON, M.F., 1990, Lower Cretaceous deposition in the southern North West Shelf. Minerals and Energy Institute of Western Australia, unpublished report 55/84.

THOMSEN, L., 1985, Biot-consistent elastic moduli of porous rocks: Low-frequency limit. Geophysics, 50, 2797-2807.

THOMSEN, L., 1986, Weak elastic anisotropy. Geophysics, **51**, 1954-1966.

TREADGOLD, G.E., RITCHIE, K., and DEY-SARKAR, S.K., 1990, AVO:an example of processing pitfalls. SEG 60th Annual International Meeting Expanded Abstracts, 1487-1490.

TSCHALENKO, J. S., 1970, Similarities between shear zones of different magnitudes. GSA Bulletin, 81, 1625-1640.

TSVANKIN, I., 1995a, Moveout analysis for transversely isotropic media with a tilted symmetry axis. SEG 65th Annual International Meeting Expanded Abstracts.

TSVANKIN, I., 1995b, Inversion of moveout velocities for horizontal transverse isotropy. SEG 65th Annual International Meeting Expanded Abstracts.

TSVANKIN, I., 1995c, Body-wave radiation patterns and AVO in transversely isotropic media. Geophysics, 60, 1409-1425.

TSVANKIN, I, and THOMSEN, L., 1994, Nonhyperbolic reflection moveout in anisotropic media: Geophysics, **59**, 1290-1304.

TSVANKIN, I., and THOMSEN, L., 1995, Inversion of reflection traveltimes for transverse isotropy. Geophysics, 60, 1095-1107.

TURA, M.A.C., and HANITZSCH, C., 1995, Influence of velocity uncertainty on AVO migration/inversion. SEG International Exposition and 65th Annual Meeting, Houston, 1995.

TURNER, B., and HEARN, S., 1995, Shear-wave splitting analysis using a single-source dynamite VSP in the Otway Basin. Exploration Geophysics, 26, 519-526.

TSINGAS, C., and KANASEWICH, E.R., 1991, Seismic reflection amplitude versus angle variation over a thermally enhanced oil recovery site. Geophysics, 56, 292-301.

URSIN, B., 1990, Offset-dependent geometrical sppreading in a layered medium. Geophysics, 55, 492-496.

URSIN, B., and DAHL, T., 1992, Seismic reflection amplitudes. Geophysical Prospecting, 40, 483-512.

URSIN, B., and EKREN, B.O., 1995, Robust AVO analysis. Geophysics, 60, 317-326.

URSIN, B., and TJAALAND, E., 1992, Information content of the elastic reflection matrix. SEG 62nd Annual International Meeting Expanded Abstracts.

UZCATEGUI, O.J., and MUJICA, D.L., 1995, Anisotropic poststack depth migration, eastern Venezuela. SEG 65th Annual International Meeting Expanded Abstracts.

VAIL, P.R., TODD, R.G., and SANGREE, J.B., 1977, Seismic stratigraphy and global changes of sea level, part 5: Chronostratigraphic significance of seismic reflections, in Payton, C.E., (ed.), Seismic Stratigraphy-applications to hydrocarbon exploration. AAPG Memoir 26, 99-116.

van den BERG, C.P., GIDLOW, P.M., DUWEKE, W.A., MULLER, B., and SMITH, G.C., 1992, AVO analysis in gold exploration: a South African case study. SEG 62nd Annual International Meeting Expanded Abstracts.

VAUGHAN, P.S., 1993, North West Shelf 3-D seismic-a decade of developments. APEA Journal, 33, 315-321.

VEENSTRA, E., 1985, Rift and drift in the Dampier sub-basin, a seismic and structural interpretation. APEA Journal, 25, 177-189.

VEEVERS, J. J., (Ed.), 1984, Phanerozoic earth history of Australia, Oxford, Clarendon.

VEEVERS, J. J., 1988, Morphotectonics of Australia's Northwestern margin - A review. In: Purcell, P.G., and Purcell, R.R. (Eds) The North West Shelf, Australia. Proceedings of the Petroleum Exploration Society of Australia Symposium, Perth, 1988, 19-27.

VERM, R.W., and HILTERMAN, F.J., 1995, Lithologic color-coded sections by AVO crossplots. Denver Geophysical Society Record, 21(2), 4-7.

VERNIK, L., AND NUR, A., 1992, Ultrasonic velocity and anisotropy of hydrocarbon source rocks: Geophysics, 57, 727-735.

VINCENT, P., AND TILBURY, L., 1988—Gas and oil fields of the Rankin Trend and northern Barrow-Dampier Sub-basin. In: Purcell, P.G., and Purcell, R.R. (Eds) The North West Shelf, Australia. Proceedings of the Petroleum Exploration Society of Australia Symposium, Perth, 1988, 341-369.

WALDEN, A.T., 1991, Making AVO sections more robust. Geophysical Prospecting, 39, 915-942.

WHITE, R., 1992, The accuracy of estimating Q from seismic data. Geophysics, 57, 1508-1511.

WIDMAIER, M.T., MULLER, T., SHAPIRO, B.A., and HUBRAL, P., 1995, Elastic P-wave AVO corrected for thin layering. SEG 65th Annual International Meeting Expanded Abstracts.

WOODSIDE OFFSHORE PETROLEUM, 1971, Angel-1 Well Completion Report Volume 1: Basic Data.

WOODSIDE OFFSHORE PETROLEUM, 1972, Angel-2 Well Completion Report Volume 1: Basic Data.

WOODSIDE OFFSHORE PETROLEUM, 1973, Angel-3 Well Completion Report Volume 1: Basic Data.

WOODSIDE OFFSHORE PETROLEUM PTY. LTD., 1988, A review of the petroleum geology and hydrocarbon prospectivity of the Barrow-Dampier sub-basin and environs. In: Purcell, P.G., and Purcell, R.R. (Eds), The North West Shelf, Australia. Proceedings of the Petroleum Exploration Society of Australia Symposium, Perth, 1988, 115-128.

WOODSIDE OFFSHORE PETROLEUM, 1989, Angel Field Petrophysical Review. Unpublished Company Report.

WOODSIDE OFFSHORE PETROLEUM, 1989b, Wanaea-1 Well Completion Report, Volume 1:Basic Data. Unpublished Company Report.

WOODSIDE OFFSHORE PETROLEUM, 1990a, A study of the present-day stress field in the Wanaea and Angel Fields. Unpublished company report.

WOODSIDE OFFSHORE PETROLEUM, 1990b, A structural study of Angel-4 cores 1-4. Unpublished company report.

WOODSIDE OFFSHORE PETROLEUM, 1990c, Angel Field 1990 Seismic Interpretation, Volume 1. Unpublished company report.

WOODSIDE OFFSHORE PETROLEUM, 1990d, Angel-4 Well Completion Report, Volume 1. Unpublished company report.

WOODSIDE OFFSHORE PETROLEUM, 1990e, Cossack-1 Well Completion Report, Volume 1: Basic Data. Unpublished Company Report.

WOODSIDE OFFSHORE PETROLEUM, 1992 Angel-4 Petrophysics. Unpublished Company Report.

WRIGHT, J., 1987, The effects of transverse isotropy on reflection amplitude versus offset: Geophysics, **52**, 564-567.

WULFF, K., 1992, Depositional history and facies analysis of the Upper Jurassic sediments in the Eastern Barrow Sub-basin. APEA Journal, 32, 104-114.

XU, GARDNER, G.H.F., and McDONALD, J.A., 1993, Some effects of velocity variation on AVO and its interpretation. Geophysics, 58, 1297-1300.

YIELDING, G., WALSH, J., and WATTERSON, J., 1992, The prediction of small-scale faulting in reservoirs. First Break, 10(12), 449-460.

YU, G., 1985, Offset-amplitude variation and controlled-amplitude processing. Geophysics, 50, 2697-2708.

APPENDIX A

Reprint of: RYAN-GRIGOR, S., and SCHULZ-ROJAHN, J.P., 1995, Seismic delineation of structure-controlled carbonate cement and potential economic implications, Angel Field, North West Shelf. The APEA Journal, 35, 280-295.

Ryan-Grigor, S., & Schulz-Rojahn, J. P. (1995). Seismic delineation of structure-controlled carbonate cement and potential economic implications, Angel Field, North West Shelf *APEA Journal, 35*(1), 280-295.